



metals

Continuous Casting

Edited by
Michael Vynnycky

Printed Edition of the Special Issue Published in *Metals*

Continuous Casting

Continuous Casting

Special Issue Editor

Michael Vynnycky

MDPI • Basel • Beijing • Wuhan • Barcelona • Belgrade



Special Issue Editor
Michael Vynnycky
University of Limerick,
Ireland

Editorial Office
MDPI
St. Alban-Anlage 66
4052 Basel, Switzerland

This is a reprint of articles from the Special Issue published online in the open access journal *Metals* (ISSN 2075-4701) from 2018 to 2019 (available at: https://www.mdpi.com/journal/metals/special_issues/continuous_casting)

For citation purposes, cite each article independently as indicated on the article page online and as indicated below:

LastName, A.A.; LastName, B.B.; LastName, C.C. Article Title. <i>Journal Name</i> Year , Article Number, Page Range.

ISBN 978-3-03921-321-4 (Pbk)

ISBN 978-3-03921-322-1 (PDF)

© 2019 by the authors. Articles in this book are Open Access and distributed under the Creative Commons Attribution (CC BY) license, which allows users to download, copy and build upon published articles, as long as the author and publisher are properly credited, which ensures maximum dissemination and a wider impact of our publications.

The book as a whole is distributed by MDPI under the terms and conditions of the Creative Commons license CC BY-NC-ND.

Contents

About the Special Issue Editor	vii
Michael Vynnycky Continuous Casting Reprinted from: <i>Metals</i> 2019 , 9, 643, doi:10.3390/met9060643	1
Seong-Mook Cho and Brian G. Thomas Electromagnetic Forces in Continuous Casting of Steel Slabs Reprinted from: <i>Metals</i> 2019 , 9, 471, doi:10.3390/met9040471	4
Jun Huang, Zhigang Yuan, Shaoyuan Shi, Baofeng Wang and Chi Liu Flow Characteristics for Two-Strand Tundish in Continuous Slab Casting Using PIV Reprinted from: <i>Metals</i> 2019 , 9, 239, doi:10.3390/met9020239	42
Zhufeng Lei and Wenbin Su Research and Application of a Rolling Gap Prediction Model in Continuous Casting Reprinted from: <i>Metals</i> 2019 , 9, 380, doi:10.3390/met9030380	52
Mujun Long, Huabiao Chen, Dengfu Chen, Sheng Yu, Bin Liang and Huamei Duan A Combined Hybrid 3-D/2-D Model for Flow and Solidification Prediction during Slab Continuous Casting Reprinted from: <i>Metals</i> 2018 , 8, 182, doi:10.3390/met8030182	66
Peiyuan Ni, Mikael Ersson, Lage Tord Ingemar Jonsson, Ting-an Zhang and Pär Göran JÖNSSON Numerical Study on the Influence of a Swirling Flow Tundish on Multiphase Flow and Heat Transfer in Mold Reprinted from: <i>Metals</i> 2018 , 8, 368, doi:10.3390/met8050368	76
Qin Qin, Ming Li and Jianlin Huang Analysis of the Influence of Segmented Rollers on Slab Bulge Deformation Reprinted from: <i>Metals</i> 2019 , 9, 231, doi:10.3390/met9020231	98
Xufeng Qin, Changgui Cheng, Yang Li, Chunming Zhang, Jinlei Zhang and Yan Jin A Simulation Study on the Flow Behavior of Liquid Steel in Tundish with Annular Argon Blowing in the Upper Nozzle Reprinted from: <i>Metals</i> 2019 , 9, 225, doi:10.3390/met9020225	116
Bingzhi Ren, Dengfu Chen, Wentang Xia, Hongdan Wang and Zhiwei Han Numerical Simulation of Electromagnetic Field in Round Bloom Continuous Casting with Final Electromagnetic Stirring Reprinted from: <i>Metals</i> 2018 , 8, 903, doi:10.3390/met8110903	132
Wenbin Su, Zhufeng Lei, Ladao Yang and Qiao Hu Mold-Level Prediction for Continuous Casting Using VMD–SVR Reprinted from: <i>Metals</i> 2019 , 9, 458, doi:10.3390/met9040458	142
Yanbin Yin, Jiongming Zhang, Qipeng Dong and Yuanyuan Li Modelling on Inclusion Motion and Entrapment during the Full Solidification in Curved Billet Caster Reprinted from: <i>Metals</i> 2018 , 8, 320, doi:10.3390/met8050320	157

Yazhu Zhang, Zhi Wen, Zengwu Zhao, Chunbao Bi, Yaxiang Guo and Jun Huang Laboratory Experimental Setup and Research on Heat Transfer Characteristics during Secondary Cooling in Continuous Casting Reprinted from: <i>Metals</i> 2019 , 9, 61, doi:10.3390/met9010061	172
Tihe Zhou, Ronald J. O'Malley, Hatem S. Zurob, Mani Subramanian, Sang-Hyun Cho and Peng Zhang Control of Upstream Austenite Grain Coarsening during the Thin-Slab Cast Direct-Rolling (TSCDR) Process Reprinted from: <i>Metals</i> 2019 , 9, 158, doi:10.3390/met9020158	185
Gaiyan Yang, Liguang Zhu, Wei Chen, Gaoxiang Guo and Baomin He Simulation of Crack Initiation and Propagation in the Crystals of a Beam Blank Reprinted from: <i>Metals</i> 2018 , 8, 905, doi:10.3390/met8110905	203
Michael Vynnycky Applied Mathematical Modelling of Continuous Casting Processes: A Review Reprinted from: <i>Metals</i> 2018 , 8, 928, doi:10.3390/met8110928	218

About the Special Issue Editor

Michael Vynnycky is a Professor of Applied Mathematics in the Department of Mathematics and Statistics at the University of Limerick in Limerick, Ireland. He holds a D. Phil. in Applied Mathematics from Oxford University in the U.K., and has previously held research posts at Tohoku National Industrial Research Institute in Sendai, Japan, at the KTH Royal Institute of Technology in Stockholm, Sweden, and at the University of São Paulo in São Carlos, Brazil. His primary research interests lie in the deterministic mathematical modelling of natural and industrial processes, involving the use of asymptotic and numerical methods. He is the author of around 110 peer-reviewed journal publications and over 20 reviewed papers in international conference proceedings.

Continuous Casting

Michael Vynnycky ^{1,2}

¹ Department of Materials Science and Engineering, The Royal Institute of Technology (KTH), Brinellvägen 23, 100 44 Stockholm, Sweden; michaelv@kth.se

² Department of Mathematics and Statistics, University of Limerick, Limerick V94 T9PX, Ireland; michael.vynnycky@ul.ie; Tel.: +353-61-213199

Received: 29 May 2019; Accepted: 31 May 2019; Published: 3 June 2019

1. Introduction and Scope

Continuous casting is a process whereby molten metal is solidified into a semi-finished billet, bloom, or slab for subsequent rolling in finishing mills; it is the most frequently used process to cast not only steel, but also aluminum and copper alloys. Since its widespread introduction for steel in the 1950s, it has evolved to achieve improved yield, quality, productivity, and cost efficiency. It allows lower-cost production of metal sections with better quality, due to the inherently lower costs of continuous, standardized production of a product, as well as providing increased control over the process through automation. Nevertheless, challenges remain and new ones appear, as methods are sought to minimize casting defects and to cast alloys that could originally only be cast via other means. This Special Issue covers a wide scope in the research field of continuous casting.

2. Contributions

Fourteen research articles have been published in this Special Issue of *Metals*. Twelve of these [1–12] relate to the continuous casting of steel, a general schematic for which is shown in Figure 1. As is evident from this figure, the overall process consists of a ladle and a tundish through which molten steel passes, a cooling mould region where solidification starts and at which electromagnetic stirring (EMS) may be applied, secondary cooling regions where water is sprayed on the solidified steel, a so-called strand electromagnetic stirrer, a further region at which final EMS is applied, and withdrawal rollers, by which point the steel has completely solidified. In addition, Figure 2 shows which stage of the continuous casting process each of the articles has focused on.

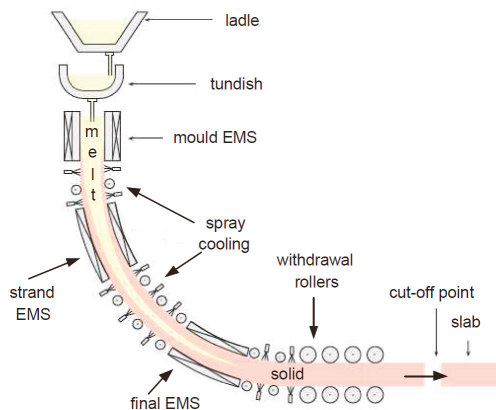


Figure 1. Schematic for the continuous casting of steel.

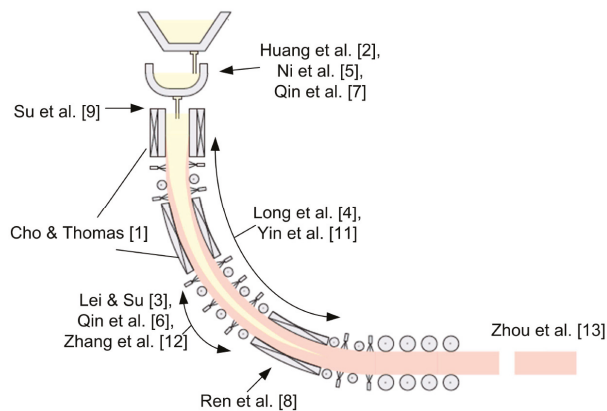


Figure 2. Schematic relating the articles in this special issue to the continuous casting of steel.

Commencing from the start of the process and working downwards [2,5,7], it is important to consider flow in the tundish. Huang et al. [2] use particle image velocimetry (PIV) and numerical simulation to investigate the flow characteristics for a two-strand tundish in continuous slab casting. On the other hand, Ni et al. [5] present a numerical study on the influence of a swirling flow tundish on multiphase flow and heat transfer in the mould, whereas Qin et al. [7] conduct a simulation study on the flow behavior of liquid steel in a tundish with annular argon blowing in the upper nozzle. Su et al. [9] use machine-learning techniques for mold-level prediction by means of variational mode decomposition and support vector regression (VMD–SVR), whereas Cho and Thomas [1] review the literature on electromagnetic forces in continuous casting of steel slabs. Yin et al. [10] consider modelling on inclusion motion and entrapment during full solidification in a curved billet caster, while Long et al. [4] develop a combined hybrid 3-D/2-D model for flow and solidification prediction during slab continuous casting. Qin et al. [6] perform an analysis of the influence of segmented rollers on slab bulge deformation, while Lei and Su [3] use machine learning in the research and application of a rolling gap prediction model. Zhang et al. [11] devise a laboratory experimental setup and consider heat transfer characteristics during secondary cooling, whereas Ren et al. [8] carry out numerical simulations of the electromagnetic field in round bloom continuous casting with final electromagnetic stirring. Zhou et al. [12] consider control of upstream austenite grain coarsening during the thin-slab cast direct-rolling (TSCDR) process, after complete solidification has occurred.

Aside from all of the above, Yang et al. [13] simulate crack initiation and propagation in the crystals of a continuously-cast beam blank, whereas Vynnycky [14] gives a review of applied mathematical modelling of continuous casting; this considers a hybrid of analytical and numerical modelling with an emphasis on the use of asymptotic techniques, and gives examples of problems not only in the continuous casting of steel, but also that of copper and aluminum alloys.

3. Conclusions and Outlook

A variety of topics have composed this Special Issue, presenting recent developments in continuous casting. Nevertheless, there are still many challenges to overcome in this research field and applications still need to be more widespread. As a Guest Editor, I hope that all of the scientific results in this Special Issue contribute to the advancement and future developments of research on continuous casting.

Finally, I would like to thank all reviewers for their invaluable efforts to improve the academic quality of published research in this Special Issue. I would also like to give special thanks to all staff at the Metals Editorial Office, especially to Toliver Guo, Assistant Editor, who managed and facilitated the publication process.

Conflicts of Interest: The author declares no conflicts of interest.

References

1. Cho, S.M.; Thomas, B.G. Electromagnetic forces in continuous casting of steel slabs. *Metals* **2019**, *7*, 471. [[CrossRef](#)]
2. Huang, J.; Yuan, Z.; Shi, S.; Wang, B.; Liu, C. Flow characteristics for two-strand tundish in continuous slab casting using PIV. *Metals* **2019**, *9*, 239. [[CrossRef](#)]
3. Lei, Z.; Su, W. Research and application of a rolling gap prediction model in continuous casting. *Metals* **2019**, *9*, 380. [[CrossRef](#)]
4. Long, M.; Chen, H.; Chen, D.; Yu, S.; Liang, B.; Duan, H. A combined hybrid 3-D/2-D model for flow and solidification prediction during slab continuous casting. *Metals* **2018**, *8*, 182. [[CrossRef](#)]
5. Ni, P.; Ersson, M.; Jonsson, L.T.I.; Zhang, T.; Jonsson, P.G. Numerical study on the influence of a swirling flow tundish on multiphase flow and heat transfer in mold. *Metals* **2018**, *8*, 368. [[CrossRef](#)]
6. Qin, Q.; Li, M.; Huang, J. Analysis of the influence of segmented rollers on slab bulge deformation. *Metals* **2019**, *9*, 231. [[CrossRef](#)]
7. Qin, X.; Cheng, C.; Li, Y.; Zhang, C.; Zhang, J.; Jin, Y. A simulation study on the flow behavior of liquid steel in tundish with annular argon blowing in the upper nozzle. *Metals* **2019**, *9*, 225. [[CrossRef](#)]
8. Ren, B.; Chen, D.; Xia, W.; Wang, H.; Han, Z. Numerical simulation of electromagnetic field in round bloom continuous casting with final electromagnetic stirring. *Metals* **2018**, *8*, 903. [[CrossRef](#)]
9. Su, W.; Lei, Z.; Yang, L.; Hu, Q. Mold-level prediction for continuous casting using VMD–SVR. *Metals* **2019**, *9*, 458. [[CrossRef](#)]
10. Yin, Y.; Zhang, J.; Dong, Q.; Li, Y. Modelling on inclusion motion and entrapment during the full solidification in curved billet caster. *Metals* **2018**, *8*, 320. [[CrossRef](#)]
11. Zhang, Y.; Wen, Z.; Zhao, Z.; Bi, C.; Guo, Y.; Huang, J. Laboratory experimental setup and research on heat transfer characteristics during secondary cooling in continuous casting. *Metals* **2019**, *9*, 61. [[CrossRef](#)]
12. Zhou, T.; O'Malley, R.J.; Zurob, H.S.; Subramanian, M.; Cho, S.H.; Zhang, P. Control of upstream austenite grain coarsening during the thin-slab cast direct-rolling (TSCDR) process. *Metals* **2019**, *9*, 158. [[CrossRef](#)]
13. Yang, G.; Zhu, L.; Chen, W.; Guo, G.; He, B. Simulation of crack initiation and propagation in the crystals of a beam blank. *Metals* **2018**, *8*, 905. [[CrossRef](#)]
14. Vynnycky, M. Applied mathematical modelling of continuous casting processes: A review. *Metals* **2018**, *8*, 928. [[CrossRef](#)]



© 2019 by the author. Licensee MDPI, Basel, Switzerland. This article is an open access article distributed under the terms and conditions of the Creative Commons Attribution (CC BY) license (<http://creativecommons.org/licenses/by/4.0/>).

Review

Electromagnetic Forces in Continuous Casting of Steel Slabs

Seong-Mook Cho¹ and Brian G. Thomas^{1,2,*}

¹ Department of Mechanical Engineering, Colorado School of Mines, 1610 Illinois Street, Golden, CO 80401, USA; seongmookcho1@mines.edu

² Department of Mechanical Science and Engineering, University of Illinois at Urbana-Champaign, 1206 West Green Street, Urbana, IL 61801, USA

* Correspondence: bgthomas@mines.edu; Tel.: +1-303-273-3309

Received: 23 March 2019; Accepted: 20 April 2019; Published: 23 April 2019

Abstract: This paper reviews the current state of the art in the application of electromagnetic forces to control fluid flow to improve quality in continuous casting of steel slabs. Many product defects are controlled by flow-related phenomena in the mold region, such as slag entrapment due to excessive surface velocity and level fluctuations, meniscus hook defects due to insufficient transport of flow and superheat to the meniscus region, and particle entrapment into the solidification front, which depends on transverse flow across the dendritic interface. Fluid flow also affects heat transfer, solidification, and solute transport, which greatly affect grain structure and internal quality of final steel products. Various electromagnetic systems can affect flow, including static magnetic fields and traveling fields which actively accelerate, slow down, or stir the flow in the mold or strand regions. Optimal electromagnetic effects to control flow depends greatly on the caster geometry and other operating conditions. Previous works on how to operate electromagnetic systems to reduce defects are discussed based on results from plant experiments, validated computational models, and lab scale model experiments.

Keywords: magnetohydrodynamics; fluid flow; bubbles; inclusions; entrapment; entrainment; heat transfer; solidification; slab mold; continuous casting

1. Introduction

Continuous casting is the dominant process to manufacture steel, producing over 96% of steel in the world [1]. Thus, even small improvements to this process can have great impact. During solidification of molten steel, many complex phenomena arise, including multiphase fluid flow, particle transport and capture, heat transfer, solidification, and solute redistribution, which are strongly interrelated and can affect various surface and internal defects if process parameters are not controlled within optimal ranges for a given caster. In the mold region, where initial solidification occurs, fluid flow greatly affects steel surface quality, according to surface turbulence, flow instability, transport and capture of argon bubbles and inclusions, superheat transport, and meniscus solidification. In addition, steel internal quality depends greatly on heat transfer, solidification, and solute and dissolved gas transport, which affect segregation, porosity, and microstructure formation in the strand region of the process. These phenomena must be controlled within acceptable process windows to avoid defects and achieve ideal grain structure, and solute distribution.

Many efforts have been made to control fluid flow in the mold, which is responsible for many surface and internal defects in steel slab casting [2–4]. To control the mold flow pattern and reduce surface instability in the mold, the effects of nozzle geometry including port shape [5–7], size [5], angle [5,8–10], bottom design [5,11], and the flow control system [12] (stopper rod vs. slide gate) have been investigated. Other studies have investigated casting conditions including casting speed [13],

argon gas injection [14–16], and nozzle submergence depth [17]. The effects of soft reduction on center segregation [18] and porosity [18,19] in the strand has been investigated to improve internal quality. Together with these process parameters, the application of electromagnetic (EM) forces is an attractive method to control phenomena related to fluid flow because the induced forces intrinsically adjust to molten steel flow variations, and field strength has the potential to be adjusted during operation. Thus, understanding and optimizing the effects of electromagnetic forces on the various continuous casting phenomena offer an important way to maintain quality and increase production for a given caster.

Tools to quantify the effects of electromagnetic forces on continuous casting phenomena include plant measurements, lab scale modeling with low melting temperature alloys, and computational modeling. In particular, computational models validated with plant data are a powerful methodology to understand the phenomena and to suggest practical strategies to optimize the operation of electromagnetic systems [20–23].

Various types of the electromagnetic systems have been developed and implemented into commercial slab casters to apply static and/or traveling magnetic fields to control fluid flow, particle transport and capture, heat transfer, and solidification during the continuous casting of steel slabs. Static magnetic fields have been widely applied as Electromagnetic Braking (EMBr) systems, including local, single-ruler, and double-ruler systems. These EMBr systems were invented to maintain a double-roll flow pattern [16] and to stabilize the fluid flow, especially at high casting speed. Local EMBr fields tend to slow down jet flow as it passes through a circular-shaped field region through the mold thickness [24], as shown in Figure 1a. Single-ruler EMBr (Figure 1b) produces a horizontal rectangular-shaped field across the entire mold width [25]. Placing the ruler above the nozzle tends to slow down surface flow and lessens surface turbulence [26]. Alternatively, positioning the ruler below the nozzle tends to deflect the jet upwards to accelerate surface flow [27–29] and also lessens mixing of the upper and lower zones, which is important during the casting of clad steel slabs [30]. Double-ruler EMBr (Figure 1c), also called Flow Control Mold (FC-Mold) [24], generates two horizontal static fields across the mold width, one above and one below the nozzle ports. Adjusting the relative strengths of the upper and lower fields enables more control of the flow field. To enable further adjustment of the static field, Multi-Mode Electromagnetic Brake (MM-EMB) has recently been developed, which aims to brake, dampen, and stabilize the flow in thin-slab casting molds [31]. Specifically, MM-EMB employs different combinations of five local static magnets: three aligned horizontally below the nozzle (one central and two near narrow faces) and two aligned above the nozzle (near narrow faces) [31].

Moving magnetic fields have been developed to control mold flow more actively than the EMBr systems. This is achieved using alternating current (AC) through a set of magnetics with increasing phase-shift, to achieve apparent motion of the magnetic field near each of the two wide faces of the mold. Four sets of magnets are installed two on each wide face, as shown in Figure 1d, and can generate three different moving fields: Electromagnetic Level Stabilizer (EMLS) which moves the fields toward the nozzle for slowing the jet; Electromagnetic Level Accelerator (EMLA), which moves the fields toward the narrow faces for accelerating the jet; and Electromagnetic Rotating Stirrer (EMRS) [32,33], also called Electromagnetic Stirring (EMS) in the Mold (M-EMS) [34,35], which move the fields in opposite directions across each wide face, for horizontally-rotating the flow around the perimeter of the mold. Alternatively, another moving field system, called Electromagnetic Casting (EMC), creates vertical rotating fields near the meniscus in the mold, to reduce oscillation mark depth and hook formation [36–38]. These fields can be set according to standard operating conditions, or adjusted continuously according to current conditions. Adjustments to the mode, moving (phase-shift) velocities, and field strengths can be accomplished manually by operators or automatically adjusted in real time, based on available plant conditions, potentially monitored with real-time sensors [32,39].

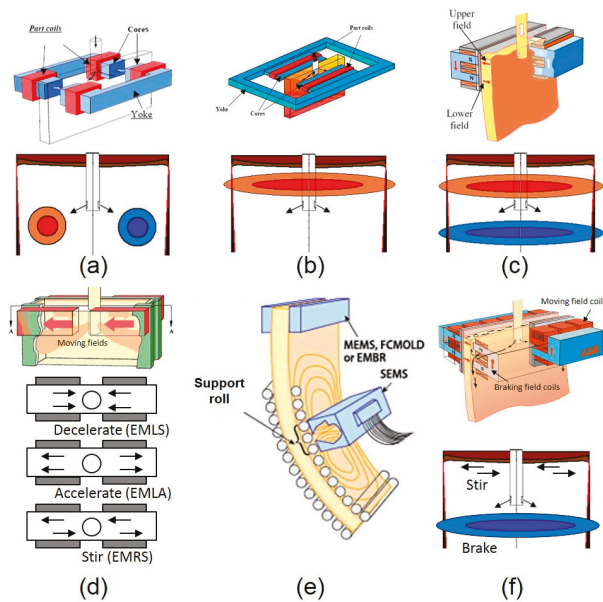


Figure 1. Types of electromagnetic systems showing hardware and field shape: (a) local Electromagnetic Braking (EMBr), (b) single-ruler EMBr, (c) double-ruler EMBr, (d) Electromagnetic Level Stabilizer (EMLS), Electromagnetic Level Accelerator (EMLA), and Electromagnetic Rotating Stirrer (EMRS) moving field systems, (e) Strand EMS (SEMS), and (f) combined fields system.

Below the mold, Strand EMS (SEMS) (Figure 1e), generates a horizontally traveling magnetic field towards one narrow face, by employing one or several box-type (behind the rolls) or in roll-type stirrers including magnets, on one or both of the strand wide faces. This slab-casting SEMS differs from S-EMS in bloom and billet casting, which can have either horizontal rotating magnetic fields around the strand perimeter as with M-EMS [33,40] or longitudinal moving fields that produce recirculating flow in the vertical plane through the strand thickness [41]. The slab-casting SEMS produces vertical recirculating flow regions across the strand width, both above and below the SEMS field region [33,40–47], which aims to control heat transfer and solidification/nucleation phenomena, to increase equiaxed grains and to reduce segregation and porosity [33,42,43].

Finally, a combined system, called FC 3rd generation system (FC3) [48], has recently been developed which combines traveling and static field systems together. An upper traveling field system similar to EMSR is applied above the nozzle ports designed to wash away particles from the meniscus region and make superheat more uniform [48]. A lower static field EMBr single-ruler system is applied below the nozzle ports, designed to lessen particle penetration deep into the mold cavity as shown in Figure 1f. Alternatively, EMC has been combined with single-ruler EMBr, to reduce both oscillation marks at the surface, and particle capture into the steel shell low in the strand [49]. With so much ability to customize the electromagnetic fields, there is a great need to understand how these systems affect fluid flow and steel quality. This has stimulated significant research over the past three decades, which is reviewed in this paper.

This paper first reviews the various research tools available to quantify the effects of electromagnetic forces on continuous steel slab casting, which include plant measurements, lab scale model experiments, and computational modeling. It then reviews current understanding of how each available electromagnetic field system affects important phenomena during slab casting, including fluid flow, surface instability, superheat transport, initial solidification, particle transport and capture, grain

structure and internal quality, and steel composition distribution during the casting of steel slabs. Based on these findings, some practical strategies are offered on how to operate electromagnetic systems to reduce defect formation and to improve the quality of the steel product.

2. Tools to Quantify Electromagnetic Effects

To understand and optimize the use of electromagnetic forces to control fluid flow and the associated complex phenomena that affect steel quality in continuous casting, previous researchers have employed several different tools: plant measurements, lab scale modeling, and computational modeling. The plant measurement method is an essential tool to quantify fundamental phenomena in the real commercial process, to validate computational modeling predictions, and to test potential improvements in practice. However, plant measurements have many limitations, owing to the harsh environment of continuous casting and the difficulty of controlling conditions to conduct controlled experiments. Lab scale physical modeling using water is difficult because electromagnetic field effects cannot be accurately mimicked. Physical modeling with low melting alloys can provide important insights into the fundamental phenomena, owing to better flow visualization methods, and better control of the process parameters related to defect formation. However, this method has its own limitations, and it can be difficult to extrapolate the results of lab experiments to the real process. Thus, the best way to investigate how electromagnetic forces should be applied in continuous casting is to develop fundamental computational models of the phenomena, to validate them via both plant measurements and lab scale model experiments, to conduct parametric modeling studies to predict optimal operations based on fundamental understanding, and finally, to test the suggested improvements in the real caster, based on long-term plant measurements to gain reliable statistical evidence.

2.1. Plant Measurements of Fluid Flow Velocity

Fluid flow velocity must be accurately measured to quantify the average mold flow pattern, and velocity fluctuations, especially at the meniscus region where defects can be generated. Methods to measure the flow of molten steel focus on velocity near the top surface in the mold, and include strain gauge, paddle-rod, and nail dipping tests. Indirect measurements of subsurface velocities include electromagnetic Mold Flow Control (MFC) sensors and dendrite angle measurements.

2.1.1. Strain Gauge Rod Tests

Dipping a refractory rod equipped with a strain gauge through the slag steel interface into the molten steel can be used to measure velocity near the top surface in the mold in two ways. Firstly, the average velocity near the top surface depends on the measured torque, which can be related to the drag force applied by the steel moving past the rod, averaged over time and length of the rod [39,50]. The Submeniscus Velocity Control (SVC) device is an example commercial implementation of this method [51]. Secondly, a more sophisticated method is to measure the shedding frequency of the Kármán vortices forming behind the rod, based on the frequency of the time-varying deflections, [52–54] as shown in Figure 2a. The vortex shedding frequency increases linearly with the fluid velocity around the rod. This method has been used to measure surface velocity from 0.05 to 0.7 m/s, which covers the range of interest in slab casting [53]. In both methods, the refractory rod should not be affected by the magnetic field or the high temperature, so should be made from an insulating, thermal shock-resistant material such as a ZrO₂ coated Mo rod [39].

2.1.2. Paddle Rod Tests

Another method to measure flow velocity and direction near the mold top surface by dipping a refractory rod, into the top surface of the molten steel pool is the paddle rod test [55–57]. As shown in Figure 2b, one end of the rod is connected to a pivot and the other end is dipped into the molten steel pool. As the molten steel flow just near the surface impinges on and pushes the rod, it rotates around

the pivot. The angle produced depends on a balance between the drag force exerted by the steel flow and the weight of the rod, which can be related to submeniscus velocity of the molten steel.

2.1.3. Nail Dipping Tests

Nail dipping tests are commonly used to quantify mold surface velocity and level due to its convenience and efficiency. This method was introduced to measure surface level profile and liquid slag layer thickness [58,59], and then extended to estimate surface velocity [60–64]. One or more stainless steel nails are immersed into the molten steel pool for a short time (~2–3 s) and removed. To quantify surface velocity, the shape of the solidified steel lump on the nail is measured shown in Figure 2c. The surface velocity is estimated according to [62]

$$U_{surface} = 0.624(\varphi_{lump})^{-0.696}(h_{lump})^{0.567} \quad (1)$$

where φ_{lump} is the diameter of the lump solidified on the stainless steel nail and h_{lump} is the height difference built up by the flow. In addition, dipping several different nails at different times enables to quantifying transient variations of the surface velocity. The nail dipping test method shows good ability to detect surface velocity variations due to changes in casting speed, and a reasonable match with SVC measurements in a real caster [62], as shown in Figure 3.

2.1.4. Electromagnetic Mold Flow Control (MFC) Sensor Measurements

The electromagnetic MFC sensor, developed by AMEPA GmbH [65], consists of a permanent magnet and pair of highly sensitive current detectors mounted behind a copper mold plate as shown in Figure 2d for the wide face. The time delay for steel flow variations to travel between the two detectors is evaluated from the measured variations in the induced current, which is generated in proportion to the local velocity of the conducting molten steel traveling through the magnetic field [66]. The time-dependent spatially-averaged velocity near the solidification front in that region of the mold is then output knowing the distance between the two detectors. The method only works in regions where the steel generally flows across the solidification front from one sensor to the other, so the sensors should be positioned at reliable locations, such as near the meniscus between the Submerged Entry Nozzle (SEN) and Narrow Face (NF) in the Wide Face (WF) mold, or perhaps vertically in the NF mold [65,67].

2.1.5. Columnar Dendrite Angle Measurements

The tangential velocity of the molten steel across the solidification front can be estimated from the angle of the columnar dendrite growth direction [68–70]. As solute is washed away from the upstream side of the dendrites, they grow towards (into) the direction of the molten steel flow [69,70]. The angle of the columnar dendrites relative to the growth direction perpendicular to the strand surface increases in direct proportion to the liquid velocity, up to ~0.3 m/s [70], with further increases showing only minor effects. This indirect method enables velocity to be measured deep into the mold cavity and strand regions, where other measurement methods are not available due to the harsh environment. This method is costly as it requires microscopy on solidified slab samples [69] and may also need calibration.

2.1.6. Other Methods

Several other methods have great potential to measure velocity magnitude and/or direction of the liquid metal. One method, which has been demonstrated in laboratory tests with nonferrous alloys, is to immerse a steel sphere into the molten steel, and then measure the melting time with embedded wire(s) [71,72]. The melting rate increases with velocity, so the decrease in time to melt the sphere correlates with the flow velocity. In addition, other methods include photographic methods, reaction probes, tracer methods, electromagnetic probes, hot wire and hot film methods, dissolution methods, and fiber optic sensor measurements, which are all reviewed elsewhere [73].

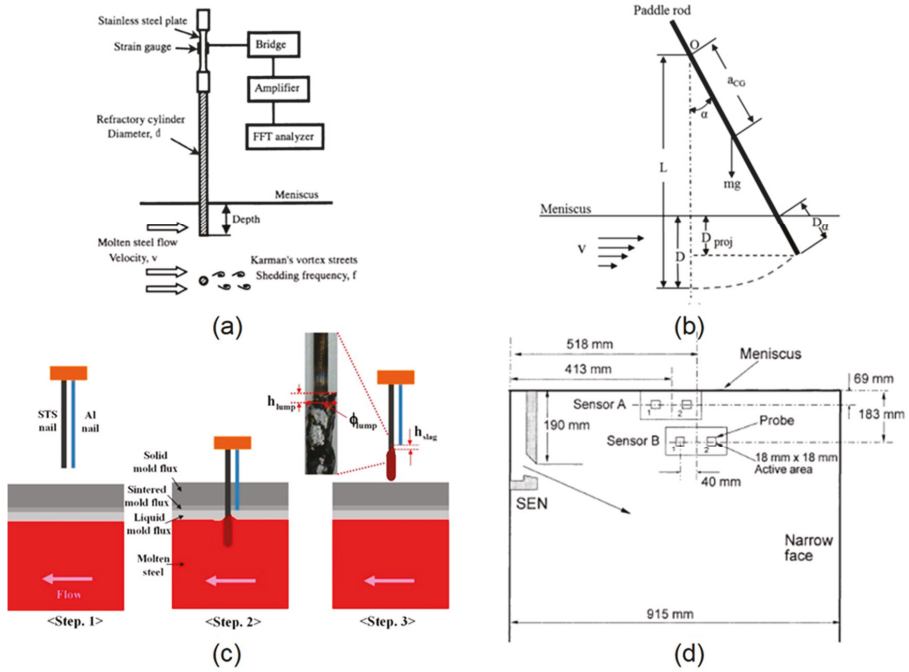


Figure 2. Plant flow–velocity measurements: (a) strain gauge test [52], (b) paddle rod test [55], (c) nail dipping method [64], and (d) electromagnetic mold flow control (MFC) test [66].

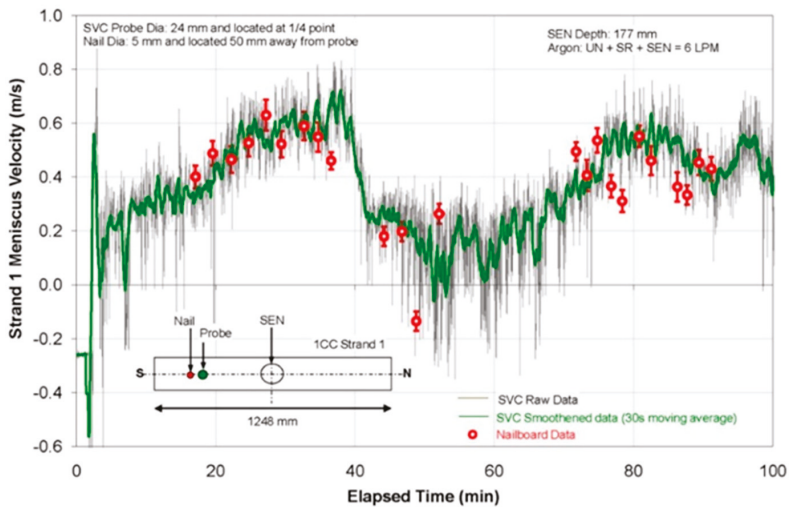


Figure 3. Comparison of surface velocity history between submeniscus velocity control (SVC) and nail dipping measurements [62].

2.2. Plant Measurements of Surface Level Profile and Fluctuations

Measurements of the surface level profile and its fluctuations are needed to understand transient phenomena related to surface defect formation. Especially, surface level fluctuations near the meniscus

are known to cause slag entrapment during initial solidification [74]. Thus, it is important to accurately measure and control the surface level during continuous casting. Eddy current sensors are widely used to measure surface level for real-time control in the plant. Other methods to measure the surface level profile include nail board, sheet dipping, and oscillation mark measurements.

2.2.1. Eddy Current Sensor Measurements

In most casters, one eddy current sensor is located above the mold top surface to detect the transient surface level, which is sent to a flow controller (stopper rod or slide gate), to control the steel flow rate. This method is also the most common way to quantify level fluctuations. However, for best control of flow rate, it is best to measure the average liquid level, which is achieved by filtering the signal to remove high-frequency level variations produced by natural turbulence which cannot be controlled, and by placing the sensor above the most stable region (such as the quarter region in the mold with a double-roll flow pattern) [60]. Thus, this measurement underestimates the level fluctuations, especially near the narrow faces and SEN, which tend to be more severe. Moreover, level fluctuations in these regions are more important to quality problems such as deep meniscus hooks, owing to the lower molten steel temperature [56]. Thus, to measure the surface level profile, it is better to keep one sensor at the most stable location (1/4 mold width) for the flow controller and to add other sensors near the narrow faces to monitor the surface level variations [75].

2.2.2. Nail Board Tests

In addition to surface velocity described in Section 2.1.3, nail dipping can also be used to measure the surface profile and its variations by using sets of “nail boards”, which are made by attaching several nails to a wood or metal board [60,64]. After dipping and removing each board, an instantaneous surface profile is made by comparing the relative heights of the steel lumps solidified on the nails [60,64]. By dipping several nail boards, transient variations of the surface profile are quantified and the surface fluctuations are calculated [60,64]. Nail dipping can also be used to measure liquid mold–flux layer thickness by adding an aluminum wire beside each stainless steel nail [59,64]. Due to the aluminum melting temperature lower than the mold flux melting temperature, the height difference between the steel lump and the aluminum wire end, h_{slag} correlated with the liquid mold–flux layer thickness as shown in Figure 2c. The slag layer thickness can also be revealed by the location of the colored bands of scale that form on each nail [76].

2.2.3. Sheet Dipping Tests

Dipping a thin sheet of steel into the top surface is an alternative method to nail boards to determine the profile of the liquid mold flux/molten steel interface. Time averages and standard deviations of the transient interface profiles, revealed by serial dipping of the sheets, are useful to validate transient computational model predictions [77].

2.2.4. Oscillation Mark Measurements

Partial overflow and freezing of the molten steel over the meniscus produces an oscillation mark during each mold oscillation cycle. The oscillation mark appears as a small transverse depression in the surface of the solidified steel slab. Thus, each mark represents the instantaneous profile of the interface between the liquid mold flux and molten steel around the mold perimeter at the time it formed. Tracing and graphing a series of oscillation marks accurately reveals the transient liquid mold flux/molten steel interface profiles, such as shown in Figure 4a. These measured profiles can be used to validate computational models of time-dependent (Figure 4b) meniscus level profiles and their fluctuations [61].

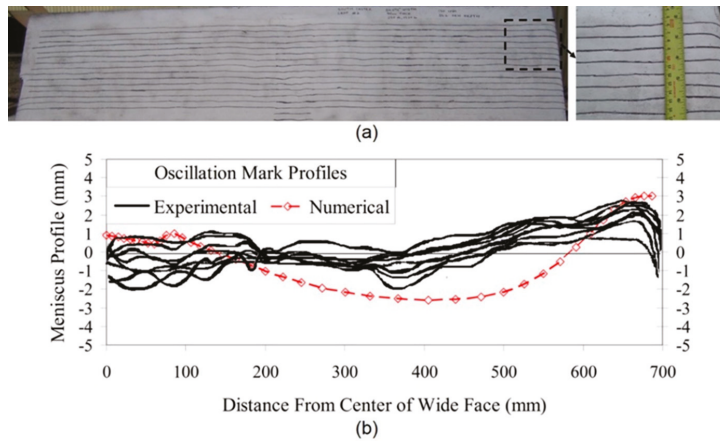


Figure 4. (a) Measurements and (b) model validation of oscillation mark profiles on steel slab surface [61].

2.3. Plant Measurements of Particle Capture

Particles, including argon bubbles, alumina, and slag inclusions, can be entrapped by the solidifying steel shell during continuous casting, and are greatly affected by the flow pattern, and EM effects. This results in surface and/or internal defects on the final steel products. Thus, it is important to quantify particle capture defects in as-cast steel slabs. Many different measurement methods are available, including ultrasonic testing, step milling, and other methods which are reviewed elsewhere [78].

2.3.1. Ultrasonic Testing (UT) Measurements

The locations of particles entrapped by the steel shell, can be measured in a steel slab in width, length, and depth directions, by using an ultrasonic detection system [79,80]. Recently, the dead zone, which is produced by reflected waves on the outer surface of the steel slab, has been reduced by using a V-shaped receiving probe and transmitting probe system with acoustic shielding between the probes [79]. This enables the detection of captured particles from 2 to 10 mm beneath the slab outer surface [79].

2.3.2. Step Milling Measurements

Step milling followed by microscopy, with automated surface scanning for particles, such as the ASPEX system [81], is a useful method to quantify both the location and size of particles captured into the solidifying steel shell [82]. Samples are cut from wide and narrow faces of an as-cast steel slab. The outer surface of each sample is milled away layer by layer, using an optical microscope to find and examine each particle observed on each exposed surface and recording the size and location of each particle. This procedure has been used to measure inclusions in slab samples in previous work [82,83], such as shown in Figure 5. Compared to the UT method, the step milling method is more difficult and expensive; but, step milling can quantify further details of the captured particles such as their shape and composition, in addition to their size and location.

2.3.3. Other Methods to Measure Particle Capture

Many other methods to measure size distribution, morphology, and composition of non-metallic oxide inclusions in the molten steel have been developed as reviewed elsewhere [78]. Direct methods include section method, volume method, extraction, and liquid evaluation methods. Section methods

include Metallographic Microscope Observation (MMO), Image Analysis (IA), Sulfur Print, Scanning Electron Microscopy (SEM), Optical Emission Spectrometry with Pulse Discrimination Analysis (OES-PDA), Laser Microprobe Mass Spectrometry (LAMMS), X-ray Photoelectron Spectroscopy (XPS), and Auger Electron Spectroscopy (AES). Volume methods include Conventional Ultrasonic Scanning (CUS), Mannesmann Inclusion Detection by Analysis Surfboards (MIDAS), Scanning Acoustic Microscope (SAM), X-ray Detection, Slime (Electrolysis), Electron Beam (EB) melting, Cold Crucible (CC) melting, and Fractional Thermal Decomposition (FTD). Extraction methods include Coulter Counter Analysis, Photo Scattering Method, and Laser Diffraction Particle Size Analyzer (LDPSA). Inclusion evaluation methods in the liquid include Ultrasonic Techniques for Liquid System, Liquid Metal Cleanliness Analyzer (LIMCA), and Confocal Scanning Laser Microscope. In addition to these direct methods, indirect ways to estimate inclusion content include measurements of total oxygen, nitrogen pickup, dissolved aluminum loss, alumina pickup in the slag, and Submerged Entry Nozzle (SEN) clogging, which are easier and less costly [78].

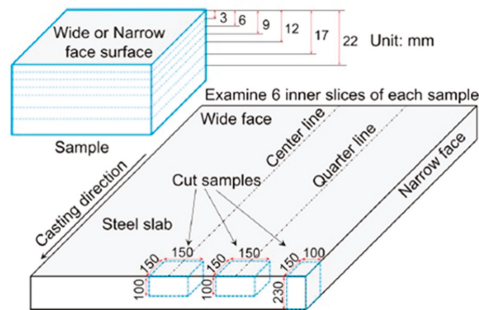


Figure 5. Step milling measurement of particles captured by the solidifying steel shell [82].

2.4. Lab Scale Modeling

Water modeling is a useful tool to simulate fluid flow phenomena of continuous steel casting due to kinematic viscosity of water similar with that of molten steel. However, the negligible electrical conductivity of water (See Table 1) prevents the study of magnetic forces that change the flow. Instead, physical devices to mimic the flow effects of electromagnetic forces have been applied to simulate stirring via two pairs of tuyeres that produce jets, and braking via a layer of beads suspended between screens that resist flow [84,85].

Table 1. Comparison of fluid properties.

Fluid	Melting Temperature (°C)	Density (kg/m ³)	Dynamic Viscosity (kg/m·s)	Electrical Conductivity (Ω·m)	Thermal Conductivity (W/m·K)
Steel	1480–1510	7000	0.0067	714,000	35.0
Water	0	998.2	0.001	0.05	0.60
Mercury	−38.8	13,534	0.001555	1,020,000	8.3
Sn ₆₀ Bi ₄₀	138–170	8250	0.0016	1,050,000	35
Ga ₆₈ In ₂₀ Sn ₁₂	10.5	6360	0.0021	3,290,000	39

A more accurate method is to use low melting temperature alloys such as mercury, Sn₆₀Bi₄₀, or eutectic Ga₆₈In₂₀Sn₁₂ alloy, in physical models, which have the benefits of being conductive to simulate induced flow from electromagnetic fields, having high surface tension and nonwettability of molten steel to simulate multiphase flow, and being liquid at or near room temperature for easy measurements (Table 1) [86]. Lab scale modeling with these liquid metals can use Ultrasound Doppler Velocimetry (UDV) and Mutual Inductance Tomography (MIT) probes to map internal velocity fields, as applied to single-ruler EMB fields in a slab casting mold [86–88], such as shown in Figure 6 [87].

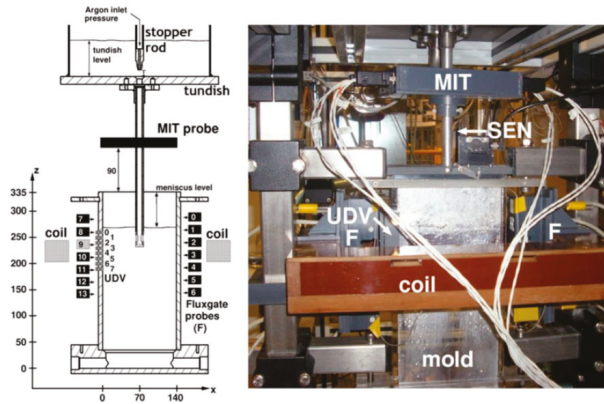


Figure 6. Low melting alloy ($\text{Ga}_{68}\text{In}_{20}\text{Sn}_{12}$) in 0.4-scale model of slab casting [87].

To maintain similarity between the low melting temperature alloy modeling and real caster conditions with electromagnetic forces, magnetohydrodynamics (MHD) dimensionless numbers, such as Hartmann number (Ha) and/or Stuart number (N), should be considered in addition to the standard fluid dynamics dimensionless numbers Froude number (Fr), Reynolds number (Re), and Weber number (We) for scaled physical models.

One way to obtain reasonable predictions of the real caster (R) from measurements in the lab scale model (M) when electromagnetic effects are present is to match both Fr and N . If the lab scale model stays fully turbulent, and multiphase flow is not dominant, then Re and We similarity is not critical [89]. First, Fr , which represents the ratio of inertial to gravitational forces, should be maintained the same in the scaled model and real caster, as follows

$$\frac{V_M}{\sqrt{gL_M}} = \frac{V_R}{\sqrt{gL_R}} \tag{2}$$

where V is a characteristic flow velocity, g is gravitational acceleration, and L is a characteristic length scale; “characteristic” refers to any pair of corresponding values in the model and real caster. This match can be achieved by choosing the casting speed in the model, $V_{Casting, M}$, by rearranging Equation (2):

$$V_{Casting, M} = V_{Casting, R} \sqrt{\frac{L_M}{L_R}} \tag{3}$$

Velocity anywhere in the real caster is then estimated by multiplying the measured velocity at the corresponding position in the scaled model by $\sqrt{\frac{L_M}{L_R}}$, according to Equation (2).

In addition, N , the ratio of electromagnetic to inertial forces, should be maintained constant, as follows

$$\left(\frac{\sigma_M}{\rho_M}\right) \frac{(B_M)^2 L_M}{V_M} = \left(\frac{\sigma_R}{\rho_R}\right) \frac{(B_R)^2 L_R}{V_R} \tag{4}$$

where σ is electric conductivity and ρ is density, as given in the property term. One way to achieve this match is to choose the magnetic field intensity in the model, B_M , as follows, which is found by rearranging Equation (4):

$$B_M = B_R \left(\frac{\rho_M \sigma_R}{\rho_R \sigma_M}\right)^{0.5} \left(\frac{L_R}{L_M}\right)^{0.5} \left(\frac{V_M}{V_R}\right)^{0.5} \tag{5}$$

To match both Fr and N in the scaled model and the real caster, B_M can be chosen as follows

$$B_M = B_R \left(\frac{\rho_M \sigma_R}{\rho_R \sigma_M} \right)^{0.5} \left(\frac{L_R}{L_M} \right)^{0.25} \quad (6)$$

which is found by replacing V_M/V_R in Equation (5) with $\sqrt{L_M/L_R}$, according to Fr in Equation (2). This approach was used successfully with a mercury model to investigate fluid flow velocities in a slab mold with static magnetic fields (local EMBr and single-ruler EMBr) during continuous casting [90].

Alternatively, it is possible to obtain reasonable predictions of the real caster from lab scale measurements on molten metal with electromagnetics, without matching Fr [27]. In this method, the casting speed in the model, $V_{Casting, M}$ is chosen to match N, by rearranging Equation (4) as follows

$$V_{Casting, M} = V_{Casting, R} \left(\frac{\rho_R \sigma_M}{\rho_M \sigma_R} \right) \left(\frac{L_M}{L_R} \right) \left(\frac{B_M}{B_R} \right)^2 \quad (7)$$

With this method, velocity anywhere in the real caster is then predicted by multiplying the measured velocity at the corresponding position in the scaled model by $\left(\frac{\rho_R \sigma_M}{\rho_M \sigma_R} \right) \left(\frac{L_M}{L_R} \right) \left(\frac{B_M}{B_R} \right)^2$, according to Equation (4). In addition, surface level in the real caster, l_R , is estimated from the measured surface level in the model, l_M , by applying the Froude number based scaling method, as follows [27]

$$l_R = l_M \left(\frac{L_R}{L_M} \right)^{0.5} \left(\frac{V_R}{V_M} \right) \quad (8)$$

Using this method, the flow pattern, velocities, and surface level predicted in a real caster matched well with both measurements and Large Eddy Simulation (LES) modeling of a scaled $\text{Ga}_{68}\text{In}_{20}\text{Sn}_{12}$ model [27]. In particular, the surface level in the real caster estimated with the Fr based scaling method (Equation (8)) showed much better agreement than a simple method of multiplying the measured surface level by the scale factor, L_R/L_M [27].

2.5. Computational Modeling: Magnetohydrodynamics (MHD) Models

Many studies of fluid flow-related phenomena in continuous steel slab casting have been conducted using three-dimensional Computational Fluid Dynamics (CFD) models, as reviewed previously [22,23]. These models solve the continuity equation for mass conservation and the Navier–Stokes equations for momentum conservation of incompressible Newtonian fluids, such as molten steel. To simulate other important phenomena, these flow equations are solved together with further coupled equations including turbulence equations, such as Reynolds-averaged Navier-Stokes (RANS)-based standard $k-\epsilon$ [91], Shear-Stress Transport (SST) $k-\omega$ [92], or LES-based subgrid-scale viscosity models such as the Wall-Adapting Local Eddy (WALE) model [93]; multiphase fluid flow equations [22] using the mixture, Eulerian, or Volume Of Fluid (VOF) methods; Lagrangian particle transport model such as the Discrete Phase Model (DPM); and advanced particle-capture criterion equations [82,94]. These equations are solved using classical finite-volume or finite difference methods, often with a commercial CFD package program, such as the ANSYS Fluent code [95], or an in-house code, such as the multi-GPU-based CUFLOW [96].

To consider effects of electromagnetic forces on fluid flow-related phenomena and Magnetohydrodynamics (MHD) models [97,98] are incorporated into the CFD models by adding a Lorentz force term to the momentum equation. Conducting fluid moving in applied magnetic fields induces current and the induced current and the magnetic fields generate Lorentz forces on the fluid flow. There are two methods including magnetic induction method and electrical potential method to calculate the Lorentz force term, as follows.

The total magnetic field, B consists of applied magnetic field, B_0 , and induced magnetic field, b .

$$B = B_0 + b \quad (9)$$

Next, to find B and the induced current density J , the magnetic induction method first finds B by solving the magnetic induction equation, derived by combining Ohm's law, Faraday's equation, and Ampère's law:

$$\frac{\partial B}{\partial t} = \nabla \times (u \times B) + \frac{1}{\mu\sigma} \nabla^2 B \quad (10)$$

where t is time, u is fluid flow velocity, μ is magnetic permeability, and σ is electrical conductivity of the fluid. Knowing B , the induced current density Ampère's equation is then solved for J :

$$J = \frac{1}{\mu} \nabla \times B \quad (11)$$

The other method to find J and B , the electric potential method, first assumes that B can be approximated by B_0 . This assumption is good for systems with high magnetic diffusion compared to magnetic induction, such as continuous casting, where the induced magnetic field b is small relative to the applied field, B_0 . With this electromagnetic condition, a Poisson equation for electric potential, φ can be derived from Ohm's law and conservation of charge, $\nabla \cdot J = 0$, as given by Equation (12).

$$\nabla^2 \varphi = \nabla \cdot (u \times B_0) \quad (12)$$

Then, from the calculated φ , the induced current density is found from Equation (13).

$$J = \sigma(-\nabla \varphi + u \times B_0) \quad (13)$$

Finally, in both methods, the Lorentz force, F_L is calculated from the calculated current density and magnetic field as follows

$$F_L = J \times B \quad (14)$$

Note that the magnetic field is always perpendicular to the flow direction due to the right-hand rule. The force direction is perpendicular to both the induced current density and the magnetic field, according to the cross product in Equation (14). Together, this means that the force direction is 180° , or directly opposite to the flow direction, so is intrinsically a braking force. The actual effect on the flow is much more complicated, however. For a static magnetic field, mass conservation often makes the flow deflect around a region of local magnetic field braking, and as a result can produce faster flow in another region. For a time-varying field, the apparent movement of the field created by a consistent phase shift in a series of magnetics can create an apparent motor force that can almost match the flow direction in some cases.

Regardless of the computational method, model validation is essential. A classic test problem for MHD CFD involves turbulent flow ($Re \sim 40,000$) in a channel with a constant static magnetic field applied uniformly over a 304-mm-long rectangular region near its center. Lorentz forces in the channel domain are shown in Figure 7. Vectors of Lorentz force predicted with both the electric potential method [99] and the magnetic induction method [61] match.

In addition, model predictions of velocity profile across the channel cross section should match with the experimental measurements, such as shown in Figure 8 [61]. An M-shaped profile is observed with higher velocities near the channel walls and lower velocities towards the center region of the channel. This is because the Lorentz forces slow down the flow in the center region, while flow accelerates near the walls to conserve mass. Validation with a test problem such as this one demonstrates that a given MHD CFD model can enable accurate investigation of the effect of electromagnetics on flow in continuous steel casting.

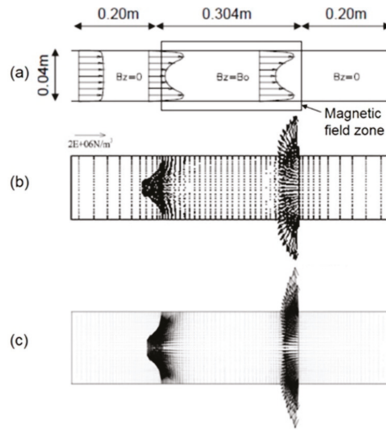


Figure 7. (a) Test channel domain of the magnetohydrodynamics (MHD) models and Lorentz force vectors calculated (b) with potential method [99] and (c) with magnetic induction method [61].

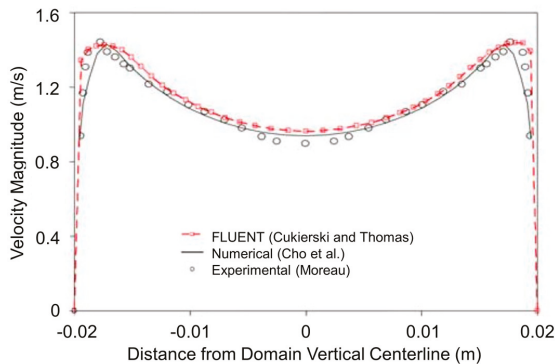


Figure 8. MHD model validation: comparison of velocity profiles in the test channel domain [61].

3. Electromagnetic Effects on Fluid Flow Pattern

The quality of continuously-cast steel slabs depends greatly on fluid flow phenomena including the flow pattern, which governs jet impingement, turbulence, surface velocity, and level variations in the mold region of the process. Excessive surface velocities, and the accompanying turbulence, large surface profile variations, and surface level fluctuations, can cause the entrainment of slag into the molten steel pool, which may lead to the entrapment of inclusions by the solidifying steel shell, and defects in the final product [74]. On the other hand, abnormally slow surface flow can result in low and nonuniform liquid temperature near the meniscus and problems associated with low superheat, which include insufficient slag melting and infiltration, meniscus freezing, and hook formation, leading to surface defects in the product [100,101]. Thus, process parameters must be controlled within optimum windows [16,32] of process operation, as shown in Figure 9 for data measured at NKK Corporation [16], to avoid these quality problems [2,16].

The flow pattern significantly affects many important phenomena in the slab mold and upper strand regions. Flow in the mold can be classified as having single-, double-, or unstable flow patterns [2,16]. Unstable flow often involves chaotic transient transitions between single- and double-roll, and should be avoided because it is the worst for steel quality, owing to severe surface instability during the flow

transitions [2,16]. Electromagnetic control of the flow pattern aims to maintain a stable double-roll flow pattern that keeps surface velocity within an optimum range for best steel quality [16,32].

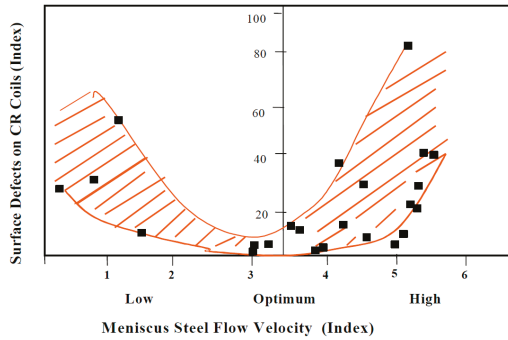


Figure 9. Slab/coil defects are minimum in an optimum window of steel meniscus velocities between weak and excessive double-roll flow conditions. NKK Corporation data; 700 to 1650 mm wide, 235-mm-thick slabs cast at 1.6 to 2.8 m/min [16].

3.1. Local EMBr

Local EMBr creates roughly circular-shaped static magnetic fields near the nozzle ports. The fields are designed to make the jet pass below the strongest core region of the magnetic field and deflected downward [24]. This results in deeper jet impingement on the narrow face, slower surface flow, and a flatter surface profile [61,102,103], as seen by comparing Figure 10a,b. These surface-flow braking effects become stronger with higher EMBr strength [102]. Note that excessive EMBr strength may produce too low surface velocity which could cause the meniscus freezing and hook formation associated with low surface temperature due to the stagnant surface flow.

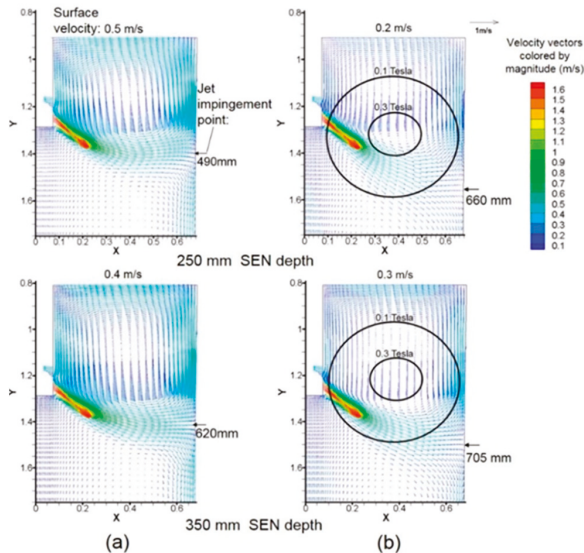


Figure 10. Mold flow pattern (a) without and (b) with local EMBr [61].

On the other hand, local EMBr causes the jet to deflect upward if the jet passes above the strongest region of the magnetic field [104]. This produces shallower jet impingement on the narrow face, higher surface velocity and larger variations in surface profile across the mold width [104]. Abnormally strong local EMBr fields may change the mold flow pattern from a double-roll to a single-roll pattern, making the jet directly go towards the surface without impinging first on the narrow faces [103]. This is usually detrimental to surface quality, and may also cause slag entrainment and other defects.

Thus, properly locating local EMBr field relative to the nozzle ports and optimizing the field strength is important to achieve surface flow conditions in a safe window of operation [105]. In addition to the EMBr magnetic field position, this also requires consideration of the SEN depth [61], nozzle port angle [90], and slab width [106] that strongly affect the jet behavior in the mold. As shown by comparing the two frames in Figure 10b, the EMBr effects on braking surface flow are weakened if the jet passes below the magnetic field region due to deeper SEN location, which leads to less deepening of the jet impingement point and less reduction in surface velocity. This trend is contrary to that without EMBr where surface velocity decreases with increasing SEN depth, as shown in Figure 10a. It is important to carefully monitor and control the SEN depth and field strength according to the casting conditions and the EMBr field location.

3.2. Single-Ruler EMBr

Single-ruler EMBr systems are designed to slow down the mold surface flow by applying a horizontal rectangular-shaped static field across the entire width of the slab mold region near the meniscus [25]. With increasing casting speed, surface flow tends to be stronger, so stronger electromagnetic braking is needed, such as in thin-slab casting at high casting speed [107,108]. This is useful to avoid excessive surface velocities and vortex formation [26], which can cause slag entrainment into the molten steel pool in the mold. Compared to local EMBr, single-ruler EMBr is more effective to brake the surface velocity in the mold because the magnetic field shape of single-ruler EMBr extends across the entire width, including the center and the narrow face regions [90]. However, excessive application of single-ruler EMBr near the meniscus can be detrimental by slowing surface velocities too much for the casting conditions. This can result in excessive cooling of the meniscus region and insufficient mixing of the surface slag layers, leading to meniscus freezing, where the accompanying subsurface hooks can capture particles including argon bubbles, alumina inclusions, and mold slag droplets into the solidifying steel shell, leading to surface defects.

On the other hand, placing the single ruler below the nozzle can increase surface velocity [27–29]. In this case, the field deflects the downward-flowing jet to become more horizontal, impinging higher on the narrow face, and causing more and faster flow up the narrow faces towards the meniscus. This can help by increasing surface velocity into the optimal range in some situations such as thick slab casting at low casting speed. Care should be taken to avoid locating the maximum of the magnetic field directly across the nozzle ports, as this produces flow instability resulting in severe jet wobbling and surface fluctuations, as discussed further in Section 4.1 [27–29]. The strong horizontal field also tends to lessen mixing between the upper and lower recirculation zones of the double-roll flow pattern. This is useful during casting of clad steels, where the field is positioned between two nozzles which deliver two different steel grades, as discussed later [30].

Vertical single-ruler EMBr, recently proposed, is designed to decrease surface velocity and surface profile variations by imposing two strong static ruler-shaped magnetic fields oriented vertically near the narrow faces [109–111]. The flow velocity up the narrow face is predicted to become slower and more uniform with vertical EMBr [110]. This is proposed to be useful for high-speed thin-slab mold casting, to avoid excessive surface flow problems. If the flow has a double-roll pattern with a downward jet, then the vertical ruler field is predicted to reduce surface velocity more than a horizontal single-ruler EMBr field [109,110], as shown in Figure 11.

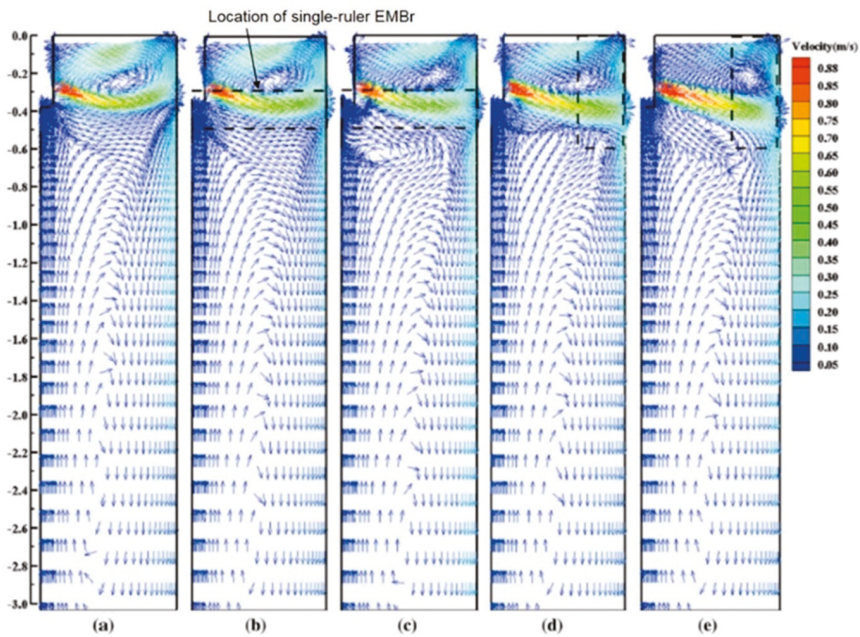


Figure 11. Mold flow pattern (a) with no magnetic field, (b) horizontal single-ruler EMBR 0.1 T, (c) 0.2 T, (d) vertical single-ruler EMBR 0.1 T, and (e) 0.2 T [109].

3.3. Double-Ruler EMBR

Double-ruler EMBR combines two horizontal rectangular-shaped static ruler magnetic fields across the mold width: one (upper ruler) above and the other (lower ruler) below the nozzle ports [24]. The upper ruler tends to decrease surface velocities and surface level variations across the mold width [17,29,112–114]. This ruler acts in several ways: stabilizing flow inside the nozzle, deflecting the jets exiting the ports downward, especially when the ruler is located just above the nozzle ports, which slows the flow up the narrow faces and finally by slowing the flow along the meniscus [29,112–114]. The lower ruler generally tends to lessen the jet penetration depth [17,79,114–119], which affects particle transport deep into the mold cavity, as discussed in Section 6.2.

Compared to local and single-ruler EMBR systems, the double-ruler EMBR has more flexibility, with independent control of the strength of two rulers offering better potential to optimize the flow pattern, by either increasing or decreasing the intensity of surface flows. However, nonoptimal choice of the ruler intensities has the potential to worsen quality problems. Excessive upper-ruler strength can make surface flow too slow, especially in low-speed operations, resulting in meniscus freezing and hook formation, which is detrimental to the slab surface quality. Alternatively, excessive lower ruler field strength could lead to excessive surface velocities, turbulence and associated defects, especially in high-speed operations.

The ruler-shaped field often tends to decrease in strength towards the narrow faces. If the strength of the lower ruler near the narrow faces is too small, then the effect of the upper ruler deflecting the jet downwards can increase flow down the narrow faces below the mold, resulting in deeper jet penetration and associated particle defects [113]. In addition, this problem may decrease flow towards the surface, resulting in slower surface flows and associated stagnation problems, even with a strong lower-ruler field and no upper field current. This is because the double-ruler still generates a magnetic field peak above the nozzle that can deflect the jet downward, which differs from the single-ruler EMBR field below the nozzle ports [17].

Finally, confining the jet between the upper and lower rulers tends to make the jet thinner, slightly faster, and with less vertical variations [113]. Thus, the locations and strengths of the double-ruler EMBr system should be adjusted to achieve optimal mold flow, keeping the surface flow velocity within the optimal range, and minimizing jet penetration deep into the mold cavity, in order to improve both surface and internal quality of steel slabs.

3.4. MM-EMB

By adjusting the strengths of the five local static fields, multi-mode EMB can be designed to change, and hopefully improve flow velocity and stability in several different ways [31,120]. With two strong local magnetic fields located near the meniscus near the narrow faces and an optional strong field just below the nozzle, MM-EMB in braking mode 1 or damping mode tends to slow down surface flow [31,120], and lessen surface level fluctuations, in order to avoid defects associated with excessive surface velocity, such as slag entrainment.

Alternatively, applying two strong local magnetic fields below the nozzle near the narrow faces, MM-EMB in braking mode 2 can achieve similar flow behavior. This mode is similar to single-ruler EMBr positioned below the nozzle, except there is no field in the center of the mold below the nozzle. The observed decrease in surface flow is likely due to the field cores being positioned above the jets near impingement on the narrow faces. Care should be taken in positioning the fields, however, because if the two fields are located below the jets near narrow-face impingement, surface flow would be expected to increase. Thus, this mode likely experiences similar behavior and operation guidelines as the local-EMBr field discussed in Section 3.1. Other MM-EMB modes are possible, which deserve further investigation.

3.5. Moving Fields: EMLS, EMLA, EMRS, M-EMS, EMC, and SEMS

Moving electromagnetic fields are generated by passing alternating currents through a series of magnets, each having a different phase shift in order to create a traveling Lorentz force to actively drive the flow tangentially across the surfaces of the solidifying steel shell in the mold. The strength and direction of the force depends on the magnet orientation, the applied current, and the effective frequency of the phase shift. Three types of horizontally-moving magnetic fields near the nozzle ports are EMLA [16,32,33,40,51,56,121], EMLS [16,32,33,40,51,56,122], and EMRS [16,32,33,40,51] or M-EMS [123,124]. Alternatively, EMC applies vertically-moving magnetic fields near the meniscus [36–38]. Other types of moving field systems—SEMS and S-EMS—are applied to the strand below the mold [33,40–47].

When surface flow is too slow, EMLA is designed to accelerate the jets in order to increase the surface velocity, turbulence, and surface temperature. This is useful for situations, such as low-speed casting and wide molds, to prevent stagnant surface flow, meniscus freezing, and the corresponding surface defects [121]. Also, EMLA can be applied when argon gas flow rate is high, to transform a detrimental single-roll pattern to a better double-roll pattern [32].

Alternatively, when surface flow is too fast, EMLS can slow down the jets in order to decrease surface velocity, surface profile variations, level fluctuations, and associated quality problems such as slag entrainment [32]. However, excessive magnetic field strength may lead to a single-roll pattern in the mold when argon gas fraction is high [51,122].

Thirdly, EMRS or M-EMS can rotate the flow around the perimeter of the mold, which is expected to wash particles away from the dendritic solidification front, in order to lessen particle entrapment, especially near the meniscus region [123,124]. In addition, the mixing effect of the rotating surface flow is designed to make the temperature distribution in the liquid near the mold top surface and meniscus region more uniform, especially in the central region of the mold near the nozzle, lessening the associated problems of meniscus freezing and lowering hook depth [123,124]. This is an alternative way to previously discussed methods to increase surface flows, with the potential benefit of less detrimental level fluctuations, if great care is taken.

Fourthly, the vertically moving magnetic fields generated by EMC induce vertical rotating flows, consisting of very small upper and lower counter-rotating recirculation regions near the meniscus in the mold, where the magnets are located [36,38]. This lessens the tendency of molten steel to overflow the meniscus during oscillation mark and hook formation. Thus, EMC can decrease surface defects including uneven slab surface and particle capture during initial solidification [36]. More details are given in Section 5.3.

Finally, SEMS in slab casting creates large vertical recirculation regions below the mold, designed to control superheat, solidification, grain structure, and solute distribution [33,40–47]. The one-way horizontally-moving fields in SEMS create Lorentz forces which directly drive the molten steel across the strand towards one of the narrow faces. After impinging on that narrow face, the flow splits vertically upward and downward. With one magnetic field or an “in-roll” pair of moving field systems on each side of the strand, this results in two large, counter-rotating vertical recirculation regions across the entire strand width, which extend far above and below the SEMS field region [41,42,45–47]. With two sets of two pairs each of in-roll-type SEMS stirrers employed, SEMS can generate three flow recirculation zones across the strand, which induce stronger effects on mixing the flow, compared to single-pair in-roll SEMS [42]. The top surface flow in the mold is not affected much by SEMS, so the importance of this mixing flow is related mainly to effects on superheat distribution, temperature gradients at the solidification front, grain structure, porosity, and segregation in the strand, which are discussed later. All of these moving-field methods deserve further investigation to understand and optimize the behavior.

3.6. Combined Traveling and Static Fields

Static and traveling magnetic fields can be combined together to offer even more flexibility to tailor electromagnetic control of the flow pattern in the mold. The FC3 system upper EMS field is designed to act like EMRS to produce the rotating flow around the perimeter of the upper mold [55,84,85], as shown in Figure 12. This aims to reduce particle capture during initial solidification and to make molten steel temperature and superheat removal more uniform around the mold perimeter. The static field in the lower mold region of FC3 is designed to slow down the jet flow to control surface flow intensity, and to shorten the jet penetration deep below the mold [55,84,85], which is designed to lessen deep particle penetration and capture. The combined effects of these two fields have great potential to reduce both surface and internal defects if they are optimized.

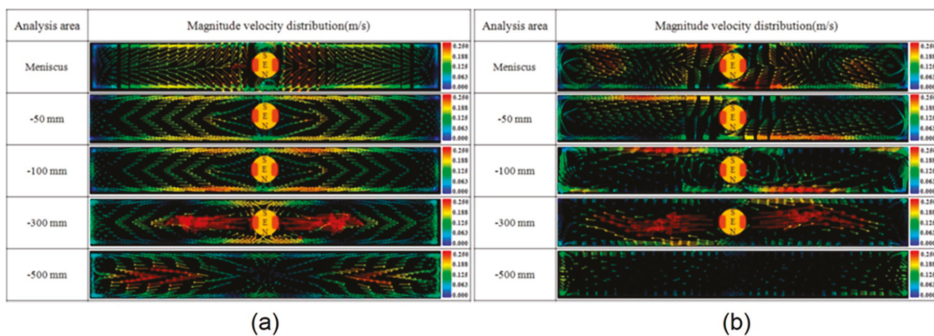


Figure 12. Flow patterns at various horizontal sections of the mold with (a) no magnetic field and (b) combined moving and static magnetic fields [55].

Another type of combined field system employs EMC near the meniscus on the narrow faces and a single-ruler static EMBr field below the nozzle ports [49]. The EMBr field is designed to brake the jet and control surface flow intensity. The moving field is designed to decrease meniscus level fluctuations to lessen slag entrapment and has been shown to greatly decrease oscillation mark depth, making a smooth slab surface with less hook formation [36].

4. Electromagnetic Flow Control and Surface Instability Effects

Surface instabilities associated with high surface velocity, velocity fluctuations, and severe level fluctuations are detrimental to surface quality of the final steel products. For many quality concerns, flow instabilities and transient events are often more important than the time-averaged flow pattern itself [16,32]. These instabilities can cause intermittent slag entrainment into the molten steel pool and slag entrapment by the solidifying steel shell, resulting in slag capture defects [74]. In addition, oscillation mark profiles become deeper and more uneven due to severe surface level fluctuations, especially near the meniscus. Electromagnetic forces affect both the flow pattern and the flow stability. Optimal application of electromagnetics to better control the surface flow and level can help to prevent these instabilities and the related quality problems.

4.1. Local and Single-Ruler EMBr

Local EMBr is designed to decrease velocity fluctuations of the jet passing below the strong magnetic field. However, the jet instability becomes severe when the local EMBr core is located below the jet, especially with excessive field strength [106]. This is because the jet deflects upwards to avoid the strong field region, and may disrupt the top surface, especially in wide slabs [106]. This further emphasizes the importance of optimizing the vertical orientation of the magnets relative to the SEN depth, according to the port angle and slab width, as discussed in Section 3.1.

The effects of single-ruler EMBr also depend strongly on the location of the ruler [27,28]. Locating a single-ruler EMBr above the nozzle decreases surface level fluctuations, resulting in a more stable surface. On the other hand, lowering the magnetic field below the nozzle ports produces shallower downward jet angles, higher surface velocities, lower turbulent kinetic energy at the surface, and better surface flow stability, especially at higher level fluctuation frequencies. In addition, vortex formation at the mold top surface, caused by biased surface flow due to nozzle misalignment between left and right sides in the mold, can be lessened with single-ruler EMBr together with optimized argon injection [125]. Applying the ruler across nozzle ports worsens the flow instability, however, producing strong unbalanced, asymmetric transient behavior (jet wobbling) and complex flow [28,29,126], as shown in Figure 13. Thus, the electromagnetic field should not be placed with its maximum directly across the nozzle ports, where it may aggravate unstable flow. When modeling these phenomena, it is important to note that the flow instability with realistic conducting walls is much less than with insulated walls [27,28,127,128], as shown in Figure 13. With single-ruler EMBr below the nozzle and electrically-conducting walls, the low-frequency oscillations of the jet flow are suppressed and results in a stable double-roll flow pattern with surface velocity within the window of safe operation, for the conditions simulated [28].

Vertical single-ruler EMBr is predicted to reduce both surface velocity and level fluctuations, especially near the meniscus [111]. The strong magnetic field oriented vertically along near the narrow faces tends to brake the upward flow produced after jet impingement on the narrow faces. Deepening SEN depth and lowering nozzle port angles (more downward) should further lessen surface fluctuations [111].

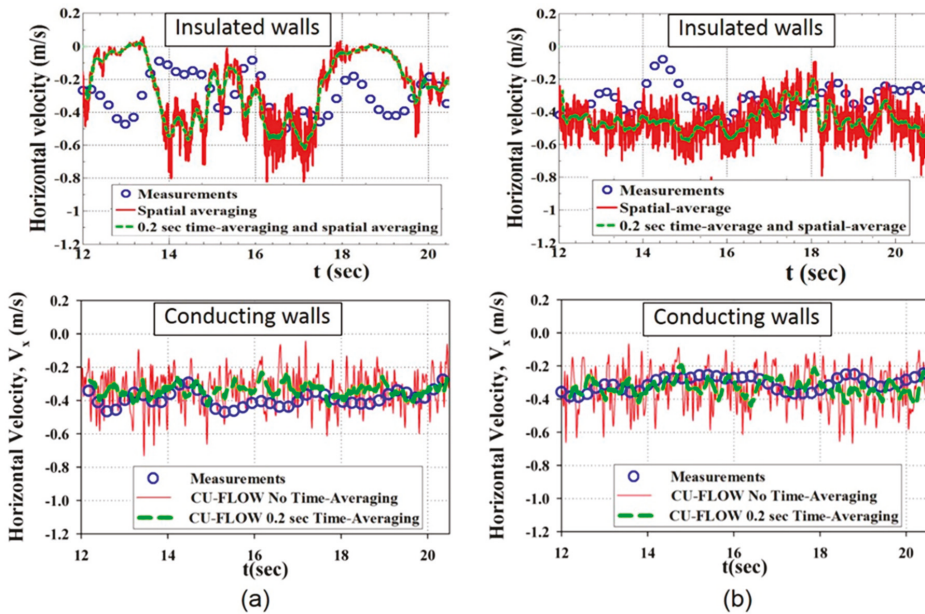


Figure 13. Transient history of jet velocity component (minus sign (–) indicates toward NF) in the mold with single-ruler EMBr locating at (a) 92 mm (near the nozzle ports) and (b) 121 mm (below the nozzle) below meniscus [28].

4.2. Double-Ruler EMBr

By surrounding the jets leaving the ports with static fields both above and below, double-ruler EMBr acts to stabilize the flow, deflecting chaotic turbulent variations in the jet direction back towards its designed path towards the narrow faces. Thus, asymmetrical flow and its associated variable surface defects tend to be reduced [79]. For example, surface level fluctuations caused by unbalanced flows in a slab mold are reduced with double-ruler EMBr [79]. Swirl flow inside the nozzle causes jet wobbling, especially with a slide-gate control system. This results in stronger variations in surface velocity and low-frequency level fluctuations [113], as shown in Figure 14a. The clockwise swirls, which have higher momentum than the counterclockwise swirls, due to shorter flowing path from the slide gate to the nozzle bottom on the right side in this orientation, produce higher surface velocity and surface level height. Thus, surface velocity and level fluctuation variations occur whenever the swirl flow direction changes in the nozzle bottom. Double-ruler EMBr reduces the surface velocity fluctuations due to the swirl direction changes as shown in Figure 14b, by dampening the momentum differences between swirl rotation directions. This is because the upper ruler field across the nozzle makes the velocity profile more uniform inside the nozzle [17,113], which then reduces jet wobbling and stabilizes the surface velocity and level across the mold width, as shown in Figures 15 and 16 [113]. This effect is also likely with single-ruler EMBr above the nozzle ports.

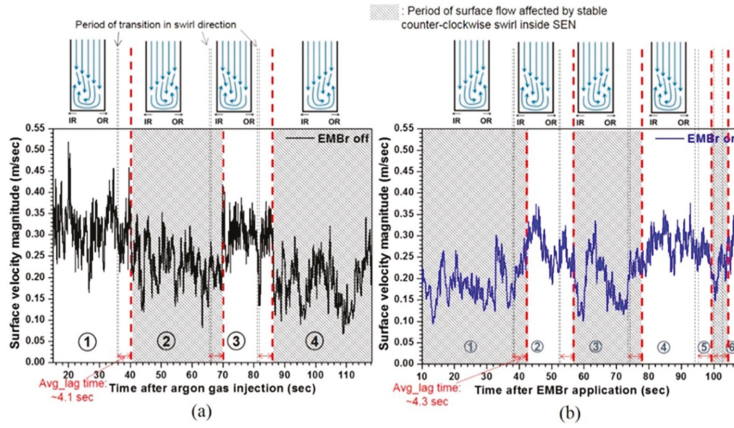


Figure 14. Surface velocity magnitude histories in the mold (a) without and (b) with double-ruler EMBr [113].

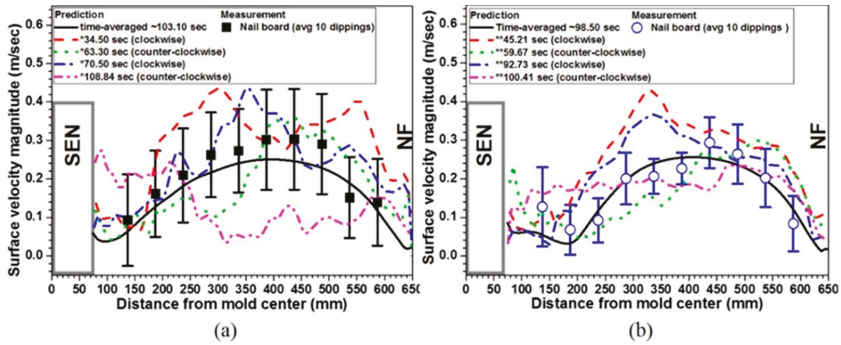


Figure 15. Surface velocity variations comparing LES modeling and measurements (a) without and (b) with double-ruler EMBr [113].

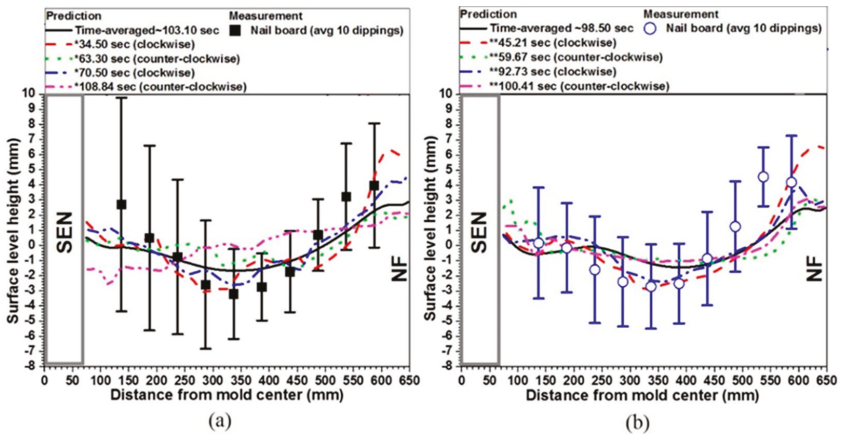


Figure 16. Surface level variations comparing LES modeling and measurements (a) without and (b) with double-ruler EMBr [113].

4.3. Moving Fields: EMLS, EMLA, and EMRS

Moving field effects on flow stability in the mold region have received less previous study [39,51,56,75], compared to that of static fields. Feedback control systems have been implemented in a few commercial operations with EMLS and EMLA, adjusting the magnetic field strength according to the current “F-value” [105], which is an estimate of surface flow strength based on SEN geometry, mold width, and casting speed [51,75]. This system is reported to maintain stable surface level in the mold [51,75]. For this to be effective, the EMLS and EMLA fields should be located just below the nozzle ports [51,75] and the flow pattern should be double-roll [16]. It is especially important to avoid unstable flow due to continuous transition between single-roll and double-roll patterns, as shown in Figure 17, as this causes severe surface level fluctuations [16]. In addition, this system needs to be improved to handle argon gas [32].

As an alternative control method, the magnetic field strength could be adjusted more actively according to local flow conditions. Two feedback control systems, based on two sensor measurements of instantaneous surface level, are expected to be better. Flow rate from the stopper rod or slide gate can be controlled to maintain a constant average liquid level, based on the first sensor, located at the quarter point. This location, found midway between the SEN and NF, is the most stable location in the mold relative to the highest amplitude wave motion [60,64,113]. The other sensor can be located near the narrow-face meniscus. Then, the magnetic field strength can be controlled to decrease the estimated surface level profile variations, as indicated by the difference between the two sensor measurements [24].

Finally, EMRS appears not increase surface level fluctuations, even the magnetic field is located near the mold surface [51].

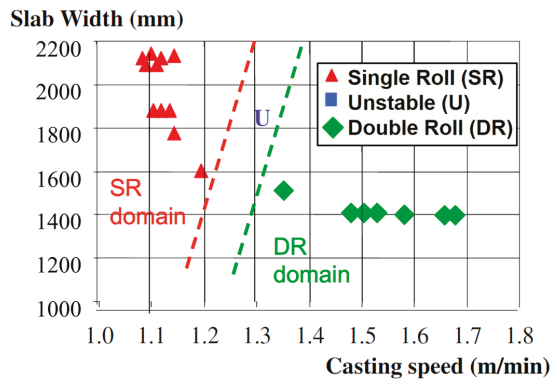


Figure 17. Unstable flow regime between single and double-roll flow patterns (4.4 t/min throughput) [16].

5. Electromagnetic Effects on Superheat Transport and Initial Solidification

Superheat is delivered with the molten steel flow towards top surface (mold flux layer), which affect initial solidification at the meniscus, and also deep into the mold cavity, which affects shell growth and potential thinning. Superheat transport depends on the mold flow pattern, which determines how the jet along with its superheat takes to reach different regions in the mold. The coldest regions tend to be found at the meniscus near the SEN and near the narrow faces. Stronger upward flow brings more superheat faster to these regions, resulting in higher meniscus temperatures. Optimal surface flow strength also mixes the liquid mold flux, which helps to melt the powder and encourage good gap infiltration and uniform lubrication. On the other hand, weaker upward flow results in a colder, stagnant meniscus, perhaps causing initial solidification problems including meniscus freezing, deeper oscillation marks and hooks, which can further increase particle capture, and slag infiltration problems.

Thus, through its effect on the flow pattern, electromagnetic forces can also help to control superheat distribution, initial solidification, and shell growth.

5.1. Static Magnetic Fields

As discussed in Sections 3.1 and 3.2, the location of static EMBr fields relative to the jet greatly affects the mold flow pattern. Thus, superheat transport is also influenced strongly by the magnetic field location [103,104,108,109,126,129,130]. Magnetic fields located below the jet deflect flow upwards towards the surface, leading to a hotter meniscus region [103,104], increasing meniscus temperature with increasing field strength, as shown in Figure 18 [104]. Optimal local EMBr fields can produce shallower oscillation marks [131].

On the other hand, magnetic fields above the jet deflect flow downwards, deeper into the mold cavity. The weaker upward flow transports less superheat to the mold upper mold, resulting in meniscus freezing, flow stagnation at the surface, and associated quality problems. In addition, local EMBr field can lessen jet intensity in the lower mold, resulting in a more uniform shell with less shell thinning at the jet impingement point [131].

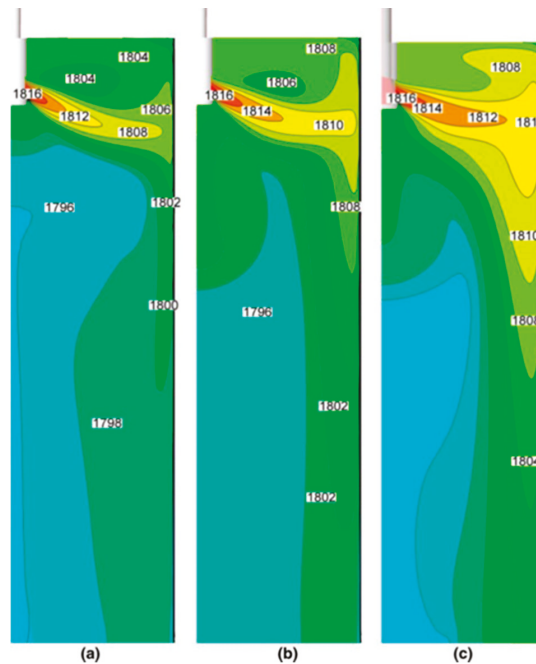


Figure 18. Temperature distribution in the mold with local EMBr field strength B_0 of (a) 0.0 T, (b) 0.2 T, and (c) 0.39 T [104].

Applying double-ruler EMBr has more flexibility to control the mold flow. Thus, superheat transport towards the stop surface is more adjustable by independent control of the field strengths of two rulers. More superheat is delivered towards the surface with stronger upward flows if the lower ruler is stronger and the upper ruler field is far above the nozzle ports [115,132]. This increases meniscus temperatures [115,132]. This can decrease the depths of oscillation marks and subsurface hooks, which are strongly related to low temperature distributions near the meniscus [100,101], as shown in Figure 19 [132]. Alternatively, abnormally high strength or low location of the upper ruler field can make the meniscus flow stagnant, causing associated surface defects.

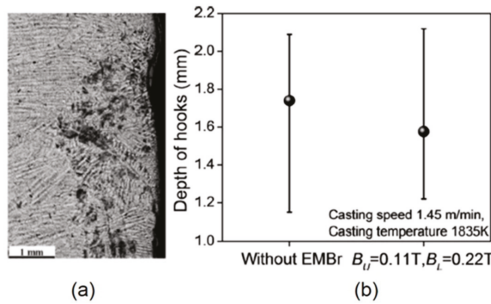


Figure 19. (a) Subsurface hooks and (b) the effect of double-ruler EMBR on hook depth in the steel slab [132].

5.2. Horizontally-moving Magnetic Fields: EMRS, M-EMS, and EMLA

The horizontally-rotating magnetic fields applied with EMRS or M-EMS produce rotating flow around the perimeter of the mold. This makes superheat transport and temperature distribution more uniform near the solidifying steel shell, especially where the meniscus tends to be cold, near the SEN and narrow faces [34]. Thus, depths of hooks and oscillation marks should be lessened. This also enables improvement of heat transfer uniformity through the slag layer in the steel shell/mold gap around the mold. Thus, the initial steel solidification around the mold is more uniform [34]. Uniformity of initial solidification can lessen defects such as longitudinal cracks, which initiate at local nonuniformities where stress can concentrate.

EMLA can increase temperature near the meniscus, by strengthening the upper flow along with delivering more superheat to the upper region of mold [32]. This is expected to have similar benefits of shallower oscillation marks and hooks.

5.3. Vertically Rotating Field near Meniscus: EMC

The moving EMC fields near the meniscus create two vertically counter-rotating recirculation zones near the meniscus [36,38]. The lower flow recirculation opposes molten steel trying to overflow the meniscus during each mold oscillation cycle. It also mixes the local superheat making temperature near the meniscus more uniform. These effects reduce oscillation mark depth and hook formation [36,38] as shown in Figure 20. This is expected to improve surface quality and to reduce particle capture defects.

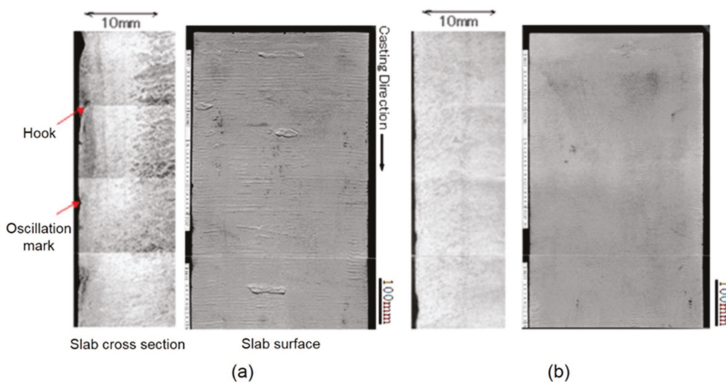


Figure 20. Oscillation marks and hooks in steel slabs (a) without and (b) with electromagnetic casting (EMC) [36].

6. Electromagnetic Effects on Particle Transport and Capture

Particles including bubbles, alumina, and slag inclusions may be transported with the flow and removed to the surface slag layer, or captured into the solidifying steel shell. Large particles are detrimental to product properties such as fatigue life, especially in high-strength steel. Bubbles are detrimental because they are usually coated with small inclusions. Captured large bubbles concentrate the inclusions into large clusters, so are detrimental to final steel product quality if they cannot be removed by further processes such as surface scarfing. Large particles are also detrimental by leading to delaminations, blisters, pencil pipes, and other defects during downstream operations [133,134].

Near the meniscus, excessive surface flow causes surface profile variations and level fluctuations, which can entrain slag as inclusions into the molten steel pool, and/or may directly entrap slag, inclusions, and bubbles into the steel shell at the meniscus [8,74]. In addition, single-roll surface flows towards narrow faces or cross-surface flows between wide faces may move particles trapped at the interface between the liquid mold slag and the molten steel pool, to the meniscus regions, where they may be captured. Alternatively, strong flow across (tangential to) the steel solidification front can wash particles away from the solidifying steel shell front, resulting in less particle capture [82,94].

Abnormally slow surface flow can lead to insufficient superheat transport to the meniscus, leading to deeper frozen hooks, as discussed in Section 5. This can cause more particle capture defects in the mold regions. Thus, the first objective of flow control is to maintain surface flows in a safe window of operation. Electromagnetic fields, combined with other casting conditions and nozzle geometry, can help to achieve this. The extra control possible with electromagnetics, however, may enable paying attention to particle transport and capture independent from surface flow.

Finally, electromagnetic fields can change the local velocity field adjacent to non-conducting particles, such as large argon bubbles, which can change the bubble shape and terminal rising velocity, relative to the flow field [135]. Thus, electromagnetic effects on the flow pattern and turbulence can significantly affect particle transport and the fraction and distributions of entrapped particles in several ways.

6.1. Local and Single-Ruler EMBr

As discussed in Sections 3–5, with local or single-ruler EMBr field located below the jets, the jets deflect upward towards the mold top surface, which could help argon bubbles and other particles carried with the flow to escape into the surface slag layer [104]. However, excessive upward flow may disrupt the top surface and allow more bubbles to accumulate beneath the slag layer, especially near the SEN, where they may be captured during initial solidification. In extreme cases, strong surface flows, such as caused by a poorly-designed local field, can push the liquid mold flux away, causing an open eye, where the molten steel is exposed to the powder and air [136]. This must be avoided because the associated reoxidation, contamination with carbon from the mold powder, bubble, and slag entrainment are all very detrimental to steel quality. Thus, the main objective of EMBr is to change the flow pattern to avoid excessive surface-directed flows to avoid particle entrapment and other defects associated with excessive surface flows.

On the other hand, if EMBr fields are located partly above the nozzle ports, so the jets are deflected downward, the flow may transport more particles deep into the strand below the mold. This will increase internal defects, as only a small fraction (lower than ~10%) of these particles are able to return to the top slag layer [137]. Thus, placing local or single-ruler EMBr fields at a proper location is important to control particle transport and capture in the mold, as expected from the effects on fluid flow pattern and surface instability, discussed in previous Sections 3.1, 3.2 and 4.1.

6.2. Double-Ruler EMBr

The upper ruler of double-ruler EMBr can help to avoid excessive surface flows and stabilizes the surface slag/molten steel interface in the mold, which tends to reduce the entrapment of inclusions due to level fluctuations [113]. These effects are similar to a single-ruler EMBr above the nozzle.

The lower ruler of double-ruler EMBr can help to lessen jet penetration and particle transport deep into the strand. As shown in Figure 21 [138], such an EMBr system causes fewer bubbles to be transported towards the narrow faces. The sizes and fractions of bubbles captured with these two flow patterns are shown in Figure 22 [138]. Small particles which contact the solidification front are easily entrapped between dendrites. On the other hand, large particles are only captured if the particle stays at the solidification front for long enough time to become surrounded by the growing shell front [82,94,138–140]. A simple criterion, which captures any particle touching the solidifying shell, overpredicts the capture of large particles, as shown in Figure 22a. Calculations with an advanced capture criterion [82,94,138] consider a potential balance of eight forces on the particle at the shell front, which include the drag from tangential velocities, which can wash away the particles from the solidification front, back into the main flow. This sophisticated capture model agrees better with plant measurements in Figure 22a, which show an average bubble diameter of ~0.1mm. Results also show that the average size of bubbles captured near the meniscus is slightly bigger than those captured deeper in the caster. Meniscus hooks, not included in the model, likely capture larger particles rising up beneath them. The change in the bubble transport with double-ruler EMBr tends to decrease the fraction of bubbles captured into the solidifying steel, as shown in Figure 22b, especially the 0.1mm size [82,138]. In addition, less deep hooks, due to more superheat towards the meniscus region with double-ruler EMBr, can reduce inclusion capture into the hooks [132] as shown in Figure 23.

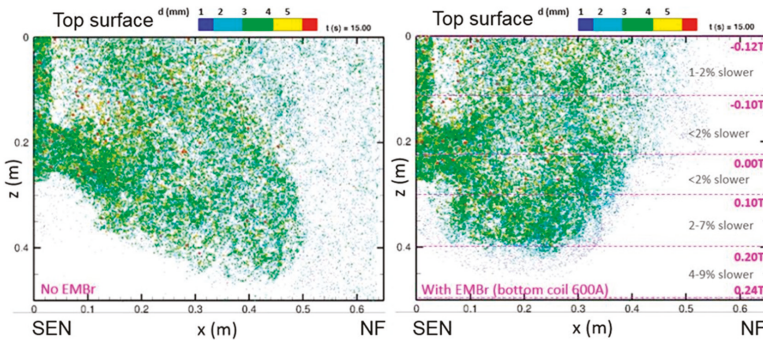


Figure 21. Bubble distributions in a slab caster centerplane without and with double-ruler EMBr [138].

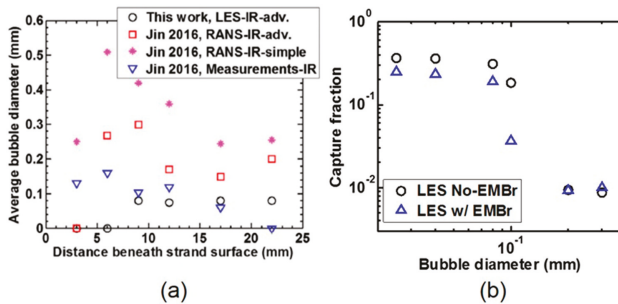


Figure 22. Captured bubble size distribution showing (a) the variation with distance beneath the strand surface and (b) the effect of double-ruler EMBr on capture fraction [138].

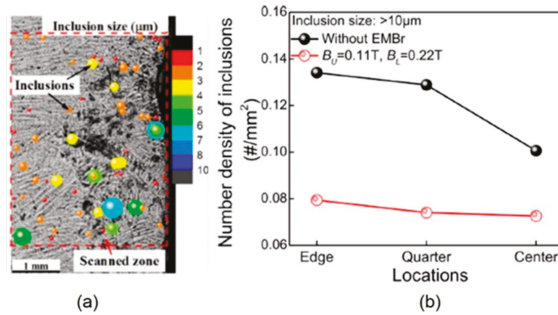


Figure 23. (a) Inclusions captured by hooks and (b) the effect of double-ruler EMBr on inclusion capture in the steel slab [132].

However, bubbles can penetrate deeper into the mold with double-ruler EMBr if the lower-ruler field strength is not enough to reduce the downward flow velocity near the narrow faces [113]. On the other hand, excessive strength of the upper ruler field can make the surface flow stagnant, leading to formation of more hooks which can entrap more slag inclusions into the shell. Thereby, optimizing the strength of both rulers is important to reduce the particle transport and capture [79,115,138], improving both surface and internal quality of the steel slabs.

6.3. Moving Magnetic Fields

Proper application of EMLS magnetic fields to stabilize surface velocity and surface level fluctuations may also help to reduce particle-related defects in the final steel product [32]. This is due to lessening the entrainment of slag inclusions and bubbles coated with inclusions and their capture into the solidifying steel shell, especially at the meniscus, as discussed in the previous section.

Horizontally-rotating magnetic fields induced by EMRS or M-EMS produce horizontally-rotating flow patterns around the perimeter of the mold. This flow pattern can wash away particles from the steel shell front in the mold [32,34,124,141–143], especially near the meniscus region, and from beneath subsurface hooks. This can significantly reduce defects related to the capture of bubbles near the surface (sometimes called pinholes or blowholes) [32,34], as shown in Figure 24, and other defects with large inclusions (slag, alumina [34], or calcium-alumina). In addition, more uniform surface temperature near the meniscus can lessen hook depth as discussed in Section 5. This in turn can reduce particle capture at the meniscus. Both the washing effect and the reduction of hooks are effective to reduce particle capture defects. Similar washing effects to lessen the capture of large inclusions might be involved with EMLA, and/or SEMS, but this needs further investigation, as previous work could not be found.

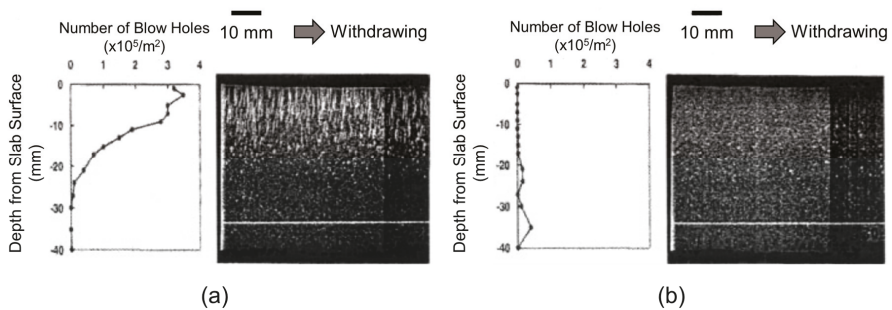


Figure 24. Subsurface-entrapped bubble defects in steel slabs (a) without and (b) with EMRS [32].

7. Electromagnetic Effects on Grain Structure and Internal Quality

Grain structure including the chill zone, columnar zone, Columnar-Equiaxed Transition (CET), and equiaxed zone is important for steel mechanical properties. Having more equiaxed grains in the slab correlates with less center segregation [144]. Many efforts have been made to increase the equiaxed zone size using electromagnetics. M-EMS can increase nuclei formation, resulting in smaller grains near the strand surface [34], perhaps due to the higher velocity flow across the solidification front melting off dendrite tips [145]. If more nuclei can survive and flow deep into the molten steel pool, this would be expected to lead to a larger fraction of equiaxed grains in the final product. Similarly, SEMs induces rotating flow below the mold, specifically in the vertical plane of the width and casting directions [33,40,42,45], which should decrease temperature gradients in the liquid, and has been shown to increase the size of the central equiaxed zone [33,40,42,45,146], as shown in Figure 25. In nonoriented electrical steel casting, the application of two sets of two pairs of in-roll SEMs magnetic fields at 400 A and 5 Hz was reported to show great improvement of grain structure, to over 60% equiaxed, as shown in Figure 26 [42].

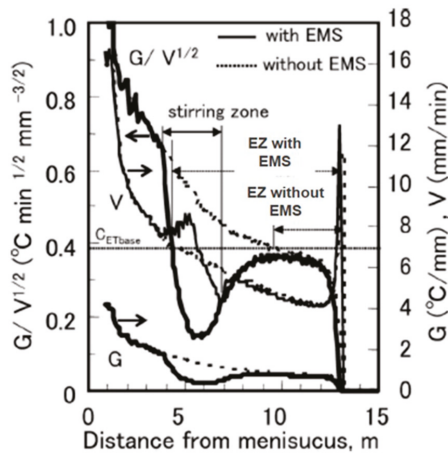


Figure 25. Effect of strand EMS on temperature gradient, dendrite tip velocity, and location of Equiaxed Zone (EZ) [146].

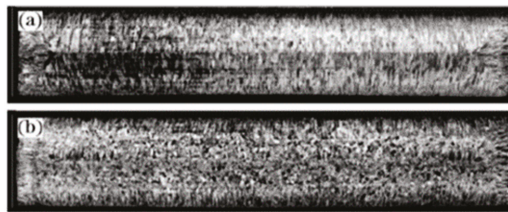


Figure 26. Microstructure of nonoriented electrical steel in slab horizontal cross-sections (a) without and (b) with SEMs rollers (54% equiaxed grains) [42].

In addition, strand EMS also affects segregation and centerline quality. Applying S-EMS together with soft reduction (Posco Heavy strAnd Reduction Process: PosHARP) has been reported to reduce center porosity and centerline segregation (abnormal high and varying solute concentration between the dendrites near final solidification) better than soft reduction alone [43], as shown in Figure 27.


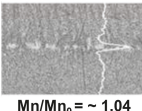

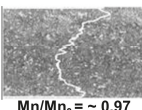
Method	Etching image	Mn segregation degree (EPMA results)	Center porosity (mm ² /g)
Soft reduction		 Mn/Mn ₀ = ~ 1.04	0.25 ~ 0.65
PosHARP		 Mn/Mn ₀ = ~ 0.97	0.09 ~ 0.20

Figure 27. Effects of SEMs with soft reduction on segregation and porosity defects [43].

However, white bands (low solute concentration) and/or dark bands (high solute concentration) in the steel microstructure are caused by tangential flow across the solidification front, due to nonuniform solute distribution in the strand region. These distinctive bands of macrosegregation can be seen in slabs cast with SEMs, always at the depth into the slab where the flow was induced [147], such as in Figure 26b. In addition, distinctive changes in the angle of the columnar dendrite growth directions can be seen in the cross-sections of slabs cast with SEMs, corresponding with the changing flow directions across the solidification front with distance down the strand. The effect of casting conditions and flow control methods with and without electromagnetic effects on segregation and grain structure needs more study to more accurately quantify the relation between fluid flow, macrosegregation, grain structure, and related steel quality.

8. Electromagnetic Control of Steel Composition Distribution: Clad Steel Casting

Another type of horizontal rectangular-shaped static magnetic field with a single-ruler, also called Level DC Magnetic Field (LMF) [30], is useful to manufacture clad steel slabs. This strong static field is employed across the slab mold in between the submergence depths of two nozzles, which deliver two different steel grades into the mold, as shown in Figure 28a. This magnetic field applied just below the mold exit produces two separated flow zones in the upper and lower pools, as shown in Figure 28b. This tends to lessen mixing of the two steel alloys, which consist of a stainless steel surface layer, which solidifies first, and a low carbon steel interior that solidifies later below the mold.

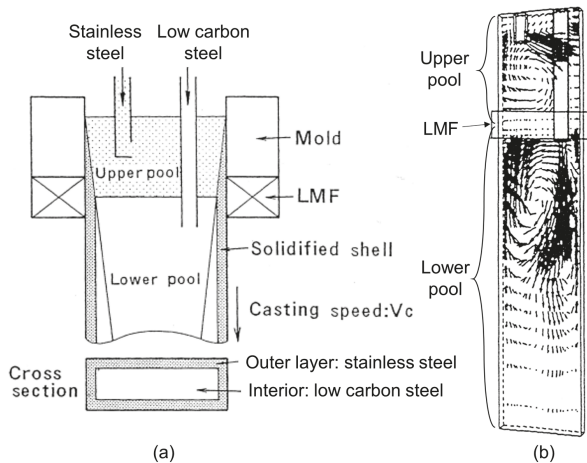


Figure 28. (a) Schematic of continuous casting and (b) flow patterns in the mold and strand region with Level DC Magnetic Field (LMF) for clad steel slabs [30].

Figure 29 shows the effects of LMF on microstructure and composition distribution in the clad steel slab. With LMF, the sharp gradient in nickel concentration at the interface between the stainless steel (outer surface layer) and the low carbon steel (interior) and the negligible nickel in the interior both indicate the effectiveness of LMF to prevent mixing of stainless steel into the interior.

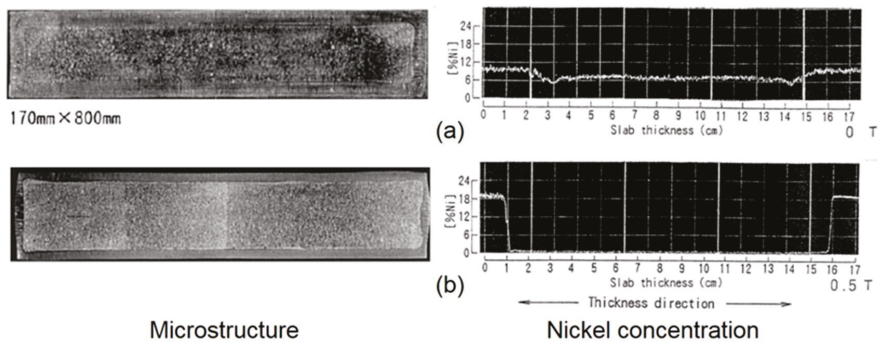


Figure 29. Comparison of microstructure and nickel distribution in the clad steel slabs (a) without and (b) with LMF [30].

9. Summary and Conclusions

This paper has reviewed the many different types of electromagnetic systems used in slab casting to affect fluid flow and related phenomena and the research tools that can be used to investigate and understand the phenomena that affect steel product quality. Some of these effects and practical strategies to operate these electromagnetic systems are summarized below.

- Combining several plant measurement methods is recommended to quantify the flow fluid and effects on quality, owing to the complexity of the continuous casting process with electromagnetics and the difficulty of making direct measurements.
- Computational modeling validated with plant measurements and lab experiments is the best way to quantify and understand the effects of electromagnetic forces on fluid flow, superheat transfer, solidification, particle transport and capture, grain structure, steel composition, and other phenomena and defects.
- Static magnetic fields (local, single-ruler, and double-ruler EMB_r and EMB), moving magnetic fields (EMLS, EMLA, EMRS/M-EMS, EMC, and SEMs), and combined systems have been developed to affect the flow pattern and flow stability, aiming to control the intensity of surface flows in the mold to reduce various defects including surface defects, slag entrainment, inclusion entrapment, and deep oscillation marks, and/or to control internal cleanliness, grain structure, segregation, and porosity.
- EMB_r, EMB, EMLS, and EMLA are designed to maintain a stable double-roll flow pattern which keeps surface velocity, profile, and level fluctuations within a safe operating window, which is most useful for higher casting speed operations, especially thin-slab casting.
- Placing static EMB_r fields at a proper location relative to the flowing jets is critical to achieving the flow objectives. A strong magnetic field above the jet core tends to deflect the jets downward, and to slow surface velocity, which decreases variations in surface level and profile. In this case, care is needed to avoid over cooling the surface if the field is too strong.
- On the other hand, a strong magnetic field below the jet core tends to deflect the jets upwards, increasing surface velocities when casting at low speed and lessening deep penetration of inclusions. In this case, care is needed to avoid upward excessive surface flows, if the field is too strong.

- Locating the core of an EMBr magnetic field directly across the jets exiting the nozzle ports should be avoided to prevent unstable jet flow and associated defects.
- A static ruler EMBr field across the nozzle above the ports helps to stabilize flow inside the nozzle, with consequent improvement of flow stability in the mold.
- Maintaining proper ruler-EMBr field strength across the mold towards the narrow faces is important to reduce surface level fluctuations near the meniscus and jet penetration deep into the mold cavity.
- Moving magnetic fields in the mold (EMLS, EMLA, EMRS, and M-EMS) actively drive the flow, providing an alternative method to achieve flow objectives. These include: EMLS moving fields towards the SEN, aiming to lower surface velocity and turbulence; EMLA moving fields towards the narrow faces, aiming to increase surface velocity and turbulence; and EMRS (M-EMS) fields rotating around the perimeter of the mold surface, aiming (in part) to wash particles away from the solidifying steel shell to lessen particle capture.
- Superheat transport and initial solidification depend greatly on the mold flow pattern. Thus, adjusting the magnetic fields to deflect (static fields) or accelerate (EMLA) the jet upwards towards the top surface in the mold can reduce meniscus freezing, hook formation, and oscillation mark depth. Furthermore, rotating magnetic fields generated by EMRS (M-EMS), or EMC can make superheat and temperature near the meniscus more uniform.
- Lessening the jet impingement depth, with a uniform ruler EMBr field across the mold below the jet, can reduce particle capture deep into the solidifying steel shell. In addition, the washing effect generated by a rotating flow pattern with EMRS or M-EMS can reduce surface defects including particle capture during initial solidification at the meniscus including subsurface hooks.
- Below the mold, horizontally-moving fields towards one narrow face (SEMS) produces vertically rotating flows in the strand region, which mixes superheat, resulting in increased equiaxed grains, and less center segregation and porosity defects.
- Strong static magnetic fields can enable clad steel casting, by helping to separate two steel alloys without mixing, by generating two separate flow recirculation zones above and below the magnetic field.
- The application of combined fields, employing a traveling field either horizontally (via EMRS or M-EMS) or vertically (EMC) in the upper part of the mold and a static field (single-ruler EMBr) in the lower part of a mold, has great potential to reduce both surface and internal defects: The horizontally-moving field around the perimeter of the mold surface can wash away particles at the solidifying steel shell front and prevent their capture. At the same time, the static field prevents the jet flow go deep into the mold cavity, thereby reducing particle penetration, capture, and internal defects.
- The vertically moving EMC field near the meniscus can greatly reduce oscillation mark and hook depth.
- One of the greatest benefits of electromagnetics over conventional flow control devices, (such as port geometry) is the potential to adjust the field strength during operation according to the current flow conditions. Even better is the potential to adjust the magnetic field according to real-time feedback from in-mold sensors, such as multiple sensors of surface level, in order to maintain the intensity of surface flows in window of safe operation real time. More work is needed to implement this into practice.

Electromagnetic systems have been designed to prevent defect formation and to improve steel quality. However, all of the process geometry and conditions including nozzle port angle, SEN depth, casting speed, and argon gas flow rate need to be considered together to find optimal flow system operation conditions including electromagnetics for a specific caster, according to its needs regarding steel quality concerns.

Author Contributions: S.-M.C. and B.G.T. reviewed the references and wrote the article. Furthermore, B.G.T. as a corresponding author supervised the paper preparation.

Funding: Support from the Continuous Casting Center at Colorado School of Mines, the Continuous Casting Consortium at University of Illinois at Urbana-Champaign, and the National Science Foundation GOALI grant (Grant No. CMMI 18-08731) are gratefully acknowledged.

Acknowledgments: Provision of FLUENT licenses through the ANSYS Inc. academic partnership program is much appreciated.

Conflicts of Interest: The authors declare no conflicts of interest.

References

1. World Steel Association. Table 4. Production of Continuously Cast Steel. In *Steel Statistical Yearbook 2018*; World Steel Association: Brussels, Belgium, 2018; pp. 9–12.
2. Thomas, B.G. Chapter 14. Fluid Flow in the Mold. In *Making, Shaping and Treating of Steel*, 11th ed.; Cramb, A., Ed.; Casting Volume; AISE Steel Foundation: Pittsburgh, PA, USA, 2003; Volume 5, pp. 14.1–14.41.
3. Thomas, B.G. Chapter 15. Continuous Casting of Steel. In *Modeling for Casting and Solidification Processing*; Yu, O., Ed.; Marcel Dekker: New York, NY, USA, 2001; pp. 499–540.
4. Thomas, B.G. Modeling of Continuous Casting Defects Related to Mold Fluid Flow. *Iron Steel Technol.* **2006**, *3*, 128–143.
5. Najjar, F.M.; Thomas, B.G.; Hershey, D.E. Numerical Study of Steady Turbulent Flow through Bifurcated Nozzles in Continuous Casting. *Metall. Mater. Trans. B* **1995**, *26B*, 749–765. [[CrossRef](#)]
6. Calderon-Ramos, I.; Morales, R.D.; Salazar-Campoy, M. Modeling Flow Turbulence in a Continuous Casting Slab Mold Comparing the use of Two Bifurcated Nozzles with Square and Circular Ports. *Steel Res. Int.* **2015**, *86*, 1610–1621. [[CrossRef](#)]
7. Salazar-Campoy, M.M.; Morales, R.D.; Najera-Bastida, A.; Calderon-Ramos, I.; Cedillo-Hernandez, V.; Delgado-Pureco, J.C. A Physical Model to Study the Effects of Nozzle Design on Dispersed Two-Phase Flows in a Slab Mold Casting Ultra-Low-Carbon Steels. *Metall. Mater. Trans. B* **2018**, *49B*, 812–830. [[CrossRef](#)]
8. Cho, S.-M.; Thomas, B.G.; Kim, S.-H. Effect of Nozzle Port Angle on Transient Flow and Surface Slag Behavior during Continuous Steel slab casting. *Metall. Mater. Trans. B* **2018**, *50B*, 52–76. [[CrossRef](#)]
9. Thomas, B.G.; Mika, L.J.; Najjar, F.M. Simulation of Fluid Flow inside a Continuous Slab-Casting Machine. *Metall. Mater. Trans. B* **1990**, *21B*, 387–400. [[CrossRef](#)]
10. Cho, S.-M.; Thomas, B.G.; Lee, H.-J.; Kim, S.-H. Effect of Nozzle Port Angle on Mold Surface Flow in Steel Slab Casting. *Iron Steel Technol.* **2017**, *14*, 76–84.
11. Chaudhary, R.; Lee, G.-G.; Thomas, B.G.; Kim, S.-H. Transient Mold Fluid Flow with Well- and Mountain-Bottom Nozzles in Continuous Casting of Steel. *Metall. Mater. Trans. B* **2008**, *39B*, 870–884. [[CrossRef](#)]
12. Gursoy, K.A.; Yavuz, M.M. Effect of Flow Rate Controllers and their Opening Levels on Liquid Steel Flow in Continuous Casting Mold. *ISIJ Int.* **2016**, *56*, 554–563. [[CrossRef](#)]
13. Wang, Y.; Zhang, L. Transient Fluid Flow Phenomena during Continuous Casting: Part II—Cast Speed Change, Temperature Fluctuation, and Steel Grade Mixing. *ISIJ Int.* **2010**, *50*, 1783–1791. [[CrossRef](#)]
14. Bai, H.; Thomas, B.G. Turbulent Flow of Liquid Steel and Argon Bubbles in Slide gate Tundish Nozzles: Part II. Effect of Operation Conditions and Nozzle Design. *Metall. Mater. Trans. B* **2001**, *32B*, 269–284. [[CrossRef](#)]
15. Liu, Z.Q.; Qi, F.S.; Li, B.K.; Cheung, S.C.P. Modeling of bubble behaviors and size distribution in a slab continuous casting mold. *Int. J. Multiphase Flow* **2016**, *79*, 190–201. [[CrossRef](#)]
16. Dauby, P.H. Continuous casting: Make better steel and more of it! *Revue de Métallurgie* **2012**, *109*, 113–136. [[CrossRef](#)]
17. Jin, K.; Vanka, S.P.; Thomas, B.G. Large Eddy Simulations of the Effects of EMBr and SEN Submergence Depth on Turbulent Flow in the Mold Region of a Steel Caster. *Metall. Mater. Trans. B* **2017**, *48B*, 162–178. [[CrossRef](#)]
18. Jacobi, H.F. Investigation of Centreline Segregation and Centreline Porosity in CC-Slabs. *Steel Res. Int.* **2003**, *74*, 667–678. [[CrossRef](#)]

19. El-Bealy, M.O. Macrosegregation Quality Criteria and Mechanical Soft Reduction for Central Quality Problems in Continuous Casting of Steel. *Mater. Sci. Appl.* **2014**, *5*, 724–744. [[CrossRef](#)]
20. Thomas, B.G. Review on Modeling and Simulation of Continuous Casting. *Steel Res. Int.* **2018**, *89*, 1700312. [[CrossRef](#)]
21. Thomas, B.G. Chapter 5. Modeling of Continuous Casting. In *Making, Shaping and Treating of Steel*, 11th ed.; Cramb, A., Ed.; Casting Volume; AISE Steel Foundation: Pittsburgh, PA, USA, 2003; Volume 5, pp. 5.1–5.24.
22. Thomas, B.G.; Zhang, L. Mathematical Modeling of Fluid Flow in Continuous Casting. *ISIJ Int.* **2001**, *41*, 1181–1193. [[CrossRef](#)]
23. Yuan, Q.; Zhao, B.; Vanka, S.P.; Thomas, B.G. Study of Computational Issues in Simulation of Transient Flow in Continuous Casting. *Steel Res. Int.* **2005**, *76*, 33–43. [[CrossRef](#)]
24. Kollberg, S.; Lofgren, P.M.; Hanley, P. Improving Quality and Productivity in Thick Slab Casting by Direct Control of ElectroMagnetic Brake (EMBR). In Proceedings of the AISTech 2004, Nashville, TN, USA, 15–17 September 2004; pp. 977–984.
25. Zeze, M.; Harada, H.; Takeuchi, E.; Ishii, T. Application of DC Magnetic Field for the Control of Flow in the Continuous Casting Strand. In Proceedings of the 76th Steelmaking Conference, Dallas, TX, USA, 28–31 March 1993; pp. 267–272.
26. Qian, Z.-D.; Wu, Y.-L. Large Eddy Simulation of Turbulent Flow with the Effects of DC Magnetic Field and Vortex Brake Application in Continuous Casting. *ISIJ Int.* **2004**, *44*, 100–107. [[CrossRef](#)]
27. Singh, R.; Thomas, B.G.; Vanka, S.P. Effects of a Magnetic Field on Turbulent Flow in the Mold Region of a Steel Caster. *Metall. Mater. Trans. B* **2013**, *44B*, 1201–1221. [[CrossRef](#)]
28. Thomas, B.G.; Singh, R.; Vanka, S.P.; Timmel, K.; Eckert, S.; Gerbeth, G. Effect of Single-Ruler Electromagnetic Braking (EMBr) Location on Transient Flow in Continuous Casting. *J. Manuf. Sci. Prod.* **2015**, *15*, 93–104. [[CrossRef](#)]
29. Chaudhary, R.; Thomas, B.; Vanka, S. Effect of Electromagnetic Ruler Braking (EMBr) on Transient Turbulent Flow in Continuous Slab Casting using Large Eddy Simulations. *Metall. Mater. Trans. B* **2012**, *43*, 532–553. [[CrossRef](#)]
30. Harada, H.; Takeuchi, E.; Zeze, M.; Tanaka, H. MHD analysis in hydromagnetic casting process of clad steel slabs. *Appl. Math. Modell.* **1998**, *22*, 873–882. [[CrossRef](#)]
31. Kunstreich, S. Recent developments of electromagnetic actuators for continuous casting of long and flat products. *MILLENNIUM STEEL* **2014**, 57–63.
32. Kunstreich, S.; Dauby, P.H. Effect of liquid steel flow pattern on slab quality and the need for dynamic electromagnetic control in the mold. *Ironmak. Steelmak.* **2005**, *32*, 80–86. [[CrossRef](#)]
33. Kunstreich, S. Electromagnetic stirring for continuous casting-Part 2. *Rev. Met. Paris.* **2003**, *100*, 1043–1061. [[CrossRef](#)]
34. Nakashima, J.; Fukuda, J.; Kiyose, A.; Kawase, T.; Ohtani, Y.; Doki, M. *Improvement of Slab Surface Quality with In-mold Electromagnetic Stirring*; Nippon Steel and Sumitomo Metal Corporation: Tokyo, Japan, 2002; pp. 61–67.
35. Fujisaki, K. In-Mold Electromagnetic Stirring in Continuous Casting. *IEEE TRANSACTIONS ON INDUSTRY APPLICATIONS* **2001**, *37*, 1098–1104. [[CrossRef](#)]
36. Tani, M.; Zeze, M.; Toh, T.; Tsunenari, K.; Umetsu, K.; Hayashi, K.; Tanaka, K.; Fukunaga, S. Electromagnetic Casting Technique for Slab Casting. *Nippon Steel Technical Report* **2013**, *104*, 62–68. [[CrossRef](#)]
37. Cha, P.-R.; Hwang, Y.-S.; Nam, H.-S.; Chung, S.-H.; Yoo, J.-K. 3D Numerical Analysis on Electromagnetic and Fluid Dynamic Phenomena in a Soft Contact Electromagnetic Slab Caster. *ISIJ Int.* **1998**, *38*, 403–410. [[CrossRef](#)]
38. Toh, T.; Takeuchi, E.; Hojo, M.; Kawai, H.; Matsumura, S. Electromagnetic Control of Initial Solidification in Continuous Casting of Steel by Low Frequency Alternating Magnetic Field. *ISIJ Int.* **1997**, *37*, 1112–1119. [[CrossRef](#)]
39. Kubota, J.; Kubo, N.; Ishii, T.; Suzuki, M.; Aramaki, N.; Nishimachi, R. Steel Flow Control in Continuous Slab Caster Mold by Traveling Magnetic Field. *NKK TECHNICAL REVIEW* **2001**, *85*, 1–9.
40. Kunstreich, S. Electromagnetic stirring for continuous casting-Part 1. *Rev. Met. Paris.* **2003**, *100*, 395–408. [[CrossRef](#)]

41. Dubke, M.; Tacke, K.-H.; Spitzer, K.-H.; Schwerdtfeger, K. Flow fields in electromagnetic stirring of rectangular strands with linear inductors: Part I. theory and experiments with cold models. *Metall. Trans. B.* **1988**, *19B*, 581–593. [[CrossRef](#)]
42. Gong, J.; Liu, H.-p.; Wang, X.-h.; Bao, Y.-p. Numerical Simulation of Electromagnetic Field and Flow Pattern in a Continuous Slab Caster with in roll-type Strand Electromagnetic Stirring. *J. Iron Steel Res. Int.* **2015**, *22*, 414–422. [[CrossRef](#)]
43. Kim, G.H.; Kwon, S.H.; Won, Y.M.; Lee, C.H. Enhancement of slab internal quality by electromagnetic stirring of molten steel. In Proceedings of the 8th International Conference on Electromagnetic Processing of Materials (EPM 2015), Cannes, France, 12–16 October 2015.
44. Kunstreich, S. Strand electromagnetic stirring (S-EMS) for thick slab casters: Box-type or In-roll stirrers? *Millennium Steel* **2008**, 122–124.
45. El-Kaddah, N.; Natarajan, T.T. Electromagnetic Stirring of Steel: Effect of Stirring Design on Mixing in Horizontal Electromagnetic Stirring of Steel Slabs. In Proceedings of the Second International Conference on CFD in the Mineral and Process Industries, Melbourne, Australia, 6–8 December 1999; pp. 339–344.
46. Dubke, M.; Tacke, K.-H.; Spitzer, K.-H.; Schwerdtfeger, K. Flow fields in electromagnetic stirring of rectangular strands with linear inductors: Part II. Computation of flow fields in billets, blooms, and slabs of steel. *Metall. Trans. B.* **1988**, *19B*, 595–602. [[CrossRef](#)]
47. Lambert, V.; Galpin, J.-M.; Hackl, H.R.; Jacobson, N.P. New Strong Strand Stirrer Boosting Quality for Ferritic Stainless Steel. *Iron Steel Technol.* **2008**, *5*, 71–79.
48. Sedén, M.; Jacobson, N.; Lehman, A.; Eriksson, J.-E. Control of Flow Behavior by FC Mold G3 in Slab Casting Process. In Proceedings of the 8th European Continuous Casting Conference, Graz, Austria, 23–26 June 2014.
49. Qian, Z.-D.; Wu, Y.-L.; Li, B.-W.; He, J.-C. Numerical Analysis of the Influences of Operational Parameters on the Fluid Flow in Mold with Hybrid Magnetic Fields. *ISIJ Int.* **2002**, *42*, 1259–1265. [[CrossRef](#)]
50. Yavuz, M.M. The Effects of Electromagnetic Brake on Liquid Steel Flow in Thin Slab Caster. *Steel Res. Int.* **2011**, *82*, 809–818. [[CrossRef](#)]
51. Domgin, J.-F.; Anderhuber, M.; Doncker, M.D.; Paepe, A.D. Optimization of an Electromagnetic Technology in ArcelorMittal Gent for Improving Products Quality in Steel Industry. *J. Manuf. Sci. Prod.* **2015**, *15*, 105–117. [[CrossRef](#)]
52. Mizukami, H.; Hanao, M.; Hiraki, S.; Kawamoto, M.; Watanabe, T.; Hayashi, A.; Iguchi, M. Measurement of Meniscus Flow Velocity in High Speed Continuous Casting Mold. *Tetsu-to-Hagane* **2000**, *86*, 265–270. [[CrossRef](#)]
53. Iguchi, M.; Terauchi, Y. Karman Vortex Probe for the Detection of Molten Metal Surface Flow in Low Velocity Range. *ISIJ Int.* **2002**, *42*, 939–943. [[CrossRef](#)]
54. Iguchi, M.; Kawabata, H.; Ogura, T.; Hayashi, A.; Terauchi, Y. A New Probe for Directly Measuring Flow Velocity in a Continuous Casting Mold. *ISIJ Int.* **1996**, *36*, S190–S193. [[CrossRef](#)]
55. Han, S.-W.; Cho, H.-J.; Jin, S.-Y.; Sedén, M.; Lee, I.-B.; Sohn, I. Effects of Simultaneous Static and Traveling Magnetic Fields on the Molten Steel Flow in a Continuous Casting Mold. *Metall. Mater. Trans. B* **2018**, *49B*, 2757–2769. [[CrossRef](#)]
56. Kubota, J.; Kubo, N.; Suzuki, M.; Ishii, T.; Nishimachi, R.; Aramaki, N. Steel Flow Control with Travelling Magnetic Field for Slab Continuous Caster Mold. *Tetsu-to-Hagane* **2000**, *86*, 69–75. [[CrossRef](#)]
57. Jin, K.; Vanka, S.P.; Thomas, B.G.; Ruan, X. Large Eddy Simulations of the Effects of Double-Ruler Electromagnetic Braking and Nozzle Submergence Depth on Molten Steel Flow in A Commercial Continuous Casting Mold. In Proceedings of the TMS Annual Meeting, CFD Modeling and Simulation in Materials Processing Symposium 2016, Nashville, TN, USA, 14–18 March 2016; pp. 159–166.
58. Dauby, P.H.; Emling, W.H.; Sobolewski, R. Lubrication in the Mold: A Multiple Variable System. *Ironmaker Steelmaker* **1986**, *13*, 28–36.
59. McDavid, R.M.; Thomas, B.G. Flow and Thermal Behavior of the Top Surface Flux/Powder Layers in Continuous Casting Molds. *Metall. Mater. Trans. B* **1996**, *27B*, 672–685. [[CrossRef](#)]
60. Cho, S.-M.; Lee, H.-J.; Kim, S.-H.; Chaudhary, R.; Thomas, B.G.; Lee, D.-H.; Kim, Y.-J.; Choi, W.-R.; Kim, S.-K.; Kim, H.-S. Measurement of Transient Meniscus Flow in Steel Continuous Casters and Effect of Electromagnetic Braking. In Proceedings of the TMS Annual Meeting Symposium 2011, San Diego, CA, USA, 27 February–3 March 2011.

61. Cukierski, K.; Thomas, B.G. Flow Control with Local Electromagnetic Braking in Continuous Casting of Steel Slabs. *Metall. Mater. Trans. B* **2008**, *38B*, 94–107. [[CrossRef](#)]
62. Liu, R.; Thomas, B.G.; Sengupta, J.; Chung, S.D.; Trinh, M. Measurements of Molten Steel Surface Velocity and Effect of Stopper-rod Movement on Transient Multiphase Fluid Flow in Continuous Casting. *ISIJ Int.* **2014**, *54*, 2314–2323. [[CrossRef](#)]
63. Rietow, B.; Thomas, B.G. Using Nail Board Experiments to Quantify Surface Velocity in the CC Mold. In Proceedings of the AISTech 2008, Pittsburgh, PA, USA, 5–8 May 2018; pp. 1–11.
64. Cho, S.-M.; Kim, S.-H.; Thomas, B.G. Transient Fluid Flow during Steady Continuous Casting of Steel Slabs: Part I. Measurements and Modeling of Two-phase Flow. *ISIJ Int.* **2014**, *54*, 845–854. [[CrossRef](#)]
65. Köhler, K.U.; Andrzejewski, P.; Julius, E.; Haubrich, H. Steel Flow Velocity Measurement and Flow Pattern Monitoring in the Mould. In Proceedings of the 78th Steelmaking Conference, Nashville, TN, USA, 2–5 April 1995; pp. 445–449.
66. Thomas, B.G.; Yuan, Q.; Sivaraj Sivaramakrishnan, S.; Shi, T.; Vanka, S.P.; Assar, M.B. Comparison of Four Methods to Evaluate Fluid Velocities in a Continuous Slab Casting Mold. *ISIJ Int.* **2001**, *41*, 1262–1271. [[CrossRef](#)]
67. Assar, M.; Dauby, P.H.; Lawson, G.D. Opening the Black Box: PIV and MFC Measurements in a Continuous Caster Mold. In Proceedings of the 83rd Steelmaking Conference, Pittsburgh, PA, USA, 26–29 March 2000.
68. Okano, S.; Nishimura, T.; Ooi, H.; Chino, T. Relation between Large Inclusions and Growth Directions of Columnar Dendrites in Continuously Cast Slabs. *Tetsu-to-Hagane* **1975**, *61*, 2982–2990. [[CrossRef](#)]
69. Esaka, H.; Toh, T.; Harada, H.; Takeuchi, E.; Fujisaki, K. Deflection of Steel Dendrite Growing in the Fluid Flow Driven by Electromagnetic Stirrer. *Tetsu-to-Hagane* **2000**, *86*, 247–251. [[CrossRef](#)]
70. Wang, X.; Wang, S.; Zhang, L.; Sridhar, S.; Conejo, A.; Liu, X. Analysis on the Deflection Angle of Columnar Dendrites of Continuous Casting Steel Billets Under the Influence of Mold Electromagnetic Stirring. *Metall. Mater. Trans. A* **2016**, *47A*, 5496–5509. [[CrossRef](#)]
71. Melissari, B.; Argyropoulos, S.A. Measurement of Magnitude and Direction of Velocity in High-Temperature Liquid Metals. Part I: Mathematical Modeling. *Metall. Mater. Trans. B* **2005**, *36B*, 691–700. [[CrossRef](#)]
72. Melissari, B.; Argyropoulos, S.A. Measurement of Magnitude and Direction of Velocity in High-Temperature Liquid Metals. Part II: Experimental Measurements. *Metall. Mater. Trans. B* **2005**, *36B*, 639–649. [[CrossRef](#)]
73. Argyropoulos, S.A. Measuring velocity in high-temperature liquid metals: A review. *Scand. J. Metall.* **2000**, *30*, 273–285. [[CrossRef](#)]
74. Hibbeler, L.C.; Thomas, B.G. Mold Slag Entrainment Mechanisms in Continuous Casting Molds. *Iron Steel Technol.* **2013**, *10*, 121–134.
75. Kubota, J.; Okitoto, K.; Shirayata, A.; Murakati, H. Meniscus Flow Control in the Mold by Traveling Magnetic Field for High Speed Slab Caster. In Proceedings of the 74th Steelmaking Conference, Washington, DC, USA, 14–17 April 1991; pp. 233–241.
76. Akhtar, A.; Thomas, B.G.; Sengupta, J. Analysis of Nail Board Measurements of Liquid Slag Layer Depth. In Proceedings of the AISTech 2016, Pittsburgh, PA, USA, 16–19 May 2016; pp. 1427–1438.
77. Yuan, Q.; Thomas, B.G.; Vanka, S.P. Study of Transient Flow and Particle Transport in Continuous Steel Caster Molds: Part I. Fluid Flow. *Metall. Mater. Trans. B* **2004**, *35B*, 685–702. [[CrossRef](#)]
78. Zhang, L.; Thomas, B.G. State of the Art in Evaluation and Control of Steel Cleanliness. *ISIJ Int.* **2003**, *43*, 271–291. [[CrossRef](#)]
79. Furumai, K.; Matsui, Y.; Murai, T.; Miki, Y. Evaluation of Defect Distribution in Continuously-Cast Slabs by Using Ultrasonic Defect Detection System and Effect of Electromagnetic Brake on Decreasing Unbalanced Flow in Mold. *ISIJ Int.* **2015**, *55*, 2135–2141. [[CrossRef](#)]
80. Lee, G.-G.; Shin, H.-J.; Thomas, B.G.; Kim, S.-H. Asymmetric Multi-phase Fluid Flow and Particle Entrapment in a Continuous Casting Mold. In Proceedings of the AISTech 2008, Pittsburgh, PA, USA, 5–8 May 2008.
81. Ren, Y.; Wang, Y.; Li, S.; Zhang, L.; Zuo, X.; Lekakh, S.N.; Peaslee, K. Detection of Non-metallic Inclusions in Steel Continuous Casting Billets. *Metall. Mater. Trans. B* **2014**, *45B*, 1291–1303. [[CrossRef](#)]
82. Jin, K.; Thomas, B.G.; Ruan, X. Modeling and Measurements of Multiphase Flow and Bubble Entrapment in Steel Continuous Casting. *Metall. Mater. Trans. B* **2016**, *47B*, 548–565. [[CrossRef](#)]
83. Demmon, F.; Gass, R.; Yin, H. Step Milling as a Tool for Characterizing Defects in Slabs at ArcelorMittal. *Iron Steel Technol.* **2015**, *12*, 82–91.
84. Yang, H.; Tehranchi, F.; Eriksson, J.-E.; Song, J. Water Modeling of Stirring and Braking Processes in a Slab Caster Mold. In Proceedings of the AISTech 2010, Pittsburgh, PA, USA, 3–6 May 2010; pp. 135–146.

85. Yang, H.; Sedén, M.; Jacobson, N.; Eriksson, J.-E.; Hackl, H. Development of the Third-Generation FC Mold by Numerical and Water Model Simulations. In Proceedings of the AISTech 2012, Atlanta, GA, USA, 7–9 May 2012.
86. Timmel, K.; Kratzsch, C.; Asad, A.; Schurmann, D.; Schwarze, R.; Eckert, S. Experimental and Numerical Modeling of Fluid Flow Processes in Continuous Casting: Results from the LIMMCAST-Project. In Proceedings of the Final LIMTECH Colloquium and International Symposium on Liquid Metal Technologies, Dresden, Germany, 19–20 September 2017; IOP Conf. Series: Materials Science and Engineering, p. 012019.
87. Wondrak, T.; Eckert, S.; Gerbeth, G.; Klotsche, K.; Stefani, F.; Timmel, K.; Peyton, A.J.; Terzija, N.; Yin, W. Combined Electromagnetic Tomography for Determining Two-phase Flow Characteristics in the Submerged Entry Nozzle and in the Mold of a Continuous Casting Model. *Metall. Mater. Trans. B* **2011**, *42B*, 1201–1210. [[CrossRef](#)]
88. Timmel, K.; Eckert, S.; Gerbeth, G. Experimental Investigation of the Flow in a Continuous-Casting Mold under the Influence of a Transverse, Direct Current Magnetic Field. *Metall. Mater. Trans. B* **2011**, *42B*, 68–80. [[CrossRef](#)]
89. Chaudhary, R.; Rietow, B.T.; Thomas, B.G. Difference between Physical Water Models and Steel Continuous Caster: A Theoretical Evaluation. In Proceedings of the Materials Science and Technology 2009, Pittsburgh, PA, USA, 25–29 October 2009; pp. 1090–1101.
90. Harada, H.; Toh, T.; Ishii, T.; Kaneko, K.; Takeuchi, E. Effect of Magnetic Field Conditions on the Electromagnetic Braking Efficiency. *ISIJ Int.* **2001**, *41*, 1236–1244. [[CrossRef](#)]
91. Launder, B.E.; Spalding, D.B. *Lectures in Mathematical Models of Turbulence*; Academic Press: London, UK, 1972.
92. Menter, F.R. Two-Equation Eddy-Viscosity Turbulence Models for Engineering Applications. *AIAA J.* **1994**, *32*, 1598–1605. [[CrossRef](#)]
93. Nicoud, F.; Ducros, F. Subgrid-Scale Stress Modelling Based on the Square of the Velocity Gradient Tensor. *Flow Turbul. Combust.* **1999**, *62*, 183–200. [[CrossRef](#)]
94. Thomas, B.G.; Yuan, Q.; Mahmood, S.; Liu, R.; Chaudhary, R. Transport and Entrapment of Particles in Steel Continuous Casting. *Metall. Mater. Trans. B* **2014**, *45B*, 22–35. [[CrossRef](#)]
95. *ANSYS FLUENT 14.5-Theory Guide*; ANSYS, Inc.: Canonsburg, PA, USA, 2012.
96. Kumar, P.; Vanka, S.P. Effects of confinement on bubble dynamics in a square duct. *Int. J. Multiphase Flow* **2015**, *77*, 32–47. [[CrossRef](#)]
97. Moreau, R. *Magnetohydrodynamics*; Kluwer Academic Publishers: Dordrecht, The Netherlands, 1990; pp. 110–164.
98. Davidson, P.A. *Introduction to Magnetohydrodynamics*, 2nd ed.; Cambridge University Press: Cambridge, UK, 2017; pp. 27–184.
99. Cho, M.J.; Kim, I.C.; Kim, S.J.; Kim, J.K. 3-D Turbulent Heat & Fluid Flow Analysis with Solidification under Electro-Magnetic Field. *Trans. KSME* **1999**, *23B*, 1491–1502.
100. Sengupta, J.; Shin, H.-J.; Thomas, B.G.; Kim, S.-H. Micrograph Evidence of Meniscus Solidification and Sub-Surface Microstructure Evolution in Continuous-Cast Ultra-Low Carbon Steels. *Acta Mater.* **2006**, *54*, 1165–1173. [[CrossRef](#)]
101. Sengupta, J.; Thomas, B.G.; Shin, H.-J.; Lee, G.-G.; Kim, S.-H. A New Mechanism of Hook Formation during Continuous Casting of Ultra-Low-Carbon Steel Slabs. *Metall. Mater. Trans. A.* **2006**, *37A*, 1597–1611. [[CrossRef](#)]
102. Takatani, K.; Nakai, K.; Kasai, N.; Watanabe, T.; Nakajima, H. Analysis of Heat Transfer and Fluid Flow in the Continuous Casting Mold with Electromagnetic Brake. *ISIJ Int.* **1989**, *29*, 1063–1068. [[CrossRef](#)]
103. Kim, D.-S.; Kim, W.-S.; Cho, K.-H. Numerical Simulation of the Coupled Turbulent Flow and Macroscopic Solidification in Continuous Casting with Electromagnetic Brake. *ISIJ Int.* **2000**, *40*, 670–676. [[CrossRef](#)]
104. Wang, Y.; Zhang, L. Fluid Flow-Related Transport Phenomena in Steel Slab Continuous Casting Strands under Electromagnetic Brake. *Metall. Mater. Trans. B* **2011**, *42B*, 1319–1351. [[CrossRef](#)]
105. Teshima, T.; Osame, M.; Okimoto, K.; Nimura, Y. Improvement of Surface Property of Steel at High Casting Speed. In Proceedings of the 71th Steelmaking Conference, Toronto, Canada, 17–20 April 1988; pp. 111–118.
106. Hwang, Y.-S.; Cha, P.-R.; Nam, H.-S.; Moon, K.-H.; Yoon, J.-K. Numerical Analysis of the Influences of Operational Parameters on the Fluid Flow and Meniscus Shape in Slab Caster with EMBR. *ISIJ Int.* **1997**, *37*. [[CrossRef](#)]

107. Tian, X.-Y.; Li, B.-W.; He, J.-C. Electromagnetic Brake Effects on the Funnel Shape Mold of a Thin Slab Caster Based on a New Type Magnet. *Metall. Mater. Trans. B* **2009**, *40B*, 596–604. [[CrossRef](#)]
108. Zhang, L.-S.; Zhang, X.-F.; Wang, B.; Liu, Q.; Hu, Z.-G. Numerical Analysis of the Influences of Operational Parameters on the Braking Effect of EMBR in a CSP Funnel- Type Mold. *Metall. Mater. Trans. B* **2014**, *45B*, 295–306. [[CrossRef](#)]
109. Xu, L.; Wang, E.; Karcher, C.; Deng, A.; Xu, X. Numerical Simulation of the Effects of Horizontal and Vertical EMBR on Jet Flow and Mold Level Fluctuation in Continuous Casting. *Metall. Mater. Trans. B* **2018**, *49B*, 2779–2793. [[CrossRef](#)]
110. Li, F.; Wang, E.; Feng, M.; Li, Z. Simulation Research of Flow Field in Continuous Casting Mold with Vertical Electromagnetic Brake. *ISIJ Int.* **2015**, *55*, 814–820. [[CrossRef](#)]
111. Li, Z.; Wang, E.; Zhang, L.; Xu, Y.; Deng, A. Influence of Vertical Electromagnetic Brake on the Steel/Slag Interface Behavior in a Slab Mold. *Metall. Mater. Trans. B* **2017**, *48B*, 2389–2402. [[CrossRef](#)]
112. Cho, S.-M.; Thomas, B.G.; Kim, S.-H. Transient Fluid Flow during Steady Continuous Casting of Steel Slabs: Part II. Effect of Double-Ruler Electro-Magnetic Braking. *ISIJ Int.* **2014**, *54*, 855–864. [[CrossRef](#)]
113. Cho, S.-M.; Thomas, B.G.; Kim, S.-H. Transient Two-Phase Flow in Slide-Gate Nozzle and Mold of Continuous Steel Slab Casting with and without Double-Ruler Electro-Magnetic Braking. *Metall. Mater. Trans. B* **2016**, *47B*, 3080–3098. [[CrossRef](#)]
114. Singh, R.; Thomas, B.G.; Vanka, S.P. Large Eddy Simulations of Double-Ruler Electromagnetic Field Effect on Transient Flow During Continuous Casting. *Metall. Mater. Trans. B* **2014**, *45B*, 1098–1115. [[CrossRef](#)]
115. Yu, H.; ZHU, M. Numerical Simulation of the Effects of Electromagnetic Brake and Argon Gas Injection on the Three-dimensional Multiphase Flow and Heat Transfer in Slab Continuous Casting Mold. *ISIJ Int.* **2008**, *48*, 584–591. [[CrossRef](#)]
116. Sarkar, S.; Singh, V.; Ajmani, S.K.; Singh, R.K.; Chanko, E.Z. Effect of Argon Injection in Meniscus Flow and Turbulence Intensity Distribution in Continuous Slab Casting Mold Under the Influence of Double Ruler Magnetic Field. *ISIJ Int.* **2018**, *58*, 68–77. [[CrossRef](#)]
117. Sarkar, S.; Singh, V.; Ajmani, S.K.; Ranjan, R.; Rajasekar, K. Effect of Double Ruler Magnetic Field in Controlling Meniscus Flow and Turbulence Intensity Distribution in Continuous Slab Casting Mold. *ISIJ Int.* **2016**, *56*, 2181–2190. [[CrossRef](#)]
118. Li, B.; Okane, T.; Umeda, T. Modeling of Molten Metal Flow in a Continuous Casting Process Considering the Effects of Argon Gas Injection and Static Magnetic-Field Application. *Metall. Mater. Trans. B* **2000**, *31B*, 1491–1503. [[CrossRef](#)]
119. Idogawa, A.; Sugizawa, M.; Takeuchi, S.; Sorimachi, K.; Fujii, T. Control of Molten Steel Flow in Continuous Casting Mold by Two Static Magnetic Fields Imposed on Whole Width. *Mater. Sci. Eng. A* **1993**, *A173*, 293–297. [[CrossRef](#)]
120. Kunstreich, S.; Gautreau, T.; Ren, J.Y.; Codutti, A.; Guastini, F.; Petronio, M. Development and Validation of Multi-Mode® EMB, a New Electromagnetic Brake for Thin Slab Casters. In Proceedings of the 8th European Continuous Casting Conference, Graz, Austria, 23–26 June 2016.
121. Kubo, N.; Kubota, J.; Suzuki, M.; Ishii, T. Molten Steel Flow Control under Electromagnetic Level Accelerator in Continuous Casting Mold. *ISIJ Int.* **2007**, *47*, 988–995. [[CrossRef](#)]
122. Kubo, N.; Ishii, T.; Kubota, J.; Ikagawa, T. Numerical Simulation of Molten Steel Flow under a Magnetic Field with Argon Gas Bubbling in a Continuous Casting Mold. *ISIJ Int.* **2004**, *44*, 556–564. [[CrossRef](#)]
123. Okazawa, K.; Toh, T.; Fukuda, J.; Kawase, T.; Toki, M. Fluid Flow in a Continuous Casting Mold Driven by Linear Induction Motors. *ISIJ Int.* **2001**, *41*, 851–858. [[CrossRef](#)]
124. Yin, Y.; Zhang, J.; Lei, S.; Dong, Q. Numerical Study on the Capture of Large Inclusion in Slab Continuous Casting with the Effect of In-mold Electromagnetic Stirring. *ISIJ Int.* **2017**, *57*, 2165–2174. [[CrossRef](#)]
125. Li, B.; Okane, T.; Umeda, T. Modeling of Biased Flow Phenomena Associated with the Effects of Static Magnetic-Field Application and Argon Gas Injection in Slab Continuous Casting of Steel. *Metall. Mater. Trans. B* **2001**, *32B*, 1053–1066. [[CrossRef](#)]
126. Moon, K.H.; Shin, H.K.; Kim, B.J.; Chung, J.Y.; Hwang, Y.S.; Yoon, J.K. Flow Control of Molten Steel by Electromagnetic Brake in the Continuous Casting Mold. *ISIJ Int.* **1996**, *36*, S201–S203. [[CrossRef](#)]
127. Liu, Z.; Vakhrushev, A.; Wu, M.; Karimi-Sibaki, E.; Kharicha, A.; Ludwig, A.; Li, B. Effect of an Electrically-Conducting Wall on Transient Magnetohydrodynamic Flow in a Continuous-Casting Mold with an Electromagnetic Brake. *Metals* **2018**, *8*, 609. [[CrossRef](#)]

128. Miao, X.; Timmel, K.; Lucas, D.; Ren, Z.; Eckert, S.; Gerbeth, G. Effect of an Electromagnetic Brake on the Turbulent Melt Flow in a Continuous-Casting Mold. *Metall. Mater. Trans. B* **2012**, *43B*, 954–972. [[CrossRef](#)]
129. Tian, X.-Y.; Zou, F.; Li, B.-W.; He, J.-C. Numerical Analysis of Coupled Fluid Flow, Heat Transfer and Macroscopic Solidification in the Thin Slab Funnel Shape Mold with a New Type EMBr. *Metall. Mater. Trans. B* **2010**, *41B*, 112–120. [[CrossRef](#)]
130. Hwang, J.Y.; Cho, M.J.; Thomas, B.G.; Cho, S.M. Numerical Simulation of Turbulent Steel CEM[®] Mold under High Mass Flow Condition. In Proceedings of the 9th International Symposium on Electromagnetic Processing of Materials (EPM2018), Hyogo, Japan, 14–18 October 2018; p. 012033.
131. Satou, Y.; Baba, N.; Kasai, N.; Mutou, A.; Hanao, M. Increase of Casting Speed of Hypo-peritectic Steel at Kashima No.3 Caster. In Proceedings of the AISTech 2009, St. Louis, MO, USA, 4–7 May 2009; pp. 663–671.
132. Wang, S.; Zhang, X.; Zhang, L.; Wang, Q. Influence of Electromagnetic Brake on Hook Growth and Inclusion Entrapment beneath the Surface of Low-Carbon Continuous Casting Slabs. *Steel Res. Int.* **2018**, *89*, 1800263. [[CrossRef](#)]
133. Zhang, L.; Aoki, J.; Thomas, B.G. Inclusion Removal by Bubble Flotation in a Continuous Casting Mold. *Metall. Mater. Trans. B* **2006**, *37B*, 361–379. [[CrossRef](#)]
134. Gass, R.; Knoepke, H.; Moscoe, J.; Shah, R.; Beck, J.; Dzierzawski, J.; Ponikvar, P.E. Conversion of Ispat Inland's No. 1 Slab Caster to Vertical Bending. In Proceedings of the ISSTech 2003 Conference, Indianapolis, Indiana, 27–30 April 2003; pp. 3–18.
135. Jin, K.; Kumar, P.; Vanka, S.P.; Thomas, B.G. Rise of an argon bubble in liquid steel in the presence of a transverse magnetic field. *Phys. Fluids* **2016**, *28*, 093301. [[CrossRef](#)]
136. Wang, Y.; Dong, A.; Zhang, L. Effect of Slide Gate and EMBr on the Transport of Inclusions and Bubbles in Slab Continuous Casting Strands. *Steel Res. Int.* **2011**, *82*, 428–439. [[CrossRef](#)]
137. Yuan, Q.; Thomas, B.G.; Vanka, S.P. Study of Transient Flow and Particle Transport in Continuous Steel Caster Molds: Part II. Particle Transport. *Metall. Mater. Trans. B* **2004**, *35B*, 703–714. [[CrossRef](#)]
138. Jin, K.; Vanka, S.P.; Thomas, B.G. Large Eddy Simulations of Electromagnetic Braking Effects on Argon Bubble Transport and Capture in a Steel Continuous Casting Mold. *Metall. Mater. Trans. B* **2018**, *49B*, 1360–1377. [[CrossRef](#)]
139. Shibata, H.; Yin, H.; Yoshinaga, S.; Emi, T.; Suzuki, M. In-situ Observation of Inclusions in Steel Melt Engulfment and Pushing by Advancing Melt/Solid of Nonmetallic Interface. *ISIJ Int.* **1998**, *38*, 149–156. [[CrossRef](#)]
140. Lee, S.-M.; Kim, S.-J.; Kang, Y.-B.; Lee, H.-G. Numerical Analysis of Surface Tension Gradient Effect on the Behavior of Gas Bubbles at the Solid/Liquid Interface of Steel. *ISIJ Int.* **2012**, *52*, 1730–1739. [[CrossRef](#)]
141. Pesteau, O. The Washing Effect in Electromagnetic Rotational Stirrers for Continuous Casting. *ISIJ Int.* **2005**, *45*, 1073–1075. [[CrossRef](#)]
142. Pesteau, O. Short Contribution to the Study of the Washing Effect in Electromagnetic Stirrers for Continuous Casting. *ISIJ Int.* **2003**, *43*, 1861–1862. [[CrossRef](#)]
143. Toh, T.; Hasegawa, H.; Harada, H. Evaluation of Multiphase Phenomena in Mold Pool under In-mold Electromagnetic Stirring in Steel Continuous Casting. *ISIJ Int.* **2001**, *41*, 1245–1251. [[CrossRef](#)]
144. Kittaka, S.; Fukukaya, T.; Maruki, Y.; Kanki, T. *Nippon Steel Strand Electro-Magnetic Stirrer "S-EMS" for Slab Caster*; Nippon Steel: Tokyo, Japan, 2003; pp. 70–74.
145. Xu, Y.; Xu, X.-J.; Li, Z.; Wang, T.; Deng, A.-Y.; Wang, E.-G. Dendrite Growth Characteristics and Segregation Control of Bearing Steel Billet with Rotational Electromagnetic Stirring. *High Temp. Mater. Proc.* **2017**, *36*, 339–346. [[CrossRef](#)]
146. Shibata, H.; Itoyama, S.; Kishimoto, Y.; Takeuchi, S.; Sekiguchi, H. Prediction of Equiaxed Crystal Ratio in Continuously Cast Steel Slab by Simplified Columnar-to-Equiaxed Transition Model. *ISIJ Int.* **2006**, *46*, 921–930. [[CrossRef](#)]
147. Bridge, M.R.; Rogers, G.D. Structural Effects and Band Segregate Formation during the Electromagnetic Stirring of Strand-Cast Steel. *Metall. Trans. B.* **1984**, *15B*, 581–589. [[CrossRef](#)]





Article

Flow Characteristics for Two-Strand Tundish in Continuous Slab Casting Using PIV

Jun Huang *, Zhigang Yuan, Shaoyuan Shi, Baofeng Wang and Chi Liu *

School of Energy and Environment, Inner Mongolia University of Science and Technology, Baotou 014010, China; 18940046801@163.com (Z.Y.); shishaoyuan@126.com (S.S.); 13327185758@163.com (B.W.)

* Correspondence: hjun8420@imust.edu.cn (J.H.); liuchiyd@163.com (C.L.);

Tel.: +86-472-595-1568 (J.H.); +86-131-9070-8932 (C.L.)

Received: 4 January 2019; Accepted: 14 February 2019; Published: 17 February 2019

Abstract: With the development of continuous casting technology, there has been an increase in the stringent requirements for the cleanliness and quality of steel being produced. The flow state of molten steel in tundish is the key to: Optimizing the residence time of molten steel in the tundish; homogenizing the temperature of molten steel; and removing inclusions by floatation. Hence, from theoretical and practical aspects, it is imperative to examine and analyze the flow field of molten steel in the tundish in order to ensure the desired molten steel flow. In this study, a two-strand tundish with 650 mm × 180 mm slab casting is considered as the subject for this research. According to the similarity theory, combined with the geometrical shape and dimension of the prototype tundish, a tundish model with a geometric similarity ratio of 2:3 is established in the laboratory. Digital particle image velocimetry (PIV) is employed to measure and examine the flow fields at different casting speeds for a tundish containing different flow control devices. The flow in the tundish is typically turbulent and also consists of a vortex motion; it exhibits both random and ordered characteristics. Results reveal that the presence of baffles with 15° holes can cause an upward-directed flow in the outlet section and give rise to a large circulation. When the casting speed is doubled, the overall velocity of the flow field and turbulent intensity increase, leading to an increase in the molten steel surface velocity.

Keywords: steel tundish; baffle; flow field; velocity; PIV

1. Introduction

The main function of the tundish is to act as a steel reservoir between the ladle and the mold, and in the case of multi-strand casters, to distribute the liquid into the molds. In addition to being a reservoir of liquid steel, the tundish is more increasingly used as a metallurgical reactor vessel aimed at improving control of steel cleanliness, temperature, and composition. Tundish metallurgy was proposed in the early 1980s as a special secondary refining technology and an important link in ensuring excellent steel quality during production from smelting and refining to the formation of slabs or billets [1]. In the past three decades, many experts and researchers have done a lot of work and published many important papers. A comprehensive review was given in the paper by Sahai [2] and the book by Sahai and Emi [3].

The basic physical phenomenon in the tundish involves the flow of molten steel. The metallurgical effect of the tundish is mainly achieved by the reasonable flow of molten steel in the tundish. The flow is intended to deliver the molten metal to the molds evenly and at a designed throughput rate and temperature with minimal contamination by, and maximize flotation of macro inclusions. Hence, the investigation of the flow phenomenon in the tundish is the foundation of tundish metallurgy.

Physical modeling has played a key role in tundish research [4–6]. In physical modeling, a low temperature aqueous analog, generally water, is used to represent molten metal in a tundish.

In particular, the kinematic viscosity of water is similar to that of molten steel. Water flow in a transparent model tundish can be used to observe melt flow physically taking place in an actual tundish. A full or reduced scale tundish model may be designed based on appropriate similarity criteria in which the flow of molten metal is simulated by the flow of water. As water flow in the model is a realistic representation of the actual tundish melt flow, it may be used to study the melt flow in a tundish.

According to the similarity principle for flow phenomena, the use of a water model to investigate the flow of molten steel in tundish is not only feasible, but also can accurately reflect the values and law of the actual flow of molten steel. However, in the actual hydraulics simulation of a tundish, it is difficult to completely maintain all forces to be equal between the model and the prototype; hence, different situations need to be considered. In a water simulation experiment using a reduced-scale model, it is imperative to use an approximate model method to ensure that the flow in the model is similar to that in the prototype.

Based on flow visualization and image processing technology, a digital image technique has been developed, which combines single point measurement technology (hotline, turbine) and flow visualization technology. Digital image measurement technology can not only achieve the overall structure and transient image field, but also obtain the velocity data of the whole flow field quantitatively. Some researchers [7–9] have measured the flow field in the tundish by the particle image velocimetry (PIV), thus that the overall structure and transient image of a planar flow field was obtained quantitatively.

Many attempts have been made to improve melt flow characteristics in existing tundish's by the installation of various flow control devices, such as weirs, dams, baffles with holes, and turbulence suppressors. The beneficial effects of various flow modification devices have been applied in actual industrial trials as well as physical and mathematical modeling studies [10,11]. Optimum placement of flow control devices has been found to result in an increase in the average residence time of fluid as well as an increase in the plug flow volume in the tundish. These flow control devices, properly installed, may create localized mixing in contained regions, which may help in inclusion agglomeration and hence, inclusion removal.

Due to the limited of view of the camera in PIV, developing an approach for measuring a water model with a length close to 5m is an important problem to be solved in this paper. In this study, the PIV flow measurement is carried out for a reduced-scale two-strand tundish model for slab production. The paper analyzes the flow characteristics in a two-strand tundish for continuous slab casting with different flow-control devices. The effect of eddies is discussed.

2. Experimental Object and Scheme

To transfer results of measurements from a model to the original tundish, apart from the geometric similarity, the fluid-dynamic similarity must be considered as well. For an isothermal water model experiment, geometrical similarity, and dynamic similarity between the model and the prototype are required. In order to maintain similarity in depth of liquid, the relationship between the velocities and hence the inlet flow rate of the fluid in the model and in the prototype is to be obtained by following either of Froude (Fr) similarity or Reynolds (Re) similarity. For the dynamic similarity, the Re number and Fr number in the model should be equivalent to those in the prototype. As steel flow in the tundish is gravity-driven, it is understood that flow inside the tundish is Froude criteria dominated. As the flow of liquid steel within the tundish is severely turbulent, the Re number of the model is in the same self-modelling region as the prototype, the Re number can meet the requirement naturally. Thus, most reduced scale-modeling studies are done mainly based on Froude similarity criteria [12].

In the experiments, a two-strand tundish of a stainless-steel slab continuous casting is used as the experimental object. The tundish model in the hydraulics experiment comprised clear glass with a 2:3 ratio to the prototype. The flow rate passing the long nozzle in the experiment is determined on the basis of the typical sectional dimension of the cast slab, i.e., 180 mm × 650 mm, and casting speed.

The typical casting speed is 1.2 m/min. The long nozzle diameter is 75 mm. The main dimensions of the water model are shown in Figure 1, all dimensions are in millimeters. The scale factor of 2:3 is defined as the ratio of lengths in the model and prototype systems to ensure geometric similarity.

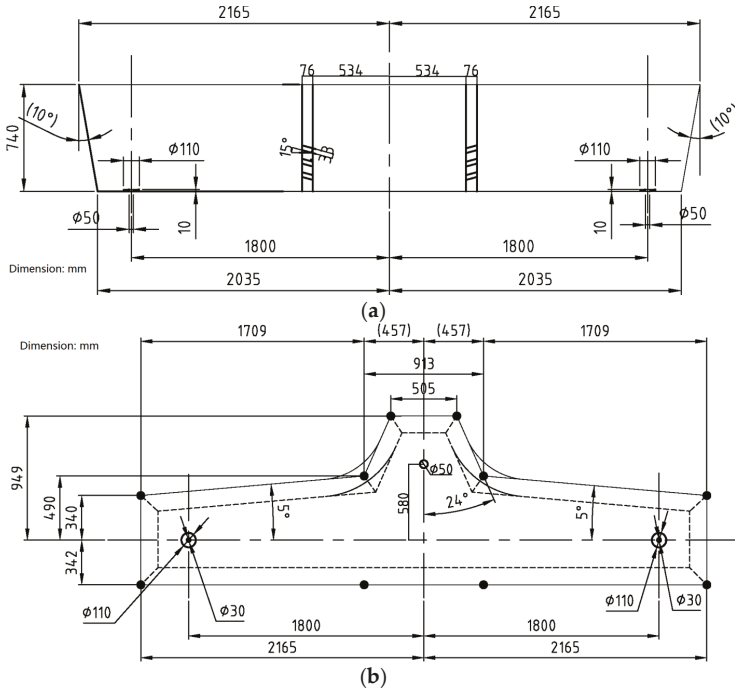


Figure 1. Two-strand tundish water model (a) shell diagram; (b) control device.

To satisfy the Froude similarity, the Froude number of the water model should be equal to that of the prototype:

$$Fr = \frac{v^2}{gl} = \frac{v'^2}{gl'} \quad (1)$$

The similarity ratio in velocity can be obtained (model velocity/prototype velocity):

$$\frac{v'}{v} = \sqrt{\frac{l'}{l}} = \lambda^{0.5} = \left(\frac{2}{3}\right)^{0.5} \quad (2)$$

The similarity ratio in the flowrate can be obtained (model flowrate /prototype flowrate):

$$\frac{Q'}{Q} = \frac{l'^2 \times v'}{l^2 \times v} = \lambda^{2.5} = \left(\frac{2}{3}\right)^{2.5} \quad (3)$$

where v and v' represent the velocity of the fluid in the tundish in the prototype and model respectively, m/s; g is the gravitational acceleration, m/s²; l is the characteristic length, m; λ is the similarity ratio, Q and Q' are the flowrate in the tundish in the prototype and model respectively, m³/h.

In the water simulation experiment, the quantity of poured steel is controlled by the flowrate at the long nozzle, meanwhile the liquid level is controlled by the level gauge in the tundish model. Table 1 summarizes the concrete experimental parameters of the tundish prototype and the water model.

Table 1. Experimental parameters of the tundish prototype and water model.

Object	Melt Depth in Tundish/mm	Volume/m ³	Long Nozzle Inserted Depth/mm	Flowrate/(m ³ /h)
Prototype	900	6.00	250	8.42
Model	600	1.78	167	3.06

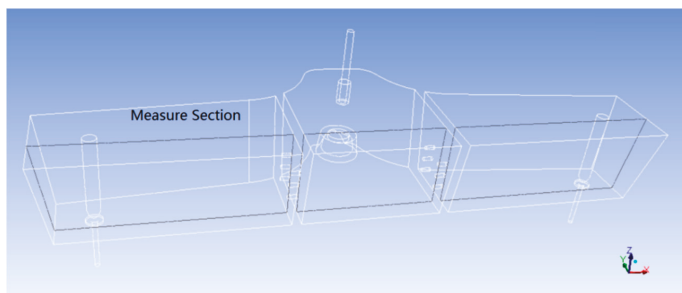
Fluid flow characteristics in the tundish with the incorporation of flow control devices is dependent on the optimum location and size. Numerical simulations have been used to optimize current control devices and installation locations. The optimized results are obtained by numerical simulation and must be validated by actual water simulation experiments. Scheme A is an optimization scheme, while the other three are in contrast to it. The installation location and size of these devices is shown in Figure 1. The flow control devices in the tundish mainly include the baffles with holes and the turbulence suppressor. Table 2 summarizes the experimental scheme. Experiments are carried out in the presence or absence of the flow control device and different casting speeds. The baffles with holes are placed in the middle of the tundish. The baffles are perpendicular to the walls of the tundish. Each baffle has six circular holes with a diameter of 33 mm and an upward inclination of 15°. To highlight the effect of the flow control device on the flow, the casting speed is doubled for comparing and manifesting the results obtained from the flow test.

Table 2. Experimental scheme and relevant processing parameters of tundish.

No.	Flow Control Device	Prototype Casting Speed/(m/min)
A	baffles with holes and suppressor	1.2
B	baffles with holes and suppressor	2.4
C	Suppressor only	1.2
D	Suppressor only	2.4

The model tundish is placed on the experimental platform, and water pipelines are connected. After setting the experimental parameters and waiting for 30 min for the flow to become steady, PIV flow measurement starts.

According to the flow path of the molten steel in the tundish, the measuring section is shown in Figure 2. The measurement section is sequentially scanned with the PIV. The photographs by PIV are processed by PIVview software, then the flow field diagrams from different locations are merged into the full section. PIVview is a compact program package for the evaluation of particle image velocimetry with the PIV-Groups of the German Aerospace Center. The software is developed in close cooperation with the Institute of Aerodynamics and Flow Technology of the German Aerospace Center in Goettingen, Germany.

**Figure 2.** Schematic of the measuring section positions in the tundish.

3. PIV Measurement Process

Figure 3 shows the hardware structure diagram of the test system developed in this study for the flow field. A certain number of tracing particles are evenly dispersed in the flow field. The 2D flow field with an approximate thickness of 3 mm is illuminated by a sheet light source comprising a laser and its lens. Two high-resolution cameras are arranged along the vertical direction of the laser to form a camera array, which can record the trajectory of the tracing particles of a particular frequency under the illumination of the sheet light source. The time interval between the two pulses of the laser that illuminate the flow field is set to meet the camera's recording frequency and synchronize the camera's recording frequency with the laser's stroboscopic frequency using the synchronizer, which are similar to commercial PIV requirements in that two continuous frames can be continuously recorded in a short time period. The use of a multi-camera array can meet the measurement for a large sight field. The machine vision systems are employed related to the acquisition and processing of data during the image recognition and velocity measurements, enabling the system to solve low-speed measurement problems at a lower cost. The motion drive unit controlled by the servo motor can meet the requirements of segmentation measurement. Combined with the camera array setting, it can meet the measurement requirement for velocity in a wider range, which also provides the necessary hardware and software conditions for implementing the different scale measurement for the flow field in the tundish.

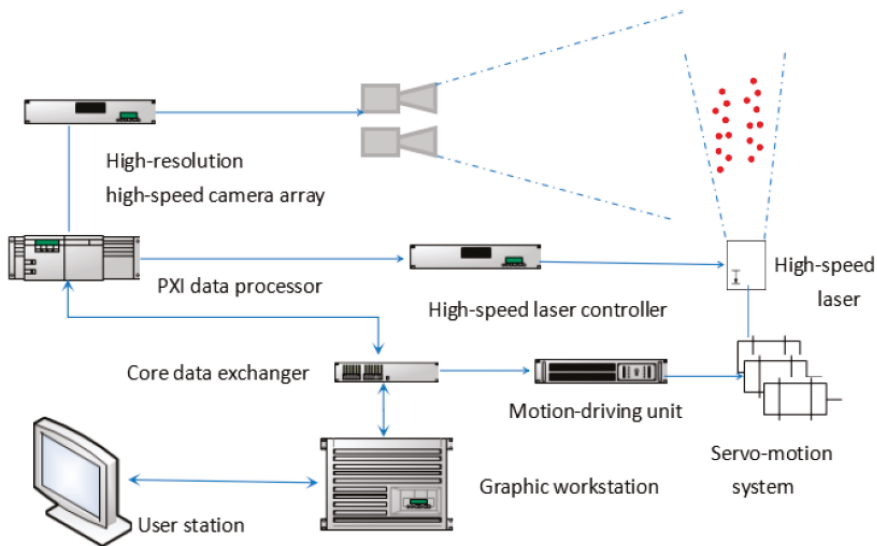


Figure 3. Diagram of the particle image velocimetry (PIV) system.

Owing to the low flow velocity in the tundish (average velocity $< 1.0 \text{ m}\cdot\text{s}^{-1}$), the continuous shooting mode of a digital camera with a fixed number of frames can meet the requirement to trace particles. The method does not require two consecutive frames in an extremely short time ($5 \mu\text{s}$) as it does by the PIV technology and only needs to ensure the synchronization between the continuous shooting speed of the digital camera and the laser strobe flash, hence, the measurement system can not only decrease the price, but also the array comprising multiple cameras can meet the requirements for obtaining a large field of view simultaneously. The image acquisition system for the flow field in the experimental tundish mainly comprises of an MGL-N-532 laser source, two Canon 5D MARK III cameras (Tokyo, Japan) and the background control and data processing software, which is shown in Figure 4. The laser emitted by the MGL-N-532 laser is the green laser with a wavelength of 532 nm

and a shooting frequency of 30 Hz. Polystyrene beads with a density of 1.02 g/cm^3 and a diameter of $50 \text{ }\mu\text{m}$ are tracing particles. Similar to a commercial PIV system, the displacement of tracing particles is obtained by the cross-correlation algorithm for the two images in the tested area, and the data are processed by the authorized PIVview software to display the two-dimensional velocity vector field within the areas in which velocity is measured [13].

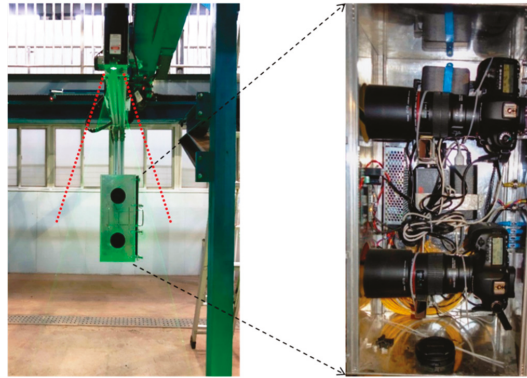


Figure 4. The image acquisition system.

As the sectional flow field of the tundish water model exceeds the shooting range of the camera array, the sectional flow field of the entire tundish water model must be obtained by the image stitching method. Although the measuring moments for different areas are not the same, the stitched image can reflect the flow distribution characteristics in the cross section.

4. Experimental Results and Discussion

Figure 5 shows the sectional flow field of the tundish with PIV measurements and numerical under schemes A. The position of the measured and simulated results is the same. The simulation shows only half. The position of two baffles with holes is indicated in the diagram. Of the black stripes that appear in the PIV measurement drawing, three are the supporting frames in the process of making the tundish model. The white stripes represent the results of different cameras at different times in Figure 5c. The results obtained from the different method are shown together.

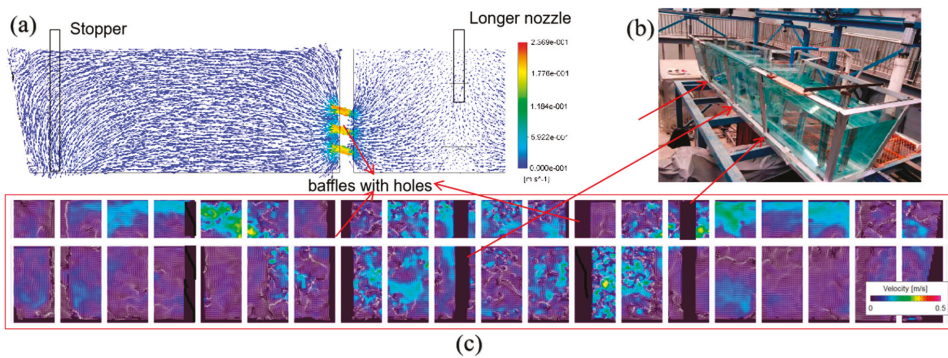


Figure 5. Flow measurement and simulation result of scheme A; (a) numerical simulation; (b) experimental setup; (c) PIV measurements.

Figure 5c shows a very detailed velocity field in which the flow is more active in the inlet section. The very marked large circulation is readily apparent from the plot. It can be seen that flow in the tundish is a local pulse, partially rendering a lot of mixing, but the overall flow shows the trend of a certain flow movement.

Figure 5a also shows the flow field for the numerical simulation results obtained by test scheme A. The commercial CFD package FLUENT with ANSYS 15.0 is used to model and solve the tundish fluid flow and it is compared with the available experiment results. The tundish with a long nozzle and exit is modelled. A non-uniform Cartesian mesh is used, with a power-law expansion of cells from the walls outwards. The finest cells are placed next to the jet-impact wall, since that is where maximum resolution is needed for the fast-moving boundary layers. A fine mesh is also used to cover the jet region. In order to test the grid independence of the results, it is necessary to test the sensitivity of the results on the number of mesh points used. A total of about 8,500,000 cells are used in the finest calculation. The mathematical model is based on the assumptions of continuum hypothesis, the standard two equation model, k - ϵ equation is used to model the turbulence. A steady-state incompressible solution is adopted, with the main dependent variables being the pressure, three velocity components and the two turbulent quantities. The SIMPLE (Semi-Implicit Method for Pressure Linked Equations) algorithm is used for the pressure-velocity coupling and QUICK (Quadratic Upstream Interpolation for Convective Kinetics) scheme is used for discretization of momentum, turbulent equations.

As can be observed from the measurement results, the flow complexity in the tundish is far from the simple recirculating flow that is obtained by the Reynolds-averaged Navier-Stokes (RANS) equations, plus an appropriate turbulence model, combining large circulation and small-scale eddies. To gain more knowledge about the transient turbulence process, which cannot be achieved via Reynolds-averaged equations solutions, large-eddy simulations (LES) of the tundish flow field are performed. Alkishriwi et al. [14,15] and Jha et al. [16,17] have carried out such simulations to investigate the turbulent flow structure and vortex dynamics. They have confirmed that the metallurgical effect of the tundish is mainly accomplished by the flow behavior. LES simulation of the flow field in a tundish is conducted to analyze the flow structure, which determines to a certain extent the steel quality. Many intricate flow details have not been observed by customary RANS approaches.

The motion of the liquid steel is generated by jets into the tundish and continuous casting mold. The flow regime is mostly turbulent, but some turbulence attenuation can occur far from the inlet. The characteristics of the flow in a tundish include jet spreading, jet impingement on the wall, wall jets, and an important decrease of turbulence intensity in the core region of the tundish far from the jet. Compared to the numerical simulation, physical simulation for the flow field provides more details on the evolution of not only velocity but also eddies. Mathematical modeling may provide a much more detailed picture of velocity, turbulence, and temperature fields as a function of location and time. In general, the numerical simulation shows the flow trend, while the water simulation work presents flow details. The two means complement each other and provide a comprehensive understanding of the flow.

Figures 6–8 shows the flow for schemes B, C, and D. C and D do not have baffles with holes. These results also show turbulent flow behavior in the tundish. Eddies can be clearly seen by measurement. Moreover, the evolution and interaction between eddies can be observed by the measurement of a large amount of transient data.

As can be seen from the results of the flow field in the tundish, the flow is typically turbulent and consists of eddies in motion. Turbulence exhibits random and orderly characteristics. One of its basic structures includes the eddies having various scales. Statistically, a large number of random small eddies form the background flow field, and large-scale eddies structures with quasi-ordered structures are statistically significant. The large eddies are limited and affected by flow boundary conditions and flow interfaces. The large eddies contain the turbulent kinetic energy, which is associated with the fluctuating velocity components. The small eddies, which are called the micro scale of turbulence, sometimes do not show up due to the limitation of image sampling setting and image resolution in

PIVview. According to turbulence theory, the turbulent kinetic energy is being dissipated in the smaller eddies. The small eddies may also play an important role in promoting the coalescence of inclusion particles [12].

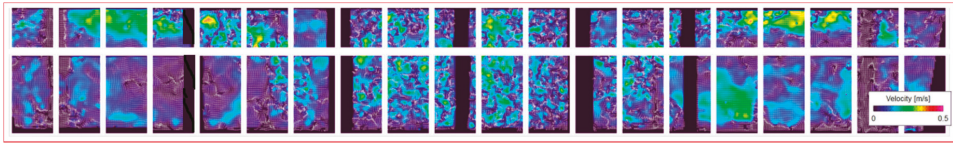


Figure 6. Flow measurement results obtained by scheme B.

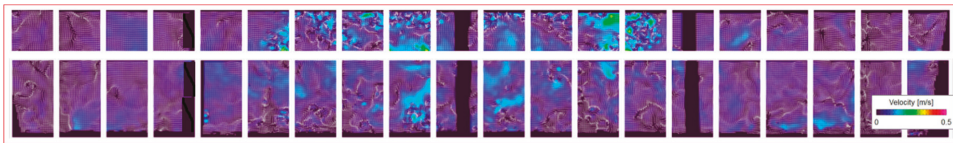


Figure 7. Flow measurement results obtained by scheme C.

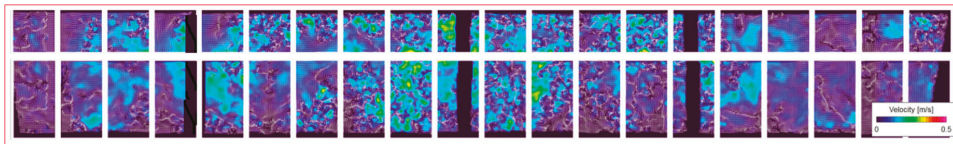


Figure 8. Flow measurement results obtained by scheme D.

The very important manifestation of turbulent flow is the presence of the eddies. The turbulent fluctuations will bring about a very effective mixing, mass (and also heat and momentum) can be readily transported by the eddies from one part of the fluid to the other [12]. The metallurgical effect of the tundish needs to be exerted via the transmission effect of these eddies.

The eddy is a flowing form, the vorticity is a physical quantity. The mathematical definition of vorticity is extremely clear. The curl of the flow field is defined as the vorticity:

$$\vec{\omega} = \nabla \times \vec{V} \quad (4)$$

where \vec{V} is the velocity, m/s; $\vec{\omega}$ is the vorticity, 1/s; ∇ is the nabla operator. From the definition of vorticity, vorticity is caused by the velocity gradient in the flow field. The positions at which the velocity gradients are large exhibit high strain rates according to Newton's law of viscosity, the flow's viscosity depends on the strain rate. A causal relationship clearly exists between the vorticity and viscosity of the fluid. For homogeneous incompressible fluids, the vorticity is generated from the fluid-solid interface. Besides moving with the flow, the vorticity diffuses like heat. At the inlet section of the tundish, the impacting jet on the turbulence suppressor generates a large number of eddies. Owing to the fluid viscosity and flow control device, a large number of eddies are generated. For preventing the entrapped slag, the molten steel is required to flow out of the tundish outlet in a stable manner. With respect to the aspects of satisfying the requirements of process and the improvement on the metallurgical effect, the application of either a flow control device or a plug rod or increase in the distance between the inlet and outlet can avoid the interference of the inlet's strong vortex flow on the outlet.

For a casting speed of $1.2 \text{ m}\cdot\text{s}^{-1}$ the theoretical velocity in the outlet section can be calculated to be $0.001 \text{ m}\cdot\text{s}^{-1}$ according to the flow rate and sectional area of the tundish. At such low relative average velocity, it is difficult to produce relatively intense heat, mass, and momentum transfer. However,

owing to the strong impacting jet action occurring near the long nozzle and the effect of the flow control device, the turbulence occurring in the tundish is clear, and a large number of eddies exist.

By the comparison between the presence and absence of the baffles with holes, the flow control device exerts a fundamental change in the flow within the tundish. In the absence of the flow control device, the turbulent areas concentrate near the long nozzle. According to the analysis related to the reason for the generation of the flow eddies in the tundish, owing to the presence of the flow control device inside the tundish and the number of fluid–solid interfaces increasing, the vorticity generating positions increase, intensifying the momentum exchange of the internal flow and making the overall flow easily uniform.

In the presence of the baffles with holes, the flow is in accordance with the requirement of the designed flow control device, especially in the flow direction and flow velocity. After flow passes through the inlet section, the flow is “thrown up” through the 15° holes to the outlet section surface and flows out from the outlet after sufficient exchange with the surface. Simultaneously, a large circulation is formed in the outlet section. The flow control devices, properly installed, may create localized mixing in contained regions, which may help in inclusion agglomeration and hence, their removal [18].

By doubling the casting speed, the shape of the flow does not significantly change. The overall velocity of the flow field and the turbulent intensity increase. In the presence of the flow control device, the surface velocity in water simulation can reach $0.3 \text{ m}\cdot\text{s}^{-1}$. After similarity conversion, the velocity of molten steel reaches $0.37 \text{ m}\cdot\text{s}^{-1}$. Such high speed may destroy the slag layer in the industrial production. Higher surface velocity could cause tundish slag entrainment at the slag/metal boundary due to turbulence arising and also cause refractory erosion near the nozzle or stopper, which requires the use of more expensive refractory practices.

By the millimeter-level spatial resolution of the tundish flow and the measurement and display at the millisecond-level time dimension scale, it is possible to achieve the precise understanding of the flow in the tundish. After combining the reality of the eddy structure and the evolution of eddies, an extremely comprehensive and precise understanding on the flow within the tundish can be achieved. These results provide a good precondition for examining the metallurgical effects of other tundishes on the basis of understanding the flow.

5. Conclusions

- (1) Based on camera array scanning, reduced-scale two-strand water tundish flow fields are obtained at different casting speeds using different flow control devices. Flow measurement results show richer flow-field details than RANS simulation.
- (2) There is a typical turbulent flow as well as vortex motions simultaneously in the tundish. The flow-control device and the boundary have an effect on the generation and dissipation of eddies, which has an important influence on the metallurgical effect of the tundish.
- (3) Baffles with 15° holes can cause an upward-directed flow in the outlet section and form a large circulation. Eddies are generated and the flow in the tundish tends to be more uniform. As the casting speed is doubled, the overall velocity of the flow field and the turbulent intensity increase, resulting in a molten steel surface velocity of up to 0.37 m/s.

Author Contributions: Conceptualization, J.H. and B.W.; methodology, J.H.; formal analysis, Z.Y.; investigation, S.S. and J.H.; resources, J.H.; data curation, S.S. and C.L.; writing—original draft preparation, B.W.; writing—review and editing, J.H.; visualization, C.L. and Z.Y.; supervision, Z.Y.; project administration, J.H.; funding acquisition, J.H. and B.W.

Funding: The work was supported by the China National Heavy Machinery Research Institute Co., Ltd. and Natural Science Foundation of Inner Mongolia under Grant 2017MSLH0534.

Acknowledgments: The author would like to thanks Baotou Lianfang High Tech Co., Ltd. for their technical support.

Conflicts of Interest: The authors declare no conflict of interest.

References

1. Mazumdar, D. Tundish metallurgy: Towards increased productivity and clean steel. *Trans. Indian Inst. Met.* **2013**, *66*, 597–610. [[CrossRef](#)]
2. Sahai, Y. Tundish technology for casting clean steel: A review. *Metall. Mater. Trans. B-Process Metall. Mater. Process. Sci.* **2016**, *47*, 2095–2106. [[CrossRef](#)]
3. Sahai, Y.; Emi, T. *Tundish Technology for Clean Steel Production*; World Scientific: Hackensack, NJ, USA, 2008; pp. 1–14.
4. Ramos-Banderas, A.; Sanchez-Perez, R.; Morales, R.D.; Palafox-Ramos, J.; Demedices-Garcia, L.; Diaz-Cruz, M. Mathematical simulation and physical modeling of unsteady fluid flows in a water model of a slab mold. *Metall. Mater. Trans. B-Process Metall. Mater. Process. Sci.* **2004**, *35*, 449–460. [[CrossRef](#)]
5. Sahai, Y. Advances in tundish technology for quality improvements of cast steel. *J. Iron Steel Res. Int.* **2008**, *15*, 643–652.
6. Braun, A.; Warzecha, M.; Pfeifer, H. Numerical and physical modeling of steel flow in a two-strand tundish for different casting conditions. *Metall. Mater. Trans. B-Process Metall. Mater. Process. Sci.* **2010**, *41*, 549–559. [[CrossRef](#)]
7. Odenthal, H.J.; Bolling, R.; Pfeifer, H. Numerical and physical simulation of tundish fluid flow phenomena. *Steel Res. Int.* **2003**, *74*, 44–55. [[CrossRef](#)]
8. Giurgea, C.; Bode, F.; Nascutiu, L.; Dudescu, C. Considerations regarding the optically transparent rigid model for piv investigations. A case study. Part 2: Notes on the failure of the model. *Energy Procedia* **2016**, *85*, 235–243. [[CrossRef](#)]
9. Cwudzinski, A. Piv method and numerical computation for prediction of liquid steel flow structure in tundish. *Arch. Metall. Mater.* **2015**, *60*, 11–17. [[CrossRef](#)]
10. Merder, T. Influence of design parameters of tundish and technological parameters of steel continuous casting on the hydrodynamics of the liquid steel flow. *Metalurgija* **2014**, *53*, 443–446.
11. Cwudzinski, A. Numerical and physical modeling of liquid steel active flow in tundish with subflux turbulence controller and dam. *Steel Res. Int.* **2014**, *85*, 902–917. [[CrossRef](#)]
12. Szekely, J.; Ilegbusi, O.J. *The Physical and Mathematical Modeling of Tundish Operations*; Springer: New York, NY, USA, 1989; pp. 1–52.
13. Huang, J.; Zhang, Y.; Zhang, Y.; Zhang, Y.; Ye, X.; Wang, B. Study of flow characteristics of tundish based on digital image velocimetry technique. *Metall. Mater. Trans. B* **2016**, *47*, 3144–3157. [[CrossRef](#)]
14. Alkishriwi, N.; Meinke, M.; Schroder, W. A large-eddy simulation method for low Mach number flows using preconditioning and multigrid. *Comput. Fluids* **2006**, *35*, 1126–1136. [[CrossRef](#)]
15. Alkishriwi, N.; Meinke, M.; Schroder, W.; Braun, A.; Pfeifer, H. Large-eddy simulations and particle-image velocimetry measurements of tundish flow. *Steel Res. Int.* **2006**, *77*, 565–575. [[CrossRef](#)]
16. Jha, P.K.; Ranjan, R.; Mondal, S.S.; Dash, S.K. Mixing in a tundish and a choice of turbulence model for its prediction. *Int. J. Numer. Methods Heat Fluid Flow* **2003**, *13*, 964–996. [[CrossRef](#)]
17. Jha, P.K.; Rao, P.S.; Dewan, A. Effect of height and position of dams on inclusion removal in a six strand tundish. *ISIJ Int.* **2008**, *48*, 154–160. [[CrossRef](#)]
18. Warzecha, M.; Merder, T.; Warzecha, P. Investigation of the flow structure in the tundish with the use of RANS and LES methods. *Arch. Metall. Mater.* **2015**, *60*, 215–220. [[CrossRef](#)]



© 2019 by the authors. Licensee MDPI, Basel, Switzerland. This article is an open access article distributed under the terms and conditions of the Creative Commons Attribution (CC BY) license (<http://creativecommons.org/licenses/by/4.0/>).

Article

Research and Application of a Rolling Gap Prediction Model in Continuous Casting

Zhufeng Lei * and Wenbin Su

School of Mechanical Engineering, Xi'an Jiaotong University, 28 West Xianning Road, Xi'an 710049, China; wbsu@mail.xjtu.edu.cn

* Correspondence: leizhufeng@stu.xjtu.edu.cn; Tel.: +86-029-8266-5304

Received: 6 March 2019; Accepted: 23 March 2019; Published: 25 March 2019

Abstract: Control of the roll gap of the caster segment is one of the key parameters for ensuring the quality of a slab in continuous casting. In order to improve the precision and timeliness of the roll gap value control, we proposed a rolling gap value prediction (RGVP) method based on the continuous casting process parameters. The process parameters collected from the continuous casting production site were first dimension-reduced using principal component analysis (PCA); 15 process parameters were chosen for reduction. Second, a support vector machine (SVM) model using particle swarm optimization (PSO) was proposed to optimize the parameters and perform roll gap prediction. The experimental results and practical application of the models has indicated that the method proposed in this paper provides a new approach for the prediction of roll gap value.

Keywords: multi-source information fusion; data stream; continuous casting; roll gap value; prediction; global optimization; support vector regression

1. Introduction

Motivation

High quality continuous casting technology has become the most internationally competitive core technology in the modern steel industry [1–4]. Due to the complexity of the continuous casting process, there are many factors that can affect the quality of continuous casting. Among them, the roll gap of the caster segment is a key parameter. Calculation of the roll gap remains an important problem in continuous casting production. Establishing a dynamic adaptive predictive model for the caster segment in continuous casting, and real-time adaptive adjustment of the roll gap according to actual working conditions, is theoretically and practically valuable for improving the quality of the slab.

The continuous casting process involves several steps as shown in Figure 1. First, the molten steel enters the mold from the tundish and a certain thickness of the shell solidifies. The slab, with a shell of a certain thickness, then enters the caster segment from the mold. Secondary cooling is then performed until the slab is completely solidified. Next, soft reduction of the slab is performed in the caster segment by adjusting the distance between the upper and lower rollers; this adjusts the internal crystal arrangement of the slab and improves the internal quality of the slab.

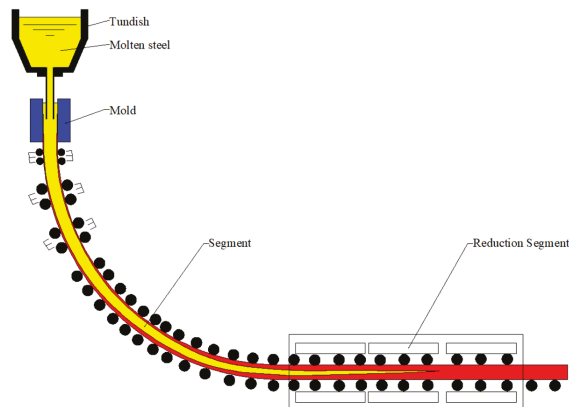


Figure 1. Continuous casting process.

There are many published studies on the prediction of continuous casting process parameters. Lait [5] developed a one-dimensional finite-difference model to calculate the temperature field and pool profile of continuously cast steel. The result obtained was reasonable for low-carbon billets over most of the mold region. Rappaz [6] described how the microscopic models of microstructure formation could be coupled to macroscopic heat flow calculations in order to predict microstructural features at the scale of the whole process. Choudhary et al. [7] developed a steady-state three-dimensional heat flow model based on the concept of artificial effective thermal conductivity. The model can be applied to various geometrical shapes of relevance to continuous casting of steel. Koric et al. [8] created an accurate multi-physics model of metal solidification at the continuum level; this model comprised of separate three-dimensional models for the thermomechanical behavior of the solidifying shell, turbulent fluid flow in the liquid pool, and thermal distortion of the mold. The model was applied to simulate continuous casting of steel. Numerical modeling is still the primary design tool used for continuous casting studies.

Artificial intelligence (AI) is a branch of the computer science discipline. AI is considered one of three cutting-edge technologies since the 1970s (those being, space technology, energy technology, and artificial intelligence). It is also considered to be one of three cutting-edge technologies of the 21st century (those being, genetic engineering, nanoscience, and artificial intelligence). AI has developed rapidly over the past three decades, has been widely used in many subject areas, and has achieved important results. AI has gradually become an independent branch of study [9]. In recent years, AI methods have been widely used in the field of intelligent manufacturing. Yang et al. [10] proposed a framework and several general guidelines for implementing big data analytics in a high-performance computing environment. AI methods have also been introduced to the field of continuous casting. Hore et al. [11] developed a model based on adaptive neural network formalism coupled with a fuzzy inference system to predict the mechanical properties of hot-rolled TRIP steel. The present model provides a predictive platform for possible application of these AI-based tools for automation, real-time process control, and operator guidance in plant operation. Liu and Gao [12] established a method for online prediction of the silicon content in blast furnace ironmaking processes. The superiority of the proposed method was demonstrated and compared with other soft sensors in terms of online prediction of the silicon content in an industrial blast furnace in China. Mahmoodkhani et al. [13] considered the friction coefficient as an input parameter in the neural network; it was optimized using an iterative method employing an equation that related the friction coefficient to the rolling force in order to rapidly predict the roll force during skin pass rolling of 980DP and 1180CP high strength steels. Tiensuu et al. [14] used statistical models to improve the dimensional accuracy of a steel plate by updating the selection of parameters for slab design. Zhang et al. [15] developed a model to predict

the critical point of interfacial instability of liquid-liquid stratified flow based on the Kelvin-Helmholtz instability. The results of the water model indicated that the prediction model was correct.

Particle swarm optimization (PSO), described by Eberhart and Kennedy in 1995, is a stochastic optimization technique based on population [16]. The particle swarm algorithm mimics the clustering behavior of insects, herds, flocks, and fish groups. These groups search for food in a cooperative way. Each member of the group changes its search mode by learning from its own experience and the experience of other members of the group. Valvano et al. [17] introduced a novel decline PSO procedure. This method was used to select the optimal parameters for sound control. Similarly, PSO was used to select the optimal parameters of the support vector machine (SVM) kernel function in this paper.

The remainder of this paper is organized as follows: The data source is introduced in Section 2. The process parameters collected at the continuous casting production site were dimension reduced by PCA, as described in Section 3. The PSO-SVM is introduced in Section 4. In Section 5, the proposed model is applied to a dataset and the results are analyzed. In Section 6, the model is applied to industrial production and compared with products produced without the model. Finally, a conclusion is presented in Section 7.

2. Continuous Casting Process Parameters

2.1. Acquisition of Continuous Casting Process Parameters

In this paper, a Chinese steel company was selected as the research object; data on the continuous casting production line was collected online from this site. The continuous casting machine under study had more than 6000 distributed sensors to record most of the process state, including the casting speed, the amount of water in each cold zone, the type of steel, and the casting temperature. Figure 2 depicts the topological structure of the continuous casting production data acquisition system. The main core equipment of the continuous casting production data acquisition system included a basic automation level Programmable Logic Controller (PLC), a man-machine interface server, a monitoring operation station, a process control-level computer database, a model application server, and a terminal client. The system collected data through the PLC controller and monitoring operation station; the data then entered the computer database. Data were analyzed and the model was updated and corrected in the model application server. Data was displayed to the operator through the terminal client; process adjustment and optimization occurred through the PLC.

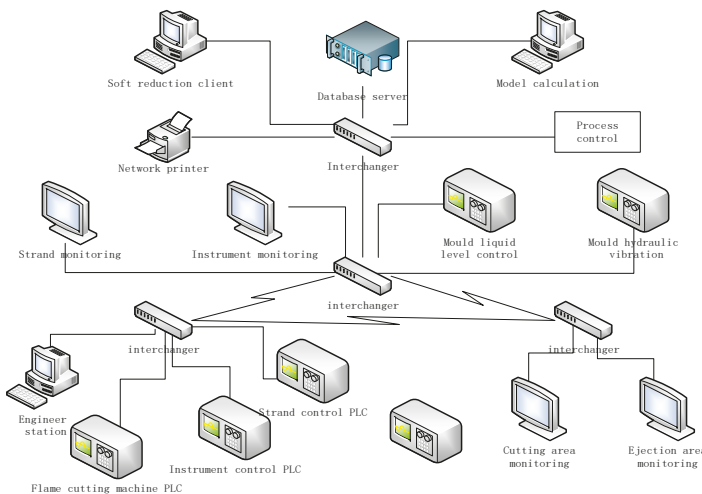


Figure 2. Topological structure of the continuous casting production data acquisition system.

In this paper, the process parameter data from the continuous casting production line were obtained with the help of field engineers; the data dimension was 6153. The process parameters included the tundish, ladle, mold, and caster segment, which were closely correlated with the roll gap value obtained; the closely related data dimension was 1020. These data were correlated with the product quality. The collection time was 1 h, the sensor recorded every 0.02 s, and the data volume was 180,000.

A correlation analysis of these process parameters was performed; the parameters that were more relevant were classified as a category. The coefficient of the association between two parameters could be obtained by:

$$r = \frac{\sum_{i=1}^n (x_i - \bar{x})(y_i - \bar{y})}{\sqrt{\sum_{i=1}^n (x_i - \bar{x})^2 \cdot \sum_{i=1}^n (y_i - \bar{y})^2}} \tag{1}$$

where r is a correlation coefficient reflecting the relationship between two variables and the related direction of this relationship, x_i is a data point in data set X , \bar{x} is the mean of X , y_i is a data point in data set Y , and \bar{y} is the mean of Y .

The analyses revealed that the correlation coefficients between each process parameter were more than 0.5; many correlation coefficients were even greater than 0.8. As a result, 15 types of continuous casting process parameters were chosen, as listed in Table 1.

Table 1. Process parameter names and abbreviations.

Name	Process Parameter	Name	Process Parameter
GSWD	Temperature of tundish molten steel	KMLL	Water flow of mold width surface
GRD	Overheating of molten steel	KMWD	Outlet temperature of mold width surface
LS	Pulling rate	ZMYL	Water pressure of mold narrow surface
ZDPL	Vibration frequency of mold	ZMLL	Water flow of mold narrow surface
ZDFZ	Vibration amplitude of mold	ZMWD	Outlet temperature of mold narrow surface
CDGYL	Average pressure of 18 drive rollers	ELSL	Average flow of 18 second cold water loops
JJQYW	Mold liquid level	ELSYL	Average pressure of 18 second cold water loops
KMYL	Water pressure of mold width surface	-	-

2.2. Data Pre-Processing

The Pauta criterion was used to detect outliers in large monitoring data sets [18]. In this paper, the Pauta criterion was used to detect outliers in the data. The detected outliers were changed to values nearby so as not to damage the sequence of the data.

Assuming that all data were measured with the same precision and in order to obtain x_1, x_2, \dots, x_n , the arithmetic mean x and the residual error $v_i = x_i - x$ ($i = 1, 2, \dots, n$) were calculated. In addition, the standard error σ was calculated using the Bessel formula. If a residual error v_b of a measured value x_b satisfied Equation (2):

$$|v_b| = |x_b - x| > 3\sigma \tag{2}$$

then x_b was an outlier, which contained a larger error, and thus, this value was replaced with the next value adjacent to it.

3. Dimension Reduction of Streaming Data from Multi-Source Information

3.1. Standardization of Continuous Casting Process Parameters

The continuous casting process is a complex continuous phase transition process. There are many links which affect the quality of the casting billet and there are many collected production process parameters. Therefore, the analysis of the data is particularly important. Analysis revealed that each process parameter could be a dimension of the data samples. The predicted roll gap of data was seen

as a label, a group of N -dimensional process parameters was seen as an input vector $x_i, x_i \in \mathbb{R}^{N \times 1}$, and another adjacent group of process parameters was seen as the second set of the input vector x_{i+1} .

The unit and magnitude of the input parameters were different. Thus, the data were standardized in order to produce data in the same range for analysis under the condition of mutual equality. A linear transformation of raw data was performed to standardize the data; this mapped the result to $[0, 1]$, according to:

$$x_{im*} = \frac{x_{im} - x_{\min}}{x_{\max} - x_{\min}} \tag{3}$$

where x_{im} was the m -dimensional process parameters of any group of input vector, x_{im*} was the standardization of x_{im} , x_{\max} was the maximum of the sample data, and x_{\min} was the minimum of the sample data.

3.2. Dimension Reduction of Continuous Casting Process Parameters

In this paper, in order to obtain a highly responsive roll gap value prediction model for the continuous casting caster segment, dimension reduction of the continuous casting process parameters was considered; this would reduce the operation time and the complexity of the algorithm.

The principal component contribution rate method was used to determine the number of parameters [19]. The variance contribution ratio and summation variance contribution ratio of each parameter is shown in Table 2.

Table 2. Variance contribution ratio of each parameter.

NO.	Feature	Variance Contribution Ratio (%)	Summation Variance Contribution Ratio (%)
1	4.79	36.97	36.97
2	3.43	32.85	69.82
3	1.76	14.74	84.56
4	1.24	5.25	89.81
5	1.01	4.74	93.55
6	0.903	3.02	96.57
7	0.605	1.92	98.49
8	0.455	0.43	98.92
9	0.350	0.32	99.24
10	0.203	0.21	99.45
11	0.113	0.15	99.6
12	0.058	0.12	99.72
13	0.044	0.1	99.82
14	0.030	0.09	99.91
15	0.008	0.09	100.00

Table 2 shows that the cumulative variance contribution ratio of the first six parameters was greater than 95%. Thus, the raw data could be fully captured with six parameters.

Figure 3 shows the classification results of principal component analysis (PCA), each color represents a principal component, there are six colors in Figure 3, representing six principal components. PCA demonstrated the effect of the dimensionality specification. The PCA results demonstrated that the data was reduced from 15 dimensions to 6.

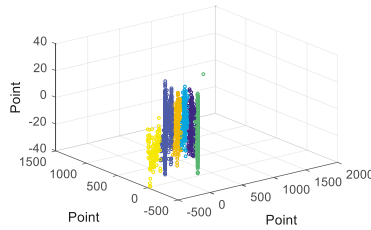


Figure 3. Dimensionality reduction results of Principal Component Analysis (PCA).

4. Establishing a Roll Gap Value Prediction Model from Multi-Source Information

4.1. PSO-SVM Model

SVM can not only solve the classification problem, but can also solve the regression problem; the basic model is the largest linear classifier defined in the feature space. SVM aims to achieve a distinction between samples by constructing a hyperplane for classification so that the sorting interval between the samples is maximized and the sample to the hyperplane distance is minimized.

Set a training data set for a feature space $D = \{(x_1, y_1), (x_2, y_2), \dots, (x_m, y_m)\}$, $x_i \in \chi = \mathbb{R}^n$, $y_i \in y = \{+1, -1\}$, $i = 1, 2, \dots, N$, where x_i is the i -th feature vector, y_i is the class tag of x_i .

The corresponding equation of the classification hyperplane was

$$h(x) = \omega \cdot x + b \tag{4}$$

where x was the input vector, ω was the weight, and b was the offset.

The classification decision function was

$$\text{Sign}(h(x)) \tag{5}$$

$$\begin{cases} h(x) > 0, y_i = 1 \\ h(x) < 0, y_i = -1 \end{cases} \tag{6}$$

The support vector machine was implemented to find the ω and b when the interval between the separation hyperplane and the nearest sample point was maximized. When the training set was linearly separable, the sample points belonging to different classes could be separated by one or several straight lines with the largest interval. The maximum interval was solved by the following formula:

$$\max \gamma_i = y_i \left(\frac{\omega}{\|\omega\|} \cdot x_i + \frac{b}{\|\omega\|} \right) \tag{7}$$

$$s.t. y_i \left(\frac{\omega}{\|\omega\|} \cdot x_i + \frac{b}{\|\omega\|} \right) \geq \gamma, i = 1, 2, \dots, N \tag{8}$$

where γ is the geometric interval.

Thus, we could obtain the linear separable support vector machine optimization problem.

$$\min_{\omega, b} \frac{1}{2} \|\omega\|^2 \tag{9}$$

$$s.t. y_i(\omega \cdot x_i + b) - 1 \geq 0, i = 1, 2, \dots, N \tag{10}$$

In the actual data set, there were many specific points, making the data set linearly inseparable; in order to solve this problem, we introduced a slack variable for each sample point $\xi_i \geq 0$, so that

$$y_i(\omega \cdot x_i + b) \geq 1 - \xi_i \tag{11}$$

for each slack variable ξ_i , pay a price ξ_i , and the optimization problem becomes

$$\frac{1}{2} \|\omega\|^2 + C \sum_{i=1}^N \xi_i \tag{12}$$

where $C > 0$ is the penalty factor.

Most of the data in the actual data were linearly inseparable. Therefore, these data could be mapped to a high-dimensional feature space through non-linear mapping, letting the non-linear problem be transformed into a linear problem. The linear indivisible problem was transformed into a linear separable problem.

Introduce kernel functions:

$$K(x_i, x_j) = \varphi(x_i) \cdot \varphi(x_j) \tag{13}$$

where the value of the kernel equaled the inner product of two vectors, x_i and x_j .

At this point, we obtained

$$W(\alpha) = \frac{1}{2} \sum_{i=1}^N \sum_{j=1}^N \alpha_i \alpha_j y_i y_j K(x_i, x_j) - \sum_{i=1}^N \alpha_i \tag{14}$$

where $\alpha_i \geq 0$, $i = 1, 2, \dots, N$ was the Lagrangian multiplier and N was the number of samples.

In this paper, the radial basis function (RBF) was chosen as the SVR kernel function, and the expression was

$$K(x_i, x) = \exp\left(\frac{-\|x_i - x\|^2}{2g^2}\right) \tag{15}$$

where g was the kernel function coefficient.

At this point, the classification function became

$$f(x) = \text{sign}\left[\sum_{i=1}^N \alpha_i y_i \exp\left(\frac{-\|x_i - x\|^2}{2g^2}\right) + b\right] \tag{16}$$

In the SVM model, training data on the cost function and the constraint condition were known. Only the penalty factor C and the kernel function parameter g could be adjusted. When the input sample points are wrongly divided, the impact of this error can be adjusted by C ; this highlights the important effect of the misclassification of sample points. The kernel function parameter g represents the kernel function parameter γ , k in the g represents the number of attributes in the input data. Thus, the hit rate of the roll gap value prediction model is governed by these two parameters [20–29].

PSO, also referred to as the particle swarm optimization algorithm or bird flock foraging algorithm, is a type of evolutionary algorithm (EA). Starting from the random solution, the optimal solution is found through iteration, and the quality of the solution is evaluated through fitness. However, the PSO algorithm rule is simpler. It searches for the global optimum by following the current optimal value. This algorithm is easy to implement, has high-precision and fast-convergence, and is suitable for solving practical problems.

PSO was used to optimize the penalty factor parameter C and kernel function parameter g in the SVM. Cross-validation of the prediction results were performed to obtain the optimal C and g so as to optimize the SVM prediction results.

Assuming that C and g are in a D -dimension target-searching space, a group was composed of m particles. The position of the i -th particle represented vector $c_i = (c_{i1}, c_{i2}, \dots, c_{iD})$, $i = 1, 2, \dots, m$, whose speed was also a D -dimension vector, $g_i = (g_{i1}, g_{i2}, \dots, g_{iD})$. The optimal location that the i -th particle had searched so far was $P_i = (P_{i1}, P_{i2}, \dots, P_{iD})$. The optimal position in which the

whole particle swarm had searched was $P_k = (P_{k1}, P_{k2}, \dots, P_{kD})$. The particle updating equation was as follows:

$$g_{id}(t + 1) = g_{id}(t) + h_1 r_1 (P_{id} - c_{id}(t)) + h_2 r_2 (P_{kd} - c_{id}(t)) \tag{17}$$

$$c_{id}(t + 1) = c_{id}(t) + g_{id}(t + 1) \tag{18}$$

while $g_{id} > G_{max}$, $g_{id} = G_{max}$;
 while $g_{id} < -G_{max}$, $g_{id} = -G_{max}$.

In the formula, $i = 1, 2, \dots, m$; $d = 1, 2, \dots, D$. h_1 and h_2 were non-negative constants, r_1 and r_2 were uniform distribution random numbers within the range of $[0, 1]$, $c_{id}(t)$ was the current position of the i -th particle, t is the current moment, P_{id} was the optimal location that the i -th particle had searched so far, and g_{id} was the current speed of the i -th particle. $g_{id} \in [-G_{max}, G_{max}]$, G_{max} , the maximum limit speed, was a negative number.

4.2. Establishing the PSO-Roll Gap Value Prediction

This section reports the process for establishing the PSO-SVM model. The SVM algorithm was used to establish the roll gap value prediction (RGVP) model of streaming data from multi-source information, as shown in Figures 4 and 5. Six types of continuous casting process parameters comprised the input data, $k(x_1, x)$; $k(x_2, x)$; ...; $k(x_N, x)$ were the kernel functions of the SVM, and the roll gap value was the output data.

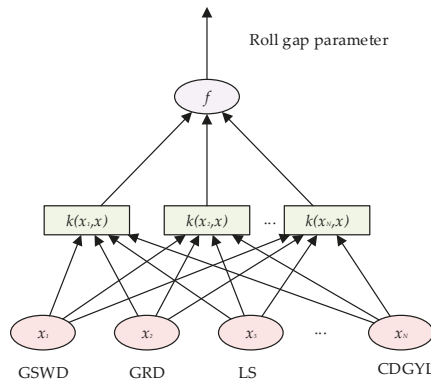


Figure 4. Roll gap value prediction model of streaming data from multi-source information. f is the output of the model.

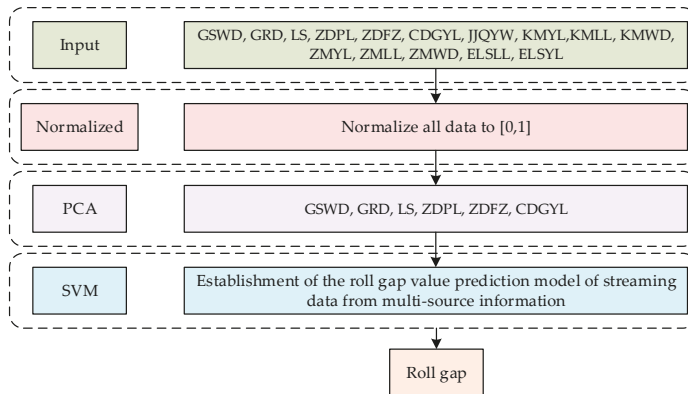


Figure 5. Common computational architecture of roll gap value prediction model.

In order to enhance the accuracy of the roll gap value prediction model, PSO was used to optimize the parameters of the PSO-RGVP.

The specific steps of the PSO-RGVP were as follows:

- Step 1: Pre-processing of process parameter data to obtain 15 types of process parameters.
- Step 2: Standardization of process parameter data and feature reduction to obtain six types of parameters.
- Step 3: Determination of the scope of C and g by PSO.
- Step 4: Testing of model parameters using the method of cross validation to obtain the optimal C and g .
- Step 5: Establishment of the roll gap value prediction model of streaming data from multi-source information.
- Step 6: Prediction of the results.

5. Experiments and Results

This section presents the results of the PSO-RGVP model and compares these results to the traditional numerical heat transfer metallurgical model; MATLAB was used to perform the experiment. This section is divided into two parts. The first was the establishment and training of the model using historical data; the second was the prediction of the test sample. Two thousand sets of process parameter data from continuous casting were collected to establish and train the model. In addition, another 500 sets of data were collected to carry out the forecast test. The experiment results are shown in Table 3.

Table 3. Results of establishment and training of the model experiment.

Parameter Optimization Results	Training Time	Mean Square Deviation
$C = 0.1; g = 0.1$	304.8 s	97.5%

Figure 6 presents the parameter optimization results of the PSO-RGVP. When the termination generation was 100 and the population number was 20 in the PSO-RGVP, it could be concluded that the optimal penalty factor $C = 0.1$ and $g = 0.1$.

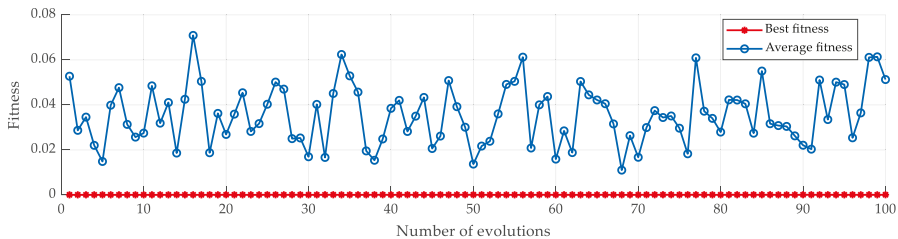


Figure 6. Parameter optimization results of PSO.

After predicting 500 sets of process parameter data that were collected with the PSO-RGVP, the predicted roll gap value was compared with the actual roll gap value, as shown in Figure 7. Relative error of prediction of the PSO-RGVP is shown in Figure 8.

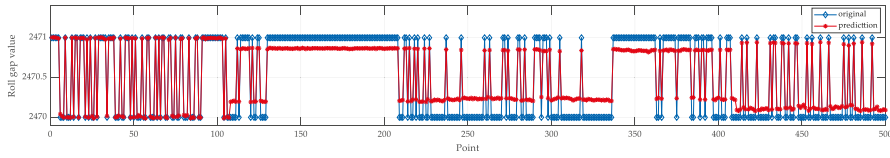


Figure 7. Prediction results of PSO-RGVP.

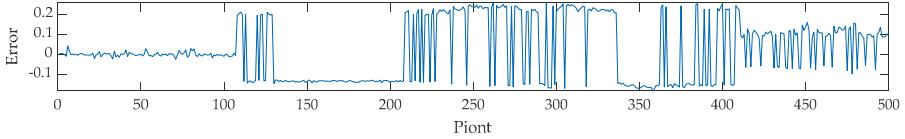


Figure 8. Relative error of prediction of the PSO-RGVP.

The PSO-RGVP is a new way to predict the value of roll gap. The maximum relative error between the predictive value and the actual value of the method proposed in this paper was 2.5%, and the prediction accuracy was 97.5%.

6. Industrial Application

This section reports the actual application of the PSO-RGVP. Modular design was used in the system; the modular structure is shown below in Figure 9.

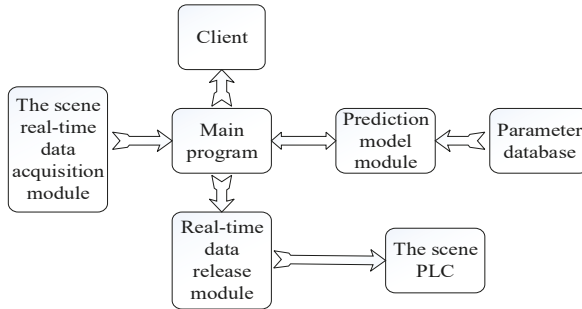


Figure 9. System modular structure diagram.

The test system had two main modules: The prediction model module and the main application program. Data interaction in the prediction model was achieved with the main application program; the program was structured and clearly defined in Figure 9.

A brief operational flow chart of the test system is shown in the following diagram (Figure 10).

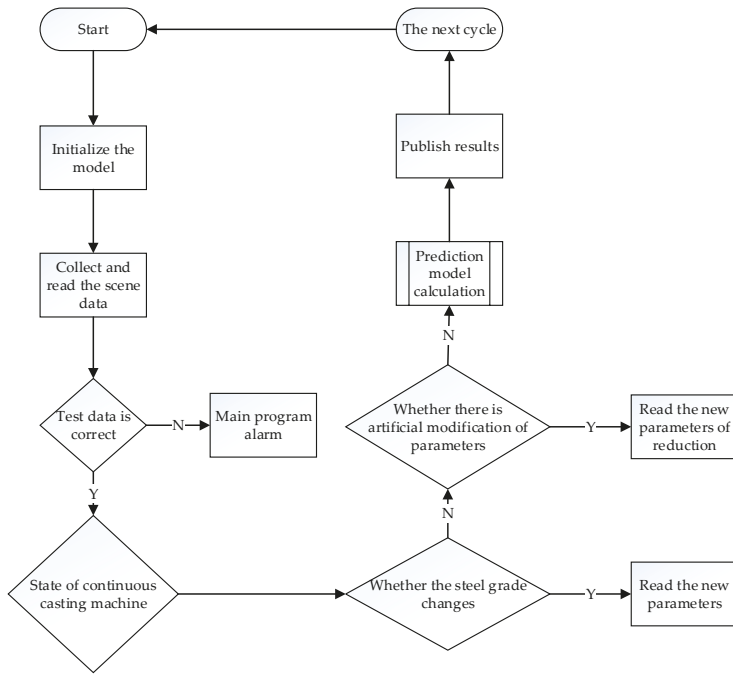


Figure 10. Test system calculation process.

As shown in Figure 10, after initializing the model, the system first acquired the real-time process parameters and filtered for correctness of the process parameters. Through the identification of real-time data, the system obtained the status of the continuous casting machine at the time and decided whether to carry out the roll gap adjustment strategy. Through the identification of the type of steel, the system read the total rolling reduction, the rolling interval, the rolling distribution, etc. The prediction model was used to obtain the roll gap prediction value, which was then released.

The prediction data was imported into the test system for trial production, then casting was performed and the quality of the slab was observed.

In order to verify the application of the model, the center segregation and center porosity of the slab, before and after use of the model, were analyzed by macroscopic examination. In particular, the continuous casting machine was compared before and after use of the model for the production of steel for Q235; the section size was 230 × 1350, the cast speed was 1.30 m/min, and the total reduction was 4 mm. The results of macroscopic examination were determined according to Chinese metallurgical standards. The results are reported in Table 4 and in Figures 11 and 12.

Table 4. Comparison of quality rating.

Serial Number	Section Size (mm × mm)	Centre Segregation	Centre Porosity	Intermediate Cracks	Triangle Area Cracks
Without proposed model	230 × 1350	B1.0	2.0	1.5	1.5
Proposed model	230 × 1350	C0.5	1.0	1.0	0.5

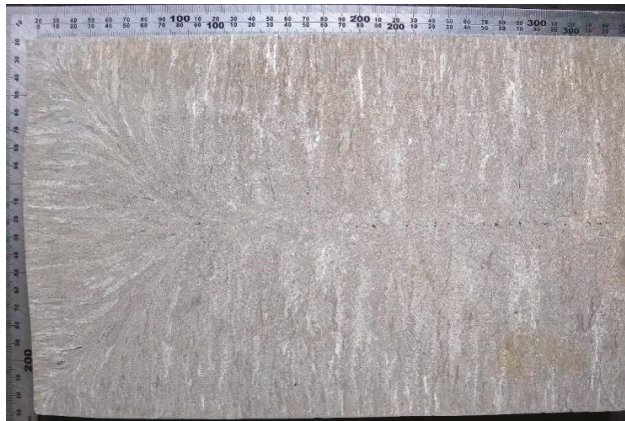


Figure 11. Macrosegregation examination of results of the proposed model.

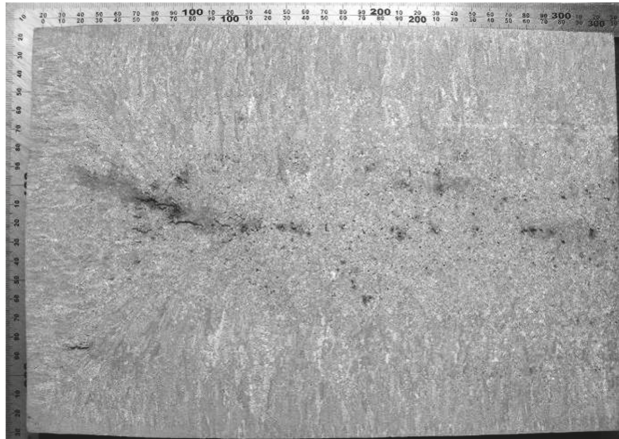


Figure 12. Macrosegregation examination of the results of the traditional method.

Figures 11 and 12 show the macrosegregation examination of the two methods: The proposed model and the traditional method. The macrosegregation sample was cut from the continuous casting slab. After polishing and pickling the surface, it was photographed under a low-power microscope. This was the main approach used to check the internal quality of a slab. It was obvious that under the same production conditions, the slab produced under the proposed model only had very few intermediate cracks; the quality rating of center segregation was C0.5; center porosity was 1.0; intermediate cracks was 1.0; triangle area cracks was 0.5. According to the quality of the intermediate cracks produced by the proposed model, the center segregation and center porosity in the slab were greatly reduced. After using the proposed model, the center segregation and center porosity in the slab were greatly reduced. In addition, the proposed model greatly reduced the labor intensity and maintenance time and improved the maintenance efficiency for production.

The results indicate that the roll gap prediction model proposed in this paper has a short computational time, can accurately predict the roll gap, and allows for real-time prediction and adjustment during production. The findings from the industrial application of this model demonstrate its accuracy. Thus, the roll gap value prediction efficiency is greatly increased in the proposed model. In this study, 2000 sets of data were collected to establish and train the model. In addition,

another 500 sets of data were collected to carry out the forecast test. The prediction accuracy was 97.5%. This showed that the PSO-RGVP was superior for prediction of the roll gap value.

7. Conclusions

In this paper, a new prediction approach, PSO-RGVP, was proposed. Multi-source information process parameters from the continuous casting process were excavated and analyzed, and PSO was used for global optimization of an adaptive prediction model for the roll gap value of the caster segment; SVM was used for the prediction of the roll gap. This method takes into account the mutual influence and restriction of the multi-source information process parameters in the actual production process; the model parameters were obtained quickly and accurately, and adaptive prediction of the roll gap value was achieved. The experimental results confirmed the efficiency of the PSO-RGVP, because actual data was used. PSO-RGVP provides a new approach for the prediction of the roll gap value.

Author Contributions: W.S. conceived and designed the research, Z.L. performed the experiment and wrote the manuscript.

Funding: This work was financially supported by the National Natural Science Foundation of China (NO. 51575429).

Acknowledgments: Q.G., X.L., H.Z., B.H., and Y.Z. are acknowledged for their valuable technical support.

Conflicts of Interest: The authors declare no conflict of interest.

References

1. Ataka, M. Rolling technology and theory for the last 100 years: The contribution of theory to innovation in strip rolling technology. *ISIJ Inter.* **2015**, *55*, 89–102. [[CrossRef](#)]
2. Ge, S.; Isac, M.; Guthrie, R.I.L. Progress of strip casting technology for steel; historical developments. *ISIJ Inter.* **2012**, *52*, 2109–2122. [[CrossRef](#)]
3. Tacke, K.H.; Schwinn, V. Recent developments on heavy plate steels. *Stahl Eisen* **2005**, *125*, 55.
4. Wolf, M.M. History of Continuous Casting. In Proceedings of the 75th Steelmaking Conference, Toronto, ON, Canada, 5–8 April 1992; pp. 47–101.
5. Lait, J. Mathematical modelling of heat flow in the continuous casting of steel. *Ironmak. Steelmak.* **1974**, *1*, 90–97.
6. Rappaz, M. Modeling of microstructure formation in solidification processes. *Int. Mater. Rev.* **1989**, *34*, 93–123. [[CrossRef](#)]
7. Choudhary, S.K.; Ganguly, S. Morphology and segregation in continuously cast high carbon steel billets. *ISIJ Inter.* **2007**, *47*, 1759–1766. [[CrossRef](#)]
8. Koric, S.; Hibbeler, L.C.; Liu, R.; Thomas, B.G. Multiphysics model of metal solidification on the continuum level. *Numer. Heat Transfer, Part B-Fundam.* **2010**, *58*, 371–392. [[CrossRef](#)]
9. Nilsson, N.J. *Principles of Artificial Intelligence*; Morgan Kaufmann Publishers: Burlington, MA, USA, 2014.
10. Yang, Y.; Cai, Y.D.; Lu, Q.; Zhang, Y.; Koric, S.; Shao, C. High-Performance Computing Based Big Data Analytics for Smart Manufacturing. In Proceedings of the ASME 2018, the 13th International Manufacturing Science and Engineering Conference, College Station, TX, USA, 18–22 June 2018.
11. Hore, S.; Das, S.K.; Banerjee, S.; Mukherjee, S. An adaptive neuro-fuzzy inference system-based modelling to predict mechanical properties of hot-rolled TRIP steel. *Ironmak. Steelmak.* **2016**, *44*, 656–665. [[CrossRef](#)]
12. Liu, Y.; Gao, Z. Enhanced just-in-time modelling for online quality prediction in BF ironmaking. *Ironmak. Steelmak.* **2015**, *42*, 321–330. [[CrossRef](#)]
13. Mahmoodkhani, Y.; Wells, M.A.; Song, G. Prediction of roll force in skin pass rolling using numerical and artificial neural network methods. *Ironmak. Steelmak.* **2016**, *44*, 281–286. [[CrossRef](#)]
14. Tiensuu, H.; Tamminen, S.; Pikkuaho, A.; Rönning, J. Improving the yield of steel plates by updating the slab design with statistical models. *Ironmak. Steelmak.* **2016**, *44*, 577–586. [[CrossRef](#)]
15. Zhang, L.; Li, Y.; Wang, Q.; Yan, C. Prediction model for steel/slag interfacial instability in continuous casting process. *Ironmak. Steelmak.* **2015**, *42*, 705–713. [[CrossRef](#)]

16. Eberhart, R.; Kennedy, J. A New Optimizer Using Particle Swarm Theory. In Proceedings of the MHS'95, the Sixth International Symposium on Micro Machine and Human Science, Nagoya, Japan, 4–6 October 1995; pp. 39–43. [\[CrossRef\]](#)
17. Valvano, S.; Orlando, C.; Alaimo, A. Design of a noise reduction passive control system based on viscoelastic multilayered plate using PDSO. *Mech. Syst. Sig. Process.* **2019**, *123*, 153–173. [\[CrossRef\]](#)
18. Zhang, M.; Yuan, H. The Pauta criterion and rejecting the abnormal value. *J. Zhengzhou Univ. Tech.* **1997**, *1*, 84–88.
19. Martinez, A.M.; Kak, A.C. PCA versus LDA. *IEEE Trans. Pattern Anal. Mach. Intell.* **2001**, *23*, 228–233. [\[CrossRef\]](#)
20. Cervantes, J.; Garcia-Lamont, F.; Rodriguez-Mazahua, L.; Lopez, A.; Ruiz-Castilla, J.; Trueba, A. PSO-based method for SVM classification on skewed data sets. *Neurocomputing* **2017**, *228*, 187–197. [\[CrossRef\]](#)
21. Chiang, J.H.; Hao, P.Y. A new kernel-based fuzzy clustering approach: Support vector clustering with cell growing. *IEEE Trans. Fuzzy Syst.* **2003**, *11*, 518–527. [\[CrossRef\]](#)
22. Fang, Y.; Hu, C.; Liu, L.; Zhang, X. Breakout prediction classifier for continuous casting based on active learning GA-SVM. *China Mech. Eng.* **2016**, *27*, 1609–1614. [\[CrossRef\]](#)
23. Gaudioso, M.; Gorgone, E.; Labbe, M.; Rodriguez-Chia, A.M. Lagrangian relaxation for SVM feature selection. *Comput. Oper. Res.* **2017**, *87*, 137–145. [\[CrossRef\]](#)
24. Zhang, G.Z.; Sun, J. Application of fuzzy control on the caster segment's gap control of slab continuous casting machine. *Electr. Drive* **2009**, *39*, 51–53.
25. Jain, A.K.; Duin, R.P.W.; Mao, J. Statistical pattern recognition: A review. *IEEE Trans. Pattern Anal. Mach. Intell.* **2000**, *22*, 4–37. [\[CrossRef\]](#)
26. Muscat, R.; Mahfouf, M.; Zughrat, A.; Yang, Y.Y.; Thornton, S.; Khondabi, A.V.; Sortanos, S. Hierarchical fuzzy support vector machine (SVM) for rail data classification. *IFAC Papersonline* **2014**, *47*, 10652–10657. [\[CrossRef\]](#)
27. Refan, M.H.; Damesghi, A.; Kamarzarrin, M. Improving RTDGPS accuracy using hybrid PSOSVM prediction model. *Aerosp. Sci. Technol.* **2014**, *37*, 55–69. [\[CrossRef\]](#)
28. Wang, J.-S.; Chiang, J.-C. A cluster validity measure with Outlier detection for support vector clustering. *IEEE Trans. Syst. Man Cybern. Part B Cybern.* **2008**, *38*, 78–89. [\[CrossRef\]](#) [\[PubMed\]](#)
29. Wei, J.; Zhang, R.; Yu, Z.; Hu, R.; Tang, J.; Gui, C.; Yuan, Y. A BPSO-SVM algorithm based on memory renewal and enhanced mutation mechanisms for feature selection. *Appl. Soft Comput.* **2017**, *58*, 176–192. [\[CrossRef\]](#)



© 2019 by the authors. Licensee MDPI, Basel, Switzerland. This article is an open access article distributed under the terms and conditions of the Creative Commons Attribution (CC BY) license (<http://creativecommons.org/licenses/by/4.0/>).

Article

A Combined Hybrid 3-D/2-D Model for Flow and Solidification Prediction during Slab Continuous Casting

Mujun Long *, Huabiao Chen, Dengfu Chen *, Sheng Yu, Bin Liang and Huamei Duan

College of Materials Science and Engineering, Chongqing University, Chongqing 400044, China; chenhuabiao@cqu.edu.cn (H.C.); jscquys@163.com (S.Y.); binliang@cqu.edu.cn (B.L.); duanhuamei@cqu.edu.cn (H.D.)

* Correspondence: longmujun@cqu.edu.cn (M.L.); chendfu@cqu.edu.cn (D.C.); Tel.: +86-23-6510-2467 (M.L. & D.C.)

Received: 11 December 2017; Accepted: 8 March 2018; Published: 14 March 2018

Abstract: A combined hybrid 3-D/2-D simulation model was developed to investigate the flow and solidification phenomena in turbulent flow and laminar flow regions during slab continuous casting (CC). The 3-D coupling model and 2-D slicing model were applied to the turbulent flow and laminar flow regions, respectively. In the simulation model, the uneven distribution of cooling water in the width direction of the strand was taken into account according to the nozzle collocation of secondary cooling zones. The results from the 3-D turbulent flow region show that the impact effect of the molten steel jet on the formation of a solidification shell is significant. The impact point is 457 mm below the meniscus, and the plug flow is formed 2442 mm below the meniscus. In the laminar flow region, grid independence tests indicate that the grids with a cell size of $10 \times 10 \text{ mm}^2$ are sufficient in simulations to attain the precise temperature distribution and solidification profile. The liquid core of the strand is not entirely uniform, and the solidification profile agrees well with the integrated distribution of cooling water in secondary cooling zones. The final solidification points are at a position of 400–500 mm in the width direction and are 17.66 m away from the meniscus.

Keywords: slab continuous casting; hybrid simulation model; uneven secondary cooling

1. Introduction

Continuous casting (CC) technology has become the primary method of producing steel strands in the steelmaking industry. During the CC process, the molten steel is continuously fed into the water-cooled mold through a submerged entry nozzle (SEN) and a solidified shell of sufficient thickness is formed. Subsequently, the strand is pulled into the secondary cooling zones and cooled by water spray or air-mist spray in order to solidify completely. The strand quality, particularly regarding surface and inner cracks, is closely related to the turbulent flow and the heat transfer during the solidification involved in a CC process [1–5]. This is particularly true given that, in the slab CC process, the solidification profile of the slab transverse section—which closely relates to the integrated distribution of cooling water in secondary cooling zones—is not entirely uniform [6–8]. This effect on centerline segregation is significant [7,9,10].

To date, both a two-dimensional (2-D) slicing model and three-dimensional (3-D) coupling model are widely used to predict the flow and solidification phenomena during the CC process. Owing to the high calculation efficiency, the 2-D slicing model is widely used to predict the temperature distribution and solidification profile during the CC process [7,10–12]. The calculation efficiency of the 2-D slicing model is improved by using an effective thermal conductivity concept to indirectly take the flow effect into account. However, the 2-D slicing model assumes that the solidification shell is a heat-transfer

slice which moves from the meniscus to the solidification end. Evidently, the effect of turbulent flow on temperature distribution and the solidification shell is not directly considered in the 2-D slicing model. In fact, especially for slab the CC process, the molten steel jet which impacts the narrow face has a significant effect on the temperature distribution and solidification shell [13]. Hence, to consider the effect of turbulent flow, the 3-D coupling model has been applied during the CC process [13–17]. Compared with the 2-D slicing model, the computational domain is much larger. Thereby, the amount of calculation is very large. Furthermore, the integrated distribution of cooling water in the width directions of secondary cooling zones is not considered in the previous 3-D calculations [13,17]. This simple treatment of the heat transfer condition would evidently affect the accurate prediction of the solidification profile. Recently, Sun et al. [18] proposed a method to divide the computational domain of the CC bloom to improve the calculation efficiency. However, in that simulation model, the grid independence tests were not carried out and the heat transfer coefficient was assumed to be constant around the strand transverse section. Moreover, compared with the bloom, the heat transfer boundary of the CC slab is more complex. In the width direction, the distribution of the cooling water is not entirely uniform. Thus far, the combined hybrid 3-D/2-D numerical model has not been used in the simulation of a slab CC process.

In the present work, to simultaneously consider the effect of turbulent flow and improve calculation efficiency, a combined hybrid 3-D/2-D numerical model was established and used to explore the transport phenomena during the slab CC process. The 3-D coupling model and 2-D slicing model were adopted in the turbulent flow region and laminar flow region, respectively. The effects of flow in the turbulent region on the temperature distribution and the location of the final solidification point are considered by the data of the interface in the 3-D turbulent flow region. These are transmitted to the 2-D slice as the initial conditions. The grid independence tests were carried out to find a suitable mesh cell size. This was then adopted in the simulation of the laminar flow region. In the present model, the distribution of cooling water in the width direction was taken into account.

2. Model Description

2.1. Mathematical Formulation

The continuity equation is

$$\frac{\partial \rho}{\partial t} + \frac{\partial(\rho u_i)}{\partial x_i} = 0 \quad (1)$$

The momentum equation is

$$\frac{\partial(\rho u_i)}{\partial t} + \frac{\partial(\rho u_i u_j)}{\partial x_j} = -\frac{\partial P}{\partial x_i} + \frac{\partial}{\partial x_i} \left[\mu_{\text{eff}} \left(\frac{\partial u_i}{\partial x_j} + \frac{\partial u_j}{\partial x_i} \right) \right] + \rho g_i + S_{i,\text{mom}} \quad (2)$$

$$\mu_{\text{eff}} = \mu + \mu_t = \mu + c_\mu \rho \frac{k^2}{\varepsilon} \quad (3)$$

and

$$S_{i,\text{mom}} = \frac{(1 - f_L)^2}{(f_L^3 + 0.01)} A_{\text{mushy}} (u_i - v_{i,p}) \quad (4)$$

$$f_L = \begin{cases} 0 & T < T_{\text{Solidus}} \\ \frac{T - T_{\text{Solidus}}}{T_{\text{Liquidus}} - T_{\text{Solidus}}} & T_{\text{Solidus}} < T < T_{\text{Liquidus}} \\ 1 & T > T_{\text{Liquidus}} \end{cases} \quad (5)$$

where ρ , t , u_i , u_j , μ_{eff} , P , g_i , f_L , A_{mushy} , $v_{i,p}$, T , T_{Solidus} , and T_{Liquidus} are molten steel density (kg/m^3), time (s), i -component of velocity (m/s), j -component of velocity (m/s), effective viscosity ($\text{kg}\cdot\text{m}^{-1}\cdot\text{s}^{-1}$), pressure (N/m^2), i -component of acceleration due to gravity (m/s^2), liquid fraction, morphology constant, i -component of casting speed (m/s), temperature (K), solidus temperature (K), and liquidus

temperature (K), respectively. The value of A_{mushy} is usually between 10^5 and 10^8 in the numerical modelling of CC processes. In addition, the higher the value of A_{mushy} , the steeper the transition of the velocity of the material to zero as it solidifies. Values between 10^4 and 10^7 are recommended for most computations (based on the user's guide of Ansys Fluent 14.0). Based on these two things, the value of A_{mushy} was set to 10^7 in the present work.

Standard k - ε equations are

$$\frac{\partial(\rho k)}{\partial t} + \frac{\partial(\rho k u_i)}{\partial x_i} = \frac{\partial}{\partial x_i} \left(\frac{\mu_t}{\sigma_k} \frac{\partial k}{\partial x_j} \right) + G - \rho \varepsilon + S_k \quad (6)$$

$$\frac{\partial(\rho \varepsilon)}{\partial t} + \frac{\partial(\rho \varepsilon u_i)}{\partial x_i} = \frac{\partial}{\partial x_i} \left(\frac{\mu_t}{\sigma_\varepsilon} \frac{\partial \varepsilon}{\partial x_j} \right) + c_1 \frac{\varepsilon}{k} G - c_2 \frac{\varepsilon^2}{k} \rho + S_\varepsilon \quad (7)$$

where

$$G = \mu_t \frac{\partial u_i}{\partial x_j} \left(\frac{\partial u_i}{\partial x_j} + \frac{\partial u_j}{\partial x_i} \right) \quad (8)$$

$$S_k = \frac{(1 - f_L)^2}{(f_L^3 + 0.01)} A_{\text{mushy}} k \quad (9)$$

$$S_\varepsilon = \frac{(1 - f_L)^2}{(f_L^3 + 0.01)} A_{\text{mushy}} \varepsilon \quad (10)$$

where G , k , ε , μ , and μ_t are the generation of turbulence kinetic energy ($\text{kg}\cdot\text{m}^{-1}\cdot\text{s}^{-3}$), turbulent kinetic energy (m^2/s^2), dissipation rate of turbulence energy (m^2/s^3), molecular viscosity ($\text{kg}\cdot\text{m}^{-1}\cdot\text{s}^{-1}$), and turbulent viscosity ($\text{kg}\cdot\text{m}^{-1}\cdot\text{s}^{-1}$), respectively. The standard values of σ_k , σ_ε , c_1 , c_2 , and c_μ recommended by Launder and Spalding are 1.0, 1.3, 1.44, 1.92, and 0.09, respectively.

The energy equation is

$$\frac{\partial(\rho H)}{\partial t} + \frac{\partial(\rho u_i H)}{\partial x_i} = \frac{\partial}{\partial x_i} \left[\left(\lambda + \frac{c_p \mu_t}{Pr_t} \right) \frac{\partial T}{\partial x_i} \right] \quad (11)$$

where

$$H = h + \Delta H = h_{\text{ref}} + \int_{T_{\text{ref}}}^T c_p dT + f_L L \quad (12)$$

where H , Pr_t , h , L , λ , and c_p , are enthalpy (J/kg), turbulent Prandtl number, sensible enthalpy (J/kg), pure solvent melting heat (J/kg), thermal conductivity ($\text{W}\cdot\text{m}^{-1}\cdot\text{K}^{-1}$), and specific heat ($\text{J}\cdot\text{kg}^{-1}\cdot\text{K}^{-1}$), respectively. The value of Pr_t was set to 0.85 (based on the theory guide of Ansys Fluent 14.0). More details about the mathematical formulation are available in reference [14].

2.2. Computational Domain

According to the geometric symmetry, the strand was assumed to be ideally symmetrical and a quarter of the strand was selected to be calculated. The geometry and working parameters of the CC process are listed in Table 1. The whole 3-D computational domain ($1530 \times 190 \times 20,362 \text{ mm}^3$) is very large. If the coupled model is adopted in it directly, the cost of computation will be very large. To cut down the great amount of calculation and improve the calculation efficiency, the computational domain is suitably divided into two parts, the 3-D turbulence region and the 2-D laminar flow region. The division method is illustrated in Figure 1. When the z -component velocity of molten steel is equal to the casting speed, the plug flow is formed. This means that the local molten steel and shell are in a relatively static status. That is, the first transverse section of the strand—where z -component velocities equal to the casting speed—is the interface between the turbulent flow region and laminar

flow region. The data of the interface in the 3-D turbulent flow region are transmitted to the initial 2-D slice in the laminar flow region using a coordinate interpolation algorithm.

Table 1. The geometry and working parameters of the CC (continuous casting) process.

Parameters	Values	Secondary Cooling	Length (mm)	Cooling Water Flow Rate (L/min)
Mold section	1530 × 190 mm ²	Zone 1	405	155
Mold length	800 mm	Zone 2	555	84
Inside size of SEN	86 × 45 mm ²	Zone 3	800	54
Outside size of SEN	141 × 100 mm ²	Zone 4	1730	65
Port size of SEN	45 × 73 mm ²	Zone 5	1927	52
Port angle	−15 degrees	Zone 6	3854	86
Casting speed	1.2 m/min	Zone 7	5806	86
Casting temperature	1811 K	Zone 8	4485	59
Steel grade	Q345	-	-	-

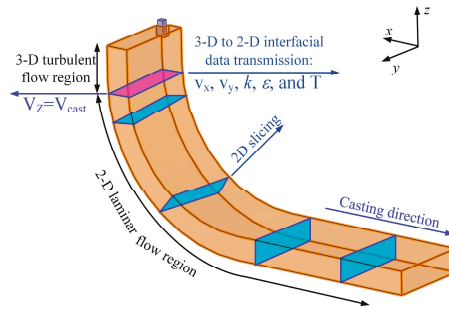


Figure 1. Illustration of 3-D turbulent flow and 2-D laminar flow regions during the CC (continuous casting) process.

In order to find out the interface between the 3-D turbulent flow region and the 2-D laminar region, a computational domain with a size of 1530 × 190 × 3250 mm³ was built and calculated. The position of this interface can be obtained by analyzing the z-component velocity variation of molten steel at the central symmetry plane of strand narrow face. The meshes created by ANSYS ICEM CFD 14.0 and adopted in 3-D turbulent flow region and 2-D laminar flow region are shown in Figure 2. The number of elements for the meshes of the 3-D part and 2-D part are 517,793 and 770, respectively.

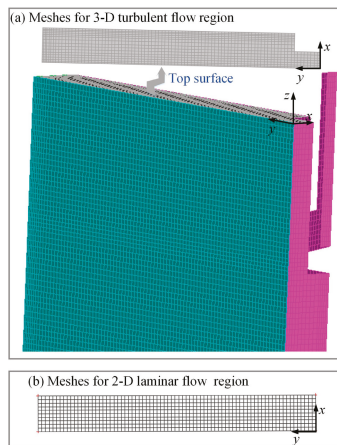


Figure 2. Meshes adopted in the (a) 3-D turbulent flow region and (b) 2-D laminar flow region.

2.3. Boundary Conditions and Physical Properties

The inlet velocity of SEN was calculated based on mass conservation. The k and ε values were estimated using the semi-empirical relations. The values of these parameters are $v_{in} = 1.502$ m/s, $k = 0.003$ m²/s², $\varepsilon = 0.0134$ m²/s³, and $T = 1811$ K. The boundary condition of the outlet in the 3-D part was set as ‘outflow’. The wall condition was employed on the meniscus without heat transfer.

The wall condition was employed on the strand surface. The heat flux of the mold surface was calculated using Equation (13) [19].

$$q_m = 2,680,000 - 276,000 \times \sqrt{\frac{60L_z}{v_c}} \tag{13}$$

where L_z and v_c are the distance from the meniscus (m) and the casting speed (m/min), respectively.

In the secondary cooling zone, the cooling types include four aspects: water spray cooling, radiation cooling, water evaporation cooling, and roll contact cooling. In the present work, four aspects of cooling types have been considered. First, we determined the heat conditions for different cooling types with the same method described in our publications [7,9]. The heat flux for the water spray cooling region was calculated using Equation (14). More detailed descriptions about the other three cooling types in the secondary cooling zone are available in our publications [7,9]. Then, to simplify this heat transfer process, we use the integrated heat transfer coefficient (in which the four cooling types have been taken into account) to describe the heat transfer process.

$$q_s = h(T_w - T_0) = \left(2950.190 \times T_w^{-0.235} \times w^{0.805}\right) (T_w - T_0) \tag{14}$$

where w , T_w , and T_0 are the spray water impingement density (L·m⁻²·s⁻¹), slab surface, and water temperature, respectively.

Due to the existence of spray water overlap, the distribution of spray water for each row of nozzles along the width direction should be identified based on the nozzle collocation, as shown in Figure 3a. More details about this technique are available in our publication [7]. According to the nozzle collocation of secondary cooling zones, the integrated distribution of cooling water from Zone 1 to Zone 8 is obtained, as shown in Figure 3b. In order to deal with the heat transfer condition conveniently, the strand surface in the width direction is divided into 26 pieces (sections No. 1 to No. 25 being 30 mm wide and section No. 26 being 15 mm wide) for heat transfer. The cooling water sprayed onto each piece is determined based on the nozzle collocation of each cooling zone. The cooling water on each piece is supposed to be uniformly distributed.

The physical properties of steel Q345 used in the calculation are listed in Table 2.

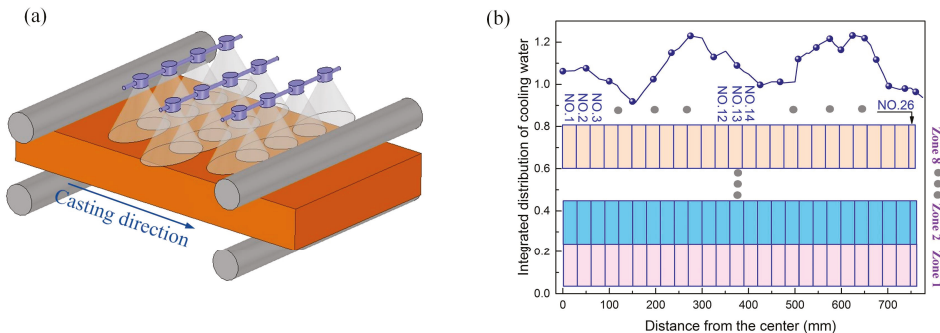


Figure 3. (a) Schematic of nozzle collocation; (b) integrated distribution of cooling water from Zone 1 to Zone 8.

Table 2. Physical properties of steel Q345.

Physical Properties	Values	Physical Properties	Values
Density, kg/m ³	7330	Viscosity, kg·(m·s) ⁻¹	0.0062
Specific heat, J (kg·K) ⁻¹	319.59 + 0.1934 × T (K)	Thermal conductivity, W (m·K) ⁻¹	57.524 – 0.0164 × T (K)
Liquidus, K	1786	Solidus, K	1715
Latent heat, J/kg	255,500	-	-

2.4. Solution Procedure

The coupled calculation model was solved using the SIMPLE method with ANSYS Fluent 14.0. For both the 3-D turbulent flow region and the 2-D laminar flow region, the time step size was set to 0.05 s. Based on the relations between the length of model and casting speed, the total number of time steps for 3-D turbulent flow region and 2-D laminar flow region were 3500 and 17,802, respectively. The calculation was performed on a computer with a 3.50-GHz Intel Core i7-3770k processor and 16.0-GB RAM. For each time step, the tolerances of continuity, *x*-velocity, *y*-velocity, *z*-velocity, *k*, *ε*, and energy were set as 0.001, 0.001, 0.001, 0.001, 0.001, 0.001, and 1 × 10⁻⁶, respectively.

3. Results and Discussion

3.1. Flow and Solidification Phenomena in the Turbulent Flow Region

Figure 4a shows the melt flow pattern in the turbulent flow region. It is seen that the molten steel jet flows through the port of SEN and impacts on the narrow face of the mold. The molten steel jet is divided into two parts at the impact point and forms upper and lower recirculation vortices. The fresh molten steel with higher temperature is brought to the impact point, where the solidification shell is remelting. The remelting phenomenon of the solidification shell is shown in Figure 4b. It is obvious that the impact effect of the molten steel jet on the formation of the solidification shell near the impact point is remarkable.

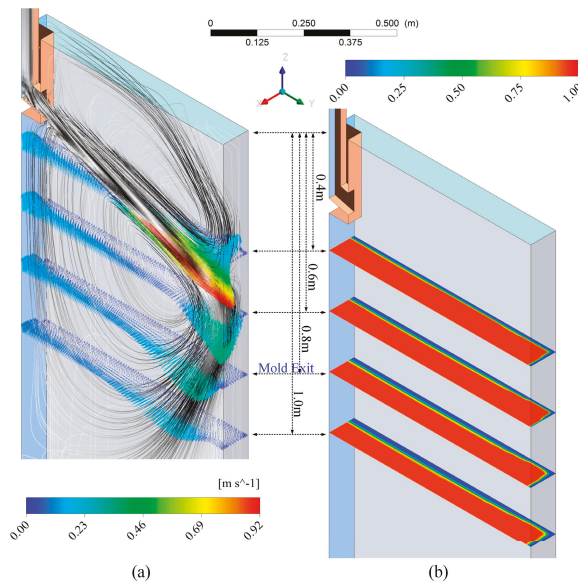


Figure 4. (a) Flow field in the turbulent flow region; (b) liquid fraction on the different transverse sections.

The impact point of the jet on the narrow face is obtained from Figure 5a,b. At the impact point, the z-component of velocity is equal to zero and the velocity magnitude reaches a valley value. In the present case, the impact point is at the position 457 mm below the meniscus. In order to find the interface between the turbulent flow region and the laminar flow region, the z-component of velocities of characteristic lines at the central symmetry plane of the strand narrow face were investigated. From Figure 5c, it can be seen that the z-component of the molten steel velocity is equal to the casting speed when arriving at the location 2442 mm below the meniscus, where it is roughly placed at the end of secondary cooling Zone 3.

To deal with the heat transfer condition for each secondary cooling zone separately, the transverse section at the end of secondary cooling Zone 3 (2560 mm below meniscus) is selected as the interface between the turbulent flow region and laminar flow region. Therefore, the 2-D slicing model is adopted in the laminar flow region from Zone 4 to Zone 8.

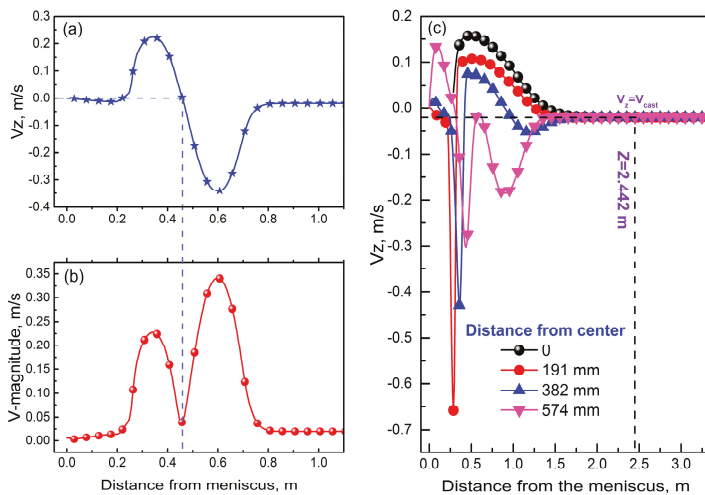


Figure 5. (a) z-component of velocity and (b) velocity magnitude variation of the line with 10 mm from the narrow face at the central symmetry plane. (c) z-component of the velocity variation of different lines at the central symmetry plane of the strand narrow face.

3.2. Grid Independence Tests for the Laminar Flow Region

To begin with, grid sizes for the laminar flow region have been carefully chosen to ensure the grid independence solution. As seen in the results of the grid independence tests shown in Figure 6, relatively larger differences exist in the solidification profile and temperature extreme in the transverse section (17.56 m from the meniscus) with different cell sizes. It is obvious that the cell size $25 \times 25 \text{ mm}^2$, as shown in Figure 6a, is too large for this case to precisely predict the solidification profile and temperature distribution. The solidification profile does not correspond with the integrated distribution of cooling water in secondary cooling zones (shown in Figure 3). Also, the lowest temperature is higher than the other cases. In comparing Figure 6b,c, where the cell size decreases from $15 \times 15 \text{ mm}^2$ to $10 \times 10 \text{ mm}^2$, there is a similar solidification profile which is corresponding with the integrated distribution of cooling water in the width direction of strand. The maximum and minimum temperatures in the case where the cell size is $15 \times 15 \text{ mm}^2$ are very close to those in the case where the cell size is $10 \times 10 \text{ mm}^2$. When the cell size reduces from $10 \times 10 \text{ mm}^2$ to $5 \times 5 \text{ mm}^2$, as shown in Figure 6d, the temperature extreme of 1181 K to 1733 K shows little change compared with that using grids with a cell size of $10 \times 10 \text{ mm}^2$. Thereby, in the present simulation, the grids with cell size $10 \times 10 \text{ mm}^2$ are sufficient to obtain the precise temperature distribution and solidification profile.

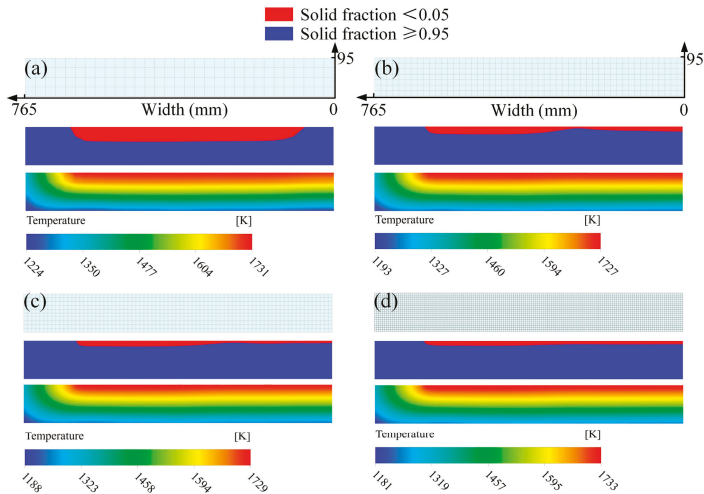


Figure 6. Solidification profile and temperature field in the transverse section (17.56 m from the meniscus) with different cell sizes: (a) $25 \times 25 \text{ mm}^2$, (b) $15 \times 15 \text{ mm}^2$, (c) $10 \times 10 \text{ mm}^2$, (d) $5 \times 5 \text{ mm}^2$.

3.3. Temperature Field and Solidification Profile

The slab center and wide surface center temperature along the casting direction predicted by the present model are compared to that predicted by our previous model, which is proven and widely employed in temperature prediction during the CC process. As the results show in Figure 7, the temperature predicted by the present model agrees well with that of the models by Long et al. [7] and Long and Chen [9]. The slab center temperature, as shown in Figure 7a, decreases slowly before complete solidification. However, after complete solidification, the slab center temperature decreases sharply. This is because there is no latent heat to maintain the temperature when the local region solidifies completely. The wide surface center temperature is shown in Figure 7b. Due to the strong cooling of the mold, the surface temperature decreases radically, and then recalesces when the strand is pulled out of the mold. In the secondary cooling zone, the surface temperature decreases gradually.

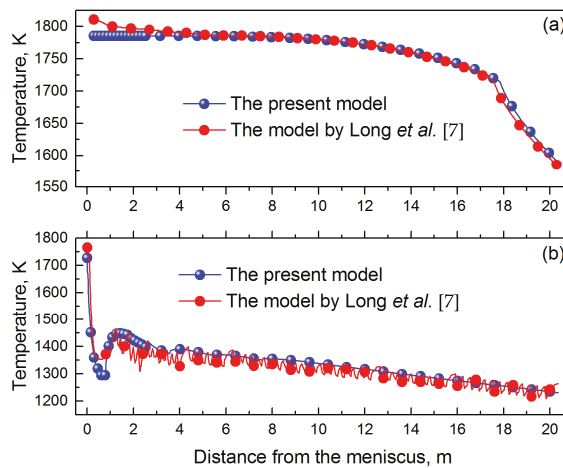


Figure 7. (a) Slab center and (b) wide surface center temperature along the casting direction.

The temperature distribution in transverse sections with different distances from the meniscus (as shown in Figure 8a) have a similar profile. The temperature decreases as the distance from the meniscus increases. Figure 8b shows the solidification profile evolution process during continuous casting. It is obvious that the liquid core of the strand is not entirely uniform. At the local region of the strand in the width direction, from roughly 400 to 500 mm, the molten steel solidifies completely owing to the minimum amount of the cooling water sprayed on it in the secondary cooling zone. The final solidification points (another one in the other half of the geometry) are 17.66 m away from the meniscus. Moreover, at the position about 150 mm in width direction, the molten steel solidifies completely a little earlier than that at the region from 400 to 500 mm. The reason is that the amount of cooling water at the former position is a little more than that at the region from 400 to 500 mm. This results from the valley of the distribution curve being very narrow at the position of about 150 mm, although the proportion of cooling water is slightly lower than that at the region from 400 to 500 mm. The solidification profile agrees well with the integrated distribution of cooling water in the secondary cooling zones.

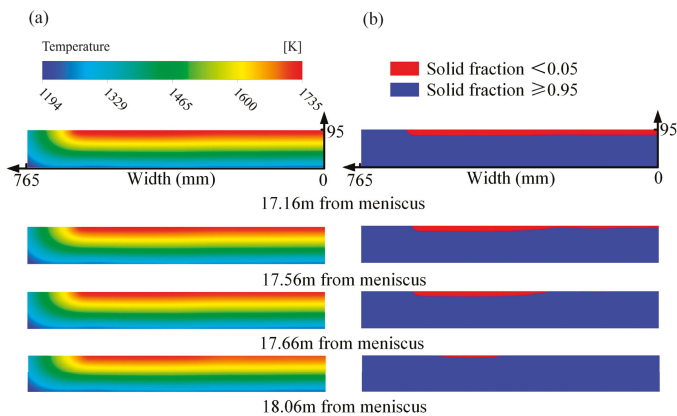


Figure 8. (a) Temperature field and (b) solidification profile in transverse sections with different distances from the meniscus.

4. Conclusions

A combined hybrid 3-D/2-D simulation model with a high calculation efficiency has been developed to investigate the flow and solidification behaviors during the slab CC process. The main conclusions are summarized as follows:

- (1) The impact effect caused by the molten steel jet on the formation of a solidification shell is significant. The impact point is at the position 457 mm below the meniscus, and the plug flow is formed 2442 mm below the meniscus.
- (2) For the simulation of the laminar flow region, the grids with a cell size of $10 \times 10 \text{ mm}^2$ are sufficient to attain a precise temperature distribution and solidification profile.
- (3) The solidification profile of the strand is not entirely uniform. The final solidification points, roughly being at the position from 400–500 mm in the width direction, are 17.66 m away from the meniscus.

Acknowledgments: The authors would like to thank the Natural Science Foundation of China (NSFC) for financial support (project No. 51504048, 51374260, 51611130062).

Author Contributions: Huabiao Chen, Mujun Long, and Dengfu Chen conceived the simulation model and the validation method. Huabiao Chen, Sheng Yu, Bin Liang, and Huamei Duan performed the calculations. All of the authors analyzed and discussed the data. Huabiao Chen wrote the paper.

Conflicts of Interest: The authors declare no conflict interest.

References

1. Ma, J.C.; Xie, Z.; Ci, Y.; Jia, G.L. Simulation and application of dynamic heat transfer model for improvement of continuous casting process. *Mater. Sci. Technol.* **2009**, *25*, 636–639. [[CrossRef](#)]
2. Zhao, Y.; Chen, D.F.; Long, M.J.; Shen, J.L.; Qin, R.S. Two-dimensional heat transfer model for secondary cooling of continuously cast beam blanks. *Ironmak. Steelmak.* **2014**, *41*, 377–386. [[CrossRef](#)]
3. Ma, J.C.; Lu, C.S.; Yan, Y.T.; Chen, L.Y. Design and application of dynamic secondary cooling control based on real time heat transfer model for continuous casting. *Int. J. Cast Met. Res.* **2014**, *27*, 135–140. [[CrossRef](#)]
4. He, D.F.; Chang, S.; Wang, H.B. Controlling transverse cracks of slab based on edge control technology. *J. Iron Steel Res. Int.* **2015**, *22*, 42–47. [[CrossRef](#)]
5. Chen, S.D.; Hu, Z.F.; Yuan, Y.Y.; Luo, Y.Z. Study on intermediate crack in continuous casting slab of medium carbon steel. *J. Iron Steel Res. Int.* **2011**, *18*, 383–388.
6. Long, M.J.; Chen, D.F.; Wang, Q.X.; Luo, D.H.; Han, Z.W.; Liu, Q.; Gao, W.X. Determination of CC slab solidification using nail shooting technique. *Ironmak. Steelmak.* **2012**, *39*, 370–377. [[CrossRef](#)]
7. Long, M.J.; Dong, Z.H.; Chen, D.F.; Liao, Q.; Ma, Y.G. Effect of uneven solidification on the quality of continuous casting slab. *Int. J. Mater. Prod. Technol.* **2013**, *47*, 216–232. [[CrossRef](#)]
8. Shen, H.F.; Hardin, R.A.; MacKenzie, R.; Beckermann, C. Simulation using realistic spray cooling for the continuous casting of multi-component steel. *J. Mater. Sci. Technol.* **2002**, *18*, 311–314.
9. Long, M.J.; Chen, D.F. Study on mitigating center macro-segregation during steel continuous casting process. *Steel Res. Int.* **2011**, *82*, 847–856. [[CrossRef](#)]
10. Ji, C.; Luo, S.; Zhu, M.; Sahai, Y. Uneven solidification during wide-thick slab continuous casting process and its influence on soft reduction zone. *ISIJ Int.* **2014**, *54*, 103–111. [[CrossRef](#)]
11. Xie, X.; Chen, D.F.; Long, H.J.; Long, M.J.; Lv, K. Mathematical modeling of heat transfer in mold copper coupled with cooling water during the slab continuous casting process. *Metall. Mater. Trans. B* **2014**, *45*, 2442–2452. [[CrossRef](#)]
12. Hardin, R.A.; Liu, K.; Kapoor, A.; Beckermann, C. A transient simulation and dynamic spray cooling control model for continuous steel casting. *Metall. Mater. Transf. B* **2003**, *34*, 297–306. [[CrossRef](#)]
13. Wang, Q.Q.; Zhang, L.F. Influence of FC-mold on the full solidification of continuous casting slab. *JOM* **2016**, *68*, 2170–2179. [[CrossRef](#)]
14. Shamsi, M.R.R.I.; Ajmani, S.K. Three dimensional turbulent fluid flow and heat transfer mathematical model for the analysis of a continuous slab caster. *ISIJ Int.* **2007**, *47*, 433–442. [[CrossRef](#)]
15. Shamsi, M.R.R.I.; Ajmani, S.K. Analysis of mould, spray and radiation zones of continuous billet caster by three-dimensional mathematical model based on a turbulent fluid flow. *Steel Res. Int.* **2010**, *81*, 132–141. [[CrossRef](#)]
16. Yang, J.W.; Du, Y.P.; Shi, R.; Cui, X.C. Fluid flow and solidification simulation in beam blank continuous casting process with 3d coupled model. *Iron Steel Res. Int.* **2006**, *13*, 17–21. [[CrossRef](#)]
17. Seyedein, S.H.; Hasan, M. A three-dimensional simulation of coupled turbulent flow and macroscopic solidification heat transfer for continuous slab casters. *Int. J. Heat Mass Transf.* **1997**, *40*, 4405–4423. [[CrossRef](#)]
18. Sun, H.B.; Zhang, J.Q. Study on the macrosegregation behavior for the bloom continuous casting: Model development and validation. *Metall. Mater. Transf. B* **2014**, *45*, 1133–1149. [[CrossRef](#)]
19. Cai, K.K. *Continuous Casting Mold*; Metallurgical Industry Press: Beijing, China, 2008; p. 6, ISBN 978-7-5024-4635-2.



© 2018 by the authors. Licensee MDPI, Basel, Switzerland. This article is an open access article distributed under the terms and conditions of the Creative Commons Attribution (CC BY) license (<http://creativecommons.org/licenses/by/4.0/>).

Article

Numerical Study on the Influence of a Swirling Flow Tundish on Multiphase Flow and Heat Transfer in Mold

Peiyuan Ni ^{1,2,*}, Mikael Ersson ³, Lage Tord Ingemar Jonsson ³, Ting-an Zhang ¹ and Pär Göran JÖNSSON ³

¹ Key Laboratory of Ecological Metallurgy of Multi-metal Intergrown Ores of Education Ministry, School of Metallurgy, Northeastern University, Shenyang 110819, China; zta2000@163.net

² Department of Materials and Manufacturing Science, Graduate School of Engineering, Osaka University, 2-1 Yamadaoka, Suita, Osaka 565-0871, Japan

³ Department of Materials Science and Engineering, KTH Royal Institute of Technology, SE-100 44 Stockholm, Sweden; bergsman@kth.se (M.E.); lage@kth.se (L.T.I.J.); parj@kth.se (P.G.J.)

* Correspondence: peiyuan_ni@163.com; Tel.: +86-024-83686283

Received: 30 April 2018; Accepted: 18 May 2018; Published: 21 May 2018

Abstract: The effect of a new cylindrical swirling flow tundish design on the multiphase flow and heat transfer in a mold was studied. The RSM (Reynolds stress model) and the VOF (volume of fluid) model were used to solve the steel and slag flow phenomena. The effect of the swirling flow tundish design on the temperature distribution and inclusion motion was also studied. The results show that the new tundish design significantly changed the flow behavior in the mold, compared to a conventional tundish casting. Specifically, the deep impingement jet from the SEN (Submerged Entry Nozzle) outlet disappeared in the mold, and steel with a high temperature moved towards the solidified shell due to the swirling flow effect. Steel flow velocity in the top of the mold was increased. A large velocity in the vicinity of the solidified shell was obtained. Furthermore, the risk of the slag entrainment in the mold was also estimated. With the swirling flow tundish casting, the temperature distribution became more uniform, and the dissipation of the steel superheat was accelerated. In addition, inclusion trajectories in the mold also changed, which tend to stay at the top of the mold for a time. A future study is still required to further optimize the steel flow in mold.

Keywords: swirling flow tundish; multiphase flow; heat transfer; mold; continuous casting

1. Introduction

The mold is the final stage during the continuous casting process of steel, where the solidification of the molten steel occurs. Multiphase flow, heat and mass transfer, slag entrainment, inclusion and bubble entrapment, inclusion removal, and solidification are very important multiphysics concerns in the continuous casting process. This is due to the fact that these issues can significantly influence the quality of the semifinal steel product. As a matter of the first importance, a desirable steel flow in mold is wanted, since the other physical phenomena are directly affected by the steel flow inside the mold.

Direct investigations of the flow phenomena in a mold face significant challenges, due to the high temperature and high cost. Therefore, as an initial step to further improve the steel flow performance in a mold, numerical and physical modeling has become a common way to study the multiphase flow phenomena under various conditions. Specifically, some factors that may affect the mold flow, such as the SEN (Submerged Entry Nozzle) type (straight or bifurcated) [1,2], SEN port design (shape, angle, thickness) [3–10], argon bubbles [11–23], SEN immersion depth [3,4,6,24], nozzle clogging [25], mold flow modifier [26], EMBr (electromagnetic braking) [13,14,20–24,27–30] and M-EMS (mold

electromagnetic stirring) [8–10,31], have been vastly investigated. Further improvements of the steel flow performance simply based on the parameter optimization become difficult. Therefore, in recent years, EMBr and M-EMS are widely applied to improve the steel flow performance in mold. It was found that EMBr can reduce the flow variation [23], suppress the flow velocity [20,30], increase the temperature near meniscus [14,29], decrease the temperature difference in mold [20,29], and reduce the impingement intensity near the narrow wall [29]. The use of M-EMS was found to contribute to a uniform temperature distribution [10,31], a large floating up rate of inclusions [31,32], a homogeneous solute distribution [10], a uniform solidified shell [10], and a high quality of the steel product [32]. However, their application relies on costly equipment, and also requires the consumption of electricity. Furthermore, it is sometimes difficult to realize a good flow pattern in a mold, since the original upstream flows from the SEN ports are unknown, due to flow fluctuations or biased flows. In addition, the effects of EMBr are directly related to some factors, such as the intensity of the magnetic field, the reciprocal position between the magnetic field and the acting region, the casting speed, the SEN depth, and so on [24,30]. Also, for the M-EMS case, the meniscus velocity magnitude and the level fluctuation height were found roughly linearly proportional to the applied current [33]. Therefore, over-stirring or insufficient stirring should be avoided, which sometimes is difficult, due to the transient steel flow in a real casting situation. Furthermore, it takes some time for the M-EMS to change the steel flow from a single port SEN in a billet or bloom casting, due to the high momentum of the impingement jet flow going deep into the mold. In summary, the performances of EMBr and M-EMS highly depend on the SEN port flow situation and application parameters. This leads to some uncertainties of their performances in applications.

An alternative way to optimize the mold flow is by a root measure to control the SEN outlet flow. This is realized by using a swirling flow SEN, which aims to produce a rotational flow component to optimize the SEN port flows, and afterwards, optimize the steel flow in a mold. The swirling flow SEN and its influence on the mold flow have been vastly studied [34–46]. It was found that the heat and mass transfer near the meniscus can be remarkably activated [34,38,40,42], and a uniform velocity distribution can be obtained within a short distance from the SEN outlet [34,38,40]. Furthermore, the penetration depth of the SEN outlet flow is remarkably decreased in a billet mold [34,42]. Industrial trial results [39] show that the swirling flow SEN effectively improved the steel product quality and reduced the clogging problem of the SEN side ports. Therefore, the swirling flow SEN has advantages in the continuous casting process.

In the past, several methods were studied both experimentally and numerically to produce a swirling flow inside a SEN. Specifically, a swirl blade method was investigated in many studies, where a swirling flow was produced by installing a swirl blade inside the SEN. It is a cost-saving method, and has been proved by plant trials [39] that it can improve the steel product quality. However, the lifespan of the swirl blade and the inclusion attachment on its surface, which may lead to nozzle clogging, restrict its application for longer casting times. Some studies have also been carried out to investigate the electromagnetic stirring method [43–46]. The swirling flow is obtained by installing the electromagnetic stirring equipment surrounding the SEN. Therefore, it is associated with an equipment cost and an electricity cost, which increases the steel product cost. Recently, Ni et al. [47–49] proposed a new method to produce a swirling flow in a SEN simply by using a cylindrical tundish design. It is a simple and cost-saving method to realize a swirling flow in the SEN. Furthermore, its effectiveness has been confirmed both by water model experiments, and also by numerical simulations [49]. However, the steel flow characteristics in the mold with this new tundish design remains to be studied.

Previous studies about the influence of a swirling flow SEN on the mold flow commonly ignored the top slag phase in the mold. The influence of a swirling flow SEN on the steel-slag interface phenomena and the steel flow in the vicinity of the solidified shell should be further studied. Moreover, swirling steel flows, produced from M-EMS and the swirling SEN, were mainly investigated by using k - ϵ type of turbulence models. However, high-intensity swirling flows normally have anisotropic turbulent fluctuations, and sometimes, a vortex core precession exists in this kind of flows [50]. A RSM

(Reynolds Stress Model) which directly solves the anisotropic turbulent fluctuations shows better performance, in general, compared to the RANS eddy-viscosity models [49,51–53]. Jakirlic et al. [53] also found that a good ability to capture the stress anisotropy in the near-wall region is very important to reproduce these types of flow. Therefore, the swirling steel flow in a cylindrical tundish design has previously been solved by using RSM coupled with the Stress-Omega submodel, where the turbulent boundary layer was also resolved with a very fine grid ($y^+ < 1$) [49]. In this study, the characteristics of the multiphase flow and heat transfer in a billet mold were studied during the casting process by using the new swirling flow tundish design. The swirling flow velocity profile on a cross section of the SEN obtained in the previous study [49] was used as the inlet flow condition for the mold flow solution to save the computational time. The RSM coupled with the Stress-Omega submodel was thereafter used to solve the flow in the mold, with a very fine grid near the solidified shell of y^+ value around 1. The VOF (volume of fluid) method was used to capture the steel-slag interface. The energy equation was solved to study the temperature distribution in the mold, and a Lagrangian particle tracking scheme was used to study the motions of non-metallic inclusions in the mold. The fluid flow, steel-slag interface fluctuation, temperature distribution, and inclusion motion in the mold were investigated. In addition, to show the change of the multiphysics in the mold, these characteristics were compared to those in a conventional tundish casting without a swirling flow effect.

2. Model Description

2.1. Model Assumptions

A three-dimensional mathematical model has been developed to describe the steel-slag-inclusion three-phase flow, and the temperature distribution in the mold. The model is based on the following assumptions:

1. Steel and slag behave as an incompressible Newtonian fluids;
2. Solidification in the mold is not considered;
3. A constant molecular viscosity for steel and slag was assumed. This is due to that the maximum temperature difference in the mold is only 30 K between 1788 K and 1818 K. The viscosity change in this temperature range is not significant, and this can be seen from a previous study [10];
4. A constant steel and slag density was used. The temperature influence on the steel density change was accounted for in the source term of the momentum equation;
5. The SEN wall was assumed to be a smooth wall;
6. Inclusions were assumed to be spherical.

2.2. Transport Equations

The conservation of a general variable ϕ within a finite control volume can be expressed as a balance among the various processes, which tends to increase or decrease the variable values. The conservation equations, e.g., continuity, volume fraction, momentum, turbulence equations, and energy equation can be expressed by the following general equation [54]:

$$\frac{\partial}{\partial t}(\rho\phi) + \frac{\partial}{\partial x_i}(\rho\phi u_i) = \frac{\partial}{\partial x_i} \left(\Gamma_\phi \frac{\partial \phi}{\partial x_i} \right) + S_\phi, \quad (1)$$

where the first term on the left-hand side is the instantaneous change of ϕ with time, the second term on the left-hand side represents the transport due to convection, the first term on the right-hand side expresses the transport due to diffusion where Γ_ϕ is the diffusion coefficient with different values for different turbulence models, or the effective thermal conductivity. Furthermore, the second term on the right-hand side is the source term.

2.3. Interface Tracking

In order to investigate the steel-slag interface fluctuation, the steel-slag interface must be properly tracked. This is done by employing the VOF model [55], where a volume fraction equation for the slag phase was solved. The sum of the slag phase fraction α_{slag} and the steel phase fraction α_{steel} is equal to 1. In addition, one set of momentum and energy equation was solved to obtain the predicted flow field in the mold. The mixed material properties in the grid cell, where the interface exists, are required by the momentum equation and can be calculated by the following equations:

$$\rho_{\text{mix}} = \alpha_{\text{steel}}\rho_{\text{steel}} + \alpha_{\text{slag}}\rho_{\text{slag}} \quad (2)$$

$$\mu_{\text{mix}} = \alpha_{\text{steel}}\mu_{\text{steel}} + \alpha_{\text{slag}}\mu_{\text{slag}} \quad (3)$$

2.4. Turbulence Modeling

As previously mentioned, one important concern about modeling the swirling flow is the anisotropic turbulent properties which commonly exist in high intensity swirling flows. Here, the RSM model [55–57] combined with the Stress-Omega submodel [55,58] was used to simulate the steel flow. The Stress-Omega submodel is good for modeling flows over the curved surfaces and swirling flows [55]. A near-wall treatment is automatically used to perform blending between the viscous sublayer and the logarithmic region [55]. In RSM model, the Reynolds stress terms emerging from the Reynolds averaging of Navier-Stokes equations are directly solved by resolving their transport equations to account for the possible anisotropic fluctuation in a swirling flow. In order to save the computational time, the realizable k - ϵ turbulence model [59], coupled with the enhanced wall treatment model [55], was first used to produce an initial flow field. Then, with this flow initialization, the RSM model calculation was carried out until a fully developed flow was obtained.

2.5. Heat Transfer

The temperature distribution in the mold was obtained by solving the following energy equation [55]:

$$\frac{\partial}{\partial t}(\rho E) + \frac{\partial}{\partial x_i}(u_i(\rho E + p)) = \frac{\partial}{\partial x_i} \left(\left(k + \frac{c_p \mu_t}{Pr_t} \right) \frac{\partial T}{\partial x_i} \right), \quad (4)$$

where E is energy in the unit of J, k is the thermal conductivity with the unit of W/(m·K), c_p is the specific heat capacity in J/(kg·K), μ_t is the turbulent viscosity, Pr_t is the turbulent Prandtl Number, ρ is fluid density in kg/m³, p is pressure in Pa, and T is temperature in K. The steel density change and subsequent natural convection due to temperature variance was accounted for by the Boussinesq model [60]. This model treats density as a constant value in all solved equations, except for the buoyancy in the momentum equation (it is normally put in the source term) as follows:

$$(\rho - \rho_0)g \approx -\rho_0\beta(T - T_0)g, \quad (5)$$

where ρ_0 is the (constant) density of the liquid steel with the unit of kg/m³, T_0 is the operating temperature in K, and β is the thermal expansion coefficient of the liquid steel. The thermal properties of the fluids and some parameters are shown in Table 1.

Table 1. Thermal properties of the steel and slag.

Parameters	Symbols	Steel	Slag
Density, kg/m ³	ρ_o	7000	2600
Viscosity, kg/(m·s)	μ	0.0064	0.09
Thermal conductivity, W/(m·K)	k	35	1.1
Specific heat, J/(kg·K)	c_p	628	1200
Thermal expansion coefficient, 1/K	β	10^{-4}	-
Interfacial tension, N/m	σ		1.6
Operating temperature, K	T_o		1788
Turbulent Prandtl number	Pr_t		0.85

2.6. Lagrangian Particle Tracking Model

The inclusion velocity u_p was obtained by solving the following momentum equation, which has been introduced in detail in a previous study [61]:

$$\frac{du_p}{dt} = \frac{(u - u_p)}{\tau_r} + g \left(1 - \frac{\rho_f}{\rho_p} \right) + \frac{1}{2} \frac{\rho_f}{\rho_p} \left(u_p \nabla u - \frac{du_p}{dt} \right) + \frac{\rho_f}{\rho_p} u_p \nabla u + \frac{2\eta v^{\frac{1}{2}} \rho_f S_{ij}}{\rho_p d_p (S_{lk} S_{kl})^{\frac{1}{4}}} (u - u_p), \quad (6)$$

where, on the right-hand side, the first term is the drag force, the second term is the force per unit inclusion mass due to gravity and buoyancy, the third term is the virtual mass force, the fourth term is the pressure gradient force, and the fifth term is the Saffman's lift force [62,63]. Furthermore, u is the continuous-phase velocity, v is the kinematic viscosity of the fluid, d_p is the diameter of an inclusion, ρ_f and ρ_p are the densities of the fluid and the inclusion, respectively. Furthermore, S_{ij} and S_{lk} are the deformation tensor, and η is a constant which is equal to 2.59 [63].

2.7. Boundary Conditions

The velocity profile on the cross section of the cylindrical tundish SEN, which has been solved in a previous study [49], was used as the inlet boundary condition for the current simulation of the mold flow. Figure 1a,b show the location of the cross section on the cylindrical tundish SEN and the steel flow characteristics [49]. The cross section is located at 0.4 m below the tundish bottom with the total SEN length of 0.65 m. It can be seen that the maximum tangential velocity is around 2.5 m/s. The swirling number is defined by using the mean tangential velocity, W , and the mean vertical velocity, V , on the cross section with the ratio of $2W/3V$, and it is 1.24 on this cross section [49]. The inlet boundary condition for the conventional tundish casting is a uniform velocity distribution at the SEN cross section, with the steel flow velocity of -1.1 m/s in Z-direction, which corresponds to the same casting speed as the swirling flow tundish casting.

The calculation domain is shown in Figure 1c. A non-slip boundary condition was imposed on the SEN wall. For the top surface of the mold, a zero-shear slip wall boundary condition was used. For the mold wall, a moving wall boundary condition with the velocity of -0.013 m/s in Z direction was used to account for the movement of the solidified shell in a real casting process. The fully developed flow condition is adopted at the mold outlet, where the normal gradients of all variables are set to zero. For the heat transfer boundary condition, a constant steel temperature of 1818 K was used at the inlet. A constant temperature of 1788 K was imposed on the solidified shell. An adiabatic condition was used both at the SEN wall and at the free surface. In addition, a "reflect" wall boundary condition was used for the inclusion tracking, and an "escape" boundary condition was used at the bottom outlet of the mold.

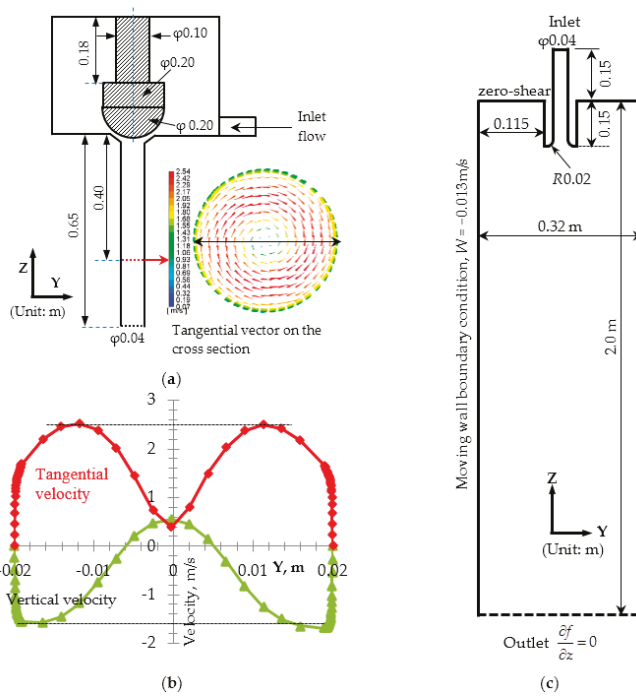


Figure 1. (a) Location of the cross section used as the inlet boundary condition of the mold simulation and the tangential velocity distribution on it, (b) velocity distribution along the line on the cross section (negative values for vertical velocity means in gravity direction), and (c) calculation domain in mold.

2.8. Solution Method

The multiphase flow and temperature distribution in the billet mold was solved by using the commercial software ANSYS FLUENT 18.0[®]. The numerical simulations were carried out based on 2.2 million grid cells to guarantee the grid-independent solution. A very fine grid was used in the near-wall region, with the y^+ value of the first grid layer around 1. The PISO scheme was used for the pressure-velocity coupling. Furthermore, the PRESTO method was adopted to discretize the pressure. The governing equations were discretized using a second order upwind scheme. The convergence criteria were as follows: the residuals of all dependent variables were smaller than 1×10^{-3} at each time step.

3. Results and Discussion

The multiphase flow and heat transfer in the mold both with a swirling flow tundish casting and also with a conventional tundish casting were firstly solved by the realizable $k-\epsilon$ model with an enhanced wall treatment for the first 75 s. After that, this solution was used as an initial condition for the RSM model calculation to 125 s for a developed flow field. The multiphysics in the mold from a conventional tundish casting and from a swirling flow tundish casting were analyzed and compared in the following.

3.1. Steel Flow Paths

Figure 2 shows the steel flow path in the mold both from a conventional tundish and from a swirling flow tundish design. It can be observed that a completely different flow pattern in the mold

was observed. With a conventional tundish casting in Figure 2a, the SEN outlet flow goes deep into the mold to the depth of around 1.5 m. This results from a large vertical momentum of the steel flow. As the steel flows downwards, the jet is entraining the surrounding fluid due to the friction. This dissipates the jet momentum and also increases the jet width. Meanwhile, the pressure in the region near the downward jet flow decreases. Therefore, the steel surrounding the impingement jet moves towards it. This leads to a vertical rotational flow in the middle region of the mold as shown in Figure 2a indicated by the red color arrows. The upwards steel flow in this rotational movement further leads to a weak rotational flow in the upper part of the mold near the meniscus. However, with a swirling flow tundish design in Figure 2b, the SEN outlet flow moves towards the solidified shell rather than goes deeply into the mold. This is due to the rotational steel flow momentum. After the steel stream reaches the solidified shell, a part of the steel flows downwards along the solidified shell with a horizontal rotational flow momentum, which can be seen from the red arrow in Figure 2b. Another part of the steel moves upwards and towards the meniscus. Therefore, the steel flow pattern undergoes a significant change compared to a conventional tundish casting. The deep impingement jet into the mold observed in Figure 2a disappeared with the use of a swirling flow tundish. This is also one of the advantages for the use of a swirling flow SEN compared to M-EMS. Due to the high steel flow inertia from the one-port SEN, the impingement jet was actually not significantly changed by the M-EMS, which shows a high downwards steel flow velocity in the center of the mold. This can be seen from some previous studies [32,33]. Therefore, in some cases, the side-port SEN was investigated in bloom castings in combination with M-EMS [8,10], which can change the high temperature SEN port flow towards the solidification front, rather than moving deeply into the mold. However, side ports are the sensitive region for nozzle clogging, and they deliver the steel into the mold from a certain direction depending on the SEN port direction, rather than along the periphery of the SEN, which is in 360° in a swirling flow SEN. Therefore, the current swirling flow tundish SEN can deliver high temperature steel uniformly distributed towards the solidified shell. Furthermore, this also avoids the strong attack by the high temperature steel on some locations of the solidified shell which is in the case with side ports.

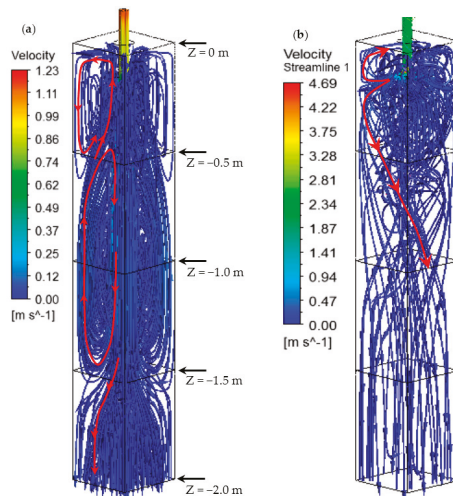


Figure 2. Comparison of steel flow paths in mold. (a) Casting with a conventional tundish and (b) casting with a swirling flow tundish.

3.2. Steel Flow Velocity

Figure 3 shows the steel flow velocity on the vertical planes at the middle of the mold. The locations of these vertical planes can be seen from the top view sketch of the mold in Figure 3. For all the vertical planes passing the mold center, the diagonal vertical plane is the largest vertical plane, and the plane perpendicular to the solid shell middle is the smallest vertical plane. Therefore, these planes are selected to show the flow characteristics. It can be seen in Figure 3a that the steel jet keeps a high velocity in the center of the mold, even for a large depth. At the top of the mold near the meniscus, the steel flow is very weak. However, with the swirling flow tundish as shown in Figure 3b, the high velocity region was located at the top region of the mold. This is expected to improve the heat transfer near the meniscus and the dissipation of the steel superheat. Furthermore, steel moves downwards at the region near the solidified shell, and it flows upwards in the center of the mold. This may be helpful to improve the mixing towards a homogeneous state in the mold. Furthermore, the velocity magnitude of the SEN outlet flow rapidly decreases to smaller than 0.4 m/s. As previously mentioned, there was no main impingement jet deep into the mold, which is different from the case of a conventional tundish casting with a straight SEN.

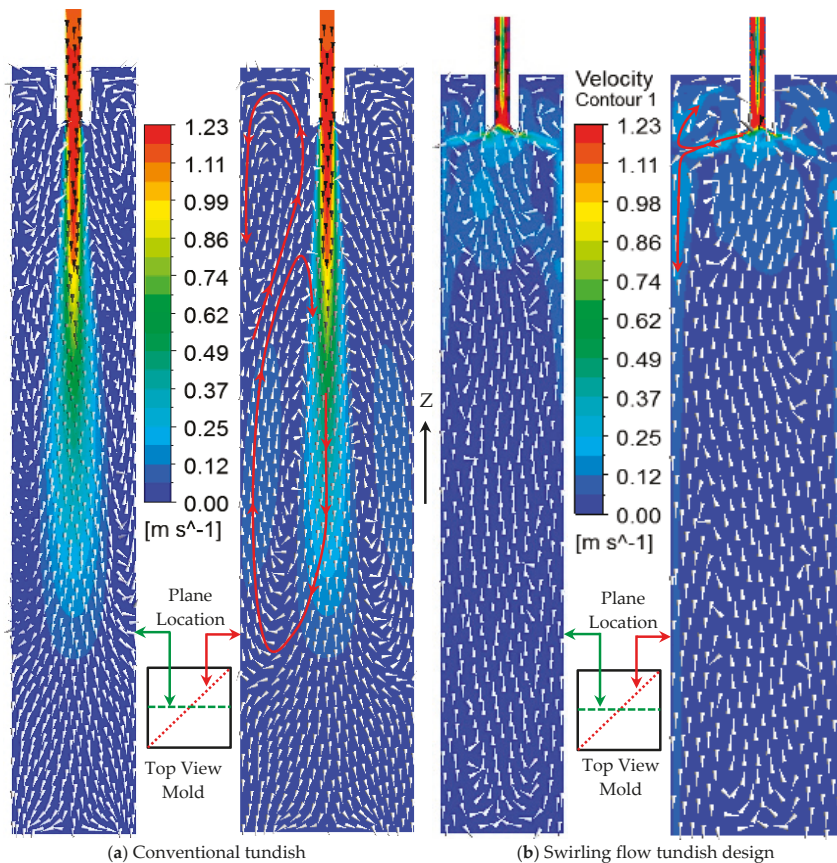


Figure 3. Steel flow velocity in the vertical middle plane of the mold. (a) Conventional tundish casting and (b) Swirling flow tundish design casting (arrows are the steel flow directions).

Figure 4 shows a comparison of the vertical velocity distributions along lines at different mold depths. It can be seen that the vertical velocity magnitude is much smaller in the mold center when a swirling flow tundish design was used. This has been clearly shown in Figure 3b. However, at the locations close to the solidified shell, its velocity is larger than that with a conventional tundish casting. This can be seen from the enlarged part in Figure 4. A large velocity near the solidified shell is helpful to shear off the dendrites from the solidification interface and promotes the nucleate, which results in an enhancement of the transition from a columnar to an equiaxed solidification [33]. For the casting with a conventional tundish, the vertical velocity of the steel flow is still around 0.1 m/s at a depth of 1.5 m in the mold center. This kind of flow pattern, with a strong downwards flow stream, is not good for some issues in a steel continuous casting process, such as the inclusion removal and the dissipation of steel superheat. Therefore, it is clear that the swirling flow tundish design is helpful for the optimization of the mold flow.

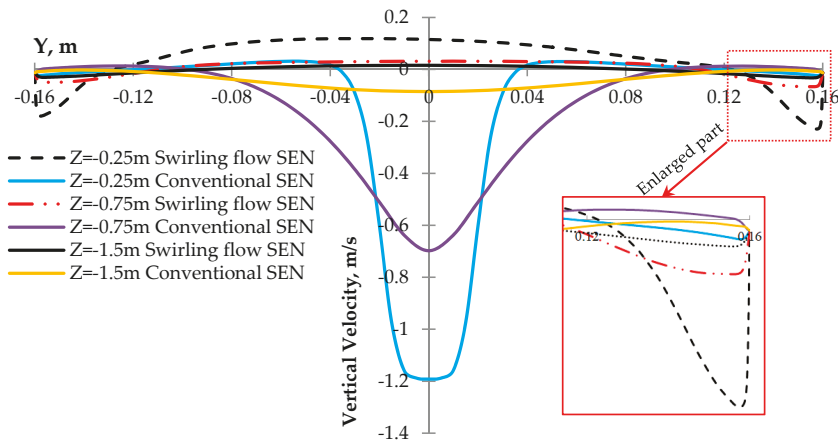


Figure 4. Vertical steel flow velocity along horizontal lines in different mold depths.

Another important characteristic about the swirling flow tundish casting is the swirling steel flow on the cross sections of the mold. Figure 5 shows the tangential velocities of the steel flow on two cross sections in different mold depths. It can be seen, in Figure 5b, that the maximum tangential velocity can reach around 0.076 m/s near the solidified shell on the cross section with a mold depth of 0.5 m. In addition, at a mold depth of 1.5 m, the maximum tangential velocity decreases to around 0.005 m/s, while the velocity distribution becomes more axisymmetric. This means that the swirling flow becomes more uniform after moving from the depth of 0.5 m to 1.5 m. Furthermore, the high tangential velocity region is still located near the solidified shell. Figure 6 shows the magnitude of the tangential velocity along different horizontal lines in different mold depths. The locations of the horizontal lines are shown in Figure 5b. It can be seen that the maximum tangential velocity gradually decreases when the steel moves downwards. This is similar as that in the mold with M-EMS, where the rotational velocity becomes smaller with an increased distance away from the stirrer midplane [33]. A large velocity gradient exists near the solidified shell, which can also be seen in Figure 4 for the vertical velocity component. In the mold with a conventional tundish, no obvious swirling flow was observed, and the steel flow velocity near the solidified shell is much smaller compared to the swirling flow tundish case. Therefore, both the tangential velocity magnitude and the axial velocity magnitude near the solidified shell are larger for the case with the swirling flow tundish casting than that with a conventional tundish casting.

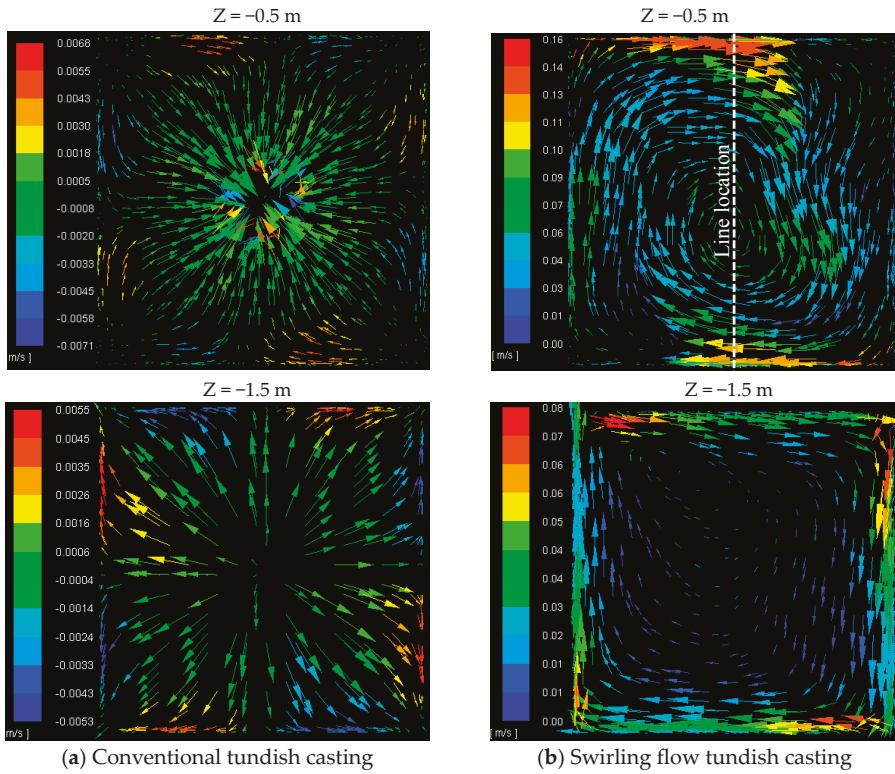


Figure 5. Tangential velocities on different cross sections of the mold. (a) Conventional tundish casting and (b) swirling flow tundish casting.

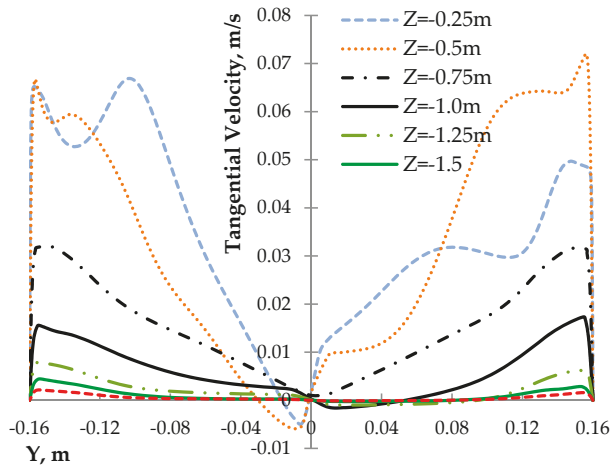


Figure 6. Tangential velocity distribution along different horizontal lines in different mold depths.

Due to the change of the steel flow pattern in mold, shear stresses on the solidified shell become different. Figure 7 shows the shear stress on the solidified shell for the first 0.5 m shell from the meniscus. It can be seen that the values of shear stresses are mostly smaller than 10 Pa both for the conventional tundish case and also for the swirling flow tundish case. Shear stress is proportional to the velocity gradient. Therefore, a large shear stress represents a large velocity gradient near the solidified shell. Due to that, a rotational flow exists in the mold as shown in Figure 5b, the shear stress values for the swirling flow tundish case are mostly larger than that with a conventional tundish. In addition, shear stresses at the locations where the SEN outlet flow hits the solidified shell are not very large, as shown in Figure 7b, with the values of around 6 Pa. This means that there is no strong flow stream towards the solidified shell, due to the uniformly spreading of the steel flow from the SEN outlet.

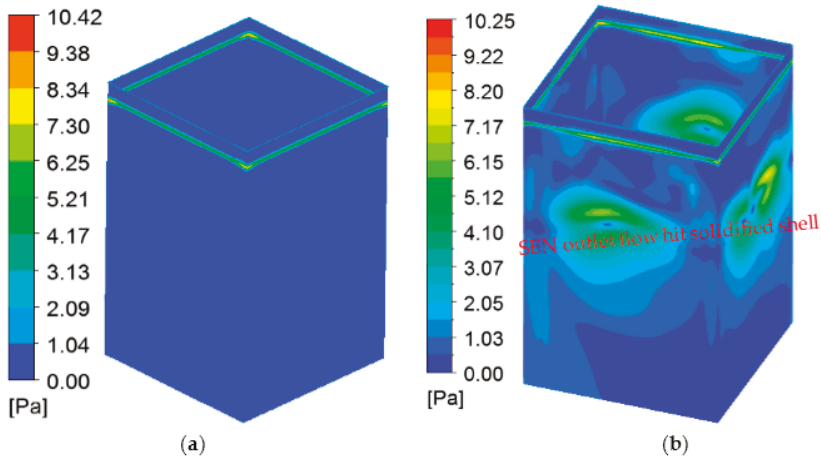


Figure 7. Shear stress on the solidified shell. (a) Conventional tundish casting and (b) swirling flow tundish casting.

3.3. Turbulence Properties

Due to the flow changes as presented above, the characteristics of the turbulence properties in the mold are also significantly changed, as shown in Figure 8. It can be seen that with a conventional tundish casting, the turbulence properties show jet flow characteristics. A high turbulent kinetic energy and Reynolds stress values exist in the region near the impingement jet, due to the shear between the jet and its surrounding steel. However, at the top of the mold, the magnitudes of the turbulence properties are very small. In addition, the turbulence properties show anisotropic characteristics. The Reynolds stress is large in the vertical direction, namely, the value of $\overline{w'w'}$ in the conventional tundish casting. With a swirling flow tundish casting, turbulence properties are sharply dissipated in the top region of the mold. This is due to the change of the steel flow pattern as previously shown in Figure 3b. Deeper in the mold, smaller values of both turbulent kinetic energy and Reynolds stresses were observed. Due to the large value of turbulent properties and the flow characteristic change with the swirling flow tundish casting, the heat transfer in the top of the mold was expected to be enhanced.

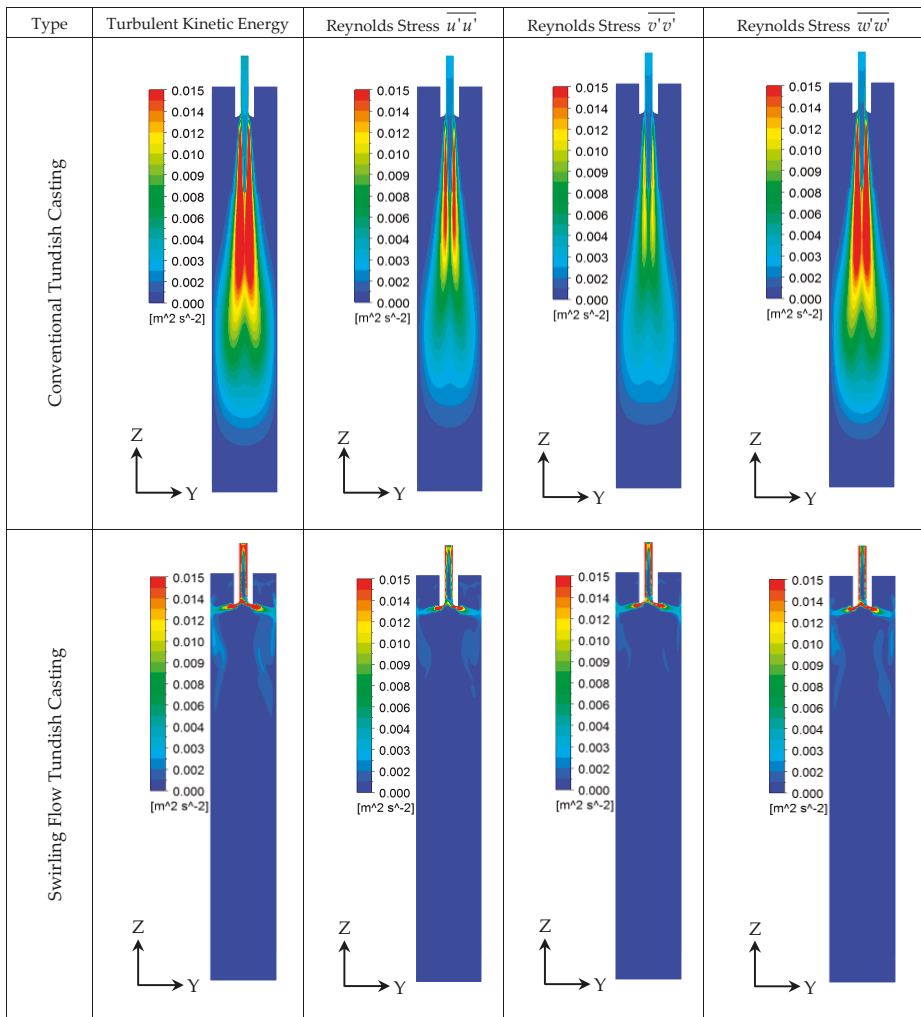


Figure 8. Turbulence properties on the YZ middle plane of the mold.

3.4. Steel/Slag Interface Phenomena

Steel/slag interface phenomena in the mold are very important during the continuous casting process. The reason is that the slag entrainment into the steel may lead to the formation of non-metallic inclusions. Therefore, a large steel/slag interface fluctuation is unwanted in the continuous casting process. Figure 9 shows the steel/slag interface and the flow pattern in the steel and slag. It can be seen that the thickness of the steel/slag interface region is larger when a swirling flow tundish was used, compared a conventional tundish. This can easily be seen from Figure 9b where the isosurface of the slag with the density of 2601 kg/m^3 was plotted (the pure slag has the density of 2600 kg/m^3). When a conventional tundish SEN was used, steel with a large momentum moves deeply into the mold, and a calm steel flow region at the top part of the mold was obtained. This can be seen from Figure 3a. However, the steel flow is activated in the top of the mold when the swirling flow tundish was used. This leads to a large level fluctuation, while it helps the heat transfer near the meniscus. In the mold

with a swirling flow tundish casting, as shown in Figure 9, the steel flowing towards the solidified shell divided into an upwards and a downwards flow. The upwards flow shown in Figure 9b directly moves towards the steel/slag interface with the velocity of around 0.2 m/s, as shown in Figure 3b. Due to the small immersion depth of the SEN in steel with the value of around 12 cm, this velocity is still high when it reaches the steel/slag interface. This should cause a large steel/slag interface fluctuation. However, a flat interface is generally observed in this study. In the case with M-EMS, the level fluctuation was also found to be increased [10,33,64]. The meniscus surface has a swirl flow and the meniscus level rises near the bloom strand wall and sinks around the SEN wall, which shows an inclined steel/slag interface [33]. Sometimes, a vortex formation near the SEN wall was found with M-EMS [64]. Therefore, the mold level fluctuation should be considered to make it as low as possible, both for M-EMS applications and for the use of swirling flow SEN.

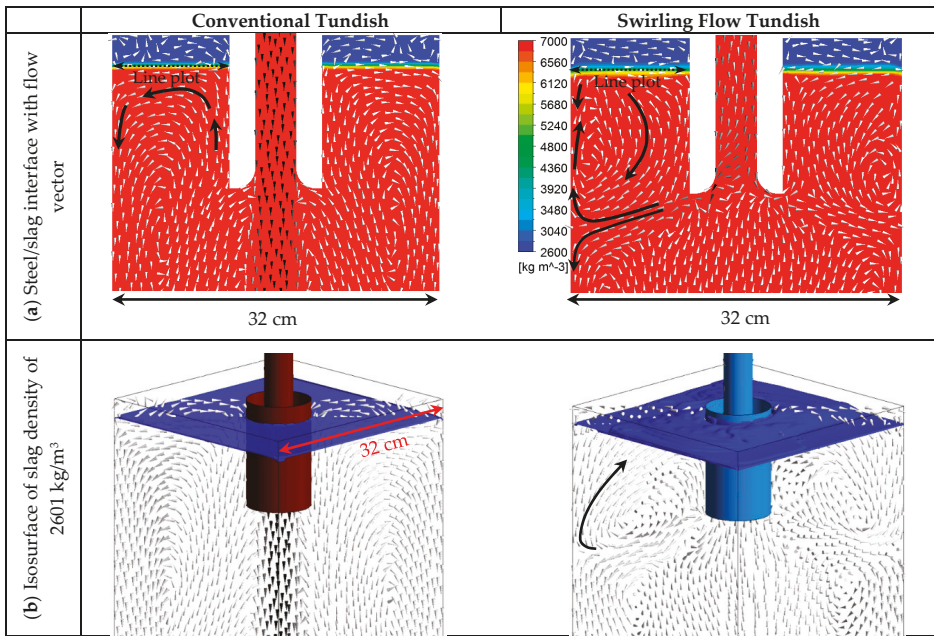


Figure 9. Steel/slag interface with steel flow vectors.

Figure 10 shows the distributions of the velocity magnitude and turbulent kinetic energy along the steel/slag interface. The location of the line plot is shown in Figure 9. It can be seen that the velocity magnitude with the swirling flow tundish case is around 3 times that of a conventional tundish, with the maximum value of 0.05 m/s. However, this maximum value is still smaller than that found in a mold with M-EMS application, where the values can reach around 0.2 to 0.3 m/s [33,64]. The turbulent kinetic energy is close to zero with a conventional tundish casting, and the maximum value is around 0.001 m²/s² for the swirling flow tundish case. This means that the turbulence intensity is slightly increased when the swirling flow tundish design was used.

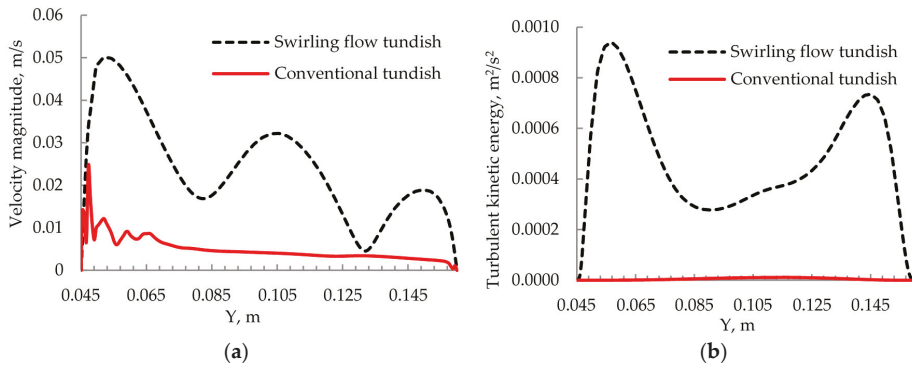


Figure 10. (a) Velocity magnitude at the steel/slag interface and (b) turbulent kinetic energy at the steel/slag interface.

According to a previous research [65], the slag entrainment into liquid steel may occur when the Weber number is greater than 12.3. The Weber number can be defined as

$$We = \frac{u_1^2 p_1}{\sqrt{\sigma g (\rho_1 - \rho_s)}}, \quad (7)$$

where u_1 is the radial steel velocity, g is gravitational acceleration, and σ is the interfacial tension between steel and slag. A slag density value of 2600 kg/m^3 was used, and the value of interfacial tension between the steel and the slag was set to 1.16 N/m [66]. The maximum total velocity at the steel-slag interface in the mold, 0.05 m/s , was used to calculate the Weber number. The calculated maximum Weber number is around 0.8 for the case with the swirling flow tundish casting. Therefore, the Weber number is still much smaller than 12.3, which means a small risk for the slag entrainment. Due to the swirling flow effect, the SEN outlet flow spreads towards the mold wall, rather than goes deep into the mold, as in a conventional tundish casting with a one-port SEN. Therefore, it is possible to increase the immersion depth of the SEN as well, where the value is 15 cm in the current study. This may help to decrease the fluctuations, as well as to further reduce the risk of the slag entrainment. In reality, the slag entrainment issue should be experimentally investigated in the future when a slag is used to protect the steel from the air reoxidation.

3.5. Temperature Distribution

Steel temperature in the mold is very important, since it significantly influences the solidification structure, which in turn determines the product quality. One important issue regarding the steel temperature is the removal of the steel superheat in the mold. Furthermore, a uniform steel temperature in the mold is also important, in order to obtain a uniform solidified shell. The influence of the swirling flow tundish casting on the temperature field in the mold was investigated, where the natural convection in the mold was also considered.

Figure 11 shows the temperature distribution in the mold. It can be seen that the swirling flow tundish design significantly change the temperature distribution in the mold. Specifically, in the mold with a conventional tundish SEN, the steel flow jet with a high temperature directly goes deeply into the mold. This leads to a high temperature region which is located deep in the center of the mold, as shown in Figure 11a. However, the temperature is low in the mold top. Therefore, the temperature field is not uniform in the mold, and it is not good for the removal of the steel superheat. In the top part of the mold, the density of steel in the region near the solidified shell is high, due to the low temperature. Therefore, steel tends to move downwards near the solidified shell. Furthermore, as

stated before, the solidified steel shell moves downwards at a speed of 0.013 m/s in order to simulate the movement of the steel shell in a real casting. In addition, the weak rotational flow in the top of the mold also leads to the steel flowing downwards near the solidified shell. These factors lead to a downwards movement of steel with a low temperature as shown in Figure 11a. In the lower part of the mold, the rotational flow leads to an upwards steel flow near the solidified shell. This upwards flow comes from the main flow jet, and thus, has a high temperature. Finally, a low temperature region was formed in the mold at a depth of around 0.5 m, as shown in Figure 11a, where the low temperature downwards flow meets the high temperature upwards flow.

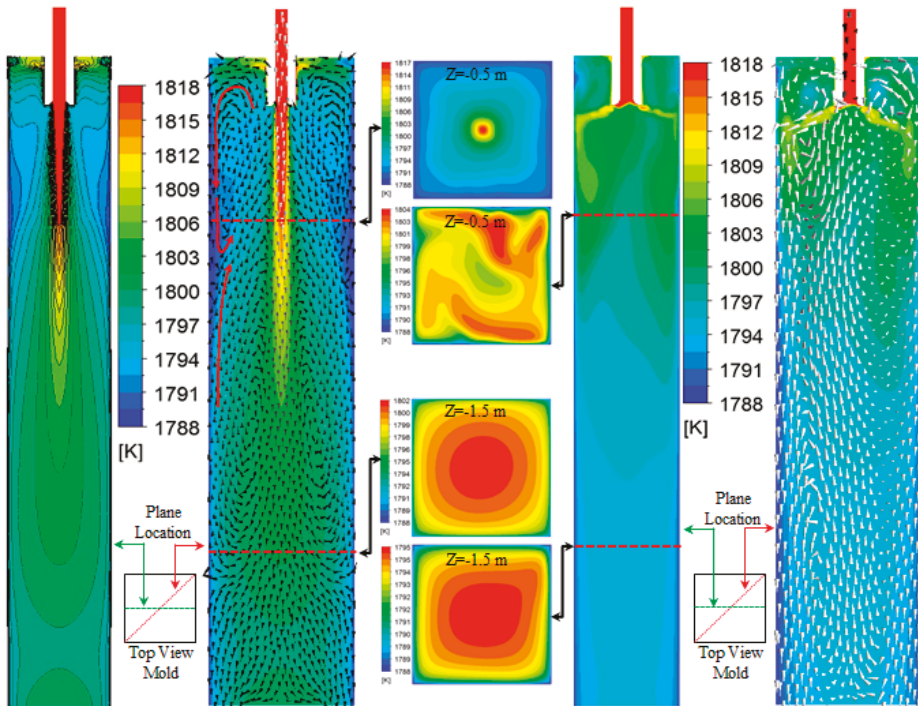


Figure 11. Temperature distribution in mold. (a) Conventional tundish casting and (b) swirling flow tundish design casting.

With a swirling flow tundish design, the temperature field in the mold changes a lot, as shown in Figure 11b. The high temperature impingement jet disappears, and the temperature field becomes more uniform in the mold. The maximum temperature gradually decreases, from the mold top to the bottom. Due to the swirling flow effect, steel with a high temperature changes the flow direction towards the solidified shell after it moves out from the SEN outlet. It increases the temperature near the solidified shell, as well as the temperature gradient there. Furthermore, this enhanced the removal of the steel superheat, and the core temperature of the billet was dramatically reduced. On the cross section at a depth of 0.5 m in the mold, the maximum temperature for the conventional tundish case and the swirling flow tundish casting is 1817 and 1804 K, respectively. These values decrease to 1802 K for the conventional tundish casting and to 1795 K for the swirling flow tundish casting at the mold depth of 1.5 m. Therefore, the swirling flow improves the steel superheat removal and leads to a more uniform temperature field in the mold. This is good for the quality of the steel solidification structure with the formation of equiaxed grains. A previous study with the application of M-EMS shows that the high temperature region was located at the mold center [32]. This is due to the impingement jet

from a straight SEN having a large inertia, and that M-EMS can only reduce the impingement depth, rather than completely remove the impingement jet. This may be the reason that the design of four horizontal side ports, with the port located in the tangential direction of the SEN circumference, was found to further improve the bloom quality cast in a M-EMS mold, compared to that with a straight SEN, due to the improvement in superheat dissipation [8].

3.6. Inclusion Behavior in Mold

In order to understand the behavior of inclusions, 30 inclusions of 1 μm , 10 μm , and 100 μm , released from the inlet, were individually tracked to see their behaviors in the mold. Figure 12 shows the trajectories of different sizes of inclusions in the mold. It can be seen that the steel flow pattern in the mold has a significant influence on the inclusion motions in the mold. Due to the impingement jet going deep into the mold, inclusions that follow the steel flow can reach a large mold depth in the conventional tundish casting. A few of them stay on the top part of the mold. This is true, even for large inclusions with a diameter of 100 μm , on which a large buoyancy force acts upon compared to small inclusions. Therefore, the steel flow pattern with a conventional tundish SEN is not beneficial for the removal of non-metallic inclusions. In the mold with a swirling flow tundish casting, some inclusions stay on the top of the mold for a time. This is due to the steel flow pattern change as previously shown in Figure 3. This may provide the chances for some inclusions to be removed. However, the buoyancy force is still not large enough to keep the large size inclusions at the top of the mold. In this study, a reflect wall boundary condition was used to show the moving path of inclusions. To realize a dynamic simulation on the inclusion removal into the slag, and the inclusion attachment on the wall, an interface capture model is required, and this is left for a future study.

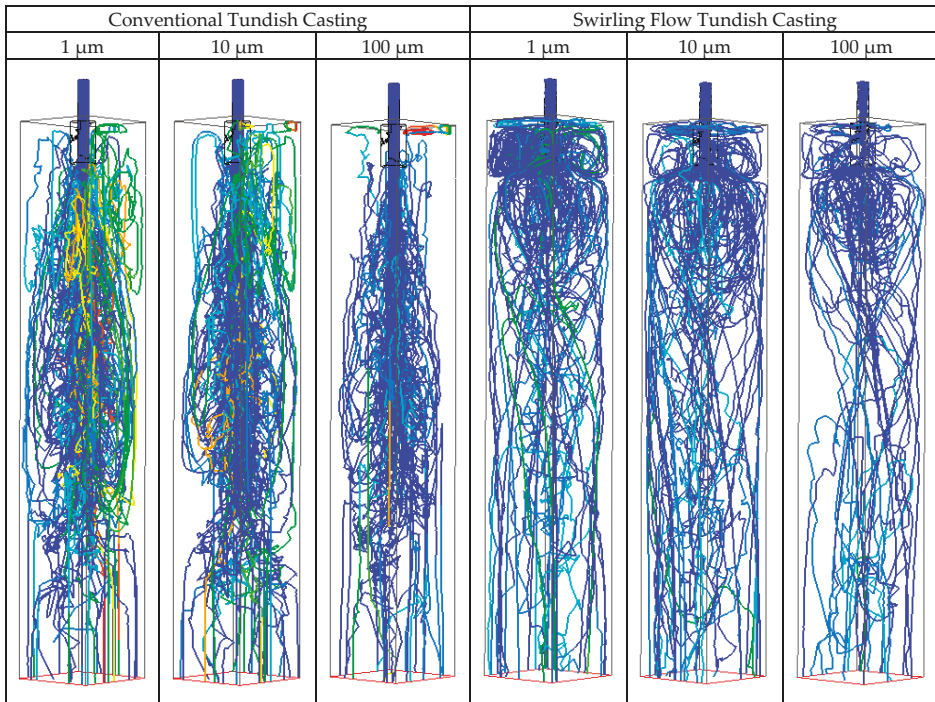


Figure 12. Trajectories of different size inclusions in the mold.

4. Concluding Discussion

A new cylindrical tundish design that produces a swirling flow in the SEN by using the steel flow potential has been investigated both by water model experiments and numerical simulations [47–49,61,67]. This study was the first to try to investigate the influence of such swirling flow tundish design on the steel flow, heat transfer, inclusion motion, and steel/slag interface stability in the mold. Previously, the effect of a swirling flow SEN on the steel flow in molds has been studied [34,38,40–42,46]. However, issues such as the steel/slag interface fluctuation, steel velocity in the vicinity of the solidified shell, and the field properties in the deep mold, are still not well investigated. In addition, the density change due to temperature variance was included in the model to consider the natural convection effect on the steel flow. In reality, there is a mushy region near the solidified shell, where the liquid volume fraction and the liquid viscosity change with the distance from the completely solidified shell; this is ignored in this study. Under this assumption, the multiphysics in the mold from a conventional tundish casting, and from the swirling flow tundish casting, are compared to show the influence of the swirling flow tundish design on the mold flow. However, a further study is still required to include the influence of the fluid property changes in the mushy region on the steel flow.

Swirling flow normally shows a certain swirl frequency [67,68], which means that the transient flow characteristics may not be axisymmetric. Therefore, a transient solver is recommended to solve this kind of flow phenomena. In this study, the plotted results are instantaneous flow field properties at 125 s, rather than the averaged flow properties in a time interval which is larger than the characteristic time of the swirling flow. This aims to give a clear observation on the swirling flow characteristics. The flow vectors in Figure 5 show that the flow is not axisymmetric. This is due to that the swirling flow in the SEN is not completely axisymmetric, as shown in Figure 1. However, the flow symmetry can be further improved by the cylindrical tundish design, such as using two tangential inlets in the cylindrical tundish in Figure 1a, which was investigated in a previous study [67]. For the study on M-EMS application, it was also found that the distribution of the electromagnetic force is not uniform in space [33]. The experimental measurements reveal that an axisymmetric flow cannot be maintained for situations with the simultaneous occurrence of the SEN jet flow and an electromagnetic stirring [64]. Therefore, efforts are still required in order to improve the flow uniformity.

The swirling flow intensity in the SEN is influenced by the cylindrical tundish design. Important design factors include the diameter of the cylinder and the steel flow velocity at the tangential inlet of the cylinder, as well as the tundish inlet area [47,49]. With a proper cylindrical tundish parameter, a certain intensity of the swirling flow in the SEN can be obtained. This should be determined by the desired flow behavior in the mold, such as the control of the mold level fluctuation. In addition, the swirling flow tundish casting can be simply realized either by connecting a small cylindrical tundish to a conventional tundish [47,48], or by installing a ceramic cylinder inside a conventional tundish [67]. Therefore, the functions of a conventional tundish, such as the inclusion removal, are not destroyed.

With a swirling flow in SEN, the steel flow has both a tangential momentum and a vertical momentum. These two momentum components influence the spreading angle of the SEN outlet flow. In addition, the steel flow in the mold is also affected by the geometry of the SEN outlet. Previous studies [8,38,40] regarding the swirling flow SEN show that a divergent nozzle can lead to the SEN outlet flow spreading more widely. In the current study, a divergent nozzle was used with only a small expansion in diameter at the SEN outlet, and it seemed to have almost no effect on the mold flow in a conventional tundish casting, where a straight impingement jet flow was observed. However, a wide spreading was observed when it was used together with the swirling flow tundish design. The spreading angle of the steel flow from the SEN is shown to be of great influence on the heat and fluid flow in the mold [38,40]. However, regarding the formation mechanism of the spreading angle, it is not well explained. Previous investigations on divergent nozzles were carried out in a swirling flow, which was produced by installing a swirl blade inside a SEN [38,40]. The mean value of tangential velocity in the SEN is around 1.72 m/s, and the averaged axial velocity is 2 m/s. A significant influence

of the divergent nozzle angle on the steel flow spreading was found. However, a large spreading of the steel flow, as that shown in Figure 3b, was also found by Ying et al. [46], with a straight nozzle used in their study, where the swirling flow was produced by installing an electromagnetic stirrer surrounding the SEN. Furthermore, the spreading angle of the steel flow was found to change with the power input, which relates to the swirling flow intensity. This means that the divergent nozzle is not the necessary factor for the steel flow spreading. Figure 13 shows the SEN outlet flow direction in the mold. Theoretically, the spreading angle of the steel flow should be determined by the ratio of the tangential velocity to the axial velocity at the moment that steel leaves the SEN. This ratio in the current study is around 1.47, which corresponds to the spreading angle α of around 56° in Figure 13a. Figure 13b shows that the spreading angle is larger than this value. This is due to the induced upwards flow by the swirling flow tundish SEN in the mold center, which shifts the SEN outlet flow upwards. Since the instantaneous flow is not axisymmetric, the left side upwards flow is stronger than that on the right side. This may create a larger spreading angle on the left side than that on the right side. In addition, the steel tends to flow along the inner wall of the divergent nozzle, due to its inertia. Therefore, the swirling flow will undergo an expansion inside a divergent nozzle, due to the expanding nozzle diameter. This expansion further reduces the pressure in the swirling flow center and increases the low-pressure area. Therefore, steel near the divergent nozzle outlet will flow into the swirling flow center, creating an upwards steel flow. This may increase the shift of the steel flow angle compared to a straight nozzle, which has been observed in a previous study [38,40]. Finally, the swirling flow leads to a horizontal movement of the steel. The shortest distance for the steel reaching the solidified shell is shown in Figure 13c. During the way to the solidified shell, the velocity of the steel flow will decrease due to the momentum dissipation. Therefore, the magnitude of the steel flow velocity near the solidified shell should be greatly influenced by this distance. This distance in the current study is different, as shown in Figure 13c. This is also the reason that a non-uniform wall shear stress in Figure 7b was observed. Furthermore, the uniformity of shear stresses is expected to be improved in a round billet mold, since the distance from the SEN to the solidified shell will be equal in all directions. In addition, the velocity magnitude near the solidified shell might be increased by using a SEN with a large gradual expansion in diameter. With this kind of SEN, the swirling flow will have a gradually expanding and developing process, instead of a sudden expansion from a small SEN diameter to the large mold cross section. This may be helpful for the optimization of the mold flow, and it is left for a future study.

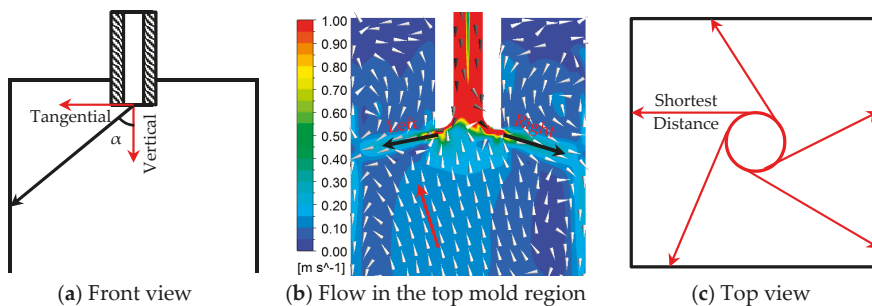


Figure 13. Steel flow direction and its collision location with solidified shell. (a) Front view schematic, (b) flow in the top mold region, and (c) top view schematic.

5. Conclusions

Multiphase flow and heat transfer in a mold with a new cylindrical tundish design during the continuous casting process were investigated by using numerical simulations. Steel and slag flow, heat transfer, and inclusion motion in the mold were analyzed. The main conclusions were the following:

1. The new cylindrical tundish design for swirling flow casting significantly changed the flow behavior in the mold. The deep impingement jet in the mold disappeared, and the steel flow moved towards the solidified shell, due to the swirling flow effect. A large velocity in the vicinity of the solidified shell was obtained.
2. The steel flow velocity in the top part of the mold was increased. The calculated Weber number was round 0.8, which indicates a small risk for the slag entrainment.
3. With the swirling flow tundish casting, the temperature distribution became more uniform, and the dissipation of the steel superheat was accelerated. Furthermore, due to the high temperature steel directly flowing to the solidified shell, the temperature near the solidified shell was increased. A high temperature region was found at the top part of the mold, rather than in the deep center of the mold in a conventional tundish casting.
4. Inclusion trajectories in the mold change a lot, due to the change of the SEN outlet flow pattern. Instead of moving deeply into the mold following the impingement jet, some inclusions tended to stay for a time at the top part of the mold. This may be helpful for their removal.

Author Contributions: P.N. and L.T.I.J. designed the paper; P.N. and M.E. did the numerical simulation; all the authors analyzed and discussed the results; P.N. wrote the paper; M.E., L.T.I.J., T.Z. and P.G.J. revised the paper.

Funding: National Natural Science Foundation of China (Grant No. 51704062).

Acknowledgments: The authors want to thank the National Natural Science Foundation of China (Grant No. 51704062) for the support on this work.

Conflicts of Interest: The authors declare no conflict of interest.

References

1. Szekely, J.; Yadaya, R.T. The physical and mathematical modelling of the flow field in the mold region of continuous casting systems. Part II. The mathematical representation of the turbulence flow field. *Metall. Mater. Trans.* **1973**, *4*, 1379–1388. [[CrossRef](#)]
2. Xu, M.; Zhu, M. Transport phenomena in a Beam-Blank continuous casting mold with two types of submerged entry nozzle. *ISIJ Int.* **2015**, *55*, 791–798. [[CrossRef](#)]
3. Thomas, B.G.; Mika, L.J.; Najjar, F.M. Simulation of fluid flow inside a continuous slab-casting machine. *Metall. Mater. Trans. B* **1990**, *21*, 387–400. [[CrossRef](#)]
4. Calderon-Ramos, I.; Morales, R.D.; Garcia-Hernandez, S.; Ceballos-Huerta, A. Effects of immersion depth on flow turbulence of liquid steel in a slab mold using a nozzle with upward angle rectangular ports. *ISIJ Int.* **2014**, *54*, 1797–1806. [[CrossRef](#)]
5. Calderon-Ramos, I.; Morales, R.D.; Salazar-Campoy, M. Modeling flow turbulence in a continuous casting slab mold comparing the use of two bifurcated nozzles with square and circular ports. *Steel Res. Int.* **2015**, *86*, 1610–1621. [[CrossRef](#)]
6. Calderon-Ramos, I.; Morales, R.D. The role of submerged entry nozzle port shape on fluid flow turbulence in a slab mold. *Metall. Mater. Trans. B* **2015**, *46*, 1314–1325. [[CrossRef](#)]
7. Salazar-Campoy, M.; Morales, R.D.; Najera-Bastida, A.; Cedillo-Hernandez, V.; Delgado-Pureco, J.C. A physical model to study the effects of nozzle design on dense two-phase flows in a slab mold casting Ultra-Low carbon steels. *Metall. Mater. Trans. B* **2017**, *48*, 1376–1389. [[CrossRef](#)]
8. Sun, H.; Zhang, J. Macroregregation improvement by swirling flow nozzle for bloom continuous castings. *Metall. Mater. Trans. B* **2014**, *45*, 936–946. [[CrossRef](#)]
9. Sun, H.; Li, L. Application of swirling flow nozzle and investigation of superheat dissipation casting for bloom continuous casing. *Ironmak. Steelmak.* **2016**, *43*, 228–233. [[CrossRef](#)]
10. Fang, Q.; Ni, H.; Zhang, H.; Wang, B.; Lv, Z. The effects of a submerged entry nozzle on flow and initial solidification in a continuous casting bloom mold with electromagnetic stirring. *Metals* **2017**, *7*, 146. [[CrossRef](#)]
11. Thomas, B.G.; Denniso, A.; Bai, H. Behavior of argon bubbles during continuous casting of steel. In Proceedings of the ISS 80th Steelmaking Conference, Chicago, IL, USA, 13–16 April 1997; pp. 375–384.

12. Thomas, B.G.; Huang, X.; Sussman, R.C. Simulation of argon gas flow effects in a continuous slab caster. *Metall. Mater. Trans. B* **1994**, *25*, 527–547. [[CrossRef](#)]
13. Li, B.; Okane, T.; Umeda, T. Modeling of biased flow phenomena associated with the effects of static magnetic-field application and argon gas injection in slab continuous casting of steel. *Metall. Mater. Trans. B* **2001**, *32*, 1053–1066. [[CrossRef](#)]
14. Wang, Y.; Zhang, L. Fluid flow-related transport phenomena in steel slab continuous casting strands under electromagnetic brake. *Metall. Mater. Trans. B* **2011**, *42*, 1319–1351. [[CrossRef](#)]
15. Liu, Z.; Li, B.; Jiang, M. Transient asymmetric flow and bubble transport inside a slab continuous casting mold. *Metall. Mater. Trans. B* **2014**, *45*, 675–697. [[CrossRef](#)]
16. Liu, Z.; Li, L.; Qi, F.; Li, B.; Jiang, M.; Tsukihashi, F. Population balance modeling of polydispersed bubbly flow in continuous casting using multiple-size-group approach. *Metall. Mater. Trans. B* **2015**, *46*, 406–420. [[CrossRef](#)]
17. Liu, Z.; Sun, Z.; Li, B. Modeling of quasi-four-phase flow in continuous casting mold using hybrid Eulerian and Lagrangian approach. *Metall. Mater. Trans. B* **2017**, *48*, 1248–1267. [[CrossRef](#)]
18. Liu, Z.; Li, B. Large-Eddy simulation of transient horizontal gas–liquid flow in continuous casting using dynamic subgrid-scale model. *Metall. Mater. Trans. B* **2017**, *48*, 1833–1849. [[CrossRef](#)]
19. Pfeiler, C.; Wu, M.; Ludwig, A. Influence of argon gas bubbles and non-metallic inclusions on the flow behavior in steel continuous casting. *Mater. Sci. Eng. A* **2005**, *413–414*, 115–120. [[CrossRef](#)]
20. Yu, H.; Zhu, M. Numerical simulation of the effects of electromagnetic brake and argon gas injection on the three-dimensional multiphase flow and heat transfer in slab continuous casting mold. *ISIJ Int.* **2008**, *48*, 584–591. [[CrossRef](#)]
21. Cho, S.; Kim, S.; Thomas, B.G. Transient fluid flow during steady continuous casting of steel slabs: Part I. measurements and modeling of two-phase flow. *ISIJ Int.* **2014**, *54*, 845–854. [[CrossRef](#)]
22. Jin, K.; Thomas, B.G.; Ruan, X. Modeling and measurements of multiphase flow and bubble entrapment in steel continuous casting. *Metall. Mater. Trans. B* **2016**, *47*, 548–565. [[CrossRef](#)]
23. Cho, S.; Thomas, B.G.; Kim, S. Transient two-phase flow in slide-gate nozzle and mold of continuous steel slab casting with and without double-ruler electro-magnetic braking. *Metall. Mater. Trans. B* **2016**, *47*, 3080–3098. [[CrossRef](#)]
24. Cukierski, K.; Thomas, B.G. Flow control with local electromagnetic braking in continuous casting of steel slabs. *Metall. Mater. Trans. B* **2008**, *39*, 94–107. [[CrossRef](#)]
25. Zhang, L.; Wang, Y.; Zuo, X. Flow transport and inclusion motion in steel continuous-casting mold under submerged entry nozzle clogging condition. *Metall. Mater. Trans. B* **2008**, *39*, 534–550. [[CrossRef](#)]
26. Gonzalez-Trejo, J.; Real-Ramirez, C.A.; Miranda-Tello, R.; Rivera-Perez, F.; Cervantes-De-La-Torre, F. Numerical and physical parametric analysis of a SEN with flow conditioners in slag continuous casting mold. *Arch. Metall. Mater.* **2017**, *62*, 927–946. [[CrossRef](#)]
27. Miao, X.; Timmel, K.; Lucas, D.; Ren, Z.; Eckert, S.; Gerbeth, G. Effect of an electromagnetic brake on the turbulent melt flow in a continuous-casting mold. *Metall. Mater. Trans. B* **2012**, *43*, 954–972. [[CrossRef](#)]
28. Liu, Z.; Li, L.; Li, B. Large eddy simulation of transient flow and inclusions transport in continuous casting mold under different electromagnetic brakes. *JOM* **2016**, *68*, 2180–2190. [[CrossRef](#)]
29. Ha, M.Y.; Lee, H.G.; Seong, S.H. Numerical simulation of three-dimensional flow, heat transfer, and solidification of steel in continuous casting mold with electromagnetic brake. *J. Mater. Process. Technol.* **2003**, *133*, 322–339. [[CrossRef](#)]
30. Yu, H.; Wang, B.; Li, H.; Li, J. Influence of electromagnetic brake on flow field of liquid steel in the slab continuous casting mold. *J. Mater. Process. Technol.* **2008**, *202*, 179–187.
31. Yu, H.; Zhu, M. Three-dimensional magnetohydrodynamic calculation for coupling multiphase flow in round billet continuous casting mold with electromagnetic stirring. *IEEE Trans. Magn.* **2010**, *46*, 82–86.
32. Yu, H.; Zhu, M. Influence of electromagnetic stirring on transport phenomena in round billet continuous casting mould and macrostructure of high carbon steel billet. *Ironmak. Steelmak.* **2012**, *39*, 574–584. [[CrossRef](#)]
33. Liu, H.; Xu, M.; Qiu, S.; Zhang, H. Numerical simulation of fluid flow in a round bloom mold with In-Mold rotary electromagnetic stirring. *Metall. Mater. Trans. B* **2012**, *43*, 1657–1675. [[CrossRef](#)]
34. Yokoya, S.; Takagi, S.; Iguchi, M.; Asako, Y.; Westoff, R.; Hara, S. Swirling effect in immersion nozzle on flow and heat transport in billet continuous casting mold. *ISIJ Int.* **1998**, *38*, 827–833. [[CrossRef](#)]

35. Yokoya, S.; Takagi, S.; Iguchi, M.; Marukawa, K.; Yasugair, W.; Hara, S. Development of swirling flow generator in immersion nozzle. *ISIJ Int.* **2000**, *40*, 584–588. [[CrossRef](#)]
36. Yokoya, S.; Takagi, S.; Kaneko, M.; Iguchi, M.; Marukawa, K.; Hara, S. Swirling flow effect in off-center immersion nozzle on bulk flow in billet continuous casting mold. *ISIJ Int.* **2001**, *41*, 1215–1220. [[CrossRef](#)]
37. Yokoya, S.; Takagi, S.; Ootani, S.; Iguchi, M.; Marukawa, K.; Hara, S. Swirling flow effect in submerged entry nozzle on bulk flow in high throughput slab continuous casting mold. *ISIJ Int.* **2001**, *41*, 1208–1214. [[CrossRef](#)]
38. Yokoya, S.; Jönsson, P.G.; Sasaki, K.; Tada, K.; Takagi, S.; Iguchi, M. The effect of swirl flow in an immersion nozzle on the heat and fluid flow in a billet continuous casting mold. *Scan. J. Metall.* **2004**, *33*, 22–28. [[CrossRef](#)]
39. Tsukaguchi, Y.; Hayashi, H.; Kurimoto, H.; Yokoya, S.; Marukawa, K.; Tanaka, T. Development of swirling-flow submerged entry nozzles for slab casting. *ISIJ Int.* **2010**, *50*, 721–729. [[CrossRef](#)]
40. Kholmatov, S.; Takagi, S.; Jonsson, L.; Jönsson, P.; Yokoya, S. Development of flow field and temperature distribution during changing divergent angle of the nozzle when using swirl flow in a square continuous casting billet mould. *ISIJ Int.* **2007**, *47*, 80–87. [[CrossRef](#)]
41. Kholmatov, S.; Takagi, S.; Jönsson, P.; Jonsson, L.; Yokoya, S. Influence of aspect ratio on fluid flow and heat transfer in mould when using swirl flow during casting. *Steel Res. Int.* **2008**, *79*, 698–707. [[CrossRef](#)]
42. Kholmatov, S.; Takagi, S.; Jonsson, L.; Jönsson, P.; Yokoya, S. Effect of nozzle angle on flow field and temperature distribution in a billet mould when using swirl flow. *Steel Res. Int.* **2008**, *79*, 31–39. [[CrossRef](#)]
43. Geng, D.; Lei, H.; He, J.; Liu, H. Effect of electromagnetic swirling flow in slide-gate SEN on flow field in square billet continuous casting mold. *Acta Metall. Sin. (Engl. Lett.)* **2012**, *25*, 347–356.
44. Wondrak, Th.; Eckert, S.; Galindo, V.; Gerbeth, G.; Stefani, F.; Timmel, K.; Peyton, A.J.; Yin, W.; Riaz, S. Liquid metal experiments with swirling flow submerged entry nozzle. *Ironmak. Steelmak.* **2012**, *39*, 1–9. [[CrossRef](#)]
45. Li, D.; Su, Z.; Chen, J.; Wang, Q.; Yang, Y.; Nakajima, K.; Marukaw, K.; He, J. Effects of electromagnetic swirling flow in submerged entry nozzle on square billet continuous casting of steel process. *ISIJ Int.* **2013**, *53*, 1187–1194. [[CrossRef](#)]
46. Yang, Y.; Jönsson, P.G.; Ersson, M.; Su, Z.; He, J.; Nakajima, K. The Influence of swirl flow on the flow field, temperature field and inclusion behavior when using a half type electromagnetic swirl flow generator in a submerged entry and mold. *Steel Res. Int.* **2015**, *86*, 1312–1327. [[CrossRef](#)]
47. Ni, P.; Jonsson, L.; Ersson, M.; Jönsson, P. A new tundish design to produce a swirling flow in the SEN during continuous casting of steel. *Steel Res. Int.* **2016**, *87*, 1356–1365. [[CrossRef](#)]
48. Ni, P.; Jonsson, L.; Ersson, M.; Jönsson, P. Non-Metallic inclusion behaviors in a new tundish and SEN design using a swirling flow during continuous casting of steel. *Steel Res. Int.* **2017**, *88*, 1600155. [[CrossRef](#)]
49. Ni, P.; Wang, D.; Jonsson, L.; Ersson, M.; Zhang, T.; Jönsson, P. Numerical and physical study on a cylindrical tundish design to produce a swirling flow in the SEN during continuous casting of steel. *Metall. Mater. Trans. B* **2017**, *48*, 2695–2706. [[CrossRef](#)]
50. Wang, S.; Yang, V.; Hsiao, G.; Hsieh, S.; Mongia, H.C. Large-eddy simulation of gas-turbine swirl injector flow dynamics. *J. Fluid Mech.* **2007**, *583*, 99–122. [[CrossRef](#)]
51. Weber, R.; Visser, B.M.; Boysan, F. Assessment of turbulence modeling for engineering predictions of swirling vortices in the near burner zone. *Int. J. Heat Fluid Flow* **1990**, *11*, 225–235. [[CrossRef](#)]
52. Hoekstra, A.; Derksen, J.; Van Den Akker, H. An experimental and numerical study on turbulent swirling flow in gas cyclones. *Chem. Eng. Sci.* **1999**, *54*, 2055–2065. [[CrossRef](#)]
53. Jakirlic, S.; Hanjalic, K.; Tropea, C. Modeling rotating and swirling turbulent flows: A perpetual challenge. *AIAA J.* **2002**, *40*, 1984–1996. [[CrossRef](#)]
54. Patankar, S.V. *Numerical Heat Transfer and Fluid Flow*; Hemisphere Publishing Corp.: New York, NY, USA, 1980.
55. ANSYS. *Fluent Theory Guide*; Release 18.0; ANSYS: Canonsburg, PA, USA, 2017.
56. Versteeg, H.K.; Malalasekera, W. *An Introduction to Computational Fluid Dynamics: The Finite Volume Method*, 2nd ed.; Pearson Education Limited: London, UK, 2007; p. 80.
57. Launder, B.E.; Reece, G.J.; Rodi, W. Progress in the development of a Reynolds-stress turbulence closure. *J. Fluid Mech.* **1975**, *68*, 537–566. [[CrossRef](#)]
58. Lien, F.S.; Leschziner, M.A. Assessment of turbulence-transport models including non-linear RNG eddy-viscosity formulation and second-moment closure for flow over a backward-facing step. *Comput. Fluids* **1994**, *23*, 983–1004. [[CrossRef](#)]

59. Shih, T.-H.; Liou, W.W.; Shabbir, A.; Yang, Z.; Zhu, J. A new $k-\epsilon$ eddy viscosity model for high Reynolds number turbulent flows. *Comput. Fluids* **1995**, *24*, 227–238. [[CrossRef](#)]
60. ANSYS. *Fluent User's Guide*; Release 18.0; ANSYS: Canonsburg, PA, USA, 2017.
61. Ni, P.; Ersson, M.; Jonsson, L.; Jönsson, P. A study on the nonmetallic inclusion motions in a swirling flow submerged entry nozzle in a new cylindrical Tundish design. *Metall. Mater. Trans. B* **2018**, *49*, 723–736. [[CrossRef](#)]
62. Saffman, P.G. The lift on a small sphere in a slow shear flow. *J. Fluid Mech.* **1965**, *22*, 385–400. [[CrossRef](#)]
63. Morsi, S.A.; Alexander, A.J. An investigation of particle trajectories in two-phase flow systems. *J. Fluid Mech.* **1972**, *55*, 193–208. [[CrossRef](#)]
64. Willers, B.; Barna, M.; Reiter, J.; Eckert, S. Experimental investigations of rotary electromagnetic mould stirring in continuous casting using a cold liquid metal model. *ISIJ Int.* **2017**, *57*, 468–477. [[CrossRef](#)]
65. Jonsson, L.; Jönsson, P. Modeling of fluid flow conditions around the slag/metal interface in a gas-stirred ladle. *ISIJ Int.* **1996**, *36*, 1127–1134. [[CrossRef](#)]
66. Shannon, G.N.; Sridhar, S. Film-drainage, separation and dissolution of Al_2O_3 inclusions at steel/interfaces. *High Temp. Mater. Process.* **2005**, *24*, 111–124. [[CrossRef](#)]
67. Ni, P.; Ersson, M.; Jonsson, L.; Jönsson, P.G. Application of a swirling flow producer in a conventional tundish during continuous casting of steel. *ISIJ Int.* **2017**, *57*, 2175–2184. [[CrossRef](#)]
68. Bai, H.; Ersson, M.; Jönsson, P. Experimental validation and numerical analysis of the swirling flow in a submerged entry nozzle and mold by using a reverse turboswirl in a billet continuous casting process. *Steel Res. Int.* **2017**, *88*, 1600399. [[CrossRef](#)]



© 2018 by the authors. Licensee MDPI, Basel, Switzerland. This article is an open access article distributed under the terms and conditions of the Creative Commons Attribution (CC BY) license (<http://creativecommons.org/licenses/by/4.0/>).

Article

Analysis of the Influence of Segmented Rollers on Slab Bulge Deformation

Qin Qin *, Ming Li and Jianlin Huang

School of Mechanical Engineering, University of Science and Technology Beijing, Beijing 100083, China; 18567937527@163.com (M.L.); S20160419@xs.ustb.edu.cn (J.H.)

* Correspondence: qinqin@me.ustb.edu.cn; Tel.: +86-10-6233-4106

Received: 26 December 2018; Accepted: 12 February 2019; Published: 14 February 2019

Abstract: The bulge deformation of the continuous casting slab must be controlled in order to improve the slab quality. In this study, a coupled three-dimensional thermomechanical model is suggested based on dynamic contact between the slab and the rollers, so as to investigate the influence of the rollers in reducing slab bulge deformation. Moreover, the rigid casting rollers in this model are replaced by elastic casting rollers in order to improve the calculation accuracy. Further, the influence of two-segment and three-segment rollers on the slab bulge deformation is systematically studied. The results indicate that the bulge deformation of the slab increased by 74.3% when elastic casting rollers were adopted instead of rigid casting rollers. This deformation was reduced by 29.7% when three-segment rollers were used instead of two-segment rollers. Moreover, the influence of the roller spacing and the roller diameter of the segmented roller on the deformation was studied in detail. In order to achieve the purpose of controlling the bulge deformation, improved segmented roller spacing and diameter were proposed, leading to a 75.4% reduction in the bulge deformation.

Keywords: continuous casting; bulge deformation; thermomechanical coupling; segmented roller; finite element analysis

1. Introduction

It is important to effectively control bulge deformation to improve the quality of continuous casting slabs. Thermal creep is one of the main factors that can cause bulge deformation in slabs, as the temperature distribution of the slab on both the wide and narrow sides affects bulge deformation. It is necessary to obtain the temperature field of a continuous casting slab during the solidification process. Some scholars have developed a two-dimensional solidification model to obtain the temperature field distribution of the slab during continuous casting [1,2]. However, they neglected the temperature field distribution of the wide sides. The two-dimensional solidification model was replaced by a three-dimensional solidification model to analyze the slab temperature field because the temperature distribution of the slab on both the wide and narrow sides could be considered in the three-dimensional model [3,4], which could better match the actual solidification process in continuous casting. This deformation calculation is very complicated. Some scholars used the theoretical analysis method [5–8] and two-dimensional thermomechanical coupling models to calculate bulge deformation [9,10]. However, the calculation accuracy of the theoretical analysis method could not be guaranteed because the bulge deformation and temperature fluctuations on the wide side of the slab in the two-dimensional model were neglected. Therefore, three-dimensional models of slab bulge deformation were developed to improve the calculation accuracy. A three-dimensional elastic–plastic and creep model was developed to calculate the slab bulge deformation on the wide side [11–13]. This model considered static contact between the continuous casting slab and the rollers. However, this model neglected the movement of the slab under the casting rollers.

In order to consider the dynamic contact between the slab and the rollers, Qin et al. suggested a 3D thermomechanical coupling model based on this dynamic contact between the slab and the rollers to compare with the 2D bulge deformation model to calculate bulge deformation [14]. Thus, Liu et al. proposed a 3D finite element viscoelastic creep model to study slab bulge deformation and the influence of temperature field distribution on this deformation [15]. However, this model neglected the slab bulge deformation on the narrow side. The slab bulge deformation on the wide side and that on the narrow side are actually mutually influential, and bulge deformation on the wide and narrow sides has been observed by some scholars [16–18]. Thus, 3D thermomechanical coupling models that included the dynamic contacts between the slab and the rollers were established to study the slab bulge deformation of the narrow side [19,20]. The 3D finite element models mentioned above mainly focused on the deformation mechanism of bulge deformation and the influence of process and structural parameters on this deformation. However, control measures of bulge deformation were hardly used in these models.

Qin et al. built a three-dimensional thermomechanical coupling model to study the temperature and bulge deformation distributions of a slab during the casting process, and the bulge deformation of this model was compared with that of the 2D bulging model [13,18]. The simulation results in the 3D bulging models were further compared with measured data from the actual production process to explore the accuracy of the simulation results in the three-dimensional bulge deformation models [17,20]. This comparison made it possible to use the finite element method to explore a method for controlling slab bulge deformation, and the fixed-gap and variable-diameter methods were suggested to reduce bulge deformation [21–24].

In the above-mentioned models, all casting rollers were assumed to be rigid, in order to save computing time, and the influence of casting roller deformation on slab bulge deformation was neglected. In fact, these casting rollers also deform during continuous casting. Therefore, this simplification would lead to an inaccurate reduction of bulge deformation values for a continuous casting slab. Moreover, segmented rollers have been widely adopted in the actual production process to control for slab bulge deformation [25–27]. The reason for this is that the stiffness of segmented rollers is much greater than that of solid rollers [28,29]. However, the structural parameters of segmented rollers have not been systematically studied for controlling slab bulge deformation.

This paper aims to discover the influence of segmented rollers on reducing slab bulge deformation and investigate the relationship between the stiffness of the segmented rollers and slab bulge deformation. A 3D thermomechanical coupling model based on the dynamic contact between the slab and the elastic casting rollers was suggested, and the structural parameters of the segmented rollers are investigated for controlling bulge deformation.

2. 3D Solidification Model Description

The temperature distribution is the foundation of this bulging analysis because the thickness of the solidified slab and the material property parameters depend on the temperature field in the slab. Therefore, the first step was to obtain the temperature field by using a solidification model.

2.1. 3D Solidification Finite Element Model

The cooling process of the continuous casting slab was a three-dimensional transient heat transfer process with heat conduction, thermal convection, and thermal radiation accompanied by phase transition. The heat transfer differential equation can be expressed as [30]:

$$\rho c_p \frac{\partial T}{\partial t} = \frac{\partial}{\partial x} \left(\lambda \frac{\partial T}{\partial x} \right) + \frac{\partial}{\partial y} \left(\lambda \frac{\partial T}{\partial y} \right) + \frac{\partial}{\partial z} \left(\lambda \frac{\partial T}{\partial z} \right) + q \quad (1)$$

The axial position z along the liquid level of crystallizer is related to casting speed u and time t . The relation function is $z = ut$. The relation function is substituted into Equation (1) and Equation (2) is shown as follows:

$$\rho c_p u \frac{\partial T}{\partial z} = \frac{\partial}{\partial x} \left(\lambda \frac{\partial T}{\partial x} \right) + \frac{\partial}{\partial y} \left(\lambda \frac{\partial T}{\partial y} \right) + \frac{\partial}{\partial z} \left(\lambda \frac{\partial T}{\partial z} \right) + q \quad (2)$$

where

ρ is the density ($kg \cdot m^{-3}$),

c_p is the specific heat capacity under constant pressure ($J \cdot (kg \cdot K)^{-1}$),

T is the temperature (K),

t is time (s),

q is the internal heat source ($W \cdot m^{-3}$),

λ is the thermal conductivity ($W \cdot (m \cdot K)^{-1}$), and

u is the casting speed, ($m \cdot min^{-1}$).

There is a solid phase zone, a liquid phase zone, and a two-phase zone in the continuous casting process, and Equation (1) can be treated as follows:

(1) The solid phase and liquid phase can be calculated as:

$$\rho c_p \frac{\partial T}{\partial t} = \frac{\partial}{\partial x} \left(\lambda \frac{\partial T}{\partial x} \right) + \frac{\partial}{\partial y} \left(\lambda \frac{\partial T}{\partial y} \right) + \frac{\partial}{\partial z} \left(\lambda \frac{\partial T}{\partial z} \right) \quad (3)$$

The heat transfer differential equation of the slab in the solid phase zone and the liquid phase zone is exactly the same Equation (3). The corresponding thermal conductivity can be obtained in the solid phase zone and the liquid phase zone separately.

For the thermal conductivity λ_L of the liquid phase zone, the forced convection heat transfer was caused due to the flow of the molten steel, which accelerated the elimination of the degree of superheat. In 1967, Mizikar [31] introduced the effective thermal conductivity for the first time to take the effects of convective heat transfer into account. The method was to treat the liquid phase zone of the slab into a "quasi-solid" and convert the convective thermal conductivity of the molten steel into an effective thermal conductivity, which was equivalent to n times compared with the thermal conductivity of the static molten steel. The value of n was generally from 2 to 7. Therefore, this method was used to calculate the thermal conductivity of the liquid phase zone in the paper and the value of n was 5. The relationship between the thermal conductivity of the solid phase zone and the thermal conductivity of the liquid phase zone was as follows:

$$\lambda_L = 5\lambda_S \quad (4)$$

where

λ_L is the thermal conductivity of the solid phase zone ($W \cdot (m \cdot K)^{-1}$), and

λ_S is the thermal conductivity of the liquid phase zone ($W \cdot (m \cdot K)^{-1}$).

(2) Since the two-phase zone has the latent heat of solidification, the internal heat source q in Equation (1) must be taken into consideration. In this study, the equivalent specific heat method was used to solve the latent heat of solidification and q is calculated as:

$$q = -\rho_{ls} \frac{\Delta H_f}{T_L - T_S} \frac{\partial T}{\partial t} \quad (5)$$

where

ΔH_f is latent heat of solidification under the action of various metals ($kJ \cdot kg^{-1}$),

T_L is the liquidus temperature (K), and T_S is the solidus temperature (K).

Equation (5) was introduced in the solidification heat transfer differential equation of the two-phase zone and Equation (1) was rearranged as:

$$\rho_{ls} c_{eff} \frac{\partial T}{\partial t} = \frac{\partial}{\partial x} \left(\lambda_{ls} \frac{\partial T}{\partial x} \right) + \frac{\partial}{\partial y} \left(\lambda_{ls} \frac{\partial T}{\partial y} \right) + \frac{\partial}{\partial z} \left(\lambda_{ls} \frac{\partial T}{\partial z} \right) \quad (6)$$

where c_{eff} is the equivalent heat capacity ($J \cdot (kg \cdot K)^{-1}$) and is calculated as:

$$c_{eff} = c_p + \frac{\Delta H_f}{T_L - T_S} \quad (7)$$

λ_{ls} is the thermal conductivity of the two-phase zone ($W \cdot (m \cdot K)^{-1}$), and is calculated as:

$$\lambda_{ls} = \lambda_s + \frac{\lambda_L - \lambda_S}{T_L - T_S} (T - T_S) \quad (8)$$

ρ_{ls} is the density of the two-phase zone ($kg \cdot m^{-3}$).

A half three-dimensional solidification finite element model was established due to the symmetry of the slab, and had dimensions of 1200 mm × 2000 mm × 250 mm. DC3D8 is an eight-node linear heat transfer hexahedral element in the ABAQUS software (6.14, Dassault Systèmes Simulia Corp., Providence, RI, USA) and was used to mesh the solidification model to perform thermal simulation analysis. The size of the element was 25 mm (length) × 25 mm (width) × 10 mm (height), and 46,080 heat transfer elements and 51,597 nodes were included in the model. The bulge deformation at the end of the foot roller section was investigated because the bulge deformation of the slab is serious when the slab leaves the foot roller section. Therefore, segmented rollers have been widely adopted to control this deformation. Then, the temperature field at the end of the foot roller section was studied for the analysis. The location of the segmented rollers and the final solidification point are listed in Figure 1.

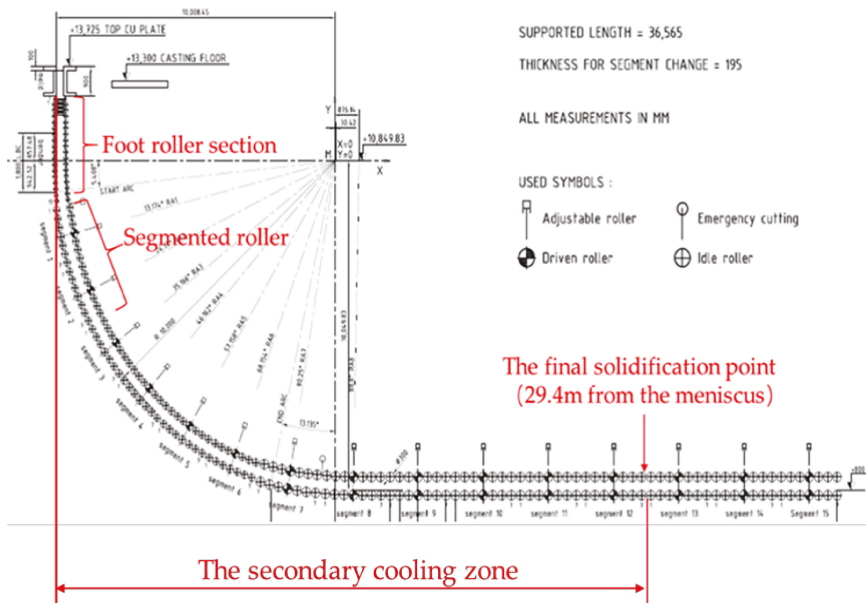


Figure 1. Slab caster roller map.

2.2. Physical Property Parameters

The material of the slab analyzed in this paper was Q235, and the material that was measured in Xiangtan Iron & Steel Co., Ltd. of Hunan Valin was AH36. The compositions of Q235 and AH36 are shown in Tables 1 and 2, respectively.

Table 1. Chemical composition and content of Q235.

Chemical Element	C	Si	Mn	P	S
Content (%)	0.18	0.20	0.40	≤0.025	≤0.022

Table 2. Chemical composition and content of AH36.

Chemical Element	C	Si	Mn	P	S	Al	Cr	Cu	Ni
Content (%)	0.157	0.2489	1.4143	0.0162	0.0044	0.0289	0.0375	0.0284	0.0177

According to the actual production process of an arc continuous casting machine, the slab geometry of the model and physical property parameters were quoted from the references [31–34] and they are listed in Table 3 and shown in Figure 2. For this study, the cooling water heat transfer, the slab surface radiation, and the heat transfer between the rollers and the slab were defined as the equivalent convection coefficient; the convection heat transfer of molten steel was expressed by effective thermal conductivity; and the latent heat of solidification was calculated by using the equivalent specific heat method.

Table 3. Simulation constants for solidification analysis.

Parameters	Values
Mold width	1200 mm
Half slab thickness	125 mm
Mold length	2000 mm
Casting speed	1.5 m·min ⁻¹
Water temperature	303 K
Inlet temperature	1808 K
Liquidus temperature	1793 K
Solidus temperature	1732 K
Specific heat capacity of the solid phase zone (c_S)	706 J · (kg · K) ⁻¹
Specific heat capacity of the liquid phase zone (c_L)	825 J · (kg · K) ⁻¹
Thermal conductivity of the solid phase zone (λ_S)	34.83 W · (m · K) ⁻¹
Thermal conductivity of the liquid phase zone (λ_L)	165 W · (m · K) ⁻¹
Latent heat of solidification under various metals (ΔH_f)	284 kJ · kg ⁻¹
Density	7400 kg·m ⁻³

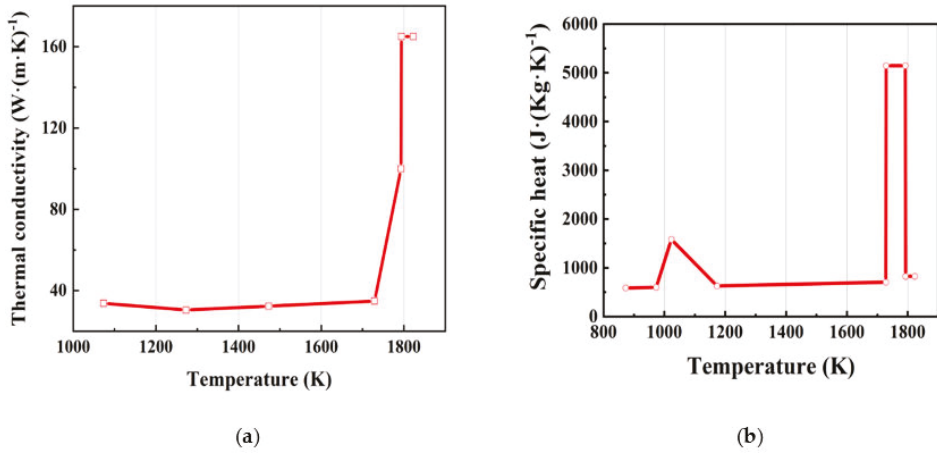


Figure 2. (a) Thermal conductivity of Q235 steel; (b) the specific heat of Q235 steel.

2.3. Boundary Conditions

(1) The comprehensive heat transfer coefficient was utilized to express the heat transfer process of the model, and the calculation expressions are as follows:

(a) The heat flux in the crystallizer was defined as follows:

$$q = 2680000 - b \sqrt{\frac{L}{v}} \quad (9)$$

where

b is determined by the actual heat balance calculation,

L is the crystallizer length (m), and

v is the casting speed ($m \cdot \text{min}^{-1}$).

(b) The heat flux in the secondary cooling zone was determined as follows, and the secondary cooling zone was from the end of the crystallizer to the final solidification point:

$$\Phi = h(T_b - T_w) \quad (10)$$

where

Φ is the heat flux ($W \cdot cm^{-2}$),

h is the heat transfer coefficient ($W \cdot (m^2 \cdot K)^{-1}$),

T_b is the slab surface temperature (K), and

T_w is the cooling water temperature (K).

(2) The initial temperature of the slab was uniformed as the inlet temperature of 1808 K.

2.4. Results and Discussion

The temperature and thickness distributions of the slab on the wide and narrow sides are shown in Figure 3. In this study, the simulation results were validated based on the actual slab temperature measurement results of the AH36 steel continuous casting process. The comparison of the measured and simulated temperatures in the center of the narrow face are exhibited in Figure 3b. As can be seen from this figure, the simulation temperature was close to the test temperature, and the maximum

relative error was less than 5%. Thus, the simulation result that agreed well with the measured data could be used as the basis temperature field for bulge deformation analysis.

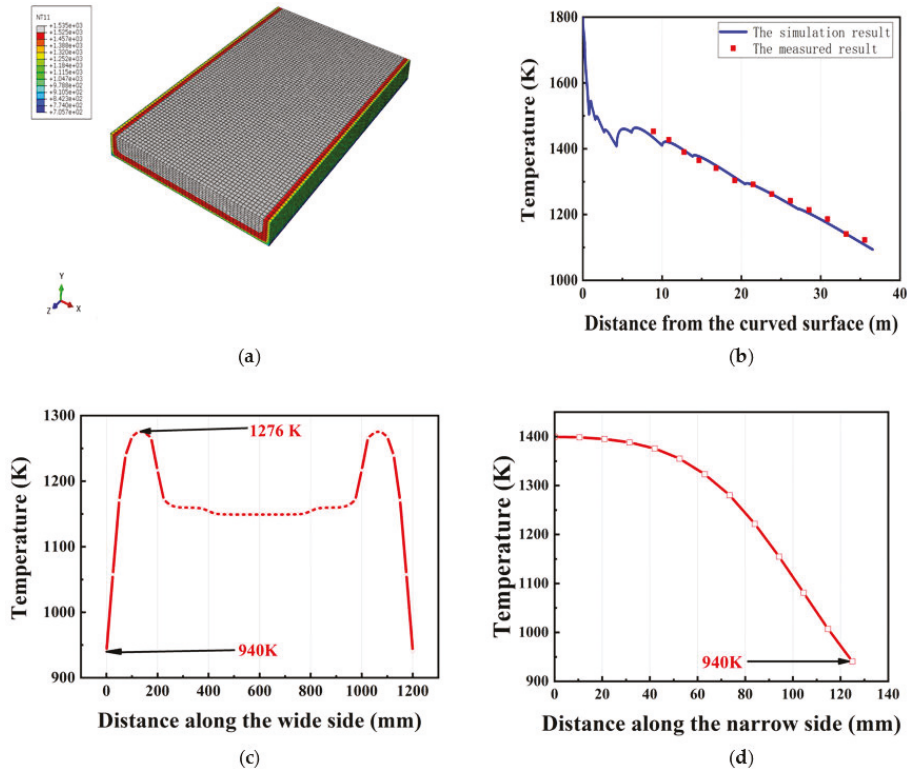


Figure 3. (a) Temperature field of the model. (b) The comparison of the measured and simulated temperature in the center of the narrow face. (c) Temperature on the wide side. (d) Temperature on the narrow side.

The temperature distributions on the wide and narrow sides are shown in Figure 3c,d. At the end of the foot roller section of the continuous slab caster, the highest temperature of the slab was 1276 K and the lowest temperature was 940 K on the wide side. The difference in temperature was 336 K, thus dropping by 26.3%. The highest temperature of the slab was 1400 K and the lowest temperature was 940 K on the narrow side. The difference in temperature was 460 K, a decrease of 32.9%. The thickness of the solidified slab at this segment was about 42.5 mm on the wide side, and the thickness of the narrow side was about 41 mm. Due to the uneven heat transfer, the temperature field of the slab was unevenly distributed overall. The lowest temperature of the slab appeared in the corner area owing to the bidirectional heat transfer characteristic.

3. The Establishment of the Bulge Deformation Model

The three-dimensional thermoelastic–plastic and creep coupling models were proposed to investigate slab bulge deformation after temperature distribution and the thickness of the solidified shell had been acquired. The relationship between the solidification heat transfer model and the slab bulge deformation model is illustrated in Figure 4. Q235 steel served as the analytical material of the casting slab. The casting roller material was 40CrMo.

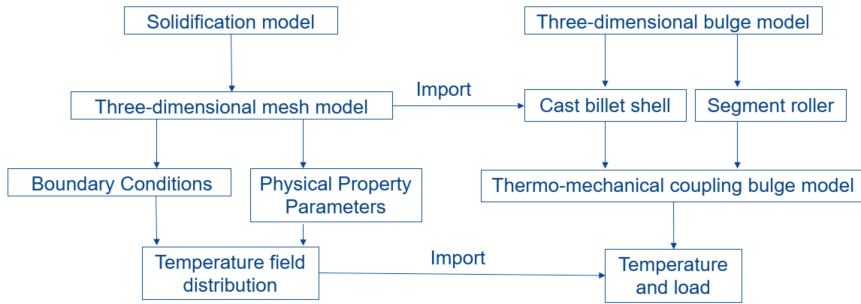


Figure 4. The relationship between the solidification model and the slab deformation model.

3.1. Physical Property Parameters

In the high-temperature continuous casting process, the bulge deformation of the slab is not only determined by the thermal process, as the high-temperature mechanical properties of the material also have an important influence on the deformation behavior of the slab. In order to accurately analyze the deformation of the casting slab, it was necessary to clarify the high-temperature mechanical properties of Q235 steel. Physical property parameters of the slab were quoted from the references [35,36] and are shown in Figure 5. According to the investigation, the material parameters of 40CrMo at the temperature of 523 K were suitable for the bulge deformation model analysis. The elastic modulus was 189.46 MPa, the Poisson ratio was 0.28, and the density was 7850 kg·m⁻³.

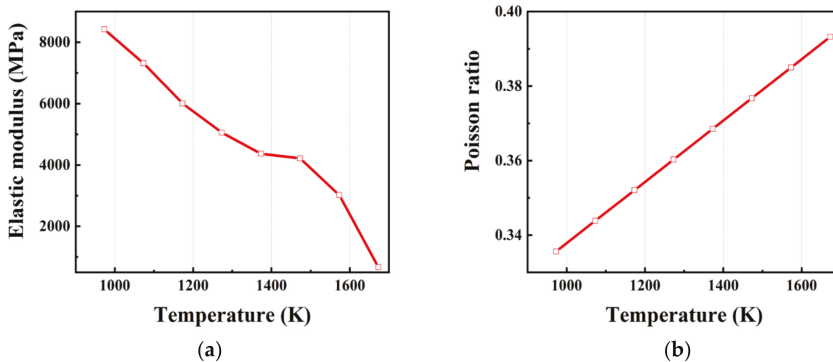


Figure 5. (a) Elastic modulus of Q235 steel; (b) Poisson ratio of Q235 steel.

3.2. Geometric Model with Various Segmented Casting Rollers

The geometric parameters of the slab and casting rollers used in the model are listed in Table 4. The three-dimensional geometric models of the interaction between the slab and the various casting rollers are shown in Figure 6, including rigid solid rollers, elastic solid rollers, elastic two-segment rollers, and elastic three-segment rollers. C3D8R was the eight-node linear three-dimensional stress hexahedron reduction integral element which was used to build the models. The casting slab was composed of 20,400 elements (C3D8R) and 40,581 nodes. In the continuous casting process, it was assumed that the casting rollers were linearly distributed, ignoring the casting blank curvature. The liquid core of the slab was removed and simplified as a cavity, and the static pressure of the molten steel in the slab was transformed into a uniform pressure on the inner surface of the slab. During the analysis, the thickness of the casting slab and the distribution of the temperature field did not change with the operation of the slab.

Table 4. Simulation constants for bulge deformations.

Parameters	Values
Thickness of the solidified slab on the wide side	42.5 mm
Thickness of the solidified slab on the narrow side	41 mm
Number of rollers	15
Roller spacing	300 mm
Radius of roller	115 mm
Length of roller	1240 mm
Casting speed	1.5 m·min ⁻¹

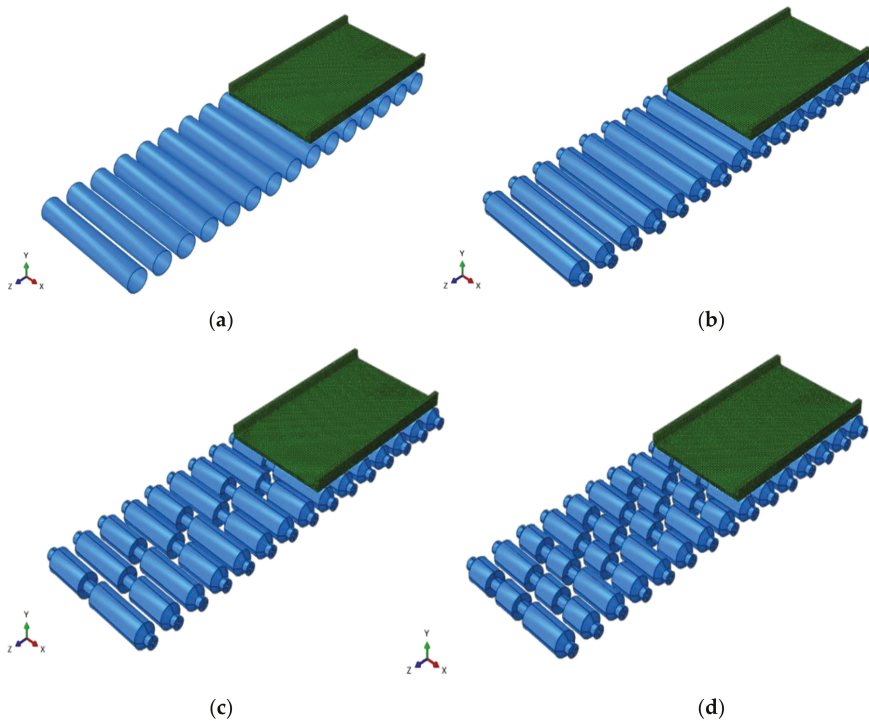


Figure 6. (a) Bulging model with rigid solid rollers. (b) Bulging model with elastic solid rollers. (c) Bulging model with two-segment rollers. (d) Bulging model with three-segment rollers.

3.3. Boundary Conditions and Contact Definition

(1) The uniform pressure was 369,634 Pa, which was to be the static pressure of the molten steel in the slab.

(2) The symmetrical displacement constraint was loaded on the slab because of the symmetry of the structure.

(3) When the longitudinal length of the slab was chosen as 2000 mm, the influence of the slab boundary on the internal structure could be neglected according to Saint-Venant's principle, and the calculation accuracy and efficiency could be guaranteed.

3.4. Creep Model

It was found that the time-hardening model could describe the creep behavior of the metal with a carbon content of 0.18% and a secondary cooling temperature range of 1173 K~T_s [37]. This could

satisfy the requirements of this paper. Therefore, the time-hardening model was used as the creep model of the casting slab material. The constitutive equation of the time-hardening model is shown as Equation (7):

$$\dot{\epsilon}_p = C \exp\left(\frac{-Q}{T}\right) \sigma^N t^m \quad (11)$$

where

$$C = 0.3091 + 0.2090(pctC) + 0.1773(pctC)^2,$$

$$Q = 17160,$$

$$N = 6.365 - 4.521 \times 10^{-3}T + 1.439 \times 10^{-6}T^2,$$

$$m = -1.362 + 5.761 \times 10^{-4}T + 1.982 \times 10^{-8}T^2,$$

$\dot{\epsilon}_p$ is the creep strain rate (s^{-1}),

C is the influence parameter of carbon content ($MPa^{-n}s^{-m-1}$),

σ is the stress (MPa),

Q is the deformation energy constant (K),

T is the temperature (K),

t is the time (s),

m is the temperature-dependent time influence index, and

N is the temperature-dependent comprehensive stress influence index.

3.5. Predefined Temperature Field

The slab temperature distribution at the end of the foot roller section was introduced into the bulging analysis as a predefined field and kept invariable in the calculation process of bulge deformation.

4. Comparisons of Slab Bulge Deformations with Different Segment Rollers

The bulge deformation of the slab was obtained by establishing the three-dimensional finite element model of the coupling interaction between the various segmented rollers and the slab. The results calculated by ABAQUS were used to analyze the influence of the segmented rollers on slab bulge deformation.

4.1. Bulge Deformation on the Wide Side

The simulation results of slab bulge deformation along the wide side are shown in Figure 7. The influence of the segmented rollers was numerically analyzed by a comparison between the average values of the bulge deformation. As can be seen in Figure 7, the following conclusions can be drawn:

(1) In the bulge deformation model with the three-segment rollers, the deformation rapidly increased to 0.90 mm from the edge to the distance of 270 mm in the direction of the wide surface. The deformation of the slab formed into a bulging platform from the distance of 270 mm to the slab center (600 mm) in the wide direction. The value of the bulging platform was 0.90 mm. The reason for this was that the edge of the solidified slab had formed a thick shell of great stiffness, and the deformation was small. The thickness of the shell decreased with the increasing distance, resulting in the decrease of slab stiffness. The bulge deformation of the slab rapidly increased under the hydrostatic pressure. Then, the platform appeared with the uniform thickness and uniform static pressure of the slab. The deformation of the slab at the contact position with the roller sectional area was greater than the average value of the platform. This was because the fixed area of the slab intermittently passed through the sectional area of the segmented rollers, and the positive creep was more effective than the reverse creep in the fixed area. In the continuous casting process, the positive creep makes the solidified shell convex outwards, and the reverse creep makes the solidified shell recess.

(2) The minimum bulge deformation was 0.82 mm in the model with rigid solid rollers. The maximum bulge deformation of 1.43 mm appeared in the model with elastic solid rollers. The difference between the deformation of the two models was about 0.61 mm, and the increase remained around 74.3%. The results showed that the stiffness of the casting rollers had a great influence on slab bulge deformation. However, the casting rollers cannot be absolutely rigid rollers in the actual production process. Thus, the elastic rollers were more suitable than the rigid rollers to simulate the bulge deformation of the casting slab in the actual production process, as a more accurate result could be obtained.

(3) The two-segment and three-segment rollers were defined by using elasticity. The bulge deformation of the casting slab in the two-segment roller model was reduced to 1.28 mm in comparison with the elastic solid rollers model. The difference in bulge deformation was 0.15 mm, meaning there was a decrease of 10.5% between the two models, while the bulge deformation of the slab with the three-segment rollers reached 0.90 mm. The bulge deformation difference was 0.53 mm, dropping by 37.1%. The result indicated that the bulge deformation with the three-segment rollers was closer to that of the rigid solid rollers. This means that the bulge deformation of the casting slab could be effectively controlled by using segmented rollers, and the influence of the three-segment rollers was more effective than that of the two-segment rollers.

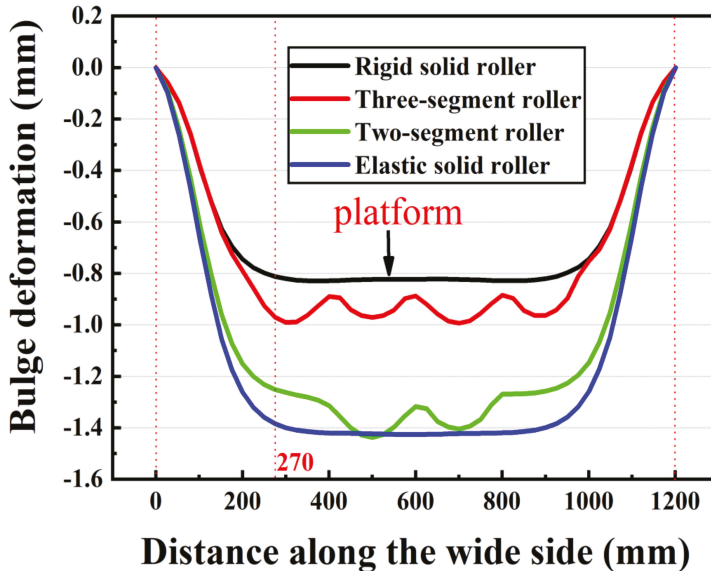


Figure 7. Bulge deformation of the slab on the wide side with different casting rollers.

4.2. Bulge Deformation on the Narrow Side

The simulation result of the slab bulge deformation along the narrow side is displayed in Figure 8.

The horizontal bulge deformation of the slab's narrow side was uneven, and the bulge deformation of the narrow side with the three-segment rollers was relatively close to that of the rigid rollers. The bulge deformation on the narrow side with the three-segment rollers reduced from 0.38 to 0.23 mm, a decrease of 39.5%. The bulge deformation on the narrow side with the two-segment rollers reduced from 0.39 to -0.008 mm, which was down by 102%. The bulge deformation on the narrow side with the rigid solid rollers reduced from 0.39 to 0.25 mm, dropping by 35.9%. The bulge deformation on the narrow side with the elastic solid rollers reduced from 0.37 to -0.08 mm, a decrease of 121.6%.

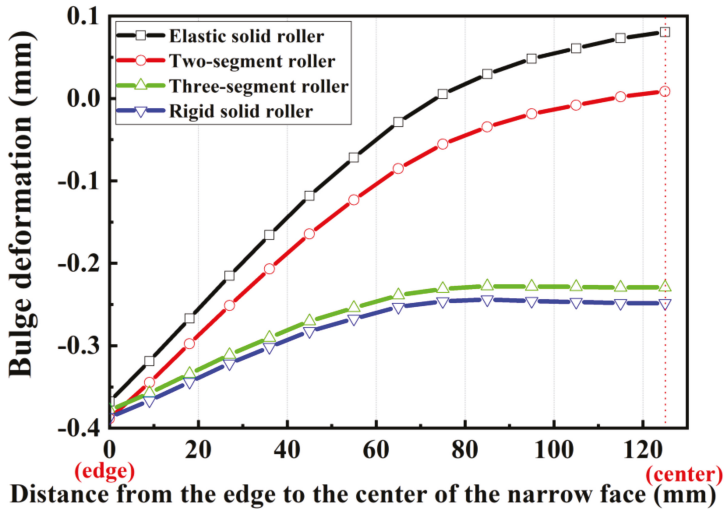


Figure 8. Bulge deformation of the slab on the narrow side with different casting rollers.

4.3. Analysis of Segmented Roller's Stiffness

The stiffness of the casting roller was an important factor affecting slab bulge deformation. In the bulging models, the vertical displacement of the elastic casting roller had occurred, which was selected to measure the stiffness of the casting roller. The results are shown in Figure 9. The vertical displacement of the elastic solid roller was a reverse parabola distribution. The maximum value of 0.14 mm appeared in the center of the solid roller. The rigid roller was not deformed, so the vertical displacement was 0 mm. The vertical displacement of the two-segment roller was evenly distributed around 0.004 mm. The displacement of the three-segment roller in the vertical direction was generally distributed around 0.0015 mm. The average vertical displacement of the roller was selected for comparison to intuitively analyze the stiffness of the casting rollers. The average vertical displacement of the elastic solid roller was 0.07 mm, the average vertical displacement of the two-segment roller was 0.004 mm, and that of the three-segment roller was 0.0015 mm. The stiffness of the two-segment roller was 17.5 times greater than that of the solid roller, and the stiffness of the three-segment roller was 46.7 times greater than that of the solid roller. As the number of sections increased, the deflection of the segment roller during the continuous casting process was smaller. This indicated that the stiffness of the segmented roller was effectively improved. Combined with the previous analysis of casting slab deformation, the conclusion could be drawn that the stiffness of the segmented roller could be better improved than that of the solid casting roller, and the bulge deformation of the slab could also be excellently reduced.

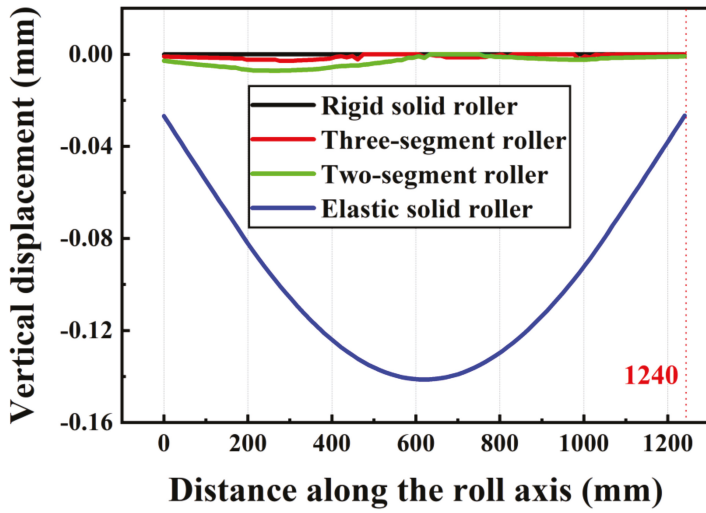


Figure 9. The vertical displacement of different casting rollers.

5. Influences of Roller Spacing and Roller Diameter on Slab Bulge Deformation

5.1. Establishment of Deformation Model with Different Roller Spacings and Diameters

In the continuous casting process, bulge deformation must be controlled to ensure the quality of the slab. There are many factors involved in slab bulge deformation in continuous casting production, among which the main parameters include casting speed, static pressure of molten steel, shell thickness, roller spacing, roller diameter, and surface temperature of the slab. The main purpose of this section is to explore and analyze the influence of the segmented roller structure parameters on bulge deformation. Under a constant casting speed condition ($1.5 \text{ m}\cdot\text{min}^{-1}$), the bulge deformation was calculated and analyzed for the casting slab. The specific simulation structural parameters are shown in Table 5. The influence of the casting process parameters was numerically analyzed by a comparison between the average values of the bulge deformation.

Table 5. Simulation parameters of bulging models.

Roller Spacing	Rigid Roller	Elastic Roller	Two-Segment Roller	Three-Segment Roller
	Roller Diameter			
300 mm	230 mm	230 mm	230 mm	230 mm
	250 mm	250 mm	250 mm	250 mm
	270 mm	270 mm	270 mm	270 mm
350 mm	230 mm	230 mm	230 mm	230 mm
400 mm	230 mm	230 mm	230 mm	230 mm

5.2. Results and Conclusions

5.2.1. Influences of Roller Spacing on Bulge Deformation

Roller spacing was adjusted by changing the gap between the rollers. Under the condition of constant casting speed ($1.5 \text{ m}\cdot\text{min}^{-1}$), the bulge deformation was calculated with 350 and 400 mm as the roller spacings. The average values of the bulge deformation were compared with that of a 300-mm roller spacing. The diameter of the roller was 230 mm. The results of slab bulge deformation on the wide side, shown in Figure 10 and Table 6, were established by the simulation model with

different roller spacings. It could be concluded that the approximate distribution of the slab bulge deformation on the wide side would not change with a 50 mm increase of the roller spacing, and the improvement of the three-segment roller for bulge deformation was most obvious. However, the bulge deformation of the slab under the same continuous casting segmented roller increased greatly with the increase of the roller spacing. The maximum increment of bulging deformation was 67.1% under the rigid roller with the roller spacing changing from 300 to 350 mm. The maximum increment of bulge deformation under the elastic roller was 47.4%, with the roller spacing changing from 350 to 400 mm. The maximum increment of bulge deformation under the two-segment roller was 37.5%, with the roller spacing changing from 300 to 350 mm. The maximum increment of bulge deformation under the three-segment roller was 60.0%, with the roller spacing changing from 300 to 350 mm. The bulging increase was about the same for the rigid roller and the three-segment roller. This also proved that the effect of the three-segment roller was closest to that of the rigid roller on slab bulge deformation. The minimum increment was 32.9% under the elastic solid roller with the roller spacing changing from 300 to 350 mm.

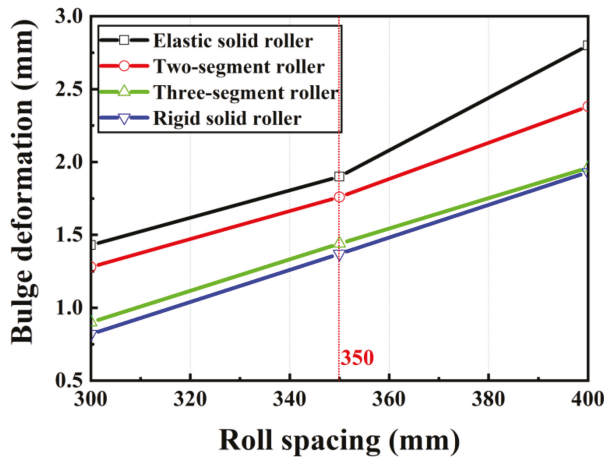


Figure 10. The bulge deformation on the wide side with different roller spacings.

Table 6. Bulge deformation on the wide side with different roller spacings.

Roller Spacing	Rigid Roller	Elastic Roller	Two-Segment Roller	Three-Segment Roller
300 mm	0.82 mm	1.43 mm	1.28 mm	0.90 mm
350 mm	1.37 mm	1.90 mm	1.76 mm	1.44 mm
400 mm	1.93 mm	2.80 mm	2.38 mm	1.96 mm

An analysis of variance (Table 6) showed that the value of variance ratio was 158.45 under different roller spacings, which was larger than the critical value of variance ratio (the critical value was 5.14). The value of variance ratio was 35.38 under different segmented rollers, which was larger than the critical value of variance ratio (the critical value was 4.76). This indicated that different roller spacings and segmented rollers all have a significant effect on slab bulge deformation. Generally, the slab bulge deformation on the wide and narrow sides increased with the increasing roller spacing. This was because the area of the slab between the two rollers increased with the increasing roller spacing. The effect of static pressure increased in the solidified shell, which indirectly reduced its stiffness. As a result, the value of slab bulge deformation became larger as the roller spacing increased. This indicated that roller spacing also played an important role in bulge deformation of the casting slab.

5.2.2. Influences of Roller Diameter on Bulge Deformation

The influence of roller diameter was observed by using the deformation models under various roller diameters and a constant roller spacing. The roller spacing was defined as 300 mm. The roller diameters of the bulging model are shown in Table 5. The results of bulge deformation on the wide side under different roller diameters are listed in Table 7. It was found that the slab bulge deformation under the rigid rollers was almost unchanged with different roller diameters. This was because the rigid roller was established by a rigid body that did not reform in the continuous casting process, and the changing roller diameters had no influence on slab bulge deformation. The average deformation of the slab on the wide side decreased by about 0.08 mm when the elastic solid roller diameter increased by 20 mm. The influence of changing roller diameters on bulging deformation was relatively small due to the low stiffness of the elastic solid roller. However, the slab bulge deformation was effectively influenced by changing the segmented roller diameter by 20 mm, including the two-segment and three-segment rollers. The maximum reduction of bulging deformation was 0.24 mm, with the two-segment roller diameter changing from 250 to 270 mm, and the decrease remained around 21.8%. The minimum reduction was 0.1 mm with the three-segment roller diameter changing from 230 to 250 mm, and the decrease remained around 11.1%. This was because the elastic roller was deformed in the model, which resulted in a larger contact area between the slab and the roller as the roller diameter increased. In other words, the rigidity of the solidified shell was indirectly increased. The bulge deformation of the continuous casting slab was effectively controlled with the improved stiffness of the solidified shell and the casting roller. An analysis of variance (Table 7) showed that the value of variance ratio was 6.30 under different roller diameters, which was larger than the critical value of variance ratio (the critical value was 5.14). The roller diameter had a significant effect on slab bulging deformation.

Table 7. Bulge deformation on the wide side with different roller diameters.

Roller Diameter	Rigid Solid Roller	Elastic Solid Roller	Elastic Two-Segment Roller	Elastic Three-Segment Roller
230 mm	0.82 mm	1.43 mm	1.28 mm	0.90 mm
250 mm	0.80 mm	1.37 mm	1.10 mm	0.80 mm
270 mm	0.80 mm	1.25 mm	0.86 mm	0.69 mm

In general, the slab bulge deformation increased with the increased roller spacing and decreased with the increased roller diameter. The comparisons of average values of bulge deformation along the wide side are shown in Figure 11. When the roller spacing was 400 mm and the roller diameter was 230 mm, the maximum average value of bulge deformation along the wide side was 2.80 mm with the elastic solid rollers. When the roller spacing was 300 mm and the roller diameter was 270 mm, the minimum average value of bulge deformation along the wide side was 0.69 mm with the three-segment rollers; the difference was of 2.11 mm in comparison with the previous one. The bulge deformation was reduced by 75.4%. The optimized structural parameters could effectively control slab bulge deformation.

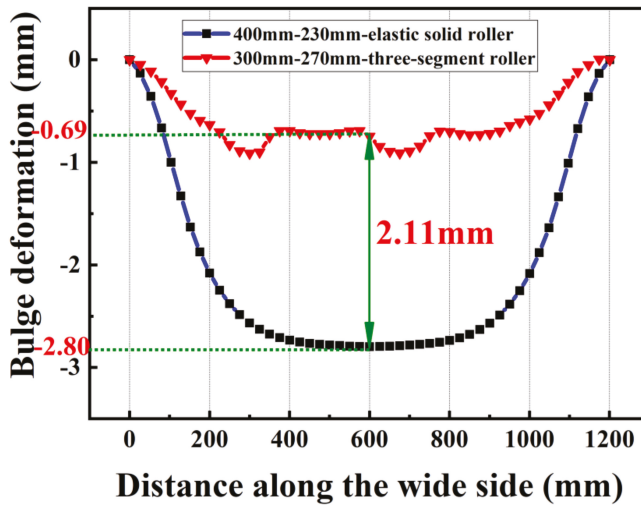


Figure 11. Comparisons of slab bulge deformation with different segment roller structure parameters.

6. Discussion

Slab bulge deformation is an important factor that affects the quality of the slab. Most researchers have focused on the deformation mechanism of the slab and rarely explored an effective way to control slab bulge deformation. Also, rigid casting rollers were most commonly used in the slab bulging models in order to simplify the calculations of slab bulge deformation. Although this simplification could greatly reduce the model's calculation time, the influence of roller deformation on slab deformation was neglected. In this paper, the influence of segmented rollers on slab bulge deformation was explored, and the structural parameters of segmented rollers were optimized to effectively control the bulge deformation of the casting slab. Also, elastic casting rollers were introduced to replace the traditional rigid casting rollers in the bulging model for simulation analysis to obtain more ideal results. The results showed that elastic casting rollers were more suitable for analyzing slab bulge deformation than rigid casting rollers. Then, by comparing the slab bulge deformation under the segmented and solid rollers separately, it was found that the stiffness of the segmented rollers was greater than that of the solid rollers, so that the bulge deformation of the slab could be effectively controlled. Finally, the roller spacing and diameter of the segmented rollers were further studied. It was found that reducing the segmented roller spacing and increasing the roller diameter could effectively control the bulge deformation of the slab. The research results in this paper could provide an effective theoretical basis for controlling slab bulge deformation in actual production.

7. Conclusions

A 3D finite element thermomechanical coupling model between segmented rollers and a casting slab was established to investigate the influence of the segmented rollers on slab bulge deformation. The traditional rigid continuous casting rollers were replaced by elastic continuous casting rollers in these models, which is an advantage that this model has over traditional models. The main conclusions are as follows:

(1) The slab bulge deformation under the elastic rollers increased by around 74.3% compared with that of traditional rigid rollers. The results indicated that the stiffness of the casting rollers would have a great influence on slab bulge deformation and the elastic rollers were more suitable for the slab bulge deformation analysis.

(2) The slab bulge deformation was 1.43 mm under the elastic solid rollers and was reduced by 10.5% under the two-segment rollers compared with elastic solid rollers, while the slab bulge deformation dropped by 37.1% under the three-segment rollers.

(3) The results showed that the bulge deformation could be controlled by reducing the roller spacing or increasing the roller diameter. The slab bulge deformation on the wide side increased when the roller spacing increased by 50 mm, with the maximum increase of 67.1% and the minimum increase of 32.9%. The average value of the slab bulge deformation was reduced by about 15% when the roller diameter was increased by 20 mm.

(4) The bulge deformation on the wide side was reduced by 75.4% when the roller diameter and spacing of the segmented rollers were optimized. This result indicates that the optimized structural parameters of casting segmented rollers could effectively control slab bulge deformation.

Author Contributions: Conceptualization, Q.Q.; methodology, Q.Q.; formal analysis, Q.Q.; investigation, M.L. and J.H.; writing—original draft preparation, M.L.; writing—review and editing, Q.Q.; visualization, M.L.; supervision, Q.Q.; funding acquisition, Q.Q.

Funding: This research was funded by the National Natural Science Foundation of China, grant number: 51375041.

Conflicts of Interest: The authors declare no conflict of interest.

References

- Janik, M.; Dyja, H.; Berski, S.; Banaszek, G. Two-dimensional thermomechanical analysis of continuous casting process. *J. Mater. Process. Technol.* **2004**, *153*, 578–582. [[CrossRef](#)]
- Ji, C.; Luo, S.; Zhu, M.; Sahai, Y. Uneven solidification during wide-thick slab continuous casting process and its influence on soft reduction zone. *ISIJ Int.* **2014**, *54*, 103–111. [[CrossRef](#)]
- Dong, Q.; Zhang, J.; Yin, Y.; Wang, B. Three-dimensional numerical modeling of macrosegregation in continuously cast billets. *Metals* **2017**, *7*, 209. [[CrossRef](#)]
- Long, M.; Chen, H.; Chen, D.; Yu, S.; Liang, B.; Duan, H. A combined hybrid 3-D/2-D model for flow and solidification prediction during slab continuous casting. *Metals* **2018**, *8*, 182. [[CrossRef](#)]
- Yoshii, A.; Kihara, S. Analysis of bulging in continuously cast slabs by bending theory of continuous beam. *Trans. Iron Steel Inst. Jpn.* **1986**, *26*, 891–894. [[CrossRef](#)]
- Liu, W.; Dai, Y. Study on the deformation of the liquid core continuous casting shell. *Heavy Mach.* **1994**, 10–16. [[CrossRef](#)]
- Sun, J.; Sheng, Y.; Zhang, X. Analysis of bulging deformation and stress in continuous cast slabs. *J. Iron Steel Res.* **1996**, 11–15. [[CrossRef](#)]
- Xu, R. Behavior analysis of bulging deformation in slab casting process. *Heavy Mach.* **2012**, 17–21. [[CrossRef](#)]
- Toishi, K.; Miki, Y. Generation mechanism of unsteady bulging in continuous casting-2-fem simulation for generation mechanism of unsteady bulging. *ISIJ Int.* **2016**, *56*, 1764–1769. [[CrossRef](#)]
- Ha, J.; Cho, J.; Lee, B.; Ha, M. Numerical analysis of secondary cooling and bulging in the continuous casting of slabs. *J. Mater. Process. Technol.* **2001**, *113*, 257–261. [[CrossRef](#)]
- Zhang, Y. Analysis of solidification heat transfer and bulging in the cast slab. Master's Thesis, Yanshan University, Hebei, China, 2011.
- Okamura, K.; Kawashima, H. Three-dimensional elasto-plastic and creep analysis of bulging in continuously cast slabs. *Tetsu-to-Hagane* **1989**, *75*, 1905–1912. [[CrossRef](#)]
- Ning, Z.; Wu, D.; Qin, Q.; Zang, Y. Three-dimensional emulation research on the bulging deformation during continuously casting slab. *Metall. Equip.* **2007**, 2.
- Qin, Q.; Shang, S.; Wu, D.; Zang, Y. Comparative analysis of bulge deformation between 2D and 3D finite element models. *Adv. Mech. Eng.* **2014**, *6*, 942719. [[CrossRef](#)]
- Liu, H.; Zhang, X.; Qian, L. 3D Finite element calculation of creep bulging system development and application. *Contin. Cast.* **2015**, *40*, 54–58.
- Camporredondo, J.E.; Acosta, F.A.; Castillejos, A.H.; Gutierrez, E.P.; De la Gonzalez, R. Analysis of thin-slab casting by the compact-strip process: Part II. Effect of operating and design parameters on solidification and bulging. *Metall. Mater. Trans. B* **2004**, *35*, 561–573. [[CrossRef](#)]

17. Zhang, J.; Shen, H.F.; Huang, T.Y. Finite element thermal-mechanical coupled analysis of strand bulging deformation in continuous casting. *Adv. Mater. Res.* **2011**, *154–155*, 1456–1461. [[CrossRef](#)]
18. Qin, Q.; Yang, Z. Finite element simulation of bulge deformation for slab continuous casting. *Int. J. Adv. Manuf. Technol.* **2017**, *93*, 4357–4370. [[CrossRef](#)]
19. Triolet, N.; Bobadilla, M.; Bellet, M.; Avedian, L.; Mabelly, P. A thermomechanical modelling of continuous casting to master steel slabs internal soundness and surface quality. *Rev. De Métallurgie-Int. J. Metall.* **2005**, *102*, 343–353. [[CrossRef](#)]
20. Fu, J.-X.; Hwang, W.-S. Numerical simulation of slab broadening in continuous casting of steel. In *Numerical Simulation-From Theory to Industry*; InTech: Rijeka, Croatia, 2012.
21. Li, B. Study about the High-temperature creep property of q460e steel and its bulging in continuous casting process. Master's Thesis, Yan Shan University, Hebei, China, 2015.
22. Han, P.; Ren, T.; Jin, X. Influence of roll misalignment on bulging of continuous casting slab. *Iron Steel* **2016**, *51*, 53–58.
23. Ohno, H.; Miki, Y.; Nishizawa, Y. Generation mechanism of unsteady bulging in continuous casting-1-development of method for measurement of unsteady bulging in continuous casting. *ISIJ Int.* **2016**, *56*, 1758–1763. [[CrossRef](#)]
24. Verma, R.; Girase, N. Comparison of different caster designs based on bulging, bending and misalignment strains in solidifying strand. *Ironmak. Steelmak.* **2006**, *33*, 471–476. [[CrossRef](#)]
25. Yu, Y.; Duan, L.; Cui, X. Brief introduction of slab caster segment rollers. *Metall. Equip.* **2016**, 45–48. [[CrossRef](#)]
26. Li, S.; Shen, B. Roller type selection of sector of WISCO three steelmaking continuous casting machine. *Metall. Equip.* **1992**, *14*, 51–52.
27. Shi, J. The advantages and theoretical argument of caster segment sub-section roller. In Proceedings of the 8th (2011) China Steel Annual Meeting, Beijing, China, 26 October 2011; p. 6.
28. Liu, W.; Wang, W. Analysis on the stiffness of segmented backing guide roll of slab continuous caster. *Bao Steel Technol.* **1994**, *12*, 58–63.
29. Liu, W.; Wang, W. The influence of structure and classified number of backup guide rolls in CCM on the deformation of slab bulge. *Shanghai Metals* **1995**, *17*, 25–30.
30. Qin, Q.; Wu, D. *Thermal and Mechanical Behavior of Continuous Casting Equipment*; Metallurgical Industry Press: Beijing, China, 2013.
31. Mizikar, E.A. Mathematical heat transfer model for solidification of continuously cast steel slabs. *Trans. Metall. Soc. AIME* **1967**, *239*, 1747–1753.
32. Cheng, J. *Continuous Casting Steel Manual*; Metallurgical Industry Press: Beijing, China, 1991.
33. Feng, K.; Chen, D.; Xu, C.; Wen, L.; Dong, L. Effect of main thermo-physical parameters of steel Q 235 on accuracy of concasting transport model. *Special Steel* **2004**, *25*, 28–31.
34. Mills, K.C.; Su, Y.; Li, Z.; Brooks, R.F. Equations for the calculation of the thermo-physical properties of stainless steel. *ISIJ Int.* **2004**, *44*, 1661–1668. [[CrossRef](#)]
35. Fu, J.; Li, J.; Wang, C.; Zhu, J. Research of Young's modulus of elasticity of steel Q235. *Mater. Rev.* **2009**, *23*, 68–70.
36. Uehara, M. Mathematical modelling of the unbending of continuously cast steel slabs. Master's Thesis, University of British Columbia, Vancouver, BC, Canada, 1983.
37. Kozłowski, P.F.; Thomas, B.G.; Azzi, J.A.; Wang, H. Simple constitutive equations for steel at high temperature. *Metall. Trans. A* **1992**, *23*, 903. [[CrossRef](#)]





Article

A Simulation Study on the Flow Behavior of Liquid Steel in Tundish with Annular Argon Blowing in the Upper Nozzle

Xufeng Qin ^{1,2}, Changgui Cheng ^{1,2,*}, Yang Li ^{1,2}, Chunming Zhang ^{1,2}, Jinlei Zhang ^{1,2} and Yan Jin ^{1,2}

¹ The State Key Laboratory of Refractories and Metallurgy, Wuhan University of Science and Technology, Wuhan 430081, China; qinxufeng@wust.edu.cn (X.Q.); liyang@wust.edu.cn (Y.L.); Zhangspringming@hotmail.com (C.Z.); Jinleiazhang@outlook.com (J.Z.); jinyan@wust.edu.cn (Y.J.)

² Hubei Provincial Key Laboratory for New Processes of Ironmaking and Steelmaking, Wuhan University of Science and Technology, Wuhan 430081, China

* Correspondence: ccghlx@wust.edu.cn; Tel.: +86-027-68862651

Received: 27 December 2018; Accepted: 12 February 2019; Published: 13 February 2019

Abstract: A three-dimensional mathematical model of gas–liquid two-phase flow has been established to study the flow behavior of liquid steel in the tundish. The effect of the argon flow rate and casting speed on the flow behavior of liquid steel, as well as the migration behavior of argon bubbles, was investigated. The results from the mathematical model were found to be consistent with those from the tundish water model. There were some swirl flows around the stopper when the annular argon blowing process was adopted; the flow of liquid steel near the liquid surface was active around the stopper. With increased argon flow rate, the vortex range and intensity around the stopper gradually increased, and the vertical flow velocity of the liquid steel in the vicinity of the stopper increased; the argon volume flow in the tundish and mold all increased. With increased casting speed, the vortex range and intensity around the stopper gradually decreased, the peak value of vertical flow velocity of liquid steel at the vicinity of the stopper decreased, and the distribution and ratio of argon volume flow between the tundish and the mold decreased. To avoid slag entrapment and purify the liquid steel, the argon flow rate should not be more than $3 \text{ L} \cdot \text{min}^{-1}$. These results provide a theoretical basis to optimize the parameters of the annular argon blowing at the upper nozzle and improve the slab quality.

Keywords: annular argon blowing; upper nozzle; flow behavior; argon gas distribution; tundish

1. Introduction

The tundish is a transitional container connecting the ladle and mold. The tundish makes the liquid steel composition and temperature uniform. It also distributes liquid steel and, more importantly, facilitates the removal of inclusions and then purifies the liquid steel. Many techniques have been adopted in the tundish to remove inclusions such as retaining walls and dams, diversion walls, tundish filtering, and electromagnetic stirring [1–4]. Moreover, the argon blowing in the tundish could effectively reduce the amount of the inclusion and purify the liquid steel. The mechanism is the injection of argon gas into the liquid steel in the tundish to form bubbles. Non-metallic inclusions could then be transported to the liquid surface in the tundish for removal.

The argon blowing patterns in the tundish mainly include the long shroud, the bottom permeable brick, the stopper, and the upper nozzle. Studies [5–7] of argon blowing through the long shroud demonstrated that the micro-bubbles generated by argon blowing could improve the removal rate of inclusions in the tundish, but these micro-bubbles had a short residence time in the tundish. Thus, the effect of removing small inclusions is less obvious.

Argon blowing through the bottom-permeable brick could effectively improve the flow pattern of liquid steel and promote the flotation and removal of fine inclusions [8–13]. The movement route of the liquid steel was more tortuous and closer to the liquid surface. This prolonged the residence time of liquid steel, improved the mixing degree of the liquid steel, and reduced the dead zone volume in the tundish. Argon blowing on the bottom-permeable brick could only stir and clean the liquid steel above the permeable brick, but this could not effectively clean the liquid steel passing through the gap between the tundish slope wall and the gas curtain. Most argon bubbles entered the tundish upper nozzle and the submerged entry nozzle (SEN) when the argon was blown by the stopper [14]. This step could clean the inner wall of the nozzle and reduce the adhesion of inclusions on the inner face of the nozzle. Moreover, some of the larger argon bubbles floated directly in the tundish and interacted with inclusions in the liquid steel during the floating process. This helped reduce the content of the inclusions in the strand [15].

The bubbles generated by the dispersed permeable portion of the upper nozzle could form a stable and continuous argon gas film between the inner wall of the nozzle and liquid steel [16–18]. This could effectively suppress the accumulation of inclusions such as Al_2O_3 on the inner wall of the nozzle and reduce the risk of nozzle clogging. Concurrently, argon bubbles generated from the ruptured gas film could wash the inclusions deposited on the inner wall of the nozzle [19].

Smirnov et al. [20–23] studied the argon-blowing process through a gas-permeable ceramic rod embedded in the nozzle pocket brick. Here, the argon bubbles raised around the stopper and formed an annular gas curtain barrier in the tundish. Their work showed that the technique could reduce the adhesion of inclusions on the inner face of the nozzle and prevent the nozzle from clogging. The loss of refractory material was significantly reduced versus argon blowing on the bottom-permeable brick. However, the void region between the permeable ceramic rods could make the liquid steel entering the tundish nozzle insufficiently clean. This would weaken the ability to remove inclusions in the liquid steel.

The preceding studies are significant for effectively controlling the liquid steel flow by argon blowing—this purifies the liquid steel in the tundish and prevents the nozzle from clogging. Here, we propose to use an annular permeable brick with a certain width set in a pocket brick on the outside of the upper nozzle to form a relatively complete annular gas curtain around the stopper. This is based on the work of Smirnov et al. and will improve the effect of controlling fluid flow in the tundish. The rising argon bubbles may promote the removal of inclusions in liquid steel of the tundish. Concurrently, the argon bubbles partially entering into the nozzle can realize the function of argon blowing with the stopper or upper nozzle to prevent the nozzle from clogging.

In this paper, we describe a three-dimensional mathematical model for the annular argon blowing at the upper nozzle in the tundish based on the actual process conditions of a continuous slab-casting tundish in a steel plant. The discrete phase model (DPM) was used to simulate the argon blowing process to analyze the effects of different argon flow rates and casting speed on the flow behavior of liquid steel and the migration behavior of argon bubbles in the tundish. In addition, the flow behavior of liquid steel with the annular argon blowing at upper nozzle was analyzed and compared with the established water model of the tundish. The results can be leveraged as a theoretical basis for the optimization of the annular argon blowing at the upper nozzle and the improvement of slab quality.

2. Model Description

2.1. Model Assumption

- (1) The effect of liquid slag on the flow behavior of liquid steel in the tundish is neglected.
- (2) The flow of liquid steel is a transient incompressible flow, and the physical properties of the liquid steel such as the density and viscosity are constant.

(3) Argon bubbles are regarded as rigid spheres, the bubble size does not change during the ascent, and the bubble diameters are distributed by Rosin–Rammeler statistics, which were obtained by the water model experiments of tundish.

(4) The transport of tracer in the tundish is an unsteady mass transfer process.

2.2. Governing Equations

The flow of the liquid steel in the tundish is a three-dimensional transient incompressible flow and mass transfer process, which satisfies the basic physical laws of mass, momentum conservation. The continuity equation and the momentum equation are described as follows.

Continuity equation:

$$\frac{\partial \rho}{\partial t} + \frac{\partial(\rho u_i)}{\partial x_i} = 0 \quad (1)$$

Momentum equation (N-S):

$$\frac{\partial(\rho u_i)}{\partial t} + \frac{\partial(\rho u_i u_j)}{\partial x_j} = -\frac{\partial P}{\partial x_i} + \frac{\partial}{\partial x_j} \left[\mu_{\text{eff}} \left(\frac{\partial u_i}{\partial x_j} + \frac{\partial u_j}{\partial x_i} \right) \right] + \rho g + F_g \quad (2)$$

where ρ is the fluid density, in $\text{kg}\cdot\text{m}^{-3}$; u_i and u_j are the velocity vectors, in $\text{m}\cdot\text{s}^{-1}$, i and j each represent the three coordinate directions (x , y , and z), and repeated indices imply summation; P is the pressure, in Pa; μ_{eff} is the turbulent effective viscosity coefficient, in $\text{Pa}\cdot\text{s}$; g is the gravitational acceleration, in $\text{m}\cdot\text{s}^{-2}$. F_g is a momentum source term, which accounts for the presence of argon bubbles, in $\text{N}\cdot\text{m}^{-3}$. Here, the standard k - ϵ turbulence equations were used in the mathematical model. The governing equations describing turbulent kinetic energy (k) and the dissipation rate of turbulence energy (ϵ) are, respectively:

$$\frac{\partial}{\partial t}(\rho k) + \frac{\partial}{\partial x_i}(\rho u_i k - \frac{\mu_{\text{eff}}}{\sigma_k} \frac{\partial k}{\partial x_i}) = G - \rho \epsilon \quad (3)$$

$$\frac{\partial}{\partial t}(\rho \epsilon) + \frac{\partial}{\partial x_i} \left(\rho u_i \epsilon - \frac{\mu_{\text{eff}}}{\sigma_\epsilon} \frac{\partial \epsilon}{\partial x_i} \right) = \frac{1}{k} (C_1 G - C_2 \rho \epsilon^2) \quad (4)$$

$$G = \mu_t \frac{\partial u_i}{\partial x_i} \left(\frac{\partial u_i}{\partial x_i} + \frac{\partial u_i}{\partial x_j} \right) \quad (5)$$

$$\mu_{\text{eff}} = \mu_0 + \mu_t = \mu_0 + \rho C_\mu \frac{k^2}{\epsilon} \quad (6)$$

where μ_0 is the dynamic viscosity, in $\text{Pa}\cdot\text{s}$; μ_t is the turbulent viscosity, in $\text{Pa}\cdot\text{s}$; k is the turbulent kinetic energy of the fluid, in $\text{m}^2\cdot\text{s}^{-2}$; ϵ is the turbulent energy dissipation rate, in $\text{m}^2\cdot\text{s}^{-3}$. Terms C_1 , C_2 , C_μ , σ_k , and σ_ϵ are empirical constants. The recommended values [11] of Launder and Spalding are $C_1 = 1.42$, $C_2 = 1.92$, $C_\mu = 0.09$, $\sigma_k = 1.0$, and $\sigma_\epsilon = 1.0$.

The trajectories and distributions of the argon bubbles are simulated using the discrete phase model (DPM). An equation for argon bubble velocity is obtained considering the drag force, buoyancy force, and virtual mass force exerted by the fluid on bubbles:

$$\frac{du_g}{dt} = \frac{18\mu}{\rho_g d_g^2} \cdot \frac{C_D \text{Re}_g}{24} (u_i - u_g) + \frac{\pi d_g^3}{6} (\rho_g - \rho) g + \frac{1}{2} \frac{\rho}{\rho_g} \frac{d}{dt} (u_i - u_g) \quad (7)$$

where u_g is the bubble velocity, in $\text{m}\cdot\text{s}^{-1}$; μ is the molecular viscosity of the fluid, in $\text{Pa}\cdot\text{s}$; ρ_g is the argon density, in $\text{kg}\cdot\text{m}^{-3}$; d_g is the bubble diameter, in m; Re_g is the relative Reynolds number of bubbles; and C_D is the drag coefficient [24], which is a function of Re_g :

$$C_D = \begin{cases} \frac{24}{\text{Re}_g} \left(1 + \frac{1}{6} \text{Re}_g^{\frac{2}{3}} \right) & \text{if } \text{Re}_g < 1000 \\ 0.44 & \text{if } \text{Re}_g \geq 1000 \end{cases} \quad (8)$$

$$\text{Re}_g = \frac{\rho d_g |u_g - u_i|}{\mu} \quad (9)$$

The momentum transfer from the discrete phase towards the melt is computed by examining their momentum change as [11,25]:

$$F_g = \sum_j^N \left(\frac{3\mu_0 C_D \text{Re}_g}{4\rho_g d_g^2} (u_{gj} - u_i) \right) m_p \Delta t \quad (10)$$

where N is the number of bubbles in a computational cell, which can be determined by the particle trajectory unsteady tracking method in Fluent software; u_{gj} is the velocity of bubble in a computational cell, in $\text{m}\cdot\text{s}^{-1}$, m_p is the mass flow rate of argon bubbles, in $\text{kg}\cdot\text{s}^{-1}$, which equals the argon density multiplied by the argon flow rate; Δt is the time step, in s, its value is 0.005 s.

In Equation (7), d_g adopts a Rosin-Rammler distribution, and the different bubble size range is divided into discrete size groups as shown in Equation (11).

$$Y_d = e^{-(d_g/\bar{d})^n} \quad (11)$$

where Y_d is the mass fraction with bubble diameter greater than d_g ; \bar{d} is the average diameter of bubbles, in m; and n is the distribution index. The mass flow with bubble diameter greater than d_g equals the mass flow rate of argon bubbles multiplied by the time step and the mass fraction with bubble diameter greater than d_g , the mass flow of different diameter range can be determined, and then the number of argon bubbles of different diameter range entering into tundish from the annular argon blowing brick can be determined.

In order to determine the residence time of liquid steel [26], the time evolution of tracer concentration C in the tundish was described by Equation (12):

$$\frac{\partial}{\partial t}(\rho C) + \frac{\partial}{\partial x_i}(\rho u_i C) = \frac{\partial}{\partial x_i}(\rho D_{\text{eff}} \frac{\partial C}{\partial x_i}) \quad (12)$$

$$D_{\text{eff}} = D_0 + \frac{\mu_{\text{eff}}}{\rho S c_t} \quad (13)$$

where C is the concentration of the tracer, in $\text{kg}\cdot\text{m}^{-3}$; D_{eff} is the effective diffusion coefficient, in $\text{m}^2\cdot\text{s}^{-1}$; D_0 is the molecular diffusion coefficient in $\text{m}^2\cdot\text{s}^{-1}$, and its value is 0; and $S c_t$ is the turbulent Schmidt number and its value is 0.7.

2.3. Boundary Conditions

(1) The model inlet of tundish was set as the velocity-inlet, and the entry velocity was calculated based on the mass conservation principle according to the section size of the strand, the casting speed, and the inner diameter of the long shroud, namely, the velocity-inlet is equal to that the cross-sectional area of strand is multiplied by the casting speed and divided by the cross section area of the long shroud. The inlet value of k , the turbulence kinetic energy, and the ε , the rate of turbulence energy dissipation, were estimated from the following relations:

$$k = 0.01 u_{\text{in}}^2 \quad (14)$$

$$\varepsilon = \frac{k^{1.5}}{0.5 D_{\text{in}}} \quad (15)$$

where u_{in} is the inlet velocity, in $\text{m}\cdot\text{s}^{-1}$, and D_{in} is the diameter of the inlet, in m. The value of D_{in} is 0.07 m. When the casting speed was controlled to be $1.05 \text{ m}\cdot\text{min}^{-1}$, $1.2 \text{ m}\cdot\text{min}^{-1}$, $1.35 \text{ m}\cdot\text{min}^{-1}$ and $1.5 \text{ m}\cdot\text{min}^{-1}$, the value of u_{in} was $1.965 \text{ m}\cdot\text{s}^{-1}$, $2.246 \text{ m}\cdot\text{s}^{-1}$, $2.527 \text{ m}\cdot\text{s}^{-1}$ and $2.808 \text{ m}\cdot\text{s}^{-1}$, respectively.

(2) The outlet of the liquid steel was set as the pressure-outlet according to the immersion depth of the SEN; the model outlet was the escape outlet for the argon bubbles.

(3) The surface of the molten pool was set as a free-surface [27], the normal velocity component and normal gradients of all other variables were assumed to be zero, and the bubbles were trapped at the liquid surface.

(4) Owing to the bilateral symmetry, only a half of the tundish is considered in the calculation in order to lower the computation cost. On symmetry plane, the boundary condition for velocity field is a zero normal component and zero gradient of tangential velocity component.

(5) The wall of the tundish was modeled as a no-slip wall boundary condition; the region near the wall was treated with a standard wall function [28].

2.4. Numerical Method

A three-dimensional mathematical model was established according to the real size of the industrial tundish. The schematic diagram of the tundish vertical view is shown in Figure 1. The half-tundish was taken as the computational domain considering the symmetry of the tundish. A schematic diagram of annular argon blowing at the upper nozzle in the tundish is shown in Figure 2. The physical properties and operational parameters are shown in Table 1.

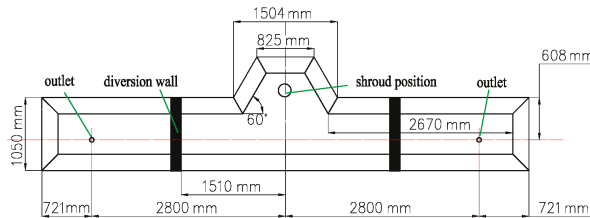


Figure 1. Schematic diagram of tundish vertical view.

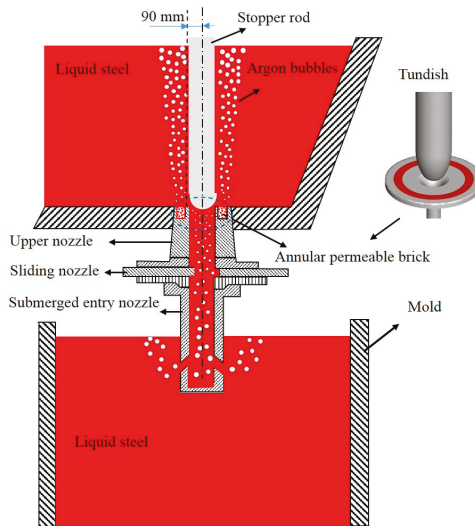
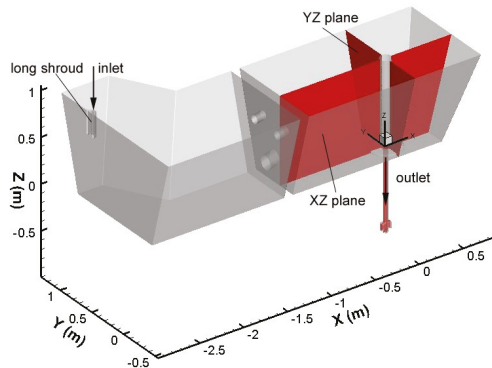


Figure 2. Schematic diagram of annular argon blowing at the tundish upper nozzle.

Table 1. Physical properties and process parameters.

Parameters	Value
Liquid steel density ($\text{kg}\cdot\text{m}^{-3}$)	7000
Liquid steel viscosity ($\text{Pa}\cdot\text{s}$)	0.0065
Argon gas density ($\text{kg}\cdot\text{m}^{-3}$)	0.27
Working liquid surface height of tundish (mm)	960
Inner and outer diameter of the shroud (mm)	70/120
Immersion depth of the shroud (mm)	250
Diameter of the stopper (mm)	127
Inner diameter of the upper nozzle (mm)	50
Sectional dimensions of the slab ($\text{mm} \times \text{mm}$)	1235 \times 175

The coordinate axis X was parallel to the intersection line of the tundish front wall and the bottom wall, and the Y direction was perpendicular to the X direction. A schematic diagram of the computational domain coordinate system is shown in Figure 3, and the flow field in XZ plane and YZ plane will be shown for analyzing the effect of the argon bubbles on the flow of liquid steel.

**Figure 3.** Schematic diagram of regional coordinate system of half tundish in the model calculation.

A mathematical model was developed using the finite-volume-based program ANSYS-FLUENT software (16.0, Ansys Inc., Canonsburg, PA, USA) based on these assumptions including the governing equations and boundary conditions described above. The velocity of liquid steel at the inlet and outlet of tundish is larger, and the flow behavior in the vicinity of stopper should be paid more attention to. So, local grid refinement was applied to simulate the behavior of blowing argon in the tundish; the meshes of the FLUENT computational domain included 6,700,000 unstructured grids using ANSYS-ICEM software (16.0, Ansys Inc.). The mesh size is 2 mm in the argon bubble action zone, and 8 mm far from the stopper. The SIMPLEC algorithm was applied to the velocity–pressure coupling. The second upwind order scheme was employed for discretization of momentum, k , and ϵ equations. The calculation was considered to be converged when the normalized residuals of all variables were smaller than 10^{-4} , when the flow field could achieve a relatively stable state. To reduce the simulation time and ensure the balance of equations at a discrete point of time, a fixed time step of 0.005 s was used in the time-dependent solution.

Considering the interaction between the continuous phase and the discrete phase, the stable flow field of the argon blowing in the tundish was obtained by calculating 15 s. Based on the stable flow field of gas–liquid two-phase, the tracer with the same properties as the liquid steel was added to the inlet of the stable flow field of the tundish for 1 s. The mixed flow of the tracer and the regional fluid were calculated by the transient mode simulation for 3000 s to obtain the residence time distribution (RTD) curve. The flow characteristics of the liquid steel in the tundish under different conditions were

obtained by analyzing the RTD curve using the modified model proposed by Hong [29]. Next, we compared the vertical velocity of the liquid steel in the vicinity of stopper to analyze the influence of different process parameters on the flow of liquid steel. This was done 90 mm from the center of the stopper. The argon gas distribution between the tundish and mold was obtained by counting the number of bubbles entering the nozzle and the tundish in one second. The experimental outline is shown in Table 2. Combined with the results of water model experiments of tundish, the parameters of Rosin–Rammler distribution used in the calculation is shown in Table 3, then the mass fraction with bubble diameter greater than d_g can be determined by using of Equation (11).

Table 2. Mathematical simulation scheme.

Case	Casting Speed (m·min ⁻¹)	Argon Flow Rate (L·min ⁻¹)	Inner and Outer Diameter of Annular Permeable Brick (mm)
Case 1	1.35	2, 3, 4, 5	220/280
Case 2	1.05, 1.20, 1.35, 1.50	3	220/280

Table 3. Parameters of Rosin–Rammler distribution used in calculation.

Argon Flow Rate (L·min ⁻¹)	Minimum Bubble Diameter (mm)	Maximum Bubble Diameter (mm)	Average Bubble Diameter (mm)	Distribution Index
2	0.6	2.85	1.6	2.82
3	0.65	2.90	1.8	4.61
4	0.7	2.95	2.0	5.08
5	0.80	3.0	2.2	7.96

3. Comparison of Flow Behavior in Mathematical Model and Water Model

The flow of liquid steel in the tundish is mainly affected by the viscous force, gravity, and inertial force. The Froude number was chosen to ensure the motion similarity between the prototype and the model. A water model of the tundish with a 1:2 scale was made to simulate the argon blowing through the annular permeable brick in this work. When the argon flow rate was 3 L·min⁻¹ and the casting speed was 1.35 m·min⁻¹, the inner and the outer diameters of the annular permeable brick were 220 mm and 280 mm, respectively. The distribution of argon bubbles in the water model and numerical simulation is shown in Figure 4, and the diffusion of the tracer in the tundish at the different times is shown in Figure 5, the left-hand diagram in Figure 5 shows the calculated flow of liquid steel in cross-section which is through the center of the lower diversion hole and the right side of the retaining wall.

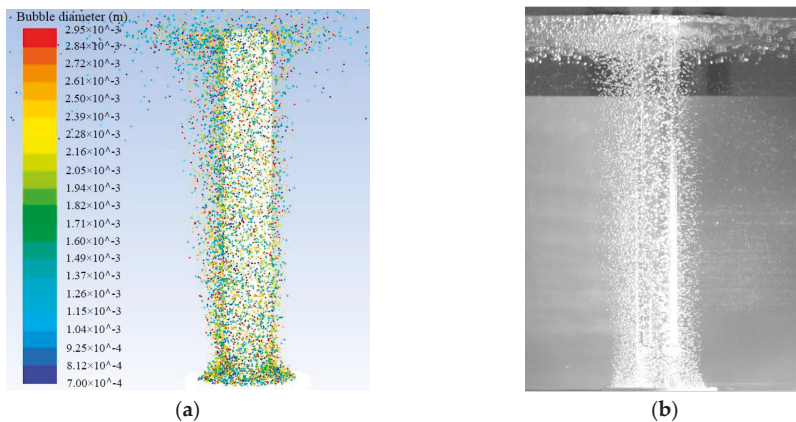


Figure 4. Distribution of argon bubbles in the tundish: (a) numerical simulation and (b) water model.

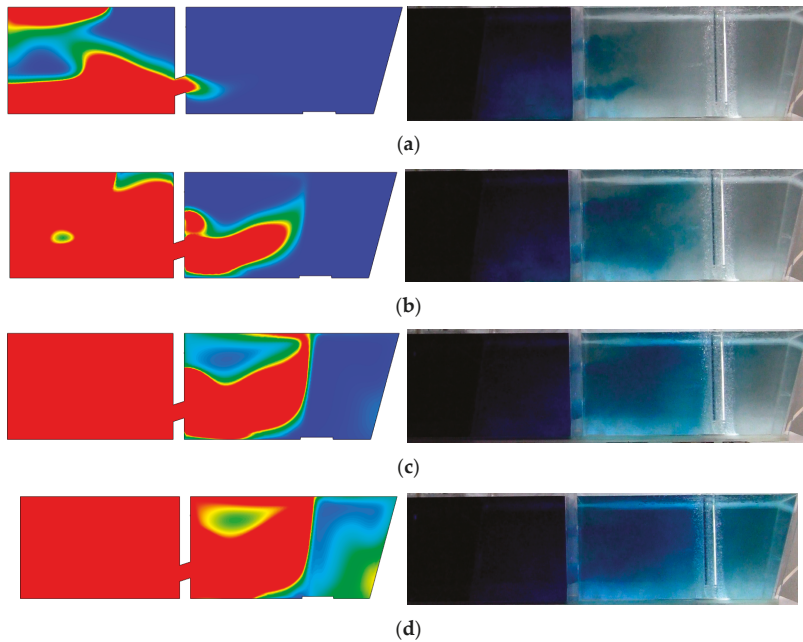


Figure 5. Flow field of the tracer in the half-tundish at different times of numerical model (left-hand diagram) and experiment (right-hand diagram): (a) 10 s, (b) 20 s, (c) 30 s, and (d) 40 s.

Figure 4 shows that the argon bubbles are asymmetrical on both sides of the stopper. The number of argon bubbles on the left side of the stopper is significantly higher than that on the right side of the stopper due to the action of the liquid steel flow.

Figure 5 demonstrates that the liquid steel departs from the diversion hole at the vicinity of the stopper and then flows upward to the liquid surface with the floating argon bubbles. The left side in Figure 5 is the flow field obtained by the mathematical modelling, right side is the flow field in water model of tundish. There are multi-swirl flow zones around the stopper. The diversion hole is not in the same XZ plane. It is part of the liquid steel that migrates from the back area of the stopper to the right wall of the tundish. There is weakened swirl flow to the right of the stopper. The distribution behavior of the argon bubbles calculated by the mathematical model is similar to that in the water model. Thus, the flow field of the liquid steel calculated by the numerical simulation is similar to that in the water model experiment.

4. Results and Discussion

4.1. Typical Flow Behavior of Liquid Steel in the Tundish with Annular Argon Blowing in the Upper Nozzle

When the casting speed was controlled at $1.35 \text{ m}\cdot\text{min}^{-1}$, the inner and outer diameter of the annular permeable brick were 220 mm and 280 mm, respectively. The velocity streamlines of liquid steel in the tundish without the argon blowing and with the argon blowing at $3 \text{ L}\cdot\text{min}^{-1}$ are shown in Figure 6.

Figure 6a demonstrates that the liquid steel entered into the tundish from the shroud, and spreads after impinging on the turbulence controller. The liquid steel then passes through the diversion holes of the retaining wall and migrates obliquely upward. For the viscous resistance of the liquid steel and the obstruction of the stopper, the velocity at the near-surface of the liquid steel around the stopper is reduced gradually when the argon blowing is not adopted. Thus, the laminar flow in the liquid surface is weak, and there is no rising flow around the stopper.

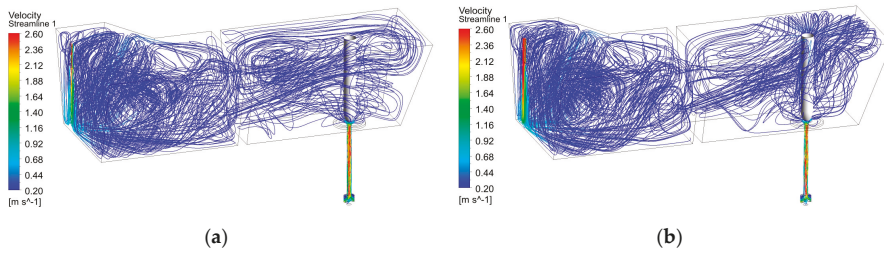


Figure 6. Velocity streamline of the liquid steel in the tundish: (a) without argon blowing and (b) with argon blowing.

When argon is blown through the annular permeable brick, the streamline of the liquid steel in the pouring area is obviously changed versus the pouring area without argon. Figure 6b demonstrates that the liquid steel is driven by the floating bubbles. It moves up to the liquid surface and diffuses to the surrounding area of the stopper. The liquid steel then moves to the vicinity of the tundish wall and flows downward; some swirl flows near the stopper are formed, which can make the level flow of liquid steel around the stopper active. The flow path of the liquid steel is extended, and the short circuit flow is significantly decreased in the tundish.

The flow characteristics of the liquid steel in the tundish with and without argon blowing by the mathematical calculation are shown in Table 4. Table 4 shows that the average residence time and the volume fraction of plug flow of liquid steel in the tundish increase with blowing argon versus no argon blowing. Thus, the annular argon blowing is beneficial to the floating and removal of inclusions in liquid steel.

Table 4. Flow characteristics of the liquid steel in the tundish with and without blowing argon.

Process Condition	Average Residence Time (s)	Volume Fraction of Plug Flow (%)	Volume Fraction of Dead Zone (%)	Volume Fraction of Mixed Flow (%)
without argon	592.12	30.91	12.75	56.34
with argon	593.56	31.59	12.53	55.88

4.2. Effect of Flow Rate of the Argon Blowing on the Flow Behavior of Liquid Steel in the Tundish

Figure 7 shows the flow behavior of the liquid steel along the XZ plane and the XY plane around the stopper in the tundish, the width of the XZ plane is only the distance between the diversion wall centerline and the right side wall of the tundish. The casting speed was $1.2 \text{ m}\cdot\text{min}^{-1}$, and the inner and outer diameters of the annular permeable area in the nozzle pocket brick were 220 mm and 280 mm, respectively. The argon flow rate was $2 \text{ L}\cdot\text{min}^{-1}$, $3 \text{ L}\cdot\text{min}^{-1}$, $4 \text{ L}\cdot\text{min}^{-1}$, and $5 \text{ L}\cdot\text{min}^{-1}$. Under the same conditions, the vertical velocity of the liquid steel in the vicinity of the stopper is shown in Figure 8. The argon flow rate of 0 in Figure 8 indicates that the argon flow was absent.

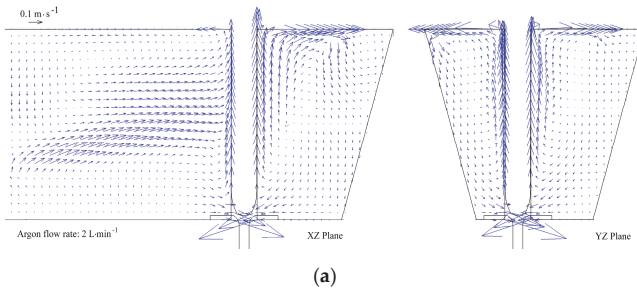


Figure 7. Cont.

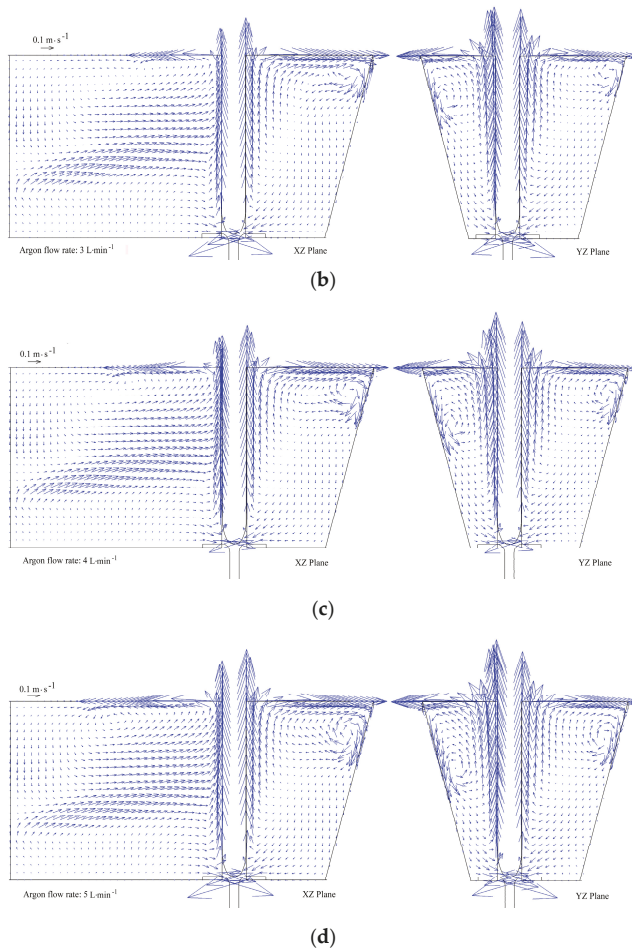


Figure 7. Flow behavior of liquid steel in the tundish under different argon flow rates: (a) $2 \text{ L}\cdot\text{min}^{-1}$, (b) $3 \text{ L}\cdot\text{min}^{-1}$, (c) $4 \text{ L}\cdot\text{min}^{-1}$, and (d) $5 \text{ L}\cdot\text{min}^{-1}$.

The vortex range and intensity around the stopper increase gradually with increased argon flowrates (Figure 7). The vortex center of liquid steel in the front, rear, and right sides of the stopper move towards the tundish wall, and then move downward along the tundish wall. The vortex center of liquid steel in the left side of the stopper moves towards the diversion wall. These flow behaviors are related to the coupling effect of the upflow of liquid steel near the stopper and the normal flow from the diversion hole. The flow intensity of the liquid steel near the tundish wall and diversion wall then increase, which decreases the dead zone of liquid steel in the tundish.

The near surface flow of liquid steel can promote floating of inclusions in the tundish, and then the increased flow rate of argon may improve the purity of liquid steel. However, an excessive surface flow velocity of liquid steel may cause slag entrapment. When the argon flowrate was $2 \text{ L}\cdot\text{min}^{-1}$, $3 \text{ L}\cdot\text{min}^{-1}$, $4 \text{ L}\cdot\text{min}^{-1}$, and $5 \text{ L}\cdot\text{min}^{-1}$, the peak value of the surface flow velocity in the tundish was $0.38 \text{ m}\cdot\text{s}^{-1}$, $0.48 \text{ m}\cdot\text{s}^{-1}$, $0.52 \text{ m}\cdot\text{s}^{-1}$, $0.57 \text{ m}\cdot\text{s}^{-1}$, respectively. Slag entrapment may occur at surface flow velocities over $0.45 \text{ m}\cdot\text{s}^{-1}$ [30]. The argon flow rate should therefore not be larger than $3 \text{ L}\cdot\text{min}^{-1}$.

As the distance from the upper nozzle surface increases, Figure 8 demonstrates that the vertical flow velocity of the liquid steel in the vicinity of the stopper first increases and then decreases.

It approaches 0 at the liquid surface in the tundish with blowing argon. These are related to the vortex flow around the stopper when the liquid steel arrives at this level. The vertical flow velocity is 0 while the horizontal flow velocity of liquid steel is the largest. In the mathematical model, the liquid surface was set to the free liquid surface in which the velocity variable at the normal direction is zero. In practical operation, the liquid surface of the tundish is covered with a slag layer. The floating argon bubbles around the stopper drive the liquid steel upward. The liquid steel from the left diversion hole impinges on the back side of the stopper, and some argon bubbles were carried by the liquid steel to the right side of the stopper as the argon bubbles floated. The vertical flow velocity is then higher than that in the left-hand of the stopper. Moreover, the distance between the front wall of the tundish and stopper is smaller, the floating argon bubbles cannot easily be dispersed. The driving effect of the floating bubbles then increases, and the vertical flow velocity of the liquid steel in the front vicinity of the stopper is higher.

There is no upflow of liquid steel without argon blowing. The liquid steel in the vicinity of the stopper flowed directly into the upper nozzle, and the vertical flow velocity in Figure 8 is negative. With increased argon flow rate, the driving effect of argon bubbles increases, and the vertical flow velocity of the liquid steel in the vicinity of the stopper increases. The peak value of vertical flow velocity of liquid steel increases with increased argon flow rate, and the peak value position also increases. The difference in peak value and peak value position with vertical flow velocity in different orientations is related to the coupling effect of the upflow of liquid steel near the stopper and the normal flow from the diversion hole.

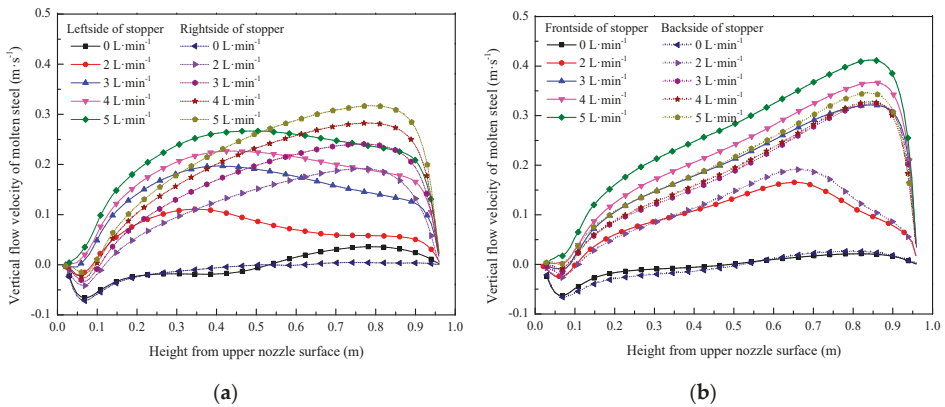


Figure 8. Vertical flow velocity of liquid steel in the vicinity of the stopper under different flow rates of argon: (a) left side and right side of the stopper; (b) front side and back sides of the stopper.

Figure 9 shows the volume flow distribution and ratio of argon in the tundish and mold under different argon flow rates. With increased argon flow rates, more argon bubbles may be released from the annular permeable brick. The number of argon bubbles entering the tundish and SEN then increases. The argon bubbles entering into the tundish nozzle can prevent the nozzle from clogging, and the high flow rate of argon may be appropriate. The bubble dimension increases with increasing argon flow rate. The larger bubbles float more easily, and the ratio of volume flow of argon between the tundish and mold then increases with increasing argon flow rate.

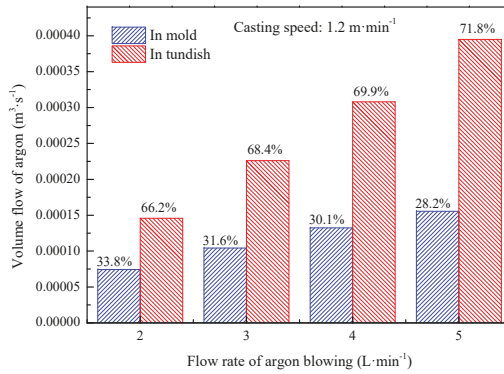


Figure 9. Volume flow distribution of argon under different argon flow rate.

4.3. Effect of Casting Speed on the Flow Behavior of Liquid Steel in the Tundish

When the flow rate of argon blowing was 3 L·min⁻¹, the inner and outer diameter of the annular permeable area in nozzle pocket brick were fixed at 220 mm and 280 mm, respectively, and the casting speed was 1.05 m·min⁻¹, 1.20 m·min⁻¹, 1.35 m·min⁻¹ and 1.50 m·min⁻¹. The flow behavior of the molten steel in the XZ plane and the XY plane at different casting speeds is shown in Figure 10. The vertical flow velocity of liquid steel in the vicinity of the stopper at different casting speeds is shown in Figure 11.

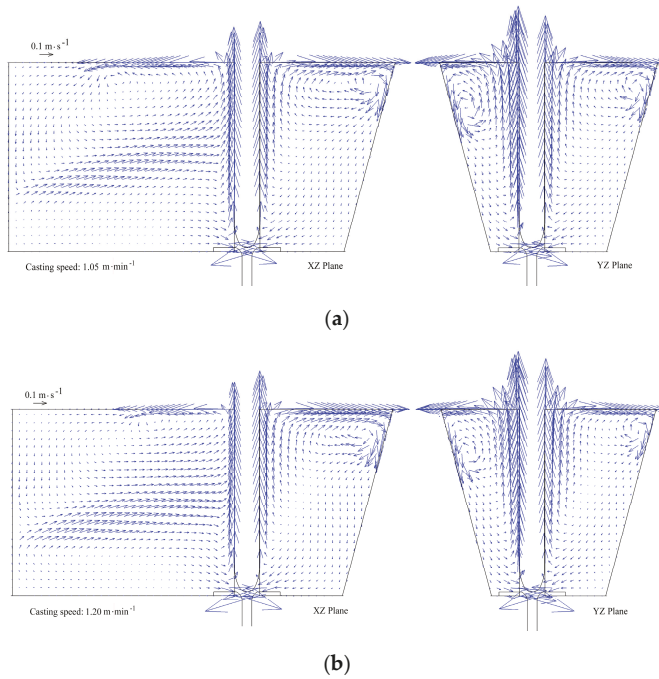


Figure 10. Cont.

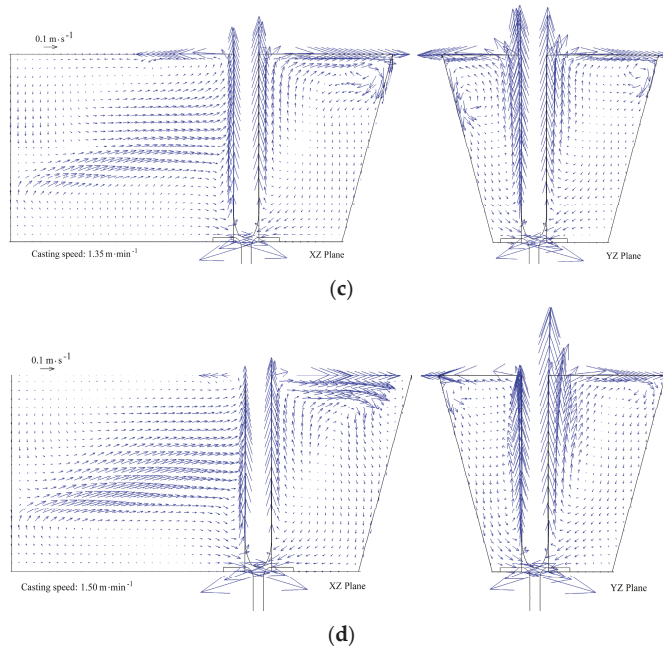


Figure 10. Flow behavior of liquid steel in the tundish under different casting speeds: (a) $1.05 \text{ m}\cdot\text{min}^{-1}$, (b) $1.20 \text{ m}\cdot\text{min}^{-1}$, (c) $1.35 \text{ m}\cdot\text{min}^{-1}$, and (d) $1.50 \text{ m}\cdot\text{min}^{-1}$.

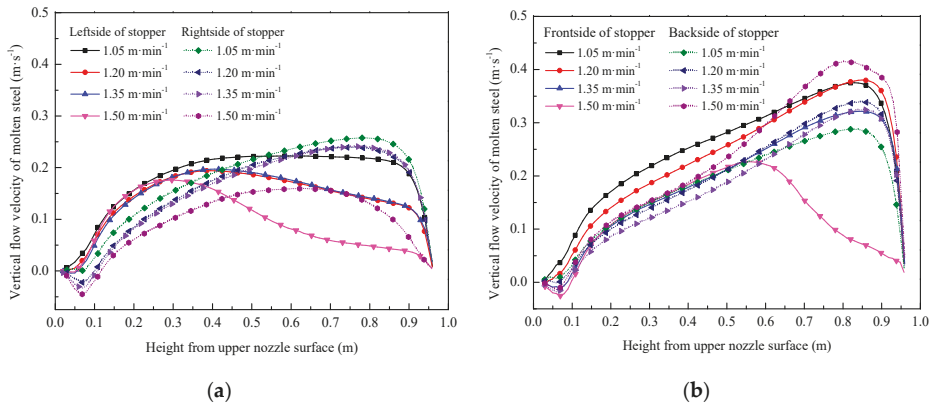


Figure 11. Vertical velocity of liquid steel in near area of stopper at different casting speeds: (a) left and right sides of the stopper; (b) front and back sides of the stopper.

Figure 10 shows that the vortex range and intensity around the stopper decrease gradually with increased casting speed. The vortex center of the liquid steel in different orientations moves towards the stopper. A higher casting speed leads to more bubbles entering the nozzle. The floating effect of the argon bubbles around the stopper weakens.

When the casting speed was 1.05 , 1.20 , 1.35 , and $1.50 \text{ m}\cdot\text{min}^{-1}$, the flow velocity peak of the liquid surface is 0.46 , 0.50 , 0.48 , and $0.59 \text{ m}\cdot\text{s}^{-1}$, respectively. The high casting speed can weaken the floating effect of the argon bubbles. The flow intensity near the back side of the stopper is high. This is related to the high flow velocity of liquid steel in the diversion hole; thus, the flow velocity peak at the

liquid surface is high when the casting speed is $1.50 \text{ m}\cdot\text{min}^{-1}$. This may lead to a slag entrapment problem, which can be eliminated by increasing the diameter of the diversion hole under the high casting speeds.

The peak value of the vertical flow velocity of liquid steel decreases with increased casting speed (Figure 11). This is seen at the left, right, and front side of the stopper; the height of peak value position also decreases. While the peak value of the vertical flow velocity of liquid steel at the back side of the stopper increases, the peak value position also moves up—this is related to the high flow velocity of liquid steel in the diversion hole, and can lead to slag entrapment. Thus, a high casting speed is disadvantageous for removal of inclusions.

Figure 12 shows the volume flow distribution and ratio of argon in the tundish and mold under different casting speeds. More argon bubbles were brought into the tundish nozzle with increased casting speed. The ratio of volume flow of argon between the tundish and mold decreases. When the casting speed is controlled to $1.05 \text{ m}\cdot\text{min}^{-1}$, the argon volume fraction in the mold is minimized accounting for 15.9% of the total volume of blowing argon. This is 38.6% when the casting speed is controlled to $1.5 \text{ m}\cdot\text{min}^{-1}$. The lower casting speed can promote the removal of nonmetallic inclusions in the tundish for a high floating effect around the stopper. This increases the residence time of the liquid steel. The high casting speed can catch more bubbles into the nozzle, which is beneficial to prevent the nozzle from clogging. It is important to regulate the floating bubbles around the stopper and the argon volume entering the nozzle.

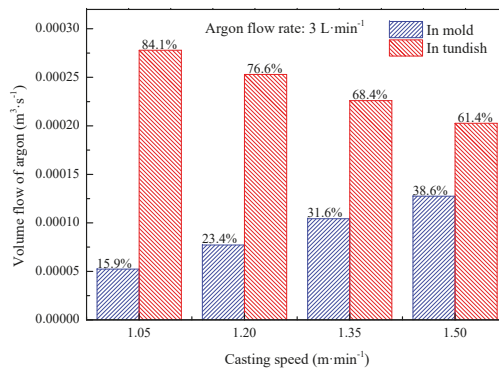


Figure 12. Volume flow distribution of argon under different casting speeds.

5. Conclusions

(1) There was some swirl flow of liquid steel around the stopper when the annular argon blowing at the upper nozzle was adopted. The liquid surface flow of liquid steel around the stopper is active, and the average residence time of liquid steel in the tundish slightly increases.

(2) With increased argon flow, the vortex range and intensity around the stopper gradually increase, and the vertical flow velocity of the liquid steel in the vicinity of the stopper increases. The argon volume flows in the tundish and the mold both increase.

(3) With increased casting speed, the vortex range and intensity around the stopper gradually decrease. The peak value of the vertical flow velocity of liquid steel at the vicinity of the stopper decreases, and the distribution and ratio of argon volume flow between the tundish and the mold decrease.

Author Contributions: X.Q. and C.C. conceived and designed the study; X.Q. and Y.L. conducted the experiment; X.Q. analyzed the experimental data and wrote the manuscript with the advice of C.C., C.Z., J.Z., and Y.J.

Funding: This research was funded by the National Nature Science Foundation of China (No. 51874215 and No. 51504172).

Acknowledgments: The authors would like to acknowledge the financial support from National Science Foundation of China (Grant No. 51874215 and No. 51504172).

Conflicts of Interest: The authors declare no conflicts of interest.

References

1. Moumtez, B.; Bellaouar, A.; Talbi, K. Numerical investigation of the fluid flow in continuous casting tundish using analysis of RTD curves. *J. Iron Steel Res. Int.* **2009**, *16*, 22–29.
2. Ding, N.; Bao, Y.P.; Sun, Q.S. Optimization of flow control devices in a single-strand slab continuous casting tundish. *Int. J. Miner. Metall. Mater.* **2011**, *18*, 292–296. [[CrossRef](#)]
3. Jin, Y.; Dong, X.S.; Yang, F. Removal mechanism of microscale non-metallic inclusions in a tundish with multi-hole-double-baffles. *Metals* **2018**, *8*, 611. [[CrossRef](#)]
4. Tripathi, A. Numerical investigation of electro-magnetic flow control phenomenon in a tundish. *ISIJ Int.* **2012**, *52*, 447–456. [[CrossRef](#)]
5. Chang, S.; Cao, X.; Zou, Z. Micro-bubble formation under non-wetting conditions in a full-scale water model of a ladle shroud Tundish system. *ISIJ Int.* **2018**, *58*, 60–67. [[CrossRef](#)]
6. Chatterjee, S.; Li, D.; Chattopadhyay, K. Modeling of liquid steel/slag/argon gas multiphase flow during Tundish open eye formation in a two-strand Tundish. *Metall. Trans. B* **2018**, *49*, 756–766. [[CrossRef](#)]
7. Chattopadhyay, K.; Hasan, M.; Isac, M. Physical and mathematical modeling of inert gas-shrouded ladle nozzles and their role on slag behavior and fluid flow patterns in a delta-shaped, four-strand tundish. *Metall. Trans. B* **2010**, *41*, 225–233. [[CrossRef](#)]
8. Cwudziński, A. Numerical and physical modeling of liquid steel flow structure for one strand tundish with modern system of argon injection. *Steel Res. Int.* **2017**, *88*, 1–14. [[CrossRef](#)]
9. Cwudziński, A. Numerical and physical modeling of liquid steel behaviour in one strand tundish with gas permeable barrier. *Arch. Metall. Mater* **2018**, *63*, 589–596.
10. Jin, Y.L.; Shen, C.; Zhang, J.P. Study on process technology of gas bubbling curtain substituting dam in the tundish of slab casting. *J. Iron Steel Res. Int.* **2011**, *18*, 256–262.
11. Chen, D.; Xie, X.; Long, M. Hydraulics and mathematics simulation on the weir and gas curtain in tundish of ultrathick slab continuous casting. *Metall. Trans. B* **2014**, *45*, 392–398. [[CrossRef](#)]
12. Vargas-Zamora, A.; Palafox-Ramos, J.; Morales, R.D. Inertial and buoyancy driven water flows under gas bubbling and thermal stratification conditions in a tundish model. *Metall. Trans. B* **2004**, *35*, 247–257. [[CrossRef](#)]
13. Zhong, L.; Li, L.; Wang, B. Water modelling experiments of argon bubbling curtain in a slab continuous casting tundish. *Steel Res. Int.* **2006**, *77*, 103–106. [[CrossRef](#)]
14. Wang, J.; Zhu, M.Y.; Zhou, H.B. Fluid flow and interfacial phenomenon of slag and metal in continuous casting tundish with argon blowing. *J. Iron Steel Res. Int.* **2008**, *15*, 26–31. [[CrossRef](#)]
15. Terzija, N.; Yin, W.; Gerbeth, G. Electromagnetic inspection of a two-phase flow of GaInSn and argon. *Flow Meas. Instrum.* **2011**, *22*, 10–16. [[CrossRef](#)]
16. Bai, H.; Thomas, B.G. Turbulent flow of liquid steel and argon bubbles in slide-gate tundish nozzles: Part I. Model development and validation. *Metall. Trans. B* **2001**, *32*, 253–267. [[CrossRef](#)]
17. Bai, H.; Thomas, B.G. Turbulent flow of liquid steel and argon bubbles in slide-gate tundish nozzles: Part II. Effect of operation conditions and nozzle design. *Metall. Trans. B* **2001**, *32*, 269–284. [[CrossRef](#)]
18. Mohammadi-Ghaleni, M.; Zaeem, M.A.; Smith, J.D. Computational fluid dynamics study of molten steel flow patterns and particle–wall interactions inside a slide-gate nozzle by a hybrid turbulent model. *Metall. Trans. B* **2016**, *47*, 3056–3065. [[CrossRef](#)]
19. Li, Y.; Cheng, C.G.; Yang, M.L. Behavior characteristics of argon bubbles on inner surface of upper tundish nozzle during argon blowing process. *Metals* **2018**, *8*, 590. [[CrossRef](#)]
20. Smirnov, A.N.; Efimova, V.G.; Kravchenko, A.V. Design of a permeable annular refractory injection block for the tundish refining of steel. *Refract. Ind. Ceram.* **2014**, *55*, 173–178. [[CrossRef](#)]
21. Smirnov, A.N.; Efimova, V.G.; Kravchenko, A.V. Flotation of nonmetallic inclusions during argon injection into the tundish of a continuous-casting machine. Part 1. *Steel Transl.* **2013**, *43*, 673–677. [[CrossRef](#)]
22. Smirnov, A.N.; Efimova, V.G.; Kravchenko, A.V. Flotation of nonmetallic inclusions during argon injection into the tundish of a continuous-casting machine. Part 2. *Steel Transl.* **2014**, *44*, 11–16. [[CrossRef](#)]

23. Smirnov, A.N.; Efimova, V.G.; Kravchenko, A.V. Flotation of nonmetallic inclusions during argon injection into the tundish of a continuous-casting machine. Part 3. *Steel Transl.* **2014**, *44*, 180–185. [[CrossRef](#)]
24. Raghavendra, K.; Sarkar, S.; Ajmani, S.K.; Denys, M.B.; Singh, M.K. Mathematical modelling of single and multi-strand tundish for inclusion analysis. *Appl. Math. Modell.* **2013**, *37*, 6284–6300. [[CrossRef](#)]
25. Pfeiler, C.; Wu, M.; Ludwig, A. Influence of argon gas bubbles and non-metallic inclusions on the flow behavior in steel continuous casting. *Mater. Sci. Eng. A* **2005**, *413–414*, 115–120. [[CrossRef](#)]
26. Merder, T.; Warzecha, M. Optimization of a six-strand continuous casting tundish: Industrial measurements and numerical investigation of the tundish modifications. *Metall. Trans. B* **2012**, *43*, 856–868. [[CrossRef](#)]
27. Ramirez, O.S.D.; Torres-Alonso, E.; Banderas, J.Á.R. Thermal and fluid-dynamic optimization of a five strand asymmetric delta shaped billet caster tundish. *Steel Res. Int.* **2018**, *89*, 1700428. [[CrossRef](#)]
28. Zhang, H.; Luo, R.H.; Fang, Q. Numerical simulation of transient multiphase flow in a five-strand bloom tundish during ladle change. *Metals* **2018**, *8*, 146. [[CrossRef](#)]
29. Lei, H. New insight into combined model and revised model for RTD curves in a multi-strand tundish. *Metall. Trans. B* **2015**, *46*, 2408–2413. [[CrossRef](#)]
30. Tang, D.T.; Li, Y.L.; Tian, Z.H. Numerical and physical simulation of bottom blowing gas rate effect on liquid steel fluidity feature in tundish. *Shanghai Met.* **2012**, *34*, 49–52. (In Chinese)



© 2019 by the authors. Licensee MDPI, Basel, Switzerland. This article is an open access article distributed under the terms and conditions of the Creative Commons Attribution (CC BY) license (<http://creativecommons.org/licenses/by/4.0/>).

Article

Numerical Simulation of Electromagnetic Field in Round Bloom Continuous Casting with Final Electromagnetic Stirring

Bingzhi Ren ^{1,2}, Dengfu Chen ^{2,*}, Wentang Xia ¹, Hongdan Wang ^{1,*} and Zhiwei Han ³

¹ School of Metallurgical and Materials Engineering, Chongqing University of Science & Technology, Chongqing 401331, China; renbingzhi@cqust.edu.cn (B.R.); wentangx@163.com (W.X.)

² College of Materials Science and Engineering, Chongqing University, Chongqing 400044, China

³ Department of Continuous Casting, CISDI Engineering Co. Ltd., Chongqing 400013, China; zhiwei.han@cisdi.com.cn

* Correspondence: chendfu@cqu.edu.cn (D.C.); wanghongdan@cqust.edu.cn (H.W.);
Tel.: +86-023-6510-2467 (D.C.); +86-023-6502-3706 (H.W.)

Received: 25 September 2018; Accepted: 1 November 2018; Published: 5 November 2018

Abstract: A 3D mathematical model was developed to simulate the electromagnetic field in $\Phi 600$ mm round bloom continuous casting with final electromagnetic stirring (F-EMS), and the model was verified using measured data for the magnetic flux density in the stirrer centre. The distribution of electromagnetic force and the influence of current intensity and frequency were investigated. The results show that the Joule heat generated by F-EMS is very small and its influence on secondary cooling heat transfer in the stirring zone can be ignored. With an increase in current frequency, the electromagnetic force density at R/2 and R/3 of the $\Phi 600$ mm round bloom first increases and then decreases, reaching a maximum at 10 Hz.

Keywords: numerical simulation; round bloom; continuous casting; final electromagnetic stirring; electromagnetic field

1. Introduction

Continuous casting is a process generally used in steel production to make the molten steel solidified into a semi-finished billet, bloom, or slab for subsequent rolling in the finishing mills. Electromagnetic stirring (EMS) technology is widely used in the continuous casting production of steel. This technology utilises electromagnetic induction to provide a non-contact electromagnetic force to enhance the molten steel flow, heat transfer, and mass transfer and to promote columnar to equiaxed transition, thereby rectifying internal defects such as central segregation and shrinkage cavities [1]. According to different installation positions, three types of EMS exist in continuous casting steel. One is situated at the caster mould, referred to as mould electromagnetic stirring (M-EMS); another is situated along the strand in the secondary cooling zone, called a strand electromagnetic stirring (S-EMS); the last one is situated near the solidification end of the strand, known as final electromagnetic stirring (F-EMS) [2]. M-EMS is used in almost all billet/bloom casters. However, for high-carbon steel or large-section strands, the use of M-EMS cannot completely improve the internal quality of the strand, and F-EMS is generally required [3], which can more effectively improve the central porosity and V-shaped segregation of the strand [4,5]. Therefore, detailed analysis of the electromagnetic field, fluid flow, and solidification behaviour of the strand is very important for evaluating the impact of F-EMS on various metallurgical operations in the continuous casting process, and the electromagnetic field is the primary problem.

In 1986, Spitzer et al. deduced the analytical formula for the 2D electromagnetic force in an infinitely long stirring system [6]. Recently, Vynnycky [7] derived another form of analytical solution

for the same issue with Ref. [6] when the tangential magnetic flux density was employed as the boundary condition. Trindade et al. [8], Yu et al. [9], and Liu et al. [10] studied the electromagnetic field of M-EMS, highlighting the obvious shielding effect of mould copper on the electromagnetic field, while that of F-EMS is different. Jiang et al. [11] and Sun et al. [3] focused mainly on fluid flow, solidification, and mass transfer of the continuous casting strand with F-EMS and rarely discussed the electromagnetic field. Therefore, this study aims to investigate the electromagnetic field in $\Phi 600$ mm round bloom continuous casting with F-EMS by numerical simulation, as well as examining the distribution features of the electromagnetic force and the influence of current intensity and frequency.

2. Mathematical Model

The continuous caster studied in this paper is produced by a domestic steel mill (Sunan Heavy Industry, Suzhou, China). Figure 1 is a structural diagram of the continuously cast round bloom with F-EMS. The origin of the coordinate is at the centre of the stirrer. The round bloom has a diameter of 600 mm and the stirrer core has a height of 300 mm.

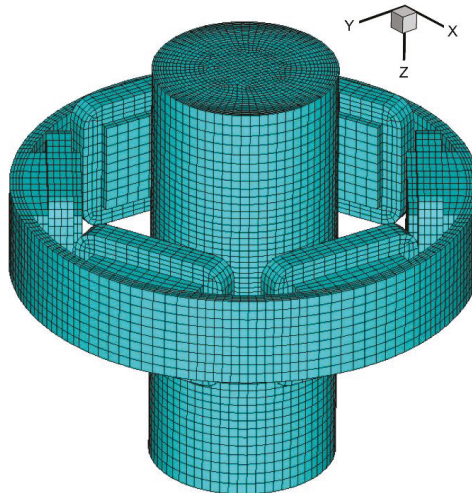


Figure 1. Schematic illustration of final electromagnetic stirring (F-EMS) for round bloom continuous casting. The air cylinder is not shown.

2.1. Basic Assumption

The fluid flow in a continuous casting round bloom with F-EMS can be described by Maxwell's equations and the Navier–Stokes equations, which are coupled by the electromagnetic force density and the flow velocity of the molten steel. In view of the complexity of the F-EMS process, several assumptions must be made in order to simplify the calculations.

1. In the F-EMS process, the magnetic Reynolds number (about 0.1) is far less than the shielding parameter (about 10) [10,12] and the angular frequency of the current intensity is much larger than the angular velocity of the molten steel; thus, the influence of the molten steel flow on the electromagnetic field is negligible [13]. Therefore, this problem can be decomposed into an electromagnetic problem and a fluid flow problem to be solved separately. In the present paper, only the electromagnetic field was calculated without regard to the flow field and solidification.
2. Since the current frequency of F-EMS is generally in the range of 4 Hz to 10 Hz, which belongs to the magnetic quasi-static field, the displacement current is ignored [8].

3. Both the outer shell and the cooling water jacket of the stirrer are approximated as an air zone for the benefit of the calculations.
4. The curve of the strand is negligible.

2.2. Control Equations

At low current frequencies, the time-varying electromagnetic field is assumed to be a magnetic quasi-static field, and Maxwell's equations can be simplified as follows [8]:

$$\nabla \cdot \mathbf{B} = 0 \quad (1)$$

$$\nabla \times \mathbf{B} = \mu_r \mu_0 \mathbf{J} \quad (2)$$

$$\nabla \times \mathbf{E} = -\frac{\partial \mathbf{B}}{\partial t} \quad (3)$$

$$\mathbf{J} = \sigma \mathbf{E} \quad (4)$$

where \mathbf{B} is the magnetic flux density, \mathbf{J} is the induced current density in the strand, μ_0 is the vacuum permeability, μ_r is the relative permeability, \mathbf{E} is the electric field intensity, σ is the electrical conductivity, and t is the time.

The electromagnetic force density at each element is calculated by harmonic analysis using Equation (5) [8]:

$$\mathbf{F}_{\text{time}} = \mathbf{J} \times \mathbf{B} \quad (5)$$

The expression for the Joule heat power density generated by the induced current is calculated from Equation (6) [14]:

$$P_{\text{time}} = |\mathbf{J}|^2 / \sigma \quad (6)$$

The time in Equations (5) and (6) refers to the real and imaginary parts of the variable at 0° and 90° , respectively.

Since F-EMS uses a sinusoidal current to generate a harmonic electromagnetic field, the magnetic flux density, electromagnetic force density and Joule heat power density change with time. However, at low current frequencies, both the shielding parameter and the interaction parameter are small, and it is feasible to use the time-averaged electromagnetic force density and Joule heat power density [15]. Hence, the time-averaged values of the two variables are calculated from Equations (7) and (8) in the post-processing to investigate the distribution characteristics [8]:

$$\mathbf{F}_{\text{em}} = (\mathbf{F}_0 + \mathbf{F}_{90}) / 2 \quad (7)$$

$$P_{\text{ave}} = (P_0 + P_{90}) / 2 \quad (8)$$

Because the time-averaged value of the magnetic flux density is 0, the time-averaged value of its modulus is transiently calculated by using Equation (9):

$$B_{\text{mag}} = f \int_{t_0}^{t_0+1/f} |\mathbf{B}| dt \quad (9)$$

where f is the current frequency.

2.3. Boundary Conditions

An air cylinder with a radius of 0.9 m and a height of 2.2 m was established around the whole stirring system to calculate the electromagnetic field. The tangential magnetic condition ($\partial\Phi/\partial n = 0$) was applied at the outer surface of the air cylinder, where Φ is the reduced scalar potential and n is

the normal unit vector to the surface [8,10]. The three-phase coil excitation was applied with source current intensity (I) and frequency.

2.4. Physical Properties

Before the $\Phi 600$ mm round bloom is completely solidified, its temperature is above 1173 K [16], which is greater than the Curie point of the steel (about 1023 K) [17]. Therefore, the strand is a paramagnetic material. In the calculation, it is considered that both the strand and the iron core of the stirrer are isotropic materials and that their relative permeability is constant. The relevant physical properties are as follows: the vacuum permeability is $1.257 \times 10^{-6} \text{ H}\cdot\text{m}^{-1}$, the relative permeability of the strand and air is 1.0, the relative permeability of the iron core is 1000, and the electrical conductivity of the strand is $7.14 \times 10^5 \text{ S}\cdot\text{m}^{-1}$.

2.5. Solution

When calculating the electromagnetic field, the length of the strand is 1.8 m. ANSYS Emag software (ANSYS 14.0, ANSYS Inc., Canonsburg, PA, USA) was used to solve Maxwell's equations by the finite element method (FEM). We employed three different meshes to verify the independence of the grid, which included 220,000, 270,000, and 350,000 elements, respectively. The comparison between simulation results and experimental data indicated that the errors of the three meshes are 7.2%, 4.6%, and 4.0%, respectively. Hence, a mesh of 270,000 elements was selected to obtain the mesh-independent results. The distribution of the electromagnetic field in the strand was obtained and the time-averaged electromagnetic force density was extracted. Except for the transient analysis of B_{mag} , other variables were calculated using harmonic analysis.

3. Results and Discussion

In order to validate the mathematical model of the electromagnetic field, the magnetic flux density in the stirrer was measured along the axial direction without the strand and compared with the numerical simulation results, as shown in Figure 2. The measurement of the magnetic flux density was carried out in a $\Phi 600$ mm round bloom continuous caster at a domestic steel mill by using a portable Gauss meter (Bell, FW5180). The calculated values agree well with the measured data, which supports the correctness of the mathematical model and the solution method for the electromagnetic field. Figure 2 also demonstrates that the magnetic flux density in the stirrer with the strand is significantly lower than that without the strand, and the maximum value decreases from 55.4 mT calculated without the strand to 51.1 mT with the strand. This is mainly due to the 'skin effect': the strand can shield the electromagnetic field, resulting in a decrease in magnetic flux density.

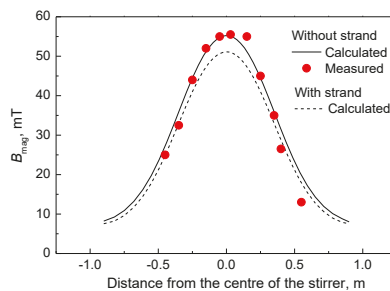


Figure 2. Profile of the magnetic flux density along the axial direction for $I = 350 \text{ A}$ and $f = 4 \text{ Hz}$.

Figure 3 shows the distribution of the magnetic flux density in both the cross-section and the longitudinal section of the $\Phi 600$ mm round bloom at 400 A and 4 Hz. The magnetic flux density in the cross-section is roughly circularly symmetrical, and it is greatest at the edge and gradually attenuates

towards the centre, as shown in Figure 3a. In the longitudinal section, the maximum value of the magnetic flux density appears in the middle of the stirrer and gradually weakens towards both ends, as shown in Figure 3b.

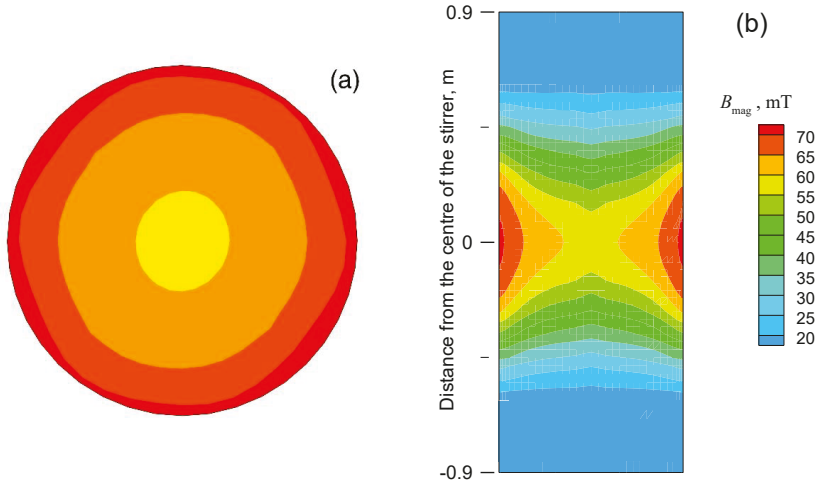


Figure 3. Contour plot of the magnetic flux density in the (a) cross-section and (b) longitudinal section for $I = 400$ A and $f = 4$ Hz.

Figure 4 displays the distribution of the time-averaged Joule heat power density in both the cross-section and the longitudinal section of the $\Phi 600$ mm round bloom at 400 A and 4 Hz. The characteristic of the Joule heat power density distribution is very similar to that of the magnetic flux density. It can also be seen from Figure 4a that the distribution of Joule heat power density has a hexagonal symmetry at the edge of the strand. This is because the iron core of the stirrer has six protruding tooth parts (see Figure 1), and the Joule heat power density at the edge of the strand near to them is large. Through the integral calculation, it is found that the Joule heat generated by F-EMS in the strand is 5.3 kW, and the quantity of the secondary cooling heat transfer (P) in this region is about 201 kW, which can be approximately calculated using Equation (10) [18]. Therefore, the Joule heat is small and negligible compared with the secondary cooling heat transfer in the stirring zone.

$$P = \varepsilon \delta (T_s^4 - T_0^4) CH / 1000 \quad (10)$$

where ε is the emissivity of the steel (0.85 in the present study), δ is the Stefan–Boltzmann constant ($5.67 \times 10^{-8} \text{ W} \cdot \text{m}^{-2} \cdot \text{K}^{-4}$), T_s is the surface temperature of the round bloom (about 1223 K), T_0 is the environmental temperature (about 373 K), C is the circumference of the round bloom, and H is the height of the stirring zone, which is 1 m.

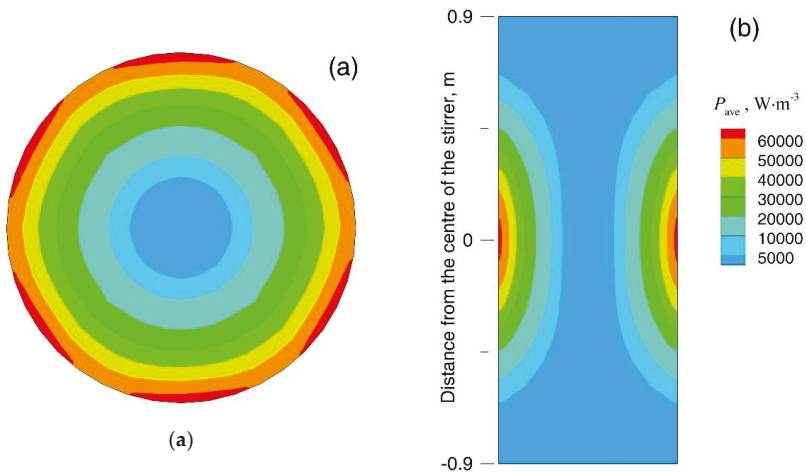


Figure 4. Contour plot of the time-averaged Joule heat power density in the (a) cross-section and (b) longitudinal section for $I = 400$ A and $f = 4$ Hz.

Figure 5a demonstrates the vector distribution of the time-averaged electromagnetic force density in the cross-section of the $\Phi 600$ mm round bloom. The electromagnetic force density is generally distributed circumferentially, thereby causing the rotation of the molten steel. It is greatest at the edge and decreases significantly towards the centre. Figure 5b shows the contour plot of the electromagnetic force density in the longitudinal section, which has a distribution similar to the magnetic flux density as well.

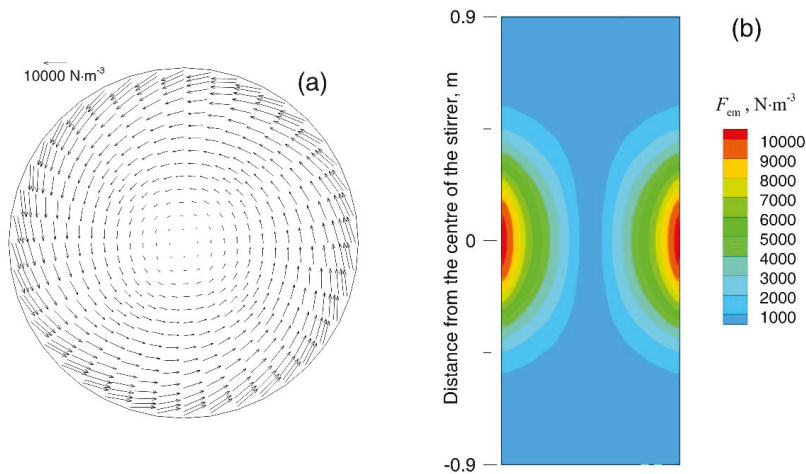


Figure 5. Distribution of the time-averaged electromagnetic force density in the (a) cross-section and (b) longitudinal section for $I = 400$ A and $f = 4$ Hz.

Figure 6 compares the electromagnetic force density calculated by FEM with that obtained from the analytical formula of the infinite-length stirring system deduced by Spitzer et al. [6]. Among the three components of the electromagnetic force density, the tangential electromagnetic force density is the largest, which is also the driving force of molten steel rotation. The tangential electromagnetic force density calculated by FEM is greater than that calculated by the analytical formula, especially at

the edge of the strand. However, in the effective area of F-EMS on the strand ($r < R/2$), the difference between the two results is not large. In addition, the difference between the radial electromagnetic force densities calculated by FEM and by the analytical formula is also not large. Finally, the axial electromagnetic force density calculated by FEM is close to zero and negligible. In short, since the electromagnetic force generated by F-EMS usually acts in a region smaller than $R/2$ in a round bloom, it can be approximately calculated by the above analytical formula for the $\Phi 600$ mm round bloom.

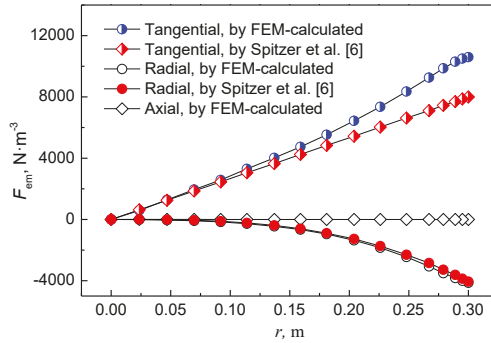


Figure 6. Comparison of FEM-calculated electromagnetic force density with that of the analytical solution by Spitzer et al. [6] in the middle plane of the stirrer for $I = 400$ A and $f = 4$ Hz.

Figure 7 illustrates the variation in the electromagnetic force density in the radial direction at different current frequencies. It can be observed that when the frequency is small, the electromagnetic force density has an approximately linear relationship with the radius, which is consistent with the analytical formula [6]. However, when the frequency is greater than 8 Hz, the electromagnetic force density is no longer linear with the radius due to the ‘skin effect’.

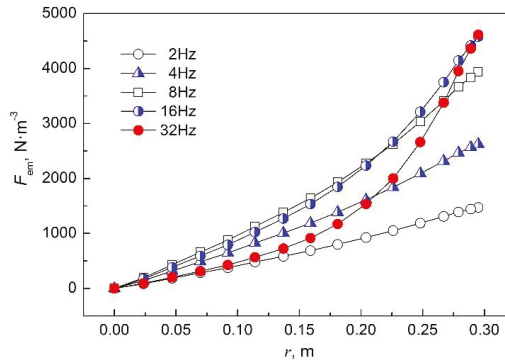


Figure 7. Electromagnetic force density profile as a function of radial distance at the middle plane of the stirrer for various current frequencies and $I = 200$ A.

Figure 8 shows the effect of the current frequency on the magnetic flux density and induced current density. It is found that different variations appear at different positions of the $\Phi 600$ mm round bloom. At the edge of the strand ($r = R$), the frequency has little effect on the magnetic flux density, while the induced current density increases significantly with increasing frequency. At $r = R/2$ of the strand, an increase in frequency leads to a decrease in magnetic flux density, and the induced current density first increases and then decreases, and the maximum value appears at 14 Hz. Since the electromagnetic force density is the cross-product of the magnetic flux density and the induced current

density, it can be inferred from Figure 8 that there is a peak in the electromagnetic force density as a function of the current frequency.

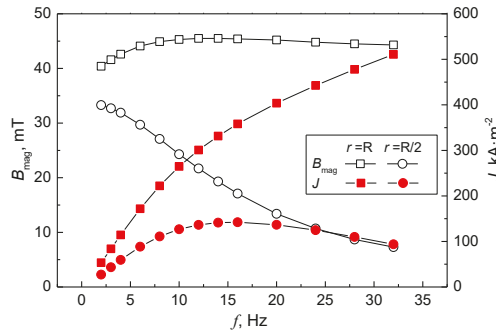


Figure 8. Effect of current frequency on the magnetic flux density and the induced current density at the middle plane of the stirrer for $I = 200$ A.

Figure 9 reveals the relationship between the electromagnetic force density and the current frequency at different radii of the $\Phi 600$ mm round bloom. At the same current intensity, the electromagnetic force density at the edge of the strand ($r = R$) gradually increases with increasing frequency and remains basically constant until the frequency is greater than 16 Hz. However, the electromagnetic force density at $r = R/2$ and $R/3$ of the strand reaches a maximum at a frequency of 10 Hz and then gradually decreases. Since the radius of the melt core is generally less than $R/2$ at the position where the strand is installed with F-EMS, the F-EMS of the $\Phi 600$ mm round bloom has the highest stirring efficiency at a frequency of 10 Hz.

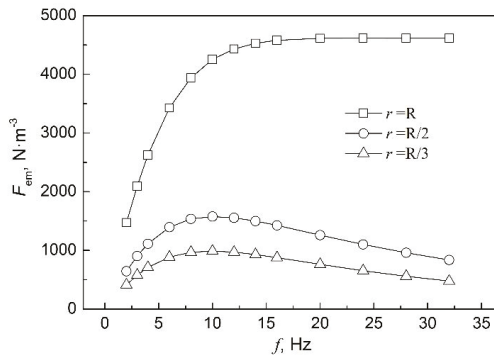


Figure 9. Effect of current frequency on the electromagnetic force density at different radii for $I = 200$ A.

Figure 10 shows the effect of current intensity on the magnetic flux density and the electromagnetic force density. The former increases linearly with an increase in current intensity, while the latter has a quadratic relationship with the current intensity, which is consistent with the analytical formula deduced by Spitzer et al. [6].

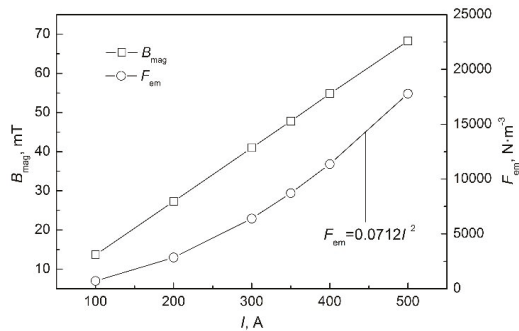


Figure 10. Effect of current intensity on the magnetic flux density and the electromagnetic force density at the middle plane of the stirrer for $f = 4$ Hz.

4. Conclusions

The three-dimensional electromagnetic field in a continuous casting round bloom with F-EMS was studied numerically, and the influence of current intensity and frequency on the electromagnetic field was discussed. The following conclusions were obtained:

1. The Joule heat generated by F-EMS in a continuous casting strand is very small, and its influence on the secondary cooling heat transfer in the stirring zone can be ignored.
2. Since the electromagnetic force generated by F-EMS usually provides stirring action in a region less than $R/2$ of a round bloom, it is feasible to calculate it approximately using the analytical formula for the infinite-length stirring system.
3. With increase in current frequency, the electromagnetic force density at $R/2$ and $R/3$ of the strand first increases and then decreases, and it reaches a maximum at 10 Hz. The results of the calculations show that the optimal current frequency of F-EMS is 10 Hz in continuous casting of a $\Phi 600$ mm round bloom.
4. The magnetic flux density increases linearly with current intensity, while the electromagnetic force density has a quadratic relationship with current intensity.

Author Contributions: B.R., W.X., and Z.H. validated the model. B.R. performed the calculation. B.R., D.C., and H.W. analyzed and discussed the data. B.R. wrote the paper. D.C. and H.W. reviewed and edited the paper. B.R., W.X., and H.W. acquired the funding.

Funding: This research was funded by the National Natural Science Foundation of China, grant number 51674057; the Chongqing Research Program of Basic Research and Frontier Technology, grant numbers cstc2016jcyjA0142 and cstc2017jcyjAX0236; the Scientific and Technological Research Program of Chongqing Municipal Education Commission, grant numbers KJ1601326 and KJ1713343; and the Research Foundation of Chongqing University of Science & Technology, grant number CK2016B19.

Conflicts of Interest: The authors declare no conflict of interest.

References

1. Barna, M.; Javurek, M.; Reiter, J.; Watzinger, J.; Kaufmann, B.; Kirschen, M. Continuous casting of round bloom strands with mould-electromagnetic stirring numerical simulations with a full coupling method. *World Iron Steel* **2012**, *12*, 29–33.
2. Hanley, P.J.; Kollberg, S.G. Electromagnetic methods for continuous casting. In *The Making, Shaping and Treating of Steel*, 11th ed.; Cramb, A.W., Ed.; Association for Iron & Steel Technology: Pittsburgh, PA, USA, 2003; pp. 287–297, ISBN 978-0-930767-04-4.
3. Sun, H.; Li, L.; Cheng, X.; Qiu, W.; Liu, Z.; Zeng, L. Reduction in macrosegregation on 380 mm \times 490 mm bloom caster equipped combination M+F-EMS by optimising casting speed. *Ironmak. Steelmak.* **2015**, *42*, 439–449. [[CrossRef](#)]

4. Mizukami, H.; Komatsu, M.; Kitagawa, T.; Kawakami, K. Effect of electromagnetic stirring at the final stage of solidification of continuously cast strand. *Tetsu-to-Hagane* **1984**, *70*, 194–200. [[CrossRef](#)]
5. Xiao, C.; Zhang, J.; Luo, Y.; Wei, X.; Wu, L.; Wang, S. Control of macrosegregation behavior by applying final electromagnetic stirring for continuously cast high carbon steel billet. *J. Iron Steel Res. Int.* **2013**, *20*, 13–20. [[CrossRef](#)]
6. Spitzer, K.H.; Dubke, M.; Schwerdtfeger, K. Rotational electromagnetic stirring in continuous casting of round strands. *Metall. Trans. B* **1986**, *17*, 119–131. [[CrossRef](#)]
7. Vynnycky, M. On an anomaly in the modeling of electromagnetic stirring in continuous casting. *Metall. Mater. Trans. B* **2018**, *49*, 399–410. [[CrossRef](#)]
8. Trindade, L.B.; Vilela, A.C.F.; Filho, Á.F.F.; Vilhena, M.T.M.B.; Soares, R.B. Numerical model of electromagnetic stirring for continuous casting billets. *IEEE Trans. Magn.* **2002**, *38*, 3658–3660. [[CrossRef](#)]
9. Yu, H.Q.; Zhu, M.Y. Influence of electromagnetic stirring on transport phenomena in round billet continuous casting mould and macrostructure of high carbon steel billet. *Ironmak. Steelmak.* **2012**, *39*, 574–584. [[CrossRef](#)]
10. Liu, H.; Xu, M.; Qiu, S.; Zhang, H. Numerical simulation of fluid flow in a round bloom mold with in-mold rotary electromagnetic stirring. *Metall. Mater. Trans. B* **2012**, *43*, 1657–1675. [[CrossRef](#)]
11. Jiang, D.; Zhu, M. Center segregation with final electromagnetic stirring in billet continuous casting process. *Metall. Mater. Trans. B* **2017**, *48*, 444–455. [[CrossRef](#)]
12. Marioni, L. *Computational Modelling and Electromagnetic-CFD Coupling Incasting Processes*; PSL Research University: Paris, France, 17 November 2017.
13. Davidson, P.A.; Hunt, J.C.R. Swirling recirculating flow in a liquid-metal column generated by a rotating magnetic field. *J. Fluid Mech.* **1987**, *185*, 67–106. [[CrossRef](#)]
14. Ren, B.Z.; Chen, D.F.; Wang, H.D.; Long, M.J.; Han, Z.W. Numerical simulation of fluid flow and solidification in bloom continuous casting mould with electromagnetic stirring. *Ironmak. Steelmak.* **2015**, *42*, 401–408. [[CrossRef](#)]
15. Barna, M.; Javurek, M.; Reiter, J.; Lechner, M. Numerical simulations of mould electromagnetic stirring for round bloom strands. *Berg Huettenmaenn. Monatsh.* **2009**, *154*, 518–522. [[CrossRef](#)]
16. Mao, B.; Ren, B.; Han, Z.; Cao, J.; Feng, K. Numerical simulation for heat transfer during solidification of round bloom continuous casting. *Ind. Heat.* **2012**, *41*, 50–53. [[CrossRef](#)]
17. Guo, G.; Ma, H.; Zhang, J.; Huang, L. The relationship of thermophysical properties to microstructure of high-carbon steel. *Phys. Test. Chem. Anal.* **2006**, *42*, 167–170.
18. Long, M.; Dong, Z.; Sheng, J.; Chen, D.; Chen, C. Universal secondary cooling structure for round blooms continuous casting of steels in various diameters. *Steel Res. Int.* **2015**, *86*, 154–162. [[CrossRef](#)]



© 2018 by the authors. Licensee MDPI, Basel, Switzerland. This article is an open access article distributed under the terms and conditions of the Creative Commons Attribution (CC BY) license (<http://creativecommons.org/licenses/by/4.0/>).

Article

Mold-Level Prediction for Continuous Casting Using VMD–SVR

Wenbin Su ¹, Zhufeng Lei ^{1,*}, Ladao Yang ² and Qiao Hu ¹

¹ School of Mechanical Engineering, Xi'an Jiaotong University, 28 West Xianning Road, Xi'an 710049, China; wbsu@mail.xjtu.edu.cn (W.S.); hqxjtu@xjtu.edu.cn (Q.H.)

² China National Heavy Machinery Research Institute Co., Ltd., 109 Dongyuan Road, Xi'an 710016, China; yld552008@163.com

* Correspondence: leizhufeng@stu.xjtu.edu.cn; Tel.: +86-177-4249-9272

Received: 5 March 2019; Accepted: 17 April 2019; Published: 18 April 2019

Abstract: In the continuous-casting process, mold-level control is one of the most important factors that ensures the quality of high-efficiency continuous casting slabs. In traditional mold-level prediction control, the mold-level prediction accuracy is low, and the calculation cost is high. In order to improve the prediction accuracy for mold-level prediction, an adaptive hybrid prediction algorithm is proposed. This new algorithm is the combination of empirical mode decomposition (EMD), variational mode decomposition (VMD), and support vector regression (SVR), and it effectively overcomes the impact of noise on the original signal. Firstly, the intrinsic mode functions (IMFs) of the mold-level signal are obtained by the adaptive EMD, and the key parameter of the VMD is obtained by the correlation analysis between the IMFs. VMD is performed based on the key parameter to obtain several IMFs, and the noise IMFs are denoised by wavelet threshold denoising (WTD). Then, SVR is used to predict each denoised component to obtain the predicted IMF. Finally, the predicted mold-level signal is reconstructed by the predicted IMFs. In addition, compared with WTD–SVR and EMD–SVR, VMD–SVR has a competitive advantage against the above three methods in terms of robustness. This new method provides a new idea for mold-level prediction.

Keywords: variational mode decomposition; empirical mode decomposition; support vector regression; mold level; continuous casting

1. Introduction

In the modern steel industry, high-efficiency continuous casting technology has become the most internationally competitive key technology [1]. The continuous casting process is a complex and continuous phase change process. Many factors affect the quality of slabs. The research into the key technology in the high-quality steel continuous-casting process is mainly focused on mold-level precision, as well as the segment and secondary cooling dynamic control [2].

At present, mold-level control is mainly based on the principle of predictive control, which combines prediction and control to improve the timeliness of prediction, but affects its accuracy. In view of the large mold-level disturbance, Guo et al. [3] used the prediction method in mold-level control. Aiming at the nonlinear characteristics of mold-level data, Tong et al. [4] carried out a constrained generalized prediction method based on the genetic algorithm. Aiming at the strong mold-level coupling characteristics, Qiao et al. [5] proposed an auto-disturbance suppression algorithm based on neural network tuning. However, these prediction methods have not effectively overcome the effects of mold-level noise.

Precise mold level monitoring is regarded as the key to improving continuous casting production quality, as shown in Figure 1 [2–4]. It is an important source of reference data for casting speed control, segment roll gap control, mold-cooling water control, and stopper rod opening control. If the mold

level fluctuates too much, the following will occur. First, it will cause impurities on the surface of the mold. Surface defects and internal defects of the slab are generated which affect the surface and internal quality of the slab. Second, it will affect the casting speed, affecting productivity and the production rhythm. Eventually, it will cause the slab and the continuous casting machine to stick together, damage the tundish slide, and even cause downtime. Accurate prediction of the mold level occupies an important position in the continuous casting production process. This paper proposes an advanced mold level signal denoising method to prepare accurate data input for future mold level prediction, realize the purpose of predictive control, and greatly reduce the occurrence of accidents affecting quality and safety in the continuous casting production process.

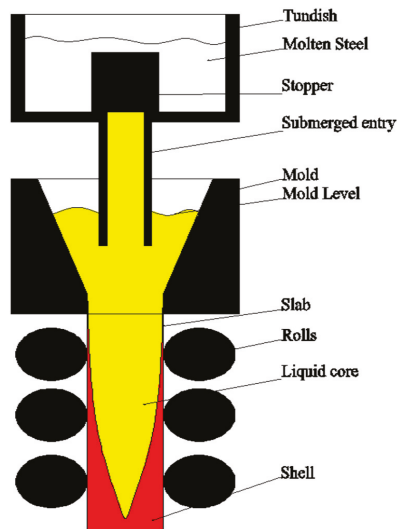


Figure 1. Mold-level model.

A data-driven method for mold-level prediction is proposed in this paper, which provides a new idea for mold-level control. The method takes variational mode decomposition (VMD) and support vector regression (SVR) as its core ideas, and creates mold-level predictions driven by data to overcome the influence of white noise caused by the casting speed and strong mold-level coupling.

Recent studies have shown that although there are many methods in the field of signal processing, none of them is applicable to all signal data. Wavelet transform (WT)-based signal processing methods are widely used, but wavelet denoising methods are limited by the selection of the wavelet basis function and affect the generalization ability of the wavelet. Although the method based on empirical mode decomposition (EMD) is widely used for the adaptability of its decomposition [6], the EMD method has serious pattern aliasing and boundary effects which seriously affect the signal decomposition. Especially in the process of signal noise processing, high-frequency components are often removed directly, resulting in loss of effective information. Signal processing techniques based on the VMD method have been widely used in recent years [7]. Compared with the EMD method, VMD effectively avoids mode aliasing and boundary effects and can realize the frequency domain splitting of signals and effective separation of components, which results in better noise and sample rate robustness.

For the prediction of time series, various prediction methods have appeared in the past several decades. Traditional time-series prediction methods, such as regression analysis and grey prediction [8], have some shortcomings, and the prediction accuracy of signals with large fluctuations needs to be improved [9]. The numerical weather prediction model for predicting future wind speed using mathematical models [10], multiple regression, exponential smoothing, the autoregressive moving

average model (ARMA), and many others are used for wind-speed prediction, power prediction, stock-trend prediction, etc. Traditional time-series prediction methods have low precision and poor robustness to nonlinear disturbances. Mold level is non-linear and non-stationary in terms of the time scale and does not satisfy Gaussian normal distribution. Traditional time-series prediction methods are not suitable for mold-level prediction.

In recent years, with the rapid development of science and technology, artificial intelligence technology has been widely used and introduced into the prediction of time series, and good prediction results have been achieved [11]. Artificial neural networks (ANN) [12] and SVR [13] methods are the main tools for dealing with non-linear, non-stationary time series. SVR is a small-sample machine-learning method based on statistical learning theory, Vapnik–Chervonenkis (VC) dimension theory, and the minimum structural risk principle. Based on limited sample information, it seeks the best compromise between model complexity and learning ability to achieve the best promotion effect [14,15]. Liu and Gao [16] established a method for the online prediction of the silicon content in blast-furnace ironmaking processes. Compared with other soft sensors, the superiority of the proposed method is demonstrated in terms of the online prediction of the silicon content in an industrial blast furnace in China. Existing studies have shown that the ANN method takes a long time to calculate and is prone to localized minimization [17–20], leading to overfitting and poor prediction results. SVR is more robust to overfitting than ANN. The parameters of SVR can be improved by means of global optimization. It can be used to improve the prediction performance of SVR.

This paper focuses on the use of a hybrid algorithm for a time-series prediction model, and it is used for mold-level prediction. After comparing and discussing the hybrid algorithm for mold-level prediction, a new idea for continuous-casting process improvement is proposed. Firstly, the model uses EMD to decompose the original mold-level signal into several intrinsic mode functions (IMFs), and the key parameter of the VMD is obtained by the correlation analysis between the IMFs. VMD is performed based on the key parameter to obtain several IMFs, and the noise IMFs are denoised by wavelet threshold denoising (WTD). Then, SVR is used to predict each denoised component to obtain the predicted IMF. Finally, the predicted IMF reconstructs the predicted mold-level signal. The rest of this paper is organized as follows. The VMD algorithm is introduced in Section 2. VMD–SVR algorithms are introduced in Section 3. The performance of the three algorithms is compared through experiments in Section 4. Section 5 concludes this paper and makes recommendations.

2. Basic Algorithm Research

2.1. Variational Mode Decomposition

VMD is a new type of signal decomposition method. This method redefines an amplitude modulation-frequency modulation signal as an IMF, whose expression is

$$u_k(t) = A_k(t) \cos(\phi_k(t)) \quad (1)$$

where $\phi_k(t) \geq 0$ is the phase, $A_k(t)$ is the amplitude, $A_k(t) \geq 0$, $\omega_k(t) = \phi'_k(t)$, and $\omega_k(t)$ is the frequency.

In the interval range of $[t - \delta, t + \delta]$, $u_k(t)$ can be regarded as a harmonic signal with amplitude $A_k(t)$ and frequency $\omega_k(t)$, and $\delta = 2\pi/\phi'_k(t)$, where the prime denotes differentiation with respect to t .

The difference between VMD and EMD is that VMD is based on solving the variational problem and uses the variational model principle in the process of obtaining the IMFs, so that the sum of the estimated bandwidths of each IMF is minimized. The optimal solution of the constrained variational model is solved. The center frequency and bandwidth of the IMF are updated in the process of solving the variational model. The signal band is adaptively segmented based on the frequency domain of the signal itself. Further, a narrowband IMF is obtained.

The variational constraint model is as follows:

$$\begin{aligned} & \min_{\{u_k\}, \{\omega_k\}} \left\{ \sum_k \left\| \partial_t \left[\left(\delta(t) + \frac{j}{\pi t} \right) \times u_k(t) \right] e^{-j\omega_k t} \right\|_2^2 \right\} \\ & \text{s.t. } \sum_k u_k = f \end{aligned} \tag{2}$$

where $j = \sqrt{-1}$; $\{u_k\} := \{u_1, u_2, \dots, u_K\}$ is the number of IMF; $\{\omega_k\} := \{\omega_1, \omega_2, \dots, \omega_K\}$ is the frequency center of each IMF; and $\sum_k := \sum_{k=1}^K$ is the sum of all modes. $\|\cdot\|_2^2$ is the square of the 2-norm.

We introduce the Lagrange function as

$$L(\{u_k\}, \{\omega_k\}, \lambda) = \alpha \sum_k \left\| \partial_t \left[\left(\delta(t) + \frac{j}{\pi t} \right) \times u_k(t) \right] e^{-j\omega_k t} \right\|_2^2 + \|f(t) - \sum_k u_k(t)\|_2^2 + \left\langle \lambda(t), f(t) - \sum_k u_k(t) \right\rangle \tag{3}$$

where α is the penalty factor and λ is the Lagrange multiplier. $\|f(t) - \sum_k u_k(t)\|_2^2$ is the second penalty. $\langle \cdot \rangle$ is the integral mean of the variables.

The problem of solving the original minimum value can be transformed into the saddle point of the extended Lagrange expression by the alternating direction method, which is the optimal solution of the below formula:

$$u_k^{n+1} = \arg_{u_k} \min L(\{u_{i<k}^{n+1}\}, \{u_{i\geq k}^{n+1}\}, \{\omega_i^n\}, \lambda^n) \tag{4}$$

$$\omega_k^{n+1} = \arg_{\omega_k} \min L(\{u_i^{n+1}\}, \{\omega_{i<k}^{n+1}\}, \{\omega_{i\geq k}^n\}, \lambda^n) \tag{5}$$

$$\lambda^{n+1} = \lambda^n + \tau \left(f(t) - \sum_k u_k^{n+1} \right) \tag{6}$$

where $\sum_k \|u_k^{n+1} - u_k^n\|_2^2 / \|u_k^n\|_2^2 < \varepsilon$ is the convergence condition; n is the number of iterations; and τ is the update parameter.

Therefore, the original signal can be decomposed into K IMFs.

The calculation process of the VMD algorithm is as follows:

- Step 1: Initialize $\{u_k^1\}$, $\{\omega_k^1\}$, λ^1 and n to zero;
- Step 2: $n = n + 1$, execute the entire loop;
- Step 3: Execute the loop $k = k + 1$ until $k = K$, update u_k : $u_k^{n+1} = \arg\min_{u_k} L(\{u_{i<k}^{n+1}\}, \{u_{i\geq k}^n\}, \{\omega_i^n\}, \lambda^n)$;
- Step 4: Execute the loop $k = k + 1$, until $k = K$, update ω_k : $\omega_k^{n+1} = \arg\min_{\omega_k} L(\{u_{i<k}^{n+1}\}, \{\omega_{i\geq k}^n\}, \{\omega_i^n\}, \lambda^n)$;
- Step 5: Use $\lambda^{n+1} = \lambda^n + \tau \left(f(t) - \sum_k u_k(t) \right)$ to update λ ;
- Step 6: Given the discrimination condition $\varepsilon > 0$, if the iteration stop condition is satisfied, all the cycles are stopped and the result is output, and K IMFs are obtained.

2.2. Support Vector Machine

SVM can not only solve the classification problem, but also solves the regression problem; the basic model is the largest linear classifier defined in the feature space. SVM aims to achieve a distinction between samples by constructing a hyperplane for classification so that the sorting interval between the samples is maximized and the sample to the hyperplane distance is minimized.

Set a training data set for a feature space $D = \{(x_1, y_1), (x_2, y_2), \dots, (x_m, y_m)\}$, $x_i \in \chi = \mathfrak{R}^n$, $y_i \in y = \{+1, -1\}$, $i = 1, 2, \dots, N$, where x_i is the i -th feature vector, y_i is the class tag of x_i .

The corresponding equation of the classification hyperplane is

$$h(x) = \omega \cdot x + b \tag{7}$$

where x is the input vector, ω is the weight, and b is the offset.

The classification decision function is

$$\text{Sign}(h(x)) \tag{8}$$

$$\begin{cases} h(x) > 0, & y_i = 1 \\ h(x) < 0, & y_i = -1 \end{cases} \tag{9}$$

The support vector machine is implemented to find ω and b when the interval between the separation hyperplane and the nearest sample point is maximized. When the training set is linearly separable, the sample points belonging to different classes can be separated by one or several straight lines with the largest interval. The maximum interval is solved by the following formula:

$$\max \gamma_i = y_i \left(\frac{\omega}{\|\omega\|} \cdot x_i + \frac{b}{\|\omega\|} \right) \tag{10}$$

$$\text{s.t. } y_i \left(\frac{\omega}{\|\omega\|} \cdot x_i + \frac{b}{\|\omega\|} \right) \geq \gamma, \quad i = 1, 2, \dots, N \tag{11}$$

where γ is the geometric interval. Thus, we can obtain the linear separable support vector machine optimization problem.

$$\min_{\omega, b} \frac{1}{2} \|\omega\|^2 \tag{12}$$

$$\text{s.t. } y_i(\omega \cdot x_i + b) - 1 \geq 0, \quad i = 1, 2, \dots, N \tag{13}$$

In the actual data set, there are many specific points, making the data set linearly inseparable; in order to solve this problem, we introduce a slack variable for each sample point $\xi_i \geq 0$, so that

$$y_i(\omega \cdot x_i + b) \geq 1 - \xi_i \tag{14}$$

For each slack variable ξ_i , pay a price ξ_i , and the optimization problem becomes

$$\min_{\omega, b, \xi} \frac{1}{2} \|\omega\|^2 + C \sum_{i=1}^N \xi_i \tag{15}$$

where $C > 0$ is the penalty factor.

Most of the data are linearly inseparable; therefore, these data should be mapped to a high-dimensional feature space through non-linear mapping, letting the non-linear problem be transformed into a linear problem. The linear indivisible problem is transformed into a linearly separable problem.

Introduce kernel functions:

$$K(x_i, x_j) = \varphi(x_i) \cdot \varphi(x_j) \tag{16}$$

where the value of the kernel equals the inner product of two vectors, x_i and x_j .

At this point, we obtain

$$W(\alpha) = \frac{1}{2} \sum_{i=1}^N \sum_{j=1}^N \alpha_i \alpha_j y_i y_j K(x_i, x_j) - \sum_{i=1}^N \alpha_i \tag{17}$$

where α is the Lagrangian multiplier, $\alpha_i \geq 0, i = 1, 2, \dots, N$, and N is the number of samples.

In this paper, the radial basis function (RBF) is chosen as the SVR kernel function, and the expression is

$$K(x_i, x) = \exp\left(\frac{-\|x_i - x\|^2}{2g^2}\right) \tag{18}$$

where g is the kernel function coefficient.

At this point, the classification function becomes

$$f(x) = \text{sign}\left[\sum_{i=1}^N \alpha_i y_i \exp\left(\frac{-\|x_i - x\|^2}{2g^2}\right) + b\right] \quad (19)$$

2.3. Empirical Mode Decomposition

EMD is an adaptive signal processing technique suitable for non-linear and non-stationary processes [21]. In 1998, Huang et al. [6] proposed the empirical mode decomposition technology. Based on time scales, EMD local features such as local maxima, local minima, and zero-crossings, we decompose the signal into several IMFs and a residual; the IMFs are orthogonal to each other. Modal decomposition is determined by the signal itself.

EMD satisfies the following basic assumptions:

- (1) In the entire data set, the number of extreme values and the number of zero crossings must be equal or at most have one point of difference.
- (2) At any point, the average defined by the local maximum envelope and the minimum envelope is zero.

Finally, the original signal is decomposed into

$$x(t) = \sum_{i=1}^N c_i + r_N \quad (20)$$

where $x(t)$ is the original signal, c_i is the IMF, N is the number of IMFs, and r_N is the residual.

2.4. Wavelet Threshold Denoising

Suppose the model of denoising based on wavelet transform is

$$x = c + \sigma e \quad (21)$$

where x is the noise signal; c is the effective signal; e is the noise component in the noise signal; and σ is the noise intensity.

The wavelet transform and its denoising process are carried out in the following steps [22]:

- (1) The noisy signal is transformed by wavelet transform. A wavelet basis is selected to determine the level N of the wavelet decomposition at the same time, and then the signal x is decomposed by the N -level wavelet.
- (2) The wavelet coefficients are thresholded. In order to keep the overall shape of the signal unchanged and keep the effective signal, the hard threshold, soft threshold or other threshold methods are used to quantify the sparseness of each layer after decomposition.
- (3) The inverse wavelet transform is performed, and the signal is reconstructed.

In this paper, a hard threshold denoising function is selected. Hard threshold processing compares the absolute value of wavelet transform coefficients with the threshold value. The coefficients smaller than or equal to the threshold value become zero, and the coefficients larger than the threshold value remain unchanged [23]. This method has better amplitude-preserving characteristics [24] and its expression is as follows:

$$S = \begin{cases} s, & |s| \geq T \\ 0, & |s| < T \end{cases} \quad (22)$$

where T is the threshold, and s is the wavelet decomposition coefficient.

3. Hybrid Algorithm Research

Mold-level prediction accuracy is influenced by many factors. In order to improve mold-level prediction accuracy, firstly, the noise in the original signal should be removed as much as possible. Then, we improve the prediction accuracy by using advanced prediction algorithms such as SVR. Thus, a prediction model based on the VMD–SVR algorithm for mold-level prediction is proposed in this paper. A hybrid algorithm flow chart is shown in Figure 2.

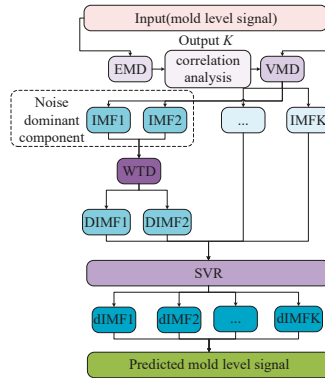


Figure 2. Hybrid algorithm flow chart. EMD—empirical mode decomposition; VMD—variational mode decomposition; IMF—intrinsic mode functions; WTD—wavelet threshold denoising; SVR—support vector regression.

Firstly, the original mold-level signal is subjected to data preprocessing to remove singular points. Then, all data are marked in the range of 0 to 1 to improve computational efficiency. Finally, the hybrid model is used for data prediction.

The hybrid algorithm flow is as follows:

- Step 1: Adaptively decompose the mold-level data based on the EMD algorithm to obtain several IMFs;
- Step 2: The K value of the key parameter of the VMD is obtained by the correlation analysis between the IMFs;
- Step 3: Perform VMD decomposition on the original signal based on K to obtain K IMFs;
- Step 4: Denoise the noise related component;
- Step 5: Perform SVR on the denoised IMFs and other IMFs to obtain the predicted IMFs;
- Step 6: Reconstruct the predicted component and obtain the predicted signal.

First, the mold-level signal is decomposed into several IMFs by the EMD, and the modal parameter K of the VMD is determined by correlation analysis between the IMFs. Then, the mold-level signal is decomposed into K IMFs by VMD, and the IMFs are analyzed to identify the noise dominant component, and the signal dominant component uses correlation analysis between the IMFs. Afterwards, in order to avoid the loss of effective information, the noise-related component is denoised by the WTD algorithm, and the effective information is effectively retained. SVR is performed on the denoised IMFs and other IMFs to obtain the predicted IMFs. Finally, the predicted IMFs are reconstructed to obtain the predicted signal.

The IMFs are obtained by adaptively decomposing the original mold-level data based on the novel VMD–SVR hybrid algorithm, the main purpose of which is to distinguish the noise-dominant IMFs and information-dominant IMFs. In order to preserve as much valid information as possible in the original mold-level data, denoising the noise-dominant IMFs can effectively remove the effects of white noise. Then, SVR is performed on all IMFs, the predicted IMFs are obtained for signal reconstruction, and the predicted mold-level data is obtained.

4. Experimental Studies

4.1. Problem Prescription

This paper presents a mold-level prediction model. This model is important for mold-level control and propose new ideas to improve continuous-casting automatic control. In order to clearly express the applicability, superiority, and generalization capability of the model application, the mold-level data of actual process parameters, collected from the continuous casting machine developed by the China National Heavy Machinery Research Institute Co., Ltd. (Xi'an, China), are used in this paper. We used an eddy current sensor to collect the mold-level signal at a steady cast speed. There are many uncertain disturbance factors in the mold-level control process, and the disturbance may change constantly at any time. Most of the disturbances are non-linear and non-stationary, and the long-term prediction model is difficult to establish.

A continuous casting production process data acquisition graph is presented in Figure 3. The time interval $\Delta t = 0.5$ h, and the sampling frequency was 2.7 Hz.

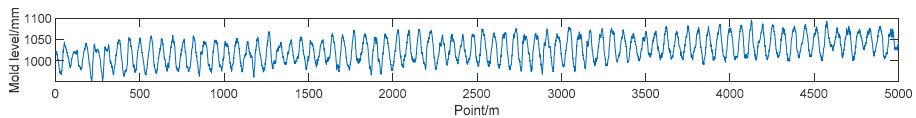


Figure 3. Mold level. The unit of the mold level is mm, while m is the number of points.

The main technical parameters of the continuous casting machine are shown in Table 1.

Table 1. Main technical parameters of the continuous casting machine.

Project	Specification
Continuous-casting machine model	Curved continuous caster
Secondary cooling category	Aerosol cooling, dynamic water distribution
Gap control	Remote adjustment, dynamic soft reduction
Basic arc radius/mm	9500
Mold length/mm	900
Metallurgical length/mm	39,200
Mold vibration frequency/time/min	25–400
Mold vibration amplitude/mm	2–10
Slab width/mm	900–2150
Slab thickness/mm	230/250
Working speed/m/min	0.8–2.03
Actual cast speed/m/min	1.3
Slab section size/mm × mm	230 × 1350
Mold oscillation frequency/Hz	1.36
Actual oscillation amplitude of mold/mm	60

4.2. Mold-Level Prediction Based on VMD–SVR Model

The VMD decomposition number is artificially determined, not adaptive. EMD is an adaptive decomposition method. Therefore, in order to minimize the interference of human factors, we decomposed the original data using EMD, and through the calculation of the correlation coefficient, a component having the largest correlation coefficient with the original signal was obtained as a boundary line between the high-frequency signal and the low-frequency signal, the high-frequency signal was integrated into one component, and the remaining components were retained to determine the number K of VMD decomposition.

First, the original data was subjected to EMD decomposition; the EMD decomposition results are shown in Figure 4.

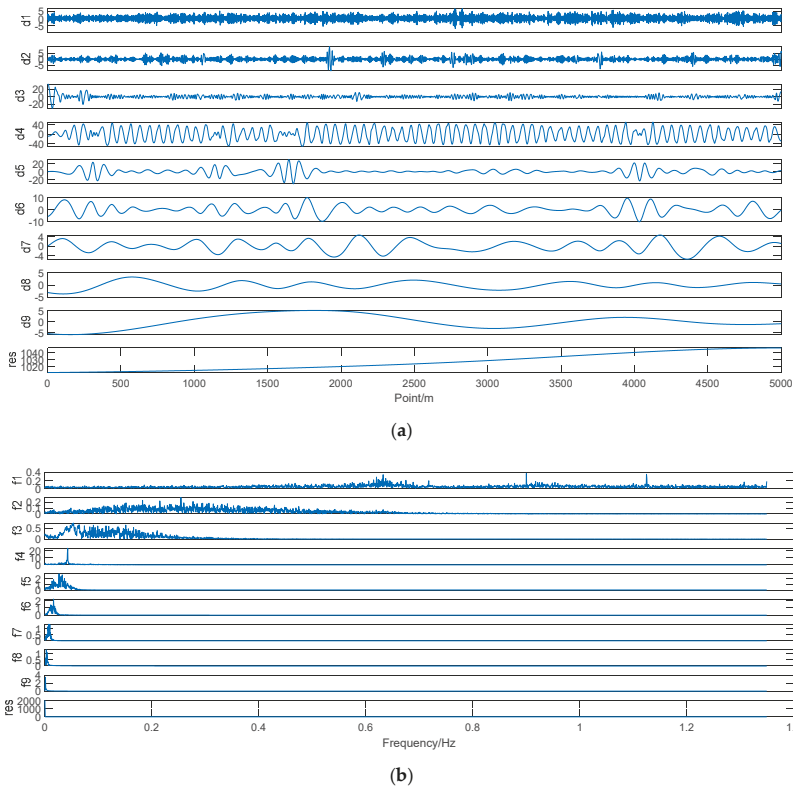


Figure 4. (a) Mold-level data EMD results; (b) spectrogram after EMD of the mold-level data; d_i is the i -th IMF, the unit of d_i is mm, m is the number of points, res is the residual, and f_i is the spectrum corresponding to the i -th IMF.

After the mold-level data is decomposed by the EMD as shown in Figure 3, the correlation coefficient between the original mold-level signal and the IMFs after EMD was determined, as shown in Table 2; IMFs 1–3 were seen to be weakly correlated with the original mold-level signal. There was a strong correlation between the original mold-level signal and the fourth IMF. We used IMFs 1–3 as a K value in the VMD decomposition, which is considered to be a high-frequency component of IMFs 1–3, and took the remaining IMF as 6 K values, thus obtaining $K = 7$, and performing VMD decomposition based on $K = 7$, which is not a simple direct merger of IMFs 1–3.

Table 2. The correlation coefficient between the original mold-level signal and the IMFs after EMD.

IMF	Correlation Coefficient
IMF 1	0.06
IMF 2	0.0906
IMF 3	0.1348
IMF 4	0.8474
IMF 5	0.1579
IMF 6	0.0196
IMF 7	0.0061
IMF 8	0.0598
IMF 9	0.0585

The VMD decomposition of the mold-level data was based on $K = 7$. The decomposition result is shown in Figure 5.

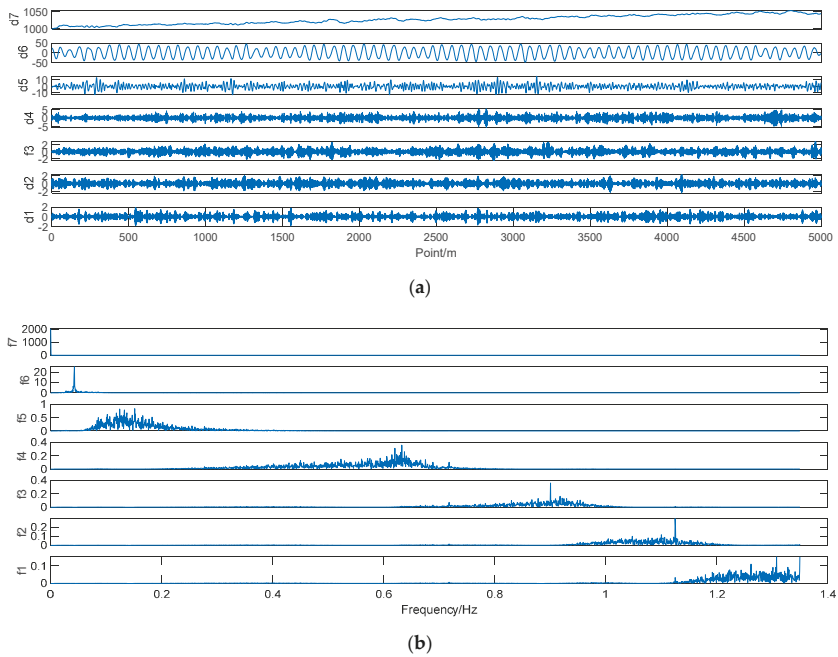


Figure 5. (a) Mold-level data VMD results; (b) spectrogram after VMD of the mold-level data; d_i is the i -th IMF, the unit of d_i is mm, m is the number of Point, and f_i is the spectrum corresponding to the i -th IMF.

It can be seen from Figure 4 that the mold-level data could clearly distinguish the center frequency of each IMF based on $K = 7$ decomposition, and no pattern aliasing occurred.

After the mold-level data was decomposed by the VMD, as shown in Figure 5, the correlation coefficient between the original mold-level signal and the IMFs after VMD was calculated, as shown in Table 3; IMFs 1–5 were weakly correlated with the original mold-level signal. There was a strong correlation between the original mold-level signal and the fourth IMF. Therefore, IMF 6 was a boundary line between the high-frequency signal and the low-frequency signal; high-frequency signals may also contain a small amount of effective information, and so, in order to minimize the loss of effective information, we performed wavelet threshold denoising on high-frequency signals (IMFs 1–5) instead of directly deleting them.

Table 3. The correlation coefficient between the original mold-level signal and the IMFs after VMD.

IMF	Correlation Coefficient
IMF 1	0.0279
IMF 2	0.0360
IMF 3	0.0429
IMF 4	0.0638
IMF 5	0.1769
IMF 6	0.8847
IMF 7	0.4560

It can be seen from Figure 6 that the noise reduction effect for IMFs 1–5 was very obvious. Both the main frequency and the amplitude had a large reduction.

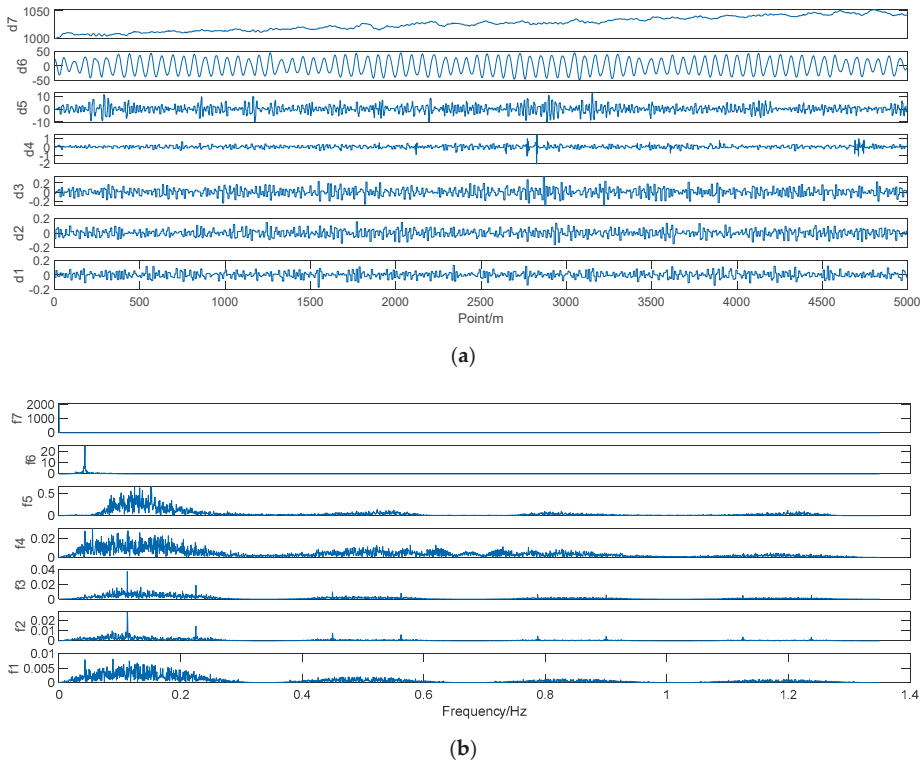


Figure 6. (a) Denoising result of IMFs 1–5; (b) spectrogram of the mold-level data after denoising; d_i is the i -th IMF, the unit of d_i is mm, m is the number of points, and f_i is the spectrum corresponding to the i -th IMF.

Then, SVR was performed on the all IMFs. In this section, the genetic algorithm was still used to globally optimize the model parameters C and g , so that the SVR model was determined. C was 15.2768 and g was 0.2018. The first 20 min of mold-level data was used as a training set, while the last 10 min of mold-level data was used as a test set in order to verify the prediction effect of the model. This method has high computational efficiency, high calculation accuracy, and can be run in real-time.

The optimization results of C and g are shown in Figure 7; fitness was the hit rate of the genetic algorithm. The predicted data of VMD–SVR are shown in Figure 8, and the VMD–SVR prediction error is shown in Figure 9.

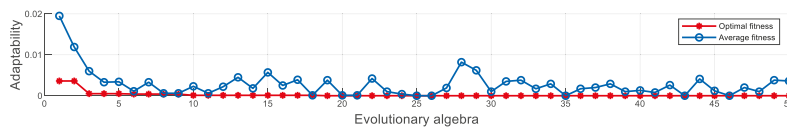


Figure 7. C and g optimization results. C is the penalty coefficient, g is the parameter of kernel function.

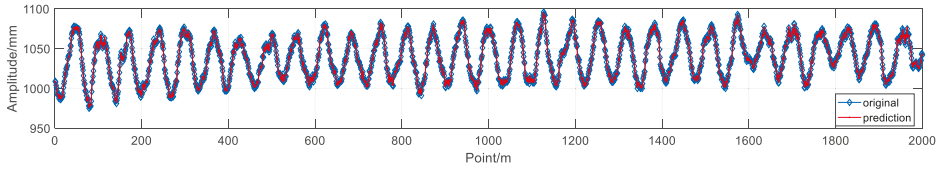


Figure 8. Comparison of VMD-SVR prediction results with original mold-level data. m is the number of points.

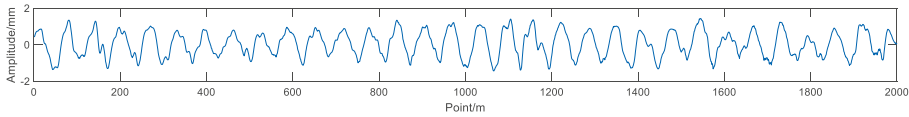


Figure 9. VMD-SVR prediction error. m is the number of points.

5. Prediction Results and Analysis

In this section, the performance of the three hybrid prediction algorithms is verified by the following four statistical indicators, which are the general purpose of the machine learning domain verification algorithm, and the optimal hybrid prediction model suitable for the mold steel level of the mold is selected.

Correlations between the original data and the predicted data, which is characterized by correlation coefficients (R):

$$R = \frac{\text{Cov}(P_i, A_i)}{\sqrt{\text{Var}(P_i) \cdot \text{Var}(A_i)}} \quad (23)$$

CC is defined as a statistical indicator and is used to reflect the close relationship between variables; the larger the CC, the better the algorithm performance.

Root mean square error (RMSE)

$$\text{RMSE} = \sqrt{\frac{\sum_{i=1}^n (P_i - A_i)^2}{n}} \quad (24)$$

RMSE is defined to reflect the degree of dispersion of a data set and to measure the deviation between the observed value and the true value; the smaller the RMSE, the better the algorithm performance.

Mean absolute error (MAE)

$$\text{MAE} = \frac{\sum_{i=1}^n |P_i - A_i|}{n} \quad (25)$$

MAE is defined as the average value of absolute error, better reflecting the actual situation of predicted error; the smaller the MAE, the better the algorithm performance.

Mean absolute percentage error (MAPE)

$$\text{MAPE} = \frac{\sum_{i=1}^n \left| \frac{P_i - A_i}{A_i} \right|}{n} \times 100 \quad (26)$$

MAPE can be used to measure the outcome of a model's predictions; the smaller the MAPE, the better the algorithm performance.

In Formulas (23)–(26), where P_i and A_i are the i -th predicted and actual values, respectively, and n is the total number of predictions.

From the test results in Table 4 and Figure 10, comparing the four indicators of the three algorithms, the test results of the average error in the algorithm described in this paper are inferior to the other two

algorithms. However, in the test results of the other three indicators, the RMSE index is improved by 36.1%, the MAPE index is improved by 37.5%, the R is improved by 3%, and the MAE index is improved by 37.6%. Compared with WT and EMD, the VMD algorithm has shown great superiority, which not only rejects the dependence of the wavelet transform on basis function, but also avoids the boundary effect and pattern aliasing of empirical mode decomposition and improves the robustness of the algorithm and generalization ability.

Table 4. Test results comparison of prediction model. R is correlation coefficients; RMSE is root mean square error; MAE is mean absolute error; MAPE is mean absolute percentage error.

Algorithm	R	RMSE	MAE	MAPE
WT-SVR	0.9733	1.0824	0.9601	0.092316
EMD-SVR	0.9691	0.9480	0.7662	0.073558
VMD-SVR	0.9992	0.6910	0.5983	0.057686

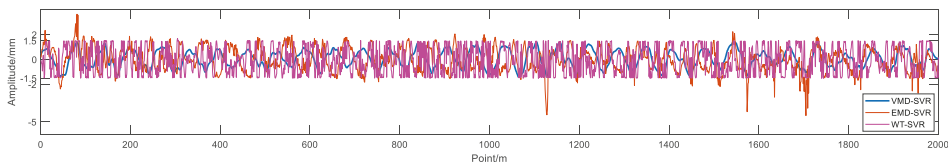


Figure 10. Prediction error between VMD-SVR and other methods. m is the number of points.

6. Conclusions

This paper proposes a prediction method based on VMD-SVR, which is suitable for mold-level prediction in continuous casting. In this method, the original mold-level data are adaptively decomposed by the EMD algorithm to obtain the effective IMF number K , via correlation coefficient analysis between the original mold-level signal and IMFs. The VMD decomposition of the original mold-level data is performed based on K , and the IMFs are obtained. Time-series prediction is performed for each IMF via SVR, and the VMD reconstruction is performed on the prediction result to obtain the final predicted mold-level signal. In order to verify the effectiveness of the proposed method, we compared the four statistical indicators of three algorithms; the conclusions are as follows.

- (1) The VMD-SVR algorithm can be used to establish the prediction model, removing noise while retaining the effective information in the data, with good denoising performance and sampling rate robustness;
- (2) In comparison with the results of the other two algorithms, the three indicators of the VMD-SVR algorithm are significantly better than those of the other two algorithms. The RMSE index is improved by 36.1%, the MAPE index are improved by 37.5%, the R is improved by 3%, and the MAE index is improved by 37.6%;
- (3) The use of mold-level prediction methods in the research on mold prediction control represents a future research direction. Accurate mold-level prediction provides a new idea for mold-level prediction control, which has important practical significance;
- (4) Using the accurately predicted mold-level data for mold-level control, the sliding nozzle and roller pressure disturbances can be well restrained. The anti-interference ability of the mold level control system is enhanced.

The potential feedback between the mold level controller and the mold level prediction will improve the accuracy and efficiency of the prediction model, which will be the focus of further research in a future paper.

Author Contributions: W.S. conceived and designed the experiments, Z.L. performed the experiments, L.Y. provided mold-level data, Q.H. analyzed the data, and Z.L. wrote the paper.

Funding: This work was financially supported by the National Natural Science Foundation of China, grant number 51575429.

Acknowledgments: Q.G., X.L., H.Z., B.H., and Y.Z. are acknowledged for their valuable technical support.

Conflicts of Interest: The authors declare no conflicts of interest.

References

1. Ataka, M. Rolling technology and theory for the last 100 years: The contribution of theory to innovation in strip rolling technology. *ISIJ Int.* **2015**, *55*, 89–102. [[CrossRef](#)]
2. Jin, X.; Chen, D.F.; Zhang, D.J.; Xie, X. Water model study on fluid flow in slab continuous casting mould with solidified shell. *Ironmak. Steelmak.* **2011**, *38*, 155–159. [[CrossRef](#)]
3. Guo, G.; Wang, W.; Chai, T. Predictive mould level control in a continuous casting line. *Control Theory Appl.* **2011**, *18*, 714–717.
4. Tong, C.; Xiao, L.; Peng, K.; Li, J. Constrained generalized predictive control of mould level based on genetic algorithm. *Control Decis.* **2009**, *24*, 1735–1739.
5. Qiao, G.; Tong, C.; Sun, Y. Study on Mould level and casting speed coordination control based on ADRC with DRNN optimization. *Acta Autom. Sin.* **2007**, *33*, 641–648.
6. Huang, N.E.; Shen, Z.; Long, S.R.; Wu, M.C.; Shih, H.H.; Zheng, Q.; Yen, N.; Tung, C.C.; Liu, H.H. The empirical mode decomposition and the Hilbert spectrum for nonlinear and non-stationary time series analysis. *Proc. R. Soc. A-Math. Phys.* **1998**, *454*, 903–995. [[CrossRef](#)]
7. Konstantin, D.; Dominique, Z. Variational mode decomposition. *IEEE Trans. Signal Process.* **2014**, *62*, 531–544.
8. Lee, W.J.; Hong, J. A hybrid dynamic and fuzzy time series model for mid-term power load predicting. *Int. J. Electr. Power Energy Syst.* **2015**, *64*, 1057–1062. [[CrossRef](#)]
9. Dai, S.; Niu, D.; Li, Y. Daily peak load predicting based on complete ensemble empirical mode decomposition with adaptive noise and support vector machine optimized by modified grey wolf optimization algorithm. *Energies* **2018**, *11*, 163. [[CrossRef](#)]
10. Lynch, P. The origins of computer weather prediction and climate modeling. *J. Comput. Phys.* **2008**, *227*, 3431–3444. [[CrossRef](#)]
11. Gaudioso, M.; Gorgone, E.; Labbe, M.; Rodriguez-Chia, A.M. Lagrangian relaxation for SVM feature selection. *Comput. Oper. Res.* **2017**, *87*, 137–145. [[CrossRef](#)]
12. Wang, J.; Shi, P.; Jiang, P.; Hu, J.; Qu, S.; Chen, X.; Chen, Y.; Dai, Y.; Xiao, Z. Application of BP neural network algorithm in traditional hydrological model for flood predicting. *Water* **2017**, *9*, 48. [[CrossRef](#)]
13. He, F.; Zhang, L. Mold breakout prediction in slab continuous casting based on combined method of GA-BP neural network and logic rules. *Int. J. Adv. Manuf. Technol.* **2018**, *95*, 4081–4089. [[CrossRef](#)]
14. Fan, G.F.; Peng, L.L.; Hong, W.C.; Sun, F. Electric load predicting by the SVR model with differential empirical mode decomposition and auto regression. *Neurocomputing* **2016**, *173*, 958–970. [[CrossRef](#)]
15. Nie, H.; Liu, G.; Liu, X.; Wang, Y. Hybrid of ARIMA and SVMs for short-term load predicting, 2012 international conference on future energy, environment, and materials. *Energy Procedia* **2012**, *16*, 1455–1460. [[CrossRef](#)]
16. Liu, Y.; Gao, Z. Enhanced just-in-time modelling for online quality prediction in BF ironmaking. *Ironmak. Steelmak.* **2015**, *42*, 321–330. [[CrossRef](#)]
17. Shen, B.Z.; Shen, H.F.; Liu, B.C. Water modelling of level fluctuation in thin slab continuous casting mould. *Ironmak. Steelmak.* **2009**, *36*, 33–38. [[CrossRef](#)]
18. Hong, W.-C. Chaotic particle swarm optimization algorithm in a support vector regression electric load predicting model. *Energy Convers. Manag.* **2009**, *50*, 105–117. [[CrossRef](#)]
19. Ghosh, S.K.; Ganguly, S.; Chattopadhyay, P.P.; Datta, S. Effect of copper and microalloying (Ti, B) addition on tensile properties of HSLA steels predicted by ANN technique. *Ironmak. Steelmak.* **2009**, *36*, 125–132. [[CrossRef](#)]
20. Voyant, C.; Muselli, M.; Paoli, C.; Nivet, M.-L. Numerical weather prediction (NWP) and hybrid ARMA/ANN model to predict global radiation. *Energy* **2012**, *39*, 341–355. [[CrossRef](#)]
21. Lei, Y.G.; Lin, J.; He, Z.J.; Zuo, M.J. A review on empirical mode decomposition in fault diagnosis of rotating machinery. *Mech. Syst. Sig. Process.* **2013**, *35*, 108–126. [[CrossRef](#)]

22. Tomic, M. Wavelet transforms with application in signal denoising. *Ann. DAAAM Proc.* **2008**, 1401–1403.
23. El B'charri, O.; Latif, R.; Elmansouri, K.; Abenaou, A.; Jenkal, W. ECG signal performance de-noising assessment based on threshold tuning of dual-tree wavelet transform. *Biomed. Eng. Online* **2017**, *16*, 26. [[CrossRef](#)] [[PubMed](#)]
24. Varady, P. Wavelet-Based Adaptive Denoising of Phonocardiographic Records. In Proceedings of the 23rd Annual International Conference on IEEE-Engineering-in-Medicine-and-Biology-Society, Istanbul, Turkey, 25–28 October 2001; pp. 1846–1849.



© 2019 by the authors. Licensee MDPI, Basel, Switzerland. This article is an open access article distributed under the terms and conditions of the Creative Commons Attribution (CC BY) license (<http://creativecommons.org/licenses/by/4.0/>).

Article

Modelling on Inclusion Motion and Entrapment during the Full Solidification in Curved Billet Caster

Yanbin Yin ¹, Jiongming Zhang ^{1,*}, Qipeng Dong ² and Yuanyuan Li ^{1,3}

¹ State Key Laboratory of Advanced Metallurgy, University of Science and Technology Beijing, Beijing 100083, China; b20150490@xs.ustb.edu.cn (Y.Y.); lyy_job@163.com (Y.L.)

² School of Iron and Steel, Soochow University, Suzhou 215137, China; qpdong@outlook.com

³ Liuzhou Iron & Steel Company, Ltd., Liuzhou 545002, China

* Correspondence: jmz2203@sina.com; Tel.: +86-010-8237-6597

Received: 12 April 2018; Accepted: 2 May 2018; Published: 6 May 2018

Abstract: Inclusions entrapped by the solidifying front during continuous casting would deteriorate the properties of the final steel products. In order to investigate the inclusion motion and the entrapment during the full solidification in curved billet caster, the present work has developed a three-dimensional numerical model coupling the flow, solidification, and inclusion motion. The predicted result indicates that the inclusion distribution inside the liquid pool of the mold is not perfectly symmetrical. Furthermore, the motion and the entrapment of micro inclusions in the mold are mainly affected by the molten steel flow pattern, however, those of macro inclusions depend both on the molten steel flow pattern and the buoyancy force of the inclusions. In the curved part of the strand, macro inclusions shift to the solidifying front of the inner radius as time goes on, while the solidifying front of the outer radius cannot entrap inclusions. The distributions of inclusions smaller than 5 μm in the solidified strand are even. However, for inclusions that are larger than 5 μm , their distributions become uneven. To validate the model, measurement of the strand surface temperature and the detection of inclusions in samples obtained from a plant have been performed. Good agreement is found between the predicted and experimental results.

Keywords: numerical simulation; molten steel flow; solidification; inclusion motion; inclusion entrapment; billet continuous casting

1. Introduction

Inclusions inside a steel matrix have a detrimental impact on the performance of steels, such as their strength, toughness, fatigability, surface appearance, etc. [1–4]. Hence, the removal of inclusions from the molten steel is a critical issue throughout the steelmaking process. In particular, continuous casting is the last opportunity for the removal of inclusions from the molten steel. Inclusions that were carried by the molten steel are injected into the continuous casting mold. It is believed that a portion of these inclusions would rise in the mold and finally be absorbed by the mold flux. However, the remainder would inevitably be entrapped by the solidifying front while they move inside the liquid pool of the strand. Therefore, an in-depth investigation on the inclusion motion, removal, and entrapment during the full solidification in a continuous casting strand is essential, and it can provide theoretical guidance for the improvement of the steel cleanliness and properties. It is very difficult to research the inclusion motion and entrapment during the continuous casting by plant measurements or physical experiments. Fortunately, numerical simulation is an appropriate method to study the inclusion motion and entrapment during the continuous casting.

In recent years, extensive research has been conducted on the particle (inclusion, bubble) behaviors during the continuous casting by method of numerical simulation [5–41]. Many previous studies have investigated particle behaviors in continuous casting strands using continuum [5,6] or

Eulerian–Eulerian multiphase flow models [7–9]. Lei H. et al. [5] studied the inclusion collision-growth in a slab continuous caster using a continuum model. The spatial distributions of the inclusion volume concentration and number density were revealed. Through coupling the electromagnetic force into the continuum model, Lei H. et al. [6] investigated the effect of in-mold electromagnetic stirring (M-EMS) on the inclusion collision-coalescence and the spatial distributions in a bloom caster. Due to the M-EMS, Archimedes force and Archimedes collision were considered for inclusions in the study. Liu Z. et al. [7–9] used the inhomogeneous Multiple Size Group (MUSIG) model or the average bubble number density (ABND) model under the Eulerian–Eulerian framework to describe the bubbly flow in slab continuous casting.

Many researchers [10–41] have studied the particle transport (motion, removal, and entrapment) in the continuous casting strand through Lagrangian descriptions for the inclusions or argon bubbles. Liu Z. et al. [14] studied the influence of electromagnetic brake (EMBr) on the transient fluid flow and inclusion transport (motion, removal) in a slab continuous casting mold through a three-dimensional (3D) mathematic model. In the study, the transport of inclusions inside the mold was calculated employing the Lagrangian approach. The results indicated that the inclusion transport inside the mold was asymmetric. When compared with no EMBr, the removal of inclusions for the EMBr arrangement was enhanced, nevertheless, that for the flow-control mold (FCM) arrangement was reduced.

Several previous works [24–41] have researched the entrapment of particles (inclusions, argon bubbles) by the solidifying front in continuous casting strand. Liu Z. et al. [37] developed a 3D numerical model coupling the fluid flow, solidification, and inclusion motion. In order to investigate the transport of inclusion clusters, an inclusion cluster model was developed based on the fractal theory and the conservation of mass. The flow and solidification of molten steel, the motion, and the entrapment of inclusion clusters in a vertical-bending continuous casting caster were studied through the coupling model. Thomas B. et al. [38] constructed a computational model coupling turbulent fluid flow and particle transports. In addition, a particle-capture model that was based on local force balances was also coupled into the computational model. Through the coupling model, the work simulated the entrapment of slag inclusions and bubbles during the thin-slab continuous casting. This paper adopted both Reynolds Average Navier-Stokes (RANS) and Large Eddy Simulation (LES) approaches to calculate the turbulence flow field. The results indicated that, particle capture depended on factors, such as particle size and density, molten steel transverse fluid, Primary Dendrite Arm Spacing (PDAS), solidification front orientation angle, and sulfur concentration gradient. Wang S. et al. [40] investigated the influence of electromagnetic parameters on the motion and the entrapment of inclusions in FCM continuous casting strands through a coupling mathematical model. The results suggested that the region about 5 mm beneath the slab surface became cleaner, and the aggregation of inclusions were eliminated while the upper and lower magnetic fields of the FCM increased. The above works researched the particle motion and the entrapment in the mold region or a part of the continuous casting strand.

Zhang L. et al. [41] conducted a study on the inclusion entrapment in the full length of a billet caster by means of numerical simulation. In the work, the geometry model was straight throughout the computational domain. However, most of the commercial continuous casters involve a curved part. The inclusion motion and entrapment in a curved continuous casting strand may have distinctive characteristics. At present, studies about the inclusion motion and entrapment during the full solidification in a curved continuous casting strand have not been reported.

The scope of the current work was to develop a three-dimensional numerical model to investigate the inclusion motion and entrapment during the full solidification in a curved billet caster. To validate the model, measurement of the strand surface temperature and the detection of inclusions in samples that were obtained from a plant have been performed.

2. Numerical Methodology

2.1. Assumptions

In the present work, the following assumptions are made in the cause of simplifying the numerical model:

1. treating the molten steel as an incompressible Newtonian fluid;
2. the influence of the mold taper and oscillation are not considered;
3. the mold flux and the level fluctuation of the molten steel are not neglected;
4. the free surface of the mold is assumed to be adiabatic;
5. the latent heat of the solid phase transformation is negligible, only the latent heat of solidification is considered;
6. the inclusion is treated as spherical alumina inclusion, and its density is constantly $3500 \text{ kg}\cdot\text{m}^{-3}$;
7. the aggregation and breakup of inclusions are not taken into account; and,
8. the influence of inclusion motion on the flow and the heat transfer of the molten steel is ignored.

2.2. The Model Details

The numerical model mainly involves two parts: the flow-solidification model and the inclusion motion model. The flow-solidification model can be found in the previous work [42], moreover, the inclusion motion model can be found in the previous work [31].

In the previous work [42], to calculate the molten steel heat transfer and solidification, the enthalpy-porosity technique was employed. In the enthalpy-porosity technique, the influence of solidification on the molten steel flow velocities is considered, through introducing a source term into the momentum conservation equation of the molten steel. The source term takes the following form:

$$S_u = \frac{(1-f)}{f^3 + e} A_{\text{mush}} \left(\vec{V} - \vec{V}_{\text{cast}} \right), \quad (1)$$

where f is liquid fraction of steel, e is a small number (0.001) to prevent division by zero, and A_{mush} is permeability coefficient. The calculation detail of A_{mush} can be found in our previous work [42].

The casting velocity, \vec{V}_{cast} , is a constant vector in the previous work. However, owing to the curved geometry model in the present work, the casting velocity should be treated as a variable varying with position.

As shown in Figure 1, in the curved part of the strand, the direction of the casting velocity at one point is parallel to the tangent of a circle at this point. Moreover, the center of the circle coincides with the center of the curved strand. Hence, the casting speed, \vec{V}_{cast} , can be expressed in Cartesian coordinate form, as follows:

$$\left(-\|\vec{V}_{\text{cast}}\| \cdot \sin \theta, 0, -\|\vec{V}_{\text{cast}}\| \cdot \cos \theta \right), \quad (2)$$

The magnitude of casting velocity at one point can be calculated by Equation (3):

$$\|\vec{V}_{\text{cast}}\| = V_{\text{center}} \cdot \frac{R}{R_{\text{caster}} - D/2}, \quad (3)$$

where R is the distance between the point and the caster center, R_{caster} is the radius of the caster, and D is the strand thickness. V_{center} is the magnitude of the casting velocity at the strand center, which is equal to the magnitude of the strand velocity at the caster exit. In the current work, V_{center} is set as $1.65 \text{ m}\cdot\text{min}^{-1}$.

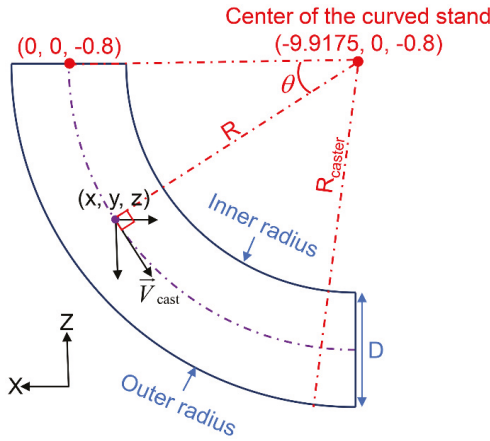


Figure 1. Schematic diagram of setting the casting velocity.

2.3. Geometry Model

As Figure 2 shows, in order to calculate the full solidification process of the billet caster, a full geometry model of the strand has been developed. The length of the computational domain is 10 m and the size of the strand cross section is 0.165 m × 0.165 m. The mold with a length of 0.8 m is vertical. The curved part of the caster initiates at the mold exit. The length of the foot roller zone (FRZ) is 0.3 m. Furthermore, the secondary cooling zone of the caster consists of three segments, which are SCZ1 (2.45 m), SCZ2 (2.4 m), and SCZ3 (1.5 m), respectively. Additionally, a part of the air cooling zone (ACZ) is involved in the computing domain, which is 2.55 m in length. The submerged entry nozzle (SEN) is a type of straight single port. The submerged depth of the SEN is 0.1 m. The inner and outer diameters of the SEN are 0.035 m and 0.075 m, respectively. To simulate the behavior of the solidified shell more accurately, the local grid refinement technology has been adopted.

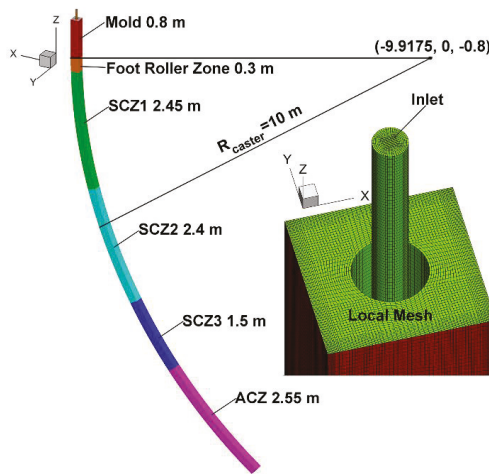


Figure 2. Geometry model and mesh in a billet caster.

2.4. Boundary Conditions

Boundary conditions for the flow-solidification simulation are set according to Dong's work [43]. To give full consideration to a statistically representative result of the inclusion entrapment and the computer capacity, 1000 inclusions per second with a consistent size are injected randomly into the SEN from the inlet. With regard to the inclusion motion, an escape boundary condition is defined for the top surface of the mold and the computational domain outlet. Moreover, a reflecting boundary is set for the walls inside and outside the SEN. In the current work, inclusions are assumed to be entrapped by the solidified shell if the local liquid fraction is below 0.6 [39,41], and the velocities of the captured inclusions are equal to the local casting velocity. Subsequently, the inclusions entrapped by the solidified shell would move together with the solidified shell.

The Material properties used in the present work are listed in Table 1.

Table 1. The Material properties and model parameters.

Parameters	Values	Dimensions
c_p , Specific heat	650	$J \cdot kg^{-1} \cdot K^{-1}$
k , Thermal conductivity	33.5	$W \cdot m^{-1} \cdot K^{-1}$
ρ , Steel density	7340	$kg \cdot m^{-3}$
L , Steel latent heat	231,637	$J \cdot kg^{-1}$
T_l , Liquid temperature	1827	K
T_s , Solid temperature	1636	K
μ , Molten steel molecular viscosity	0.00461	$kg \cdot s^{-1} \cdot m^{-1}$
T_{tun} , Tundish temperature	1758	K
d_p , Inclusion size	3.5, 5, 7, 10, 15, 20, 25, 50, 100, 200	μm

2.5. Numerical Procedure Details

The numerical model in the present work is solved using the CFD package OpenFOAM (Version 2.1.1). The solving process consists of two steps: first, the numerical simulation of the molten steel flow-solidification is executed for 600 s under transient mode, providing an initial condition for the second step; second, the calculation of inclusion motion coupling the molten steel flow and solidification is performed in the transient mode. With reference to the second step, the total calculation time was about 500 s, which could ensure that inclusions enter and exit the computational domain.

3. Results and Discussion

3.1. Solidification Model Validation

For the prediction of inclusion entrapment, an accurate solidification profile is of great importance. In order to validate the solidification model, four surface center temperatures of the strand were measured with infrared thermometers that were placed at the SCZ2, SCZ3, and at two positions in the ACZ. Figure 3 shows the variation of the predicted surface center temperature, which is in good agreement with the measured temperatures along the casting direction, and it therefore validates the solidification model. The solidified shell (liquid fraction: 0.6) thickness profile of the strand is also shown in Figure 3, where the predicted solidification end is located at 9.6 m below the meniscus. A re-melting zone of the solidified shell in the mold, resulting from the recirculation flow of the molten steel, will be discussed in the next section. After exiting from the mold, the thickness of the solidified shell increases with distance below the meniscus.

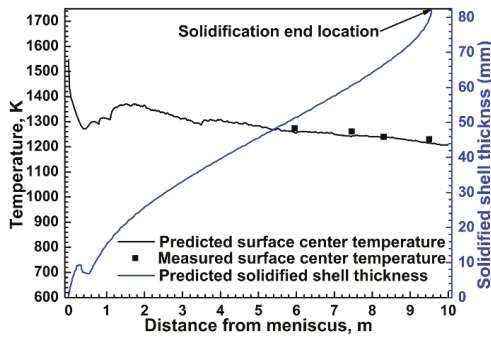


Figure 3. Solidification and temperature profiles along the casting direction.

3.2. Inclusion Motion and Entrapment in Mold

Figure 4 demonstrates the distribution of 5 μm inclusions inside the liquid pool of the mold at different moments. The solidifying front is represented by the gray iso-surface of the 0.6 liquid fraction of steel. The green spheres represent inclusions. It can be observed that inclusions that are injected into the mold are carried by the strong downward molten steel jet from the SEN port, at 0.5 s and 1.5 s after injection. At 5 s after injection, the inclusion motion that is carried by the molten steel jet flow continues, while some inclusions rise. Many inclusions concentrate in the lower part of the mold as a result of the weakening jet flow. At 15 s after injection, inclusions continue concentrating in the mold lower part, and some inclusions flow out of the mold, while the number of the rising inclusions increases. The rising inclusions move close to the solidifying front, which may be entrapped by the solidified shell, and then the inclusions move toward the mold top surface along the outer wall of the SEN. At 30 s after injection, some of the inclusions rise to the mold top surface and are removed, while many inclusions are transported into the liquid pool once again, following the molten steel. At 45 s after injection, the distribution of 5 μm inclusions in the liquid pool reaches a dynamic balance. It should be mentioned that the inclusion distribution inside the liquid pool of the mold is not perfectly symmetrical, which may be attributed to the random injection of inclusions from the inlet and the effect of the molten steel turbulence.

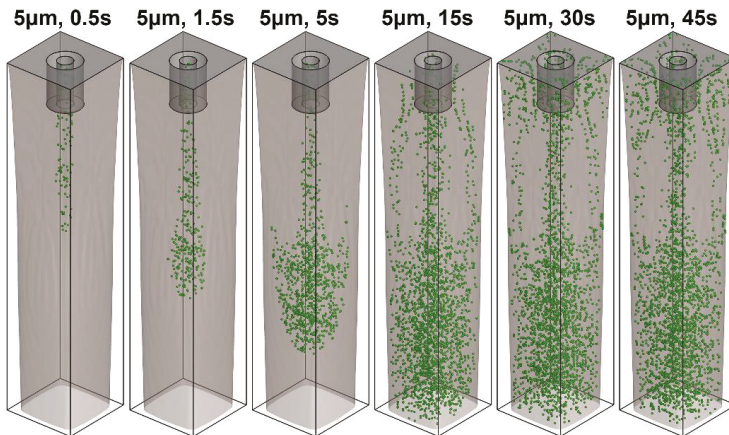


Figure 4. Transient distributions of 5 μm inclusions inside the liquid pool of the mold.

Figure 5 presents the inclusion distribution and the molten steel 3D streamline in the mold at 50 s after injection. As revealed by the predicted 3D streamline distribution, it can be seen that the molten steel is poured into the mold from the SEN port, leading to an impinging jet flow. A part of the poured molten steel flows straight downward and it exits the mold. However, the remainder flows upward along the solidified shell and creates an obvious recirculation flow zone (lower recirculation zone, LRZ) around the impinging jet in the upper zone of the mold. Subsequently, the molten steel flows toward the outer wall of the SEN, resulting in a relatively small recirculation zone (upper recirculation zone, URZ) around the SEN. It is the flow characteristic of the molten steel in the mold that leads to the transient motion and distribution of inclusions, as seen in Figure 4.

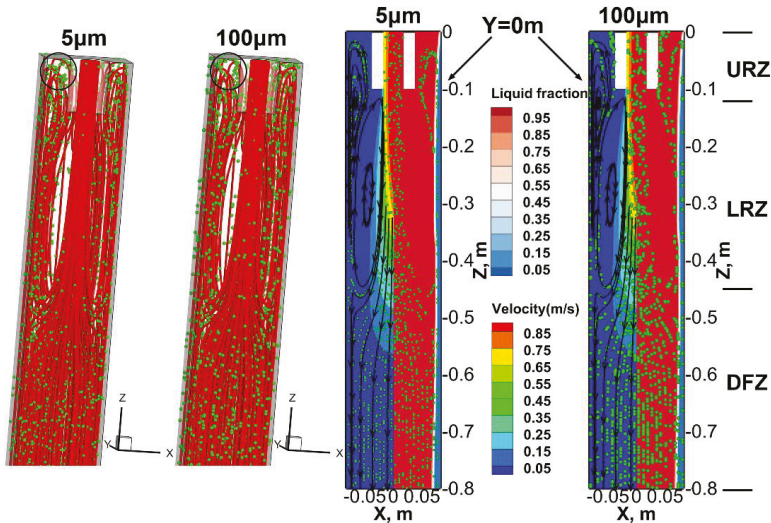


Figure 5. The inclusion (shown as green spheres) distribution, the molten steel streamline and contour plots of liquid fraction and velocity in the mold at 50 s after injection.

Figure 5 also shows the predicted two-dimensional (2D) molten steel streamline and contour plots of liquid fraction and velocity on the $Y = 0$ m plane in the mold at 50 s after injection. In addition, the inclusion distribution on the $Y = 0$ m plane, which is obtained by means of projecting the positions of inclusions between the $Y = -0.005$ m and the $Y = 0.005$ m planes onto the $Y = 0$ m plane, can be seen in Figure 5. The velocity magnitude of the molten steel in the impinging jet zone is obviously larger than that in other zones. Moreover, the velocity magnitude in the impinging jet zone decreases as the distance from the SEN port. The velocity magnitude of the molten steel becomes uniform at the mold lower region (downward flow zone, DFZ). Through the combination of the streamlines, liquid fraction contour plot, and the inclusion distribution on the $Y = 0$ m plane, it can be seen that inclusions that were carried by the downward molten steel would be entrapped by the solidifying front at the DFZ. Additionally, the lower recirculation flow of the molten steel leads to the solidified shell re-melting and inclusion entrapment. Similarly, at the URZ, the molten steel recirculation flow can also carry the inclusions to the solidifying front and make the inclusions be entrapped by the solidified shell.

At 50 s after injection, the 3D distribution of 5 μm inclusions has reached a dynamic balance. The 3D distribution of 100 μm inclusions in the mold has also achieved a dynamic balance. The inclusion distributions of the two size classes are similar, except at the black circle zone, where more inclusions in 100 μm rise to the top surface of the mold and are removed. The phenomenon is clearer on the $Y = 0$ m plane. Furthermore, the entrapping position of 100 μm inclusions is higher than that of 5 μm inclusions in the URZ. The entrapping positions of 100 μm inclusions at the DFZ and the LRZ are also

relatively higher than those of the 5 μm inclusions. It is assumed that this is due to the buoyancy force of the inclusions.

The predicted initial entrapment positions of inclusions with different sizes in the mold reveal that the larger inclusions are closer to the billet surface (Figure 6). This is because the entrapping positions of larger inclusions are higher than those of the smaller inclusions in the URZ with the effect of the buoyancy force. A higher entrapping position of inclusions in the URZ indicates that these inclusions are entrapped by a thinner solidified shell. Figure 6 also shows the variation of the predicted removal ratio of the inclusions with different sizes from the mold top surface with time. It can be seen from the predicted result that the removal ratios of the micro inclusions ($\leq 25 \mu\text{m}$) are apparently small, compared with those of the macro inclusions ($\geq 50 \mu\text{m}$). It is concluded that the motion and the entrapment of micro inclusions in the mold are mainly affected by the molten steel flow pattern, since the buoyancy force of micro inclusions is negligible. However, the motion and the entrapment of macro inclusions in the mold depend both on the molten steel flow pattern and the buoyancy force.

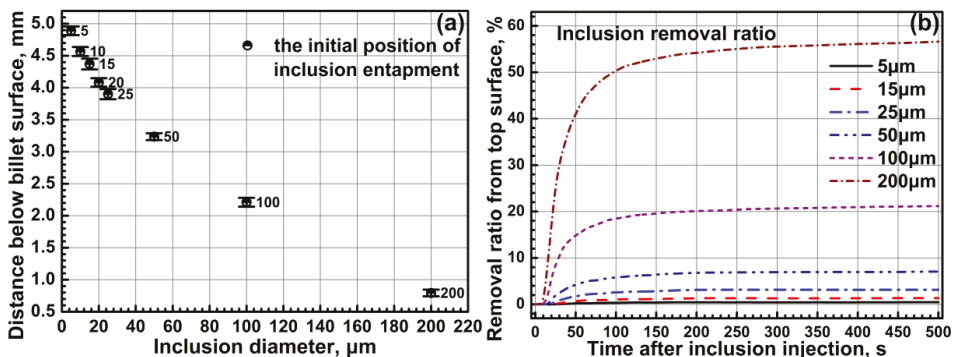


Figure 6. Predicted initial entrapment position (a) and removal ratio of inclusions with different sizes (b) in the mold.

3.3. Inclusion Motion and Entrapment in the Curved Part of the Strand

Figure 7 shows the distributions of 100 μm inclusions inside the liquid pool of the curved part of the strand at different times. The solidifying front is represented by the gray iso-surface of the 0.6 liquid fraction of steel. The green spheres represent inclusions. At 25 s after injection, the inclusions move into the FRZ, which is carried by the molten steel. At 50 s after injection, the inclusions move into the SCZ1. It is interesting to note that 100 μm inclusions shift to the solidifying front of the inner radius in the curved part of the strand as time goes on, while the solidifying front of the outer radius cannot entrap the inclusions. At 150 s after injection, the entrapment 100 μm inclusions terminates at the solidifying front of the inner radius.

In order to analyze the statistical entrapment positions of macro inclusions along the casting direction at 400 s after injection, the computational domains between the meniscus and the solidification end (9.6 m below the meniscus) are divided into 12 equal zones, respectively. Figure 8 shows the predicted entrapment ratios of the macro inclusions along the casting direction, and additionally, the terminal entrapment positions of 50 μm , 100 μm , and 200 μm inclusions at 400 s after injection. The entrapment ratio of the 100 μm inclusion decreases first, increases later, and then decreases to zero in the curved part of the strand. In addition, the entrapment ratio of the 100 μm inclusions reaches its peak value at the region of 2.4–3.2 m below the mold top surface. Moreover, the entrapment of the 100 μm inclusions terminates at the inner radius solidifying front at about 3.3 m below the meniscus. It is assumed that the flow pattern in the mold and the buoyancy force of inclusions lead to this phenomenon. A strong impinging jet flow of the molten steel is created by the straight port

SEN, resulting in many inclusions being transported into the curved part of the strand and then being entrapped by the local solidifying front. The buoyancy force leads to a deviation of the inclusion motion to the inner radius in the curved part of the strand. This phenomenon is more notable for 200 μm inclusions, as the buoyancy force of these inclusions is larger (Figure 8). This also explains why the entrapment of 50 μm inclusions terminates at a lower position under the meniscus.

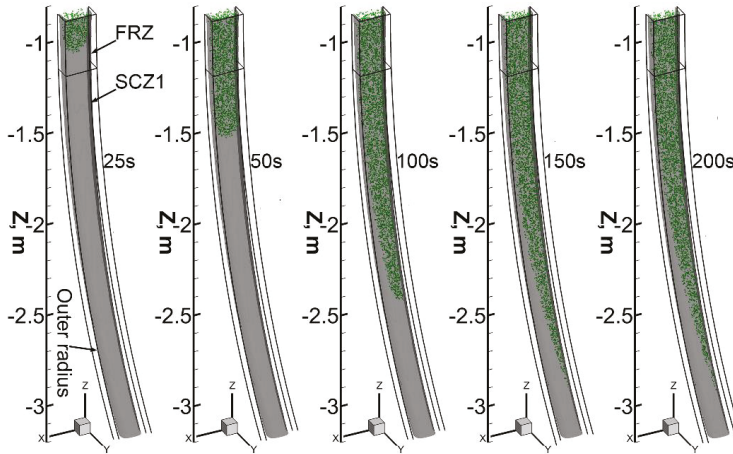


Figure 7. Transient distributions of 100 μm inclusions inside the liquid pool of the curved part of the strand.

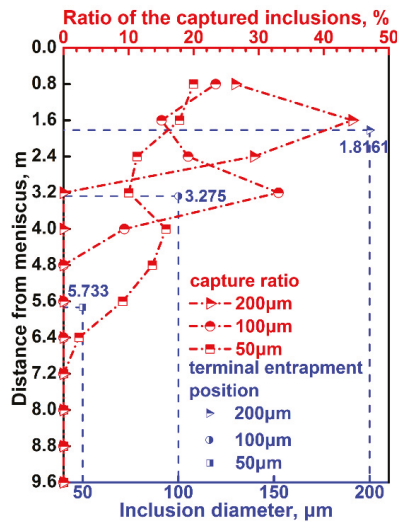


Figure 8. The predicted terminal entrapment positions and entrapment ratios of the macro inclusions along the casting direction.

3.4. Inclusion Distribution in the Solidified Strand

Due to the shift of the macro inclusions to the solidifying front of the inner radius while they move inside the liquid pool of the curved strand, an uneven distribution of the macro inclusions may

exist in the solidified strand. Figure 9 presents the distribution of inclusions on the cross section of the solidified strand, through projecting the positions of inclusions of each size class in the region of 9.6–10 m below the meniscus at 500 s onto a plane. Rectangles were used in order to indicate the approximate concentrating zone of inclusions. Inclusions that are inside the solidified shell profile at the mold exit indicate that they are entrapped in the curved part of the strand. It can be observed that the distribution of 3.5 μm inclusions in the solidified strand is uniform. However, the distribution of 7 μm inclusions in the solidified strand becomes inhomogeneous. The aggregation of 7 μm inclusions is found between the billet center and the inner radius. Furthermore, with the increase of the inclusion diameter, the aggregation is intensified, and the inclusions are closer to the inner radius.

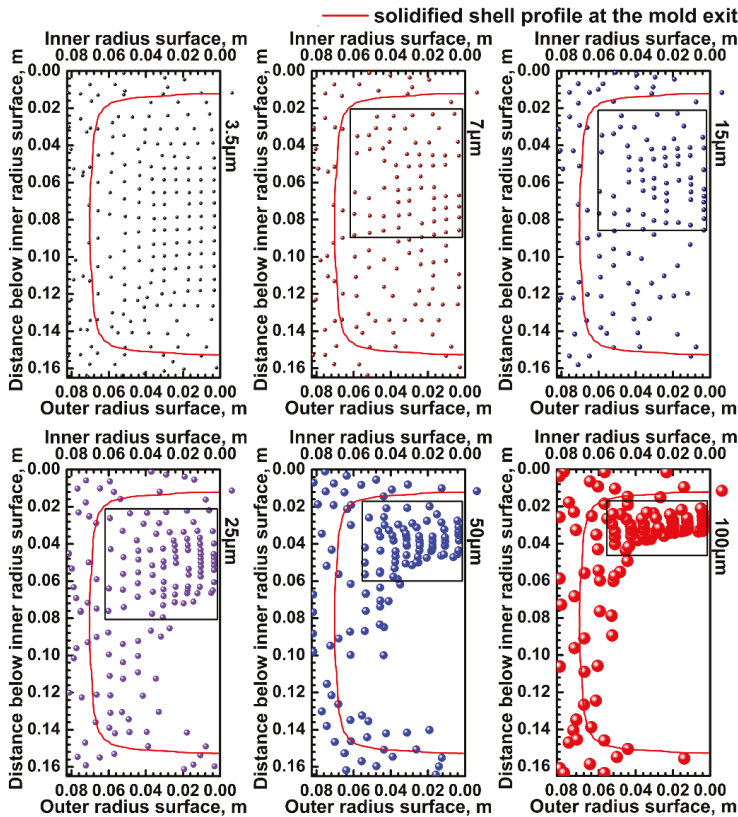


Figure 9. The predicted distributions of inclusions with different sizes on the cross section of the solidified strand.

In order to analyze the uneven distributions of inclusions in the solidified strand, a 15 mm thick zone in the center of the solidified strand has been selected (Figure 10). The positions of inclusions in each size class in the analysis zone have been gathered, and the median of the distances of these inclusions that are below the inner radius have been calculated. Moreover, a statistical parameter, coefficient of skewness, has been adopted to evaluate the distribution inhomogeneity of inclusions. To a certain extent, the distribution inhomogeneity of inclusions in the solidified strand can be reflected by the median and coefficient of skewness. The distributions of 3.5 μm and 5 μm inclusions in the solidified strand are even. However, for inclusions that are larger than 5 μm , the distributions become

uneven. Furthermore, through the coefficient of skewness, it can be found that the inhomogeneity is enhanced with the increase of the inclusion diameter.

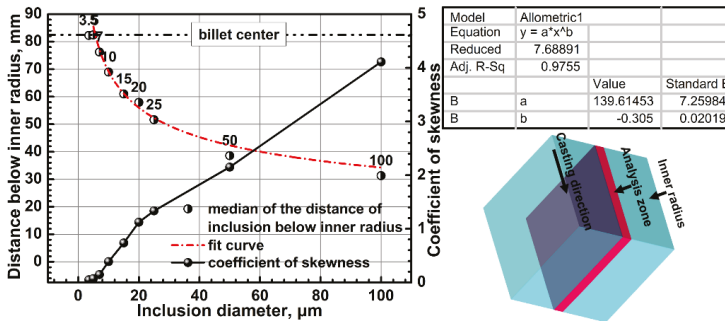


Figure 10. Variation of the distribution deviation of inclusions in the solidified strand.

3.5. Comparison Between the Predicted and the Experimental Results

Samples with the same process parameters and material properties adopted in the current work were obtained from a steel plant. The sampling schematic diagram can be seen in Figure 11. The steel samples were machined into 15 mm × 15 mm × 15 mm metallographic samples, and then these samples were polished and examined using EVO18, ZEISS scanning electron microscope (SEM). The numbers of inclusions in steel samples were automatically counted using the SEM control software INCAFeature (Oxford Instruments, Oxfordshire, England). The analyzed area of each steel sample was 11 × 11 mm². The inclusion size was determined by the equivalent circle diameter (ECD). Only inclusions that were above 2 μm ECD were counted. Manganese sulfide (MnS) inclusions that were precipitated during the solidification process were not counted. In total, 1263 inclusions were detected in the 11 steel samples (Figure 11). The number of inclusions in the samples decreases as the inclusion diameter increases. The largest of those detected inclusions is 38.78 μm . The measured inclusion number density reaches a maximum at the fourth steel sample from the inner radius, which is located between the inner radius and the center of the solidified strand.

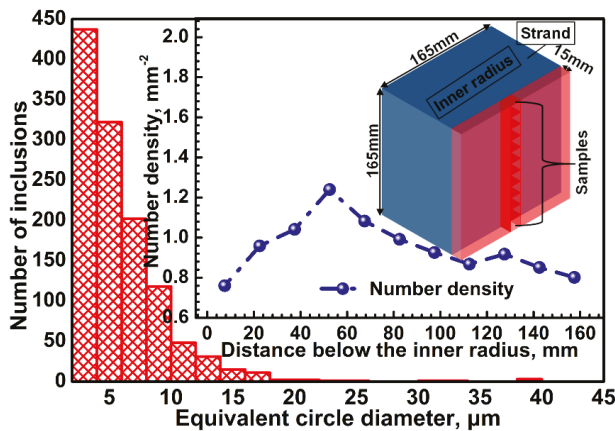


Figure 11. Sampling schematic diagram and the experimental result.

In order to compare the predicted result with the experimental result further, the detected inclusions in these steel samples are divided into four groups (2–5 μm , 5–10 μm , 10–20 μm , >20 μm),

according to size. For the four groups, their size weighted averages are 3.30 μm , 6.90 μm , 12.67 μm , and 30.00 μm , respectively. The predicted results are collected in the analysis zone shown in Figure 11.

Figure 12 presents the comparison between the predicted and the experimental results. Good agreement is found between the predicted result of inclusions in 3.5 μm and the experimental result of inclusions in 2–5 μm . Likewise, the predicted distribution of inclusions in 7 μm is in good agreement with the distribution of inclusions in 5–10 μm , according to the experiment. For the predicted result of inclusions in 15 μm and the experimental result of inclusions in 10–20 μm , their variation trends are similar (Figure 12c). The relatively large deviation between the inclusion size in the predicted result and the weighted average size in the experimental result may result in the deviation between the experimental and predicted results. Inclusions that were larger than 20 μm were rarely detected in the steel samples. As Figure 12d shows, the variation trend in the experimental result of inclusions larger than 20 μm is similar to that in the predicted results of 25 μm , 50 μm , and 100 μm inclusions. Through the experimental result, it can also be found that the distribution of inclusions smaller than 5 μm in the solidified strand is even. However, for inclusions that were larger than 5 μm , their distributions become uneven. This is consistent with the predicted result discussed above. The comparison between the predicted and the experimental results indicates that the inclusion motion model is valid.

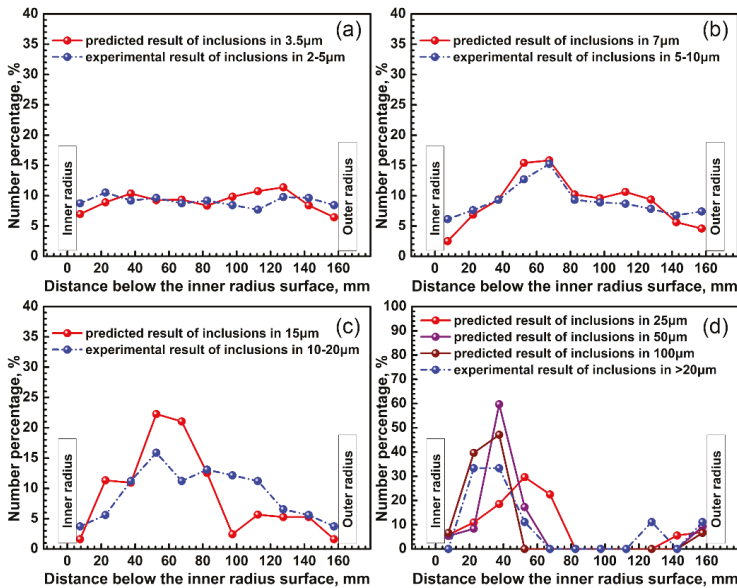


Figure 12. Comparison between the predicted and the experimental results: (a) 2–5 μm ; (b) 5–10 μm ; (c) 10–20 μm ; (d) >20 μm .

4. Conclusions

The present work has developed a three-dimensional numerical model coupling the flow field, solidification, and inclusion motion for a curved strand. Through the coupling model, we have investigated the inclusion motion and entrapment during the full solidification in a curved billet caster. The characteristics of the inclusion motion and entrapment in the mold and the curved part of the strand have been revealed. Moreover, the inclusion distributions in the solidified strand have also been presented. The conclusions are as follows:

1. the inclusion distribution inside the liquid pool of the mold is not perfectly symmetrical, resulting from the random injection of inclusions from the inlet and the effect of the molten steel turbulence;

2. the entrapping positions of larger inclusions are higher than those of smaller inclusions in the URZ with the effect of the buoyancy force. As a result, the initial entrapping positions of larger inclusions are more close to the billet surface;
3. the motion and entrapment of micro inclusions in the mold are mainly affected by the molten steel flow pattern, since the buoyancy force of micro inclusions is negligible. However, the motion and entrapment of macro inclusions in the mold depend both on the molten steel flow pattern and the buoyancy force;
4. owing to the effect of the buoyancy force, macro inclusions shift to the solidifying front of the inner radius in the curved part of the strand as time goes on, while the solidifying front of the outer radius cannot entrap the inclusions;
5. the distributions of inclusions smaller than 5 μm in the solidified strand are even. However, for inclusions that are larger than 5 μm , their distributions become uneven. Furthermore, the inhomogeneity is enhanced with the increase of the inclusion diameter; and,
6. good agreement is found between the predicted and experimental results. The comparison between the predicted and the experimental results indicates that the inclusion motion model is valid.

Author Contributions: J.Z. and Y.Y. conceived and designed the study; Y.Y. and Q.D. performed the numerical calculation; Y.Y. and Y.L. conducted the experiment. Y.L. and Q.D. analyzed the experimental data; Y.Y. and J.Z. wrote the paper.

Acknowledgments: The authors gratefully express their appreciation to the National Natural Science Foundation of China (51474023) for sponsoring this work.

Conflicts of Interest: The authors declare no conflict of interest.

References

1. Zhang, L. Nucleation, growth, transport, and entrapment of inclusions during steel casting. *JOM* **2013**, *65*, 1138–1144. [[CrossRef](#)]
2. Hu, Y.; Chen, W.; Wan, C.; Wang, F.; Han, H. Effect of deoxidation process on inclusion and fatigue performance of spring steel for automobile suspension. *Metall. Mater. Trans. B* **2018**, *49*, 569–580. [[CrossRef](#)]
3. Deng, X.; Ji, C.; Cui, Y.; Tian, Z.; Yin, X.; Shao, X.; Yang, Y.; McLean, A. Formation and evolution of macro inclusions in IF steels during continuous casting. *Ironmak. Steelmak.* **2017**, *44*, 739–749. [[CrossRef](#)]
4. Wang, X.; Li, X.; Li, Q.; Huang, F.; Li, H.; Yang, J. Control of stringer shaped non-metallic inclusions of Cao-Al₂O₃ system in API X80 linepipe steel plates. *Steel Res. Int.* **2014**, *85*, 155–163. [[CrossRef](#)]
5. Lei, H.; Geng, D.; He, J. A continuum model of solidification and inclusion collision-growth in the slab continuous casting caster. *ISIJ Int.* **2009**, *49*, 1575–1582. [[CrossRef](#)]
6. Lei, H.; Jiang, J.; Yang, B.; Zhao, Y.; Zhang, H.; Wang, W.; Dong, G. Mathematical model for collision-coalescence among inclusions in the bloom continuous caster with M-EMS. *Metall. Mater. Trans. B* **2018**, *49*, 666–676. [[CrossRef](#)]
7. Liu, Z.; Li, B. Large-eddy simulation of transient horizontal gas–liquid flow in continuous casting using dynamic subgrid-scale model. *Metall. Mater. Trans. B* **2017**, *48*, 1833–1849. [[CrossRef](#)]
8. Liu, Z.; Qi, F.; Li, B.; Jiang, M. Multiple size group modeling of polydispersed bubbly flow in the mold: An analysis of turbulence and interfacial force models. *Metall. Mater. Trans. B* **2015**, *46*, 933–952. [[CrossRef](#)]
9. Liu, Z.; Li, B.; Qi, F.; Cheung, S.C.P. Population balance modeling of polydispersed bubbly flow in continuous casting using average bubble number density approach. *Powder Technol.* **2017**, *319*, 139–147. [[CrossRef](#)]
10. Yu, H.; Zhu, M. Three-dimensional magnetohydrodynamic calculation for coupling multiphase flow in round billet continuous casting mold with electromagnetic stirring. *IEEE Trans. Magn.* **2010**, *46*, 82–86. [[CrossRef](#)]
11. Ho, Y.; Hwang, W. Numerical simulation of inclusion removal in a billet continuous casting mold based on the partial-cell technique. *ISIJ Int.* **2003**, *43*, 1715–1723. [[CrossRef](#)]
12. Li, B.; Tsukihashi, F. Numerical estimation of the effect of the magnetic field application on the motion of inclusion in continuous casting of steel. *ISIJ Int.* **2003**, *43*, 923–931. [[CrossRef](#)]

13. Liu, Z.; Li, B.; Jiang, M.; Fumitaka, T. Euler-Euler-Lagrangian modeling for two-phase flow and particle transport in continuous casting mold. *ISIJ Int.* **2014**, *54*, 1314–1323. [[CrossRef](#)]
14. Liu, Z.; Li, L.; Li, B. Large eddy simulation of transient flow and inclusions transport in continuous casting mold under different electromagnetic brakes. *JOM* **2016**, *68*, 2180–2190. [[CrossRef](#)]
15. Liu, Z.; Sun, Z.; Li, B. Modeling of quasi-four-phase flow in continuous casting mold using hybrid Eulerian and Lagrangian approach. *Metall. Mater. Trans. B* **2017**, *48*, 1248–1267. [[CrossRef](#)]
16. Trindade, L.; Nadalon, J.; Vilela, A.; Vilhena, M.; Soares, R. Numerical modeling of inclusion removal in electromagnetic stirred steel billets. *Steel Res. Int.* **2007**, *78*, 708–713. [[CrossRef](#)]
17. Wang, S.; De Toledo, G.; Välimaa, K.; Louhenkilpi, S. Magnetohydrodynamic phenomena, fluid control and computational modeling in the continuous casting of billet and bloom. *ISIJ Int.* **2014**, *54*, 2273–2282. [[CrossRef](#)]
18. Wang, Y.; Zhang, L. Fluid flow-related transport phenomena in steel slab continuous casting strands under electromagnetic brake. *Metall. Mater. Trans. B* **2011**, *42*, 1319–1351. [[CrossRef](#)]
19. Yang, Y.; Jönsson, P.; Ersson, M.; Nakajima, K. Inclusion behavior under a swirl flow in a submerged entry nozzle and mold. *Steel Res. Int.* **2015**, *86*, 341–360. [[CrossRef](#)]
20. Yang, Y.; Jönsson, P.; Ersson, M.; Su, Z.; He, J.; Nakajima, K. The influence of swirl flow on the flow field, temperature field and inclusion behavior when using a half type electromagnetic swirl flow generator in a submerged entry and mold. *Steel Res. Int.* **2015**, *86*, 1312–1327. [[CrossRef](#)]
21. Yu, H.; Zhu, M. Influence of electromagnetic stirring on transport phenomena in round billet continuous casting mould and macrostructure of high carbon steel billet. *Ironmak. Steelmak.* **2012**, *39*, 574–584. [[CrossRef](#)]
22. Zhang, L.; Aoki, J.; Thomas, B. Inclusion removal by bubble flotation in a continuous casting mold. *Metall. Mater. Trans. B* **2006**, *37*, 361–379. [[CrossRef](#)]
23. Zhang, L.; Wang, Y.; Zuo, X. Flow transport and inclusion motion in steel continuous-casting mold under submerged entry nozzle clogging condition. *Metall. Mater. Trans. B* **2008**, *39*, 534–550. [[CrossRef](#)]
24. Wang, Q.; Zhang, L. Determination for the entrapment criterion of non-metallic inclusions by the solidification front during steel centrifugal continuous casting. *Metall. Mater. Trans. B* **2016**, *47*, 1933–1949. [[CrossRef](#)]
25. Liu, Z.; Li, B. Effect of vertical length on asymmetric flow and inclusion transport in vertical-bending continuous caster. *Powder Technol.* **2018**, *323*, 403–415. [[CrossRef](#)]
26. Pfeiler, C.; Wu, M.; Ludwig, A. Influence of argon gas bubbles and non-metallic inclusions on the flow behavior in steel continuous casting. *Mater. Sci. Eng. A* **2005**, *413–414*, 115–120. [[CrossRef](#)]
27. Liu, Z.; Li, L.; Li, B.; Jiang, M. Large eddy simulation of transient flow, solidification, and particle transport processes in continuous-casting mold. *JOM* **2014**, *66*, 1184–1196. [[CrossRef](#)]
28. Jin, K.; Vanka, S.; Thomas, B. Large eddy simulations of electromagnetic braking effects on argon bubble transport and capture in a steel continuous casting mold. *Metall. Mater. Trans. B* **2018**. [[CrossRef](#)]
29. Jin, K.; Thomas, B.; Ruan, X. Modeling and measurements of multiphase flow and bubble entrapment in steel continuous casting. *Metall. Mater. Trans. B* **2016**, *47*, 548–565. [[CrossRef](#)]
30. Lei, S.; Zhang, J.; Zhao, X.; He, K. Numerical simulation of molten steel flow and inclusions motion behavior in the solidification processes for continuous casting slab. *ISIJ Int.* **2014**, *54*, 94–102. [[CrossRef](#)]
31. Yin, Y.; Zhang, J.; Lei, S.; Dong, Q. Numerical study on the capture of large inclusion in slab continuous casting with the effect of in-mold electromagnetic stirring. *ISIJ Int.* **2017**, *57*, 2165–2174. [[CrossRef](#)]
32. Jin, K.; Thomas, B.; Liu, R.; Vanka, S.; Ruan, X. Simulation and validation of two-phase turbulent flow and particle transport in continuous casting of steel slabs. *IOP Conf. Ser. Mater. Sci. Eng.* **2015**, *84*, 012095. [[CrossRef](#)]
33. Pfeiler, C.; Thomas, B.; Wu, M.; Ludwig, A.; Kharicha, A. Solidification and particle entrapment during continuous casting of steel. *Steel Res. Int.* **2008**, *79*, 599–607. [[CrossRef](#)]
34. Lei, S.; Zhang, J.; Zhao, X.; Dong, Q. Study of molten steel flow and inclusions motion behavior in the solidification processes for high speed continuous casting slab by numerical simulation. *Trans. Indian Inst. Met.* **2016**, *69*, 1193–1207. [[CrossRef](#)]
35. Yuan, Q.; Thomas, B.; Vanka, S. Study of transient flow and particle transport in continuous steel caster molds: Part I. Fluid flow. *Metall. Mater. Trans. B* **2004**, *35*, 685–702. [[CrossRef](#)]
36. Yuan, Q.; Thomas, B.; Vanka, S. Study of transient flow and particle transport in continuous steel caster molds: Part II. Particle transport. *Metall. Mater. Trans. B* **2004**, *35*, 703–714. [[CrossRef](#)]

37. Liu, Z.; Li, B. Transient motion of inclusion cluster in vertical-bending continuous casting caster considering heat transfer and solidification. *Powder Technol.* **2016**, *287*, 315–329. [[CrossRef](#)]
38. Thomas, B.; Yuan, Q.; Mahmood, S.; Liu, R.; Chaudhary, R. Transport and entrapment of particles in steel continuous casting. *Metall. Mater. Trans. B* **2014**, *45*, 22–35. [[CrossRef](#)]
39. Liu, Z.; Li, B.; Zhang, L.; Xu, G. Analysis of transient transport and entrapment of particle in continuous casting mold. *ISIJ Int.* **2014**, *54*, 2324–2333. [[CrossRef](#)]
40. Wang, S.; Zhang, L.; Wang, Q.; Yang, W.; Wang, Y.; Ren, L.; Cheng, L. Effect of electromagnetic parameters on the motion and entrapment of inclusions in FC-mold continuous casting strands. *Metall. Res. Technol.* **2016**, *113*, 205. [[CrossRef](#)]
41. Zhang, L.; Wang, Y. Modeling the entrapment of nonmetallic inclusions in steel continuous-casting billets. *JOM* **2012**, *64*, 1063–1074. [[CrossRef](#)]
42. Dong, Q.; Zhang, J.; Liu, Q.; Yin, Y. Magneto-hydrodynamic calculation for electromagnetic stirring coupling fluid flow and solidification in continuously cast billets. *Steel Res. Int.* **2017**, *88*, 1700067. [[CrossRef](#)]
43. Dong, Q.; Zhang, J.; Yin, Y.; Wang, B. Three-dimensional numerical modeling of macrosegregation in continuously cast billets. *Metals* **2017**, *7*, 209. [[CrossRef](#)]



© 2018 by the authors. Licensee MDPI, Basel, Switzerland. This article is an open access article distributed under the terms and conditions of the Creative Commons Attribution (CC BY) license (<http://creativecommons.org/licenses/by/4.0/>).

Article

Laboratory Experimental Setup and Research on Heat Transfer Characteristics during Secondary Cooling in Continuous Casting

Yazhu Zhang ^{1,2}, Zhi Wen ^{1,*}, Zengwu Zhao ^{2,*}, Chunbao Bi ², Yaxiang Guo ² and Jun Huang ²

¹ School of Energy and Environment Engineering, University of Science and Technology Beijing, Beijing 100083, China; zhangyazhu212@imust.edu.cn

² Key Laboratory of Integrated Exploitation of Bayan Obo Multi-Metal Resources, Inner Mongolia University of Science and Technology, Baotou 014010, China; 15942914079@163.com (C.B.); 15847652053@163.com (Y.G.); hjun8420@imust.edu.cn (J.H.)

* Correspondence: wenzhi@me.ustb.edu.cn (Z.W.); zhengwu@imust.edu.cn (Z.Z.); Tel.: +86-137-01110-4376 (Z.W.); +86-186-0472-1886 (Z.Z.)

Received: 23 November 2018; Accepted: 4 January 2019; Published: 10 January 2019

Abstract: Spray cooling is a key technology in the continuous casting process and has a marked influence on the product quality. In order to obtain the heat transfer characteristics, which are closer to the actual continuous casting to serve the design, prediction and simulation, we created an experimental laboratory setup to investigate heat transfer characteristics of air mist spray cooling during the continuous casting secondary cooling process. A 200-mm thick sample of carbon steel was heated above 1000 °C, and then cooled in a water flux range of 0.84 to 3.0 L/(m²·s). Determination of the boundary conditions involved experimental work comprising an evaluation of the thermal history and the heat flux and heat transfer coefficient (HTC) at the casting surface using inverse heat conduction numerical schemes. The results show that the heat fluxes were characterized via boiling curves that were functions of the slab surface temperatures. The heat flux was determined to be 2.9×10^5 W/m² in the range of 1100 to 800 °C with a water flux of 2.1 L/(m²·s). The critical heat flux increased with the increase of water flux. The HTC was close to a linear function of water flux. We also obtained the relation between the HTC and the water flux in the transition boiling region for surface temperatures of 850 to 950 °C.

Keywords: air mist spray cooling; continuous casting; heat flux; HTC; secondary cooling

1. Introduction

In continuous casting, molten steel is poured from a tundish into a water-cooled mould and a partially solidified billet or slab is withdrawn from the bottom of the mould. The billet or slab is then cooled by a water spray (this is the secondary cooling process) so that the solidified billet or slab is produced constantly and continuously. Continuous casting is a bridge between steelmaking and rolling. Secondary cooling is an essential part of continuous casting and can strongly influence the quality of billets or slabs. The cooling must be controlled relative to the casting speed to avoid the formation of internal and surface cracks.

Steel solidification behavior is influenced by heat transportation under the specific cooling conditions. In the secondary cooling zone, the heat transfer behavior of the billet or slab surface is directly linked to the characteristics of the spray. These can be manipulated to control the solidification process, and in turn the billet or slab quality and the casting productivity. In an attempt to meet high billet or slab quality requirements, heat transfer in the mould and the secondary cooling have received much research attention. Due to requirements for high quality, the secondary cooling technology of

continuous casting has been developed with specially designed nozzles, finer waterway control, and a more effective water injection strategy.

In recent years, numerical simulation has been widely applied to design and optimize the secondary cooling process. An accurate simulation, however, is strongly dependent on the level of understanding of the physical mechanism of the casting process, the high-temperature properties of the material involved, and thermal boundary conditions. Laboratory experiments can provide a database that can be used to specify the boundary conditions in mathematical models of secondary cooling. Thermal boundary conditions that characterize the boiling heat transfer in secondary cooling are applicable for industrial processes after validation with reliable experiments.

Important work on spray cooling can be found in the literature [1–6]. The main cooling effect derives from evaporation. Heat transfer is influenced by water flow, droplet size, and velocity. Most studies either focused on the macroscopic effect of the sprays on the heat transfer rate or attempted to characterize the heat transfer processes during the impact of the spray on a surface. Many efforts have been made to understand the effect of changing the magnitude of the heat flux or the heat transfer coefficient (HTC) in different boiling heat transfer regimes. Thomas et al. [7,8] carried out laboratory measurements of water flow and heat transfer during spray cooling. Their research focused on the conditions of the surface of the steel strand in the secondary spray cooling zones with water jet–air mist cooling. The steel surface temperature range was 1200 °C to 200 °C. Ramstorfer et al. [9] developed a dynamic spray cooling experimental platform where they measured the HTCs due to spray cooling using an experimental setup, allowing spray cooling up to a surface temperature of 1250 °C. Horský et al. [10] developed experimental methods and numerical models for spray-cooled surface heat transfer. Those papers discussed heat transfer during spray cooling and optimization of the cooling process. Ito et al. [11] also investigated the effects of the hydraulic pressure and water flow rate of a cooling water spray on cooling intensity and developed a more efficient secondary cooling system with a high-pressure water spray. Tsutsumi et al. [12] did laboratory experiments on the cooling capacities of hydraulic and mist spray cooling by several kinds of spray nozzles. They proposed an equation for HTC that considered the spray thickness and collision pressure. El-Bealy [13] studied the degree to which homogeneity of cooling conditions with air mist nozzles improved slab quality. The Brno University of Technology Heat Transfer and Fluid Flow Laboratory [14] established reliable techniques to measure the effects of individual nozzles and combinations of nozzles to determine the HTCs. They also discussed methods for determining the HTCs and using them in a solidification model.

Most industrial spray nozzles are polydispersed, which allows them to generate water droplets with a wide range of sizes and velocities. This, in addition to the complex interaction of spray droplets, makes it difficult to predict (by single or multiple sprays) the performance of an industrial spray nozzle. Extensive laboratory studies have been done on the heat transfer of drops and sprays at low mass flux or for a single spray nozzle. However, data on industrial spray nozzles with high mass flux or on multiple spray nozzles are very scarce. Meanwhile, thinner samples with short cooling times are used in laboratory studies, which have led to a measured data shortage in high-temperature ranges. Due to fewer measurement data, the measurement error has become larger. It has become essential to use thicker samples and closer to the actual billet or slab. Experiments closely emulating the actual process of secondary cooling in continuous casting are particularly important.

In the paper, we developed a multifunctional experimental setup, enabling a quantitative understanding of the secondary cooling of a continuous casting. The objective was to explore and obtain data that characterized heat transfer at high temperatures using multiple air mist spray nozzles. The calculated temperature profile, heat flux and HTCs provided insight and useful data for the development of cooling strategies for continuous casting.

2. Establishing the Experimental Setup

Compared with industrial secondary cooling of continuous casting, a laboratory-scale simulator is cost effective because it is not necessary to interrupt actual steel production. The laboratory simulator

provides more flexibility to change the range of operational parameters required for optimizing the secondary cooling process and developing new continuous casting technologies. By separating the secondary cooling from the casting in the experimental setup, we avoid the operational risk associated with using liquid metal. This enables us to simulate air-mist spray cooling in the secondary cooling process.

An overview of the system configuration is shown in Figure 1a,b. The experimental setup consisted of an air–water spray, slab heating, slab cooling and data acquisition and analysis systems. To simulate the features of an industrial air mist spray, a laboratory air–water spray system was designed, as shown in Figure 2. The system consisted of water tanks, pumps, an air compressor, an air pressure tank, electromagnetic flowmeters, temperature transmitters, pressure transmitters, electric control valves, metal hoses and spray racks.

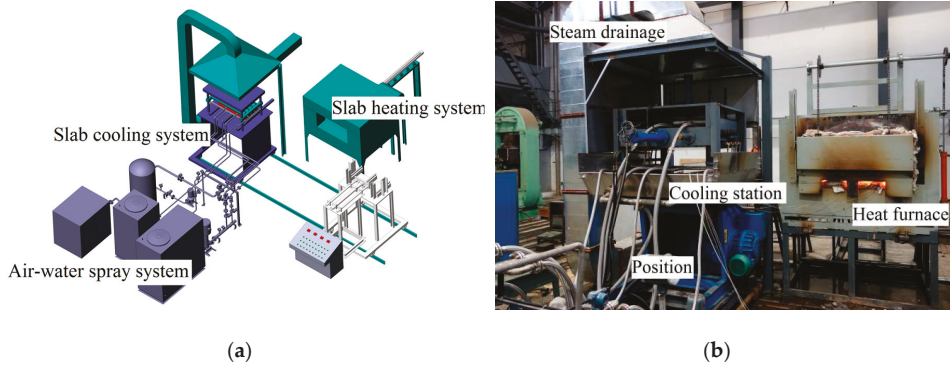


Figure 1. Schematic presentation (a) and equipment (b) of the experimental setup.



Figure 2. Air-water spray system.

Cooling water was supplied to the setup from the water tank. A valve was used to adjust the flow to the desired flowrate and pressure. The flow parameters were measured with the flowmeters and pressure gauges, which were controlled by the control software.

Nozzle alignments and cooling parameters are the main factors influencing the secondary cooling of continuous casting. The experimental setup was designed to meet the requirements of different nozzles with an extensive range of mass fluxes. The system could be adjusted to test the cooling effects of different spray configurations. The slab heating system comprised a feeding car, a heating furnace and a discharging electric actuator. After the desired temperature was reached, the slab was transported into the cooling station by a rack and pinion structure actuated by a motor. The slab cooling system included the cooling station, a slab depressing device, a reciprocating motion device,

a drainage pipe, water pumps, electromagnetic flowmeters and the steam drainage system. It enabled spray rack replacement, slab movement simulation, adjustment of the slab cooling angle, and water and vapor discharge. Depending on the dynamic adjustment of the slab position by hydraulic pressure, it was possible to continuously simulate the position of the slab throughout the entire secondary cooling zone. The cooling station was placed in the positioner with 0° to 90° tilting to meet the slab arc change from initial mould position to final level position.

Figure 3 shows the top side cooling device that used three rows and four columns of nozzles with a 120° impingement angle. According to the nozzle angle, the overlap between the two nozzles was designed with nozzle manufacturer's suggestion. The jets coalesced into a mist curtain on the slab surface.

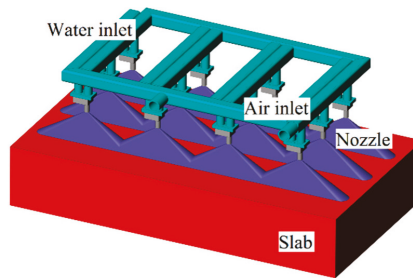


Figure 3. Schematic of the arrangement of the nozzles.

In this way, the slab contact conditions (e.g., surface structure and clamping roller) could be manipulated to be similar to those used in industrial practice. There were four clamping rollers with a 120-mm diameter and a 160-mm separation distance that could clamp a slab with a 100- to 350-mm thickness.

Figure 4 shows the clamping rollers with the top spray configuration. During the tests, the slab surface was exposed to the air mist nozzles through the gap between the rollers. The heat was conducted to the slab surface and removed by the cooling air and water. The cooling process consumed much water and air, and heat was released during the process. Vapor and cooling water were collected and directed into a drain while the apparatus operated.

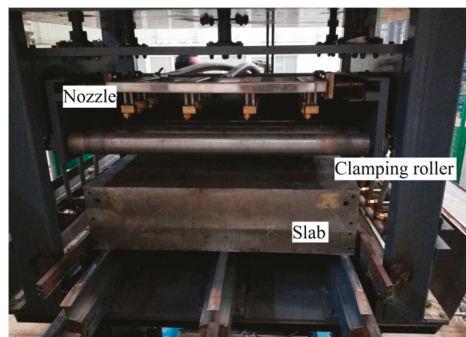


Figure 4. The clamping rollers with no contact slab.

A data acquisition system was used to monitor the temperature, pressure, flow rate, and so forth during heating and cooling. It comprised a computer, a data acquisition box, K-type thermocouples and a software package, which were used for process parameter acquisition, calculation and data display. The thermocouples were inserted into the subsurfaces of the slabs. The slabs were then

preheated to a desired initial temperature and transported to the cooling system. The measured temperature was used as an input for calculating the inverse heat conduction. By using the calculated results, we could evaluate the local heat flux at the boundaries. The heat flux was expressed via a boiling curve with different variables. The experimental setup provided the flexibility to adjust the operational parameters (mass flux, heating temperature, casting speed, etc.), enabling study of the heat transfer in secondary cooling. The technical parameters of the setup are shown in Table 1.

Table 1. Technical parameters of the pilot experimental set-up.

Condition	Parameter
Max. heating slab size	1100 × 600 × 350 mm(thickness)
Max. heating temperature	1250 °C
Max. water flow	18.0 m ³ /h
Max. air flow	6.0 m ³ /min
Max. water pressure	1.0 MPa
Max. air pressure	0.4 MPa
Max. nozzle array	3 rows and 4 columns
Max. temperature synchronous acquisition frequency	5 Hz
Cooling condition	Single or multi-side cooling

3. Inverse Heat Conduction Problem

Normally, it is difficult to measure surface heat flux and temperature of a slab undergoing air mist spray cooling. When thermocouples are set at a certain distance from the surface of the slab to measure temperatures at different positions, a mathematical model can be used to calculate the surface heat flux and surface temperature [15,16]. The heat boundary condition can be calculated by recording the temperature as a function of time, which is in the form of an inverse heat transfer problem [17].

We used thermocouples embedded in the slab at certain depths to measure cooling curves at different positions. The surface temperature and heat flux of the slab were calculated using the Beck's sequential function specification method [18,19]. As a result of the calculation, the relation between the HTC and the slab surface temperature could be obtained. In this study, we regarded the internal heat transfer in the slab as one-dimensional unsteady heat conduction along the direction of the spray cooling, ignoring the heat loss from the side of the slab. Figure 5 shows the physical model of the inverse heat conduction problem during the cooling.

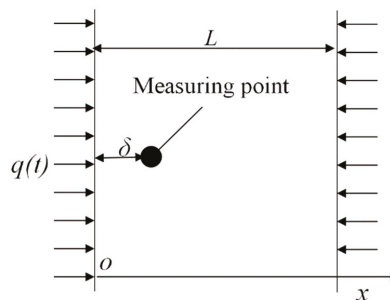


Figure 5. Schematic of the physical model of the inverse heat conduction problem.

The slab was heated to T_0 and cooled by the heat flux $q(t)$. A thermocouple was embedded at $x = \delta$ to record the temperature history at a time interval of Δt . The aim was to calculate $q(t)$ using the

measured temperature data with known initial conditions and the thermophysical properties of the materials involved in the system. The governing equation and boundary conditions were

$$\begin{aligned} \rho C_p(T) \frac{\partial T}{\partial t} &= \frac{\partial}{\partial x} \left(k(T) \frac{\partial T}{\partial x} \right) \\ T(x, 0) &= T_0 \\ T|_{x=\delta} &= Y(t) \\ -k \partial T / \partial x|_{x=L} &= 0 \\ q(t) &= -k \partial T / \partial x|_{x=0} \end{aligned} \quad (1)$$

where ρ is the slab density, δ is the distance between the outer surface of the slab and the thermocouple, k is the conductivity, T is the slab temperature, T_0 is the initial slab temperature, C_p is heat capacity, x is the thickness direction coordinate, and $Y(t)$ is the measured temperature. In the model, T_0 and $Y(t)$ were known; only the surface heat flux $q(t)$ had to be solved. Since air mist cooling is a transient process, the temperature field and the heat flux q_M at a certain time t_M can be solved for if the temperature field $T_{M-1}(x)$ and the heat flux q_{M-1} at t_{M-1} have been determined. Assuming $q(t) = q_M$, which is constant when $t_{M-1} < t < t_M$, Equation (1) can be modified as Equation (2):

$$\begin{aligned} \rho C_p(T) \frac{\partial T}{\partial t} &= \frac{\partial}{\partial x} \left(k(T) \frac{\partial T}{\partial x} \right) \\ -k \partial T / \partial x|_{x=0} &= \begin{cases} q_M = \text{Const} & t_{M-1} < t < t_M \\ q(t) & t > t_M \end{cases} \\ -k \partial T / \partial x|_{x=L} &= 0 \\ T(x, t_{M-1}) &= T_{M-1}(x) \end{aligned} \quad (2)$$

In this work, a sensitivity coefficient $Z(x, t) = \partial T(x, t) / \partial q_M$ was introduced to evaluate the sensitivity of the measured temperature point error. In Beck's method, the heat flux $q(t)$, is discretized into a series of q_i over a measurement interval Δt . The heat flux guess is kept constant within a period of time, $r\Delta t$, where r is the number of future time steps. Solved as a forward heat conduction problem, the predicted temperature by using the applied heat flux guess q_i can be obtained at $t = i + r\Delta t$. In this way, the value of q_i in each time interval can be found to minimize the difference between the measured and calculated temperatures. The surface heat flux at different times is therefore calculated by defining the least squares error function. A program was written in Fortran to solve the one-dimensional transient heat conduction problem. In the process of calculation, the measurement interval Δt was 0.25 s, and the number of future time steps r was 10. Thermocouples were embedded at $x = 20$ mm to record the temperature history. The thermal properties of the materials used in the calculation were functions of temperature and are shown in Table A1. In the course of calculation, it was considered that the steel density 7850 Kg/m^3 was constant. After programming, one of the parameters about the number of mesh points needed to be tested to investigate the grid independence of the results. When the number of mesh points was greater than 400, the results do not change. The number of mesh points used in this paper was 1000.

4. Experimental Results and Discussion

One of the goals of the setup was to obtain experimental data under industrial heat flux boundary conditions for describing the boiling heat transfer in the secondary cooling of continuous casting. Precise temperature measurement was a key for a reliable heat transfer measurement [20]. Several 8-mm diameter holes were drilled 180 mm deep from the side of the 200-mm-thick slab perpendicular to the casting direction. The holes were drilled with flat bottoms to ensure that the tips of the thermocouples could touch the bottoms of the holes. A short distance from the cooling surface to the holes was required to reduce the time delay as the thermocouples responded to the changes in surface heat flux. In this experiment, the thermocouples were inserted 20 mm from the cooling surface. The thermocouples' fastening devices were welded to the surface of the slab to push

the thermocouples' tips into contact with the bottoms of the holes. The gaps in the holes were filled with refractory cotton.

Figure 6 shows the armored K-type thermocouples that were inserted into the holes and "locked" inside by fastening devices. The locations of thermocouples numbered 1 to 5 are also shown in the figure. The thermocouples were far away from the edge of the slab to ensure a reduced heat loss effect. The thermocouple NO.1 and NO.3 were arranged inside the slab under the clamping roller respectively. The NO.2 was in the middle of the two clamping rollers. The slab was tilted 15° from the horizontal position to simulate the slab position.

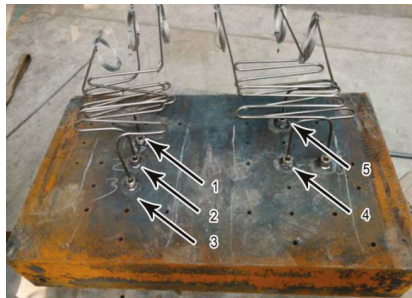


Figure 6. Sketch of the locations of thermocouples.

The air mist spray characteristics, such as water distribution profiles, droplet velocity and the Sauer mean diameter, had an effect on heat transfer. These parameters depended on atomization and gas-water parameters of the nozzle. The main experiment parameters are shown in Table 2. Due to the swing of the spray cooling racks and the overlapping between the nozzles, the uniformity of the water distribution in the vertical and horizontal casting direction was guaranteed. It could be considered that the slab surface cooling was homogeneous. The paper focused on the average convection heat transfer coefficient in secondary cooling. The average water flux was defined as a ratio of water flow to the area of the cooling surface of the slab. The water flux was 0.84 to 3.0 L/(m²·s) in the experiment. The nozzle arrangements with three rows and four columns were derived from the industrial continuous casting in this paper. The experimental nozzle model used was HPZ5.0-120B2.

Table 2. Parameters.

Experimental Condition	Parameter Value
Slab size	1100 × 600 × 200 mm
Material	ASTM A572 Gr.50
Air pressure	0.2 MPa
Water flux	2.1 L/(m ² ·s)
Nozzle distance from slab surface	180 mm
Heating target temperature	1150 °C
Temperature sampling frequency	4 Hz
Cooling condition	Top cooling
Water temperature	15.2 °C
Experimental nozzle model	HPZ5.0-120B2

Figure 7. shows a typical slab cooling in the experiment setup for a top spray configuration at a water temperature of 15.2 °C. Clearly, much vapor was generated during cooling, and the slab was cooled from the surface.



Figure 7. Slab cooling process.

Typical temperature readings relative to time curves during the spray cooling are shown in Figure 8. Regardless of the thermocouple location, the time–temperature curves were similar. A high cooling rate was observed, and the slab temperature dropped drastically. Due to the strong relation between the heat flux and the surface temperature, heat extraction rates changed rapidly with time.

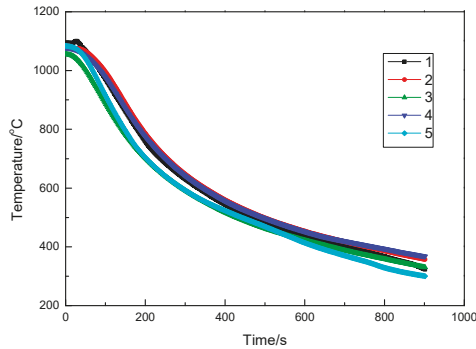


Figure 8. Temperature evolution during cooling at positions 1 to 5.

The inverse heat transfer algorithm was applied to calculate heat fluxes by using the measured temperature profile data. The calculated heat fluxes were plotted as functions of surface temperatures at each thermocouple location to determine the boiling curve.

Figure 9 shows the relation between the surface temperature and the heat flux at different measuring positions. It can be seen that the heat flux was not linearly related to the surface temperature. The five thermocouples' average heat flux of the slab first increased to a maximum value when the slab was cooled to approximately 574.2 °C, and then decreased from the peak value with further cooling. The maximum average heat flux was $5.0 \times 10^5 \text{ W/m}^2$ at 572.4 °C. At 1000 °C, the average heat flux was $2.2 \times 10^5 \text{ W/m}^2$. In the temperature range from 1100 to 800 °C, the average heat flux was $2.9 \times 10^5 \text{ W/m}^2$. Comparing the heat flux at the different thermocouple positions, better vapor discharge conditions resulted in faster cooling and a higher heat flux.

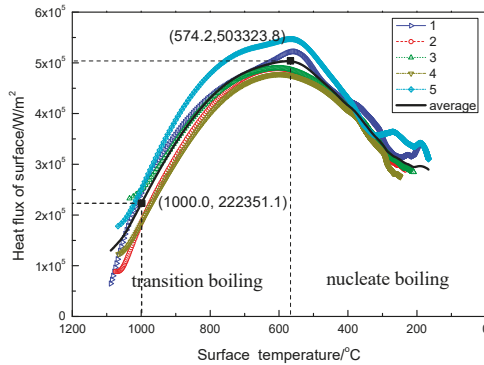


Figure 9. Relationship between surface temperature and heat flux.

As the simulated casting speed was 1.8 m/min, all thermocouples areas were cooled by sprays and support rolls. Each thermocouple reflected the average heat transfer on the surface. The NO.5 thermocouple was located in the lower part of the sample. Good steam exhaust conditions resulted in the greater heat flux.

The surface temperature history experienced two distinct regimes. The boiling curve allowed a better understanding of the physical state of the surface [21]. The first turn in the curve coincided with the starting time of the spray cooling, from radiation to transition boiling. The second turn coincided with the critical heat flux (CHF), from transition boiling to nucleate boiling. At high surface temperatures, where film boiling was dominant, a vapor film near the solid hot surface minimized direct droplet contact time with the surface, resulting in a low heat-transfer rate. As the surface temperature decreased, the droplets began to penetrate the vapor film, and a sharp increase in the heat transfer rate was observed. After reaching the CHF, the heat flux decreased, going through the nucleate boiling regime and finally to convection or one-phase cooling.

The air mist spray heat transfer curve was similar to that of pool boiling in all the boiling regimes. However, we found that the cooling curve did not experience the Leidenfrost point due to the absence of stable film boiling. This can be explained by the following four circumstances. First, the distance between the thermocouple and the cooled surface was 20 mm, the thermocouple's measurement delay resulted in the experiment not showing any Leidenfrost temperature. Second, the air and water flow rate are high in industrial conditions, but the residence time was short in the high-temperature region under experiment conditions. Therefore, the temperature point of Leidenfrost was not obvious. Third, the liquid droplets on the slab did not form a layer under the air mist spray cooling because the spray carried substantial momentum, which pushed the residual droplets away [22]. Fourth, the cooling steel surface oxidized, forming an oxide layer that increased the slab roughness. The oxidation of the surface had the effect of raising the gasification nucleation number.

Figure 10 shows the relation between surface temperature and HTC. It could be seen that the HTC linearly varies with the temperature from 1100 to 500 °C. As temperatures decreased from 1100 to 800 °C, the average HTC linearly increased from 120.0 W/m²·K to 542.6 W/m²·K. At a CHF temperature of 574.2 °C, the average HTC was 888.9 W/m²·K.

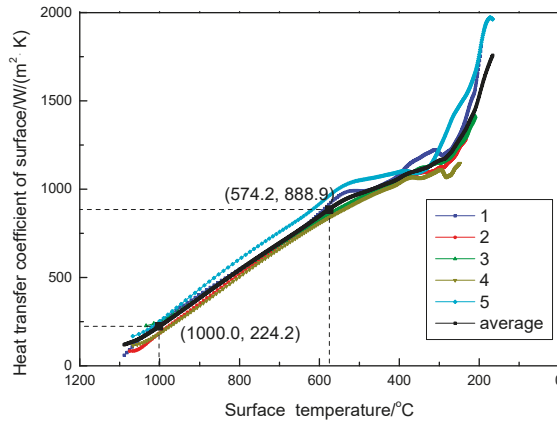


Figure 10. Relationship between surface temperature and HTC.

Using the method developed by this paper, we measured the heat transfer boiling curve of another condition with water fluxes of 0.84 L/(m²·s) and 3.0 L/(m²·s). The effect of the cooling water flux was assessed by comparing the heat transfer characteristics of the tests.

Similar slopes for the transition boiling and nucleate boiling regime were observed for different water fluxes during cooling and shown in Figure 11a. The HTC curve showed a typical linear relation, as shown in Figure 11b. The heat flux with a water flux of 3.0 L/(m²·s) was higher, especially the CHF. There was a clear trend of increased CHF with water flux. Higher water flux led to more droplets breaking the vapor film and accelerating the steam discharge, strengthening the heat transfer on the slab surface.

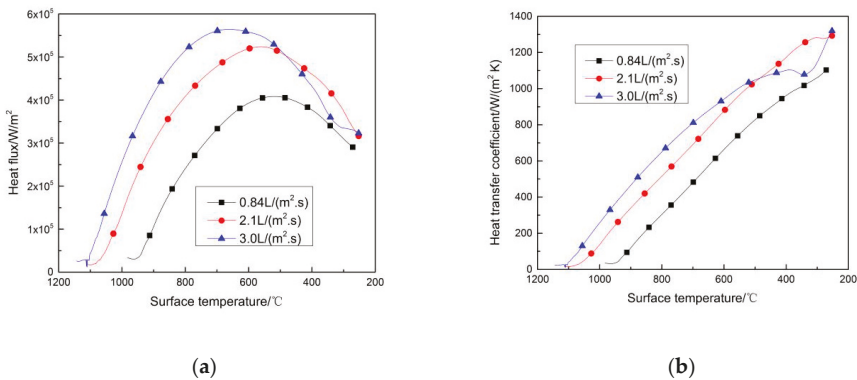


Figure 11. Heat characteristics with different water flux for (a) heat flux; (b) HTC.

The HTC as a function of the temperature difference between the steel surface and the water flux was found to be particularly useful to apply to the solidification model, as shown in Figure 12. We concluded that the HTC was a close linear function of water mass flux for surface temperatures of 850 to 950 °C. The integrated HTC for the section can be described by the generic equation $HTC = aG^b$, where a and b are constants determined experimentally. The following relation for heat transfer in the transition film boiling region for surface temperatures of 850 to 950 °C is suggested:

$$HTC = 152 \times G^{1.06} \text{ (W/m}^2\text{·K)}, \text{ where } 0.84 \leq G \leq 3.0 \text{ (L/m}^2\text{·s)}$$

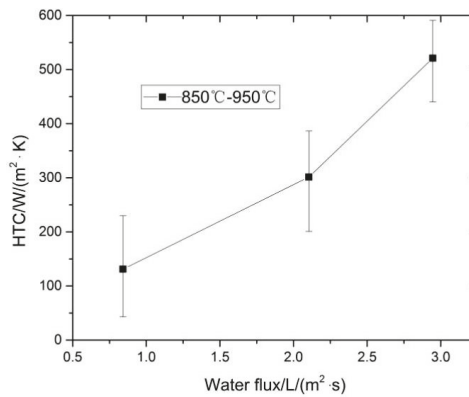


Figure 12. The HTC as a function of water flux.

HTC indicated the heat transfer efficiency between the surface of slab and cooling water, and the effect of heat transfer was high when HTC was large. In general, it needed to be measured by experiment and statistics, and expressed by empirical formula. Significant work regarding spray cooling could be found in the literature. Most researchers studied the macroscopic heat transfer rate. Different researchers had given different empirical formulas according to the test conditions and these formulas had different forms. Gan [23] summarized some of the formula as follows:

$$\text{HTC} = 360 \times G^{0.556}, \text{ where } 0.8 < G < 2.5 \text{ (L/m}^2\cdot\text{s)}, 727 \text{ }^\circ\text{C} < T_s < 1027 \text{ }^\circ\text{C}$$

$$\text{HTC} = 423 \times G^{0.556}, \text{ where } 1 < G < 7 \text{ (L/m}^2\cdot\text{s)}, 627 \text{ }^\circ\text{C} < T_s < 927 \text{ }^\circ\text{C}$$

$$\text{HTC} = 581G^{0.451} (1 - 0.0075T_w), \text{ where } T_w \text{ is the water temperature}$$

$$\text{HTC} = \alpha(708G^{0.75}T_s^{-1.2} + 0.116), \text{ where } \alpha \text{ is a calibration factor, } T_s \text{ is the slab temperature}$$

$$\text{HTC} = 157G^{0.55} (1 - 0.0075T_w), \text{ where } T_w \text{ is the water temperature}$$

$$\text{HTC} = 130 + 350G$$

Compared with the formula in the paper, there were some differences between the researches. In some cases, the difference was striking. HTC was related to the factors of water flux, spray pressure, spray distance, nozzle structure, surface temperature of slab, water temperature etc. All of these factors had an impact on the relation.

An optimized transition boiling can help to improve heat transfer for specific spray characteristics. The test model was for carbon steel, but the results equally apply to other materials [24]. However, deviations should be expected due to the surface characteristics of the spray-cooled surface [25].

In summary, heat flux and HTC are critical for the theoretical heat design of an industrial process. The experimental setup provides a powerful tool for a quantitative understanding of the heat transportation phenomena of not only continuous casting but also other industries.

5. Conclusions

In this work, an experimental setup to simulate the secondary cooling of continuous casting was developed. This provided a powerful tool for optimizing the continuous casting operation and for better continuous casting machine designs. An inverse heat conduction algorithm was used to calculate the surface heat fluxes during the slab cooling. The main conclusions derived from this study are:

- (1) Transition boiling was the primary heat transfer characteristic in the range from 1100 to 800 °C during secondary cooling for the continuous casting of steel.

- (2) In the experimental spray cooling, the average heat flux was measured to be $2.9 \times 10^5 \text{ W/m}^2$ in the range of 1100 to 800 °C with water injection of 2.1 L/(m²·s). The surface HTC increased linearly from 120.0 W/m²·K to 542.6 W/m²·K as the temperature decreased from 1100 to 800 °C.
- (3) The relation between HTC and water flux in the transition boiling region for surface temperatures of 850 to 950 °C was suggested to be $\text{HTC} = 152 \times G^{1.06}$.

Author Contributions: Conceptualization, Y.Z. and Z.W.; methodology, Y.Z., J.H. and Z.W.; formal analysis, Y.Z.; investigation, Y.Z. and J.H.; resources, Z.Z.; data curation, C.B. and Y.G.; writing—original draft preparation, Y.Z.; writing—review and editing, Z.Z.; visualization, C.B. and Y.G.; supervision, Y.Z.; project administration, J.H.; funding acquisition, Z.Z. and Z.W.

Funding: The work was supported by National Natural Science Foundation of China under Grant 51264030; National Key R & D Program of China under Grant 2016YFC0401201; and Natural Science Foundation of Inner Mongolia under Grant 2017MSLH0534.

Conflicts of Interest: The authors declare no conflicts of interest.

Appendix A

Table A1. Thermophysical property.

$T/^\circ\text{C}$	$C_p/\text{J}(\text{kg}\cdot\text{K})^{-1}$	$k/\text{W}(\text{m}\cdot\text{K})^{-1}$
20	462	44.55
100	481	42.95
200	508	41.02
300	530	38.23
400	560	35.74
500	605	33.20
600	680	30.81
700	824	29.39
765	1360	38.38
800	718	25.39
900	615	26.13
1000	604	25.57
1100	685	23.71
1200	858	20.55

References

1. Wendelstorf, J.; Spitzer, K.H.; Wendelstorf, R. Spray water cooling heat transfer at high temperatures and liquid mass fluxes. *Int. J. Heat Mass Transf.* **2008**, *51*, 4902–4910. [[CrossRef](#)]
2. Petrus, B.; Zheng, K.; Zhou, X.; Thomas, B.G.; Bentsman, J. Real-Time, Model-Based Spray-Cooling Control System for Steel Continuous Casting. *Metall. Mater. Trans. B* **2011**, *42*, 87–103. [[CrossRef](#)]
3. Ramstorfer, F.; Roland, J.; Chimani, C.; Mörwald, K. Investigation of Spray Cooling Heat Transfer for Continuous Slab Casting. *Mater. Manuf. Process* **2011**, *26*, 165–168. [[CrossRef](#)]
4. Hauksson, A.T.; Fraser, D.; Prodanovic, V.; Samarasekera, I. Experimental study of boiling heat transfer during subcooled water jet impingement on flat steel surface. *Ironmak Steelmak* **2004**, *31*, 51–56. [[CrossRef](#)]
5. Minchaca, J.I.; Castillejos, A.H.; Acosta, F.A. Size and Velocity Characteristics of Droplets Generated by Thin Steel Slab Continuous Casting Secondary Cooling Air-Mist Nozzles. *Metall. Mater. Trans. B* **2011**, *42*, 500–515. [[CrossRef](#)]
6. Zhang, J.; Chen, D.F.; Zhang, C.Q.; Wang, S.G.; Hwang, W.S.; Han, M.R. Effects of an even secondary cooling mode on the temperature and stress fields of round billet continuous casting steel. *J. Mater. Process. Technol.* **2015**, *222*, 315–326. [[CrossRef](#)]
7. Hernandez, C.A.; Minchaca, J.I.; Humberto, C.E.; Acosta, F.A.; Zhou, X.; Thomas, B.G. Measurement of heat flux in dense air-mist cooling: Part II—The influence of mist characteristics on steady-state heat transfer. *Exp. Therm. Fluid Sci.* **2013**, *44*, 161–173. [[CrossRef](#)]

8. Hernandez, C.A.; Castillejos, A.H.; Acosta, F.A.; Zhou, X.; Thomas, B.G. Measurement of heat flux in dense air-mist cooling: Part I—A novel steady-state technique. *Exp. Therm. Fluid Sci.* **2013**, *44*, 147–160. [[CrossRef](#)]
9. Ramstorfer, F.; Roland, J.; Chimani, C.; Mörwald, K. Modelling of air-mist spray cooling heat transfer for continuous slab casting. *Int. J. Cast Met. Res.* **2013**, *22*, 39–42. [[CrossRef](#)]
10. Horský, J.; Raudenský, M.; Pohanka, M. Experimental Study of Heat Transfer in Hot Rolling and Continuous Casting. *Mater. Sci. Forum* **2005**, *473–474*, 347–354. [[CrossRef](#)]
11. Ito, Y.; Murai, T.; Miki, Y.; Mitsuzono, M.; Goto, T. Development of Hard Secondary Cooling by High-pressure Water Spray in Continuous Casting. *ISIJ Int.* **2011**, *51*, 1454–1460. [[CrossRef](#)]
12. Tsutsumi, K.; Kubota, J.; Hosokawa, A.; Ueoka, S.; Nakano, H.; Kuramoto, A.; Sumi, I. Effect of Spray Thickness and Collision Pressure on Spray Cooling Capacity in a Continuous Casting Process. *Steel Res. Int.* **2018**, *89*, 9. [[CrossRef](#)]
13. El-Bealy, M.O. Air-Water Mist and Homogeneity Degree of Spray Cooling Zones for Improving Quality in Continuous Casting of Steel. *Steel Res. Int.* **2011**, *82*, 1187–1206. [[CrossRef](#)]
14. Moravec, R.; Blazek, K.; Horský, J.; Graham, C.; Fiegle, S.; Dombovic, T.; Kaurich, T. Coupling of Solidification model And Heat Transfer Coefficients to Have Valuable Tool for Slab Surface Temperatures Prediction. In Proceedings of the METEC 7th InSteelCon, Düsseldorf, Germany, 27 June–1 July 2011; pp. 1–9.
15. Chen, L.; Askarian, S.; Mohammadzaheri, M.; Samadi, F. Simulation and Experimental study of Inverse Heat Conduction Problem. *Fund. Chem. Eng.* **2011**, *233–235*, 2820–2823. [[CrossRef](#)]
16. Buczek, A.; Telejko, T. Inverse determination of boundary conditions during boiling water heat transfer in quenching operation. *J. Mater. Process. Technol.* **2004**, *155–156*, 1324–1329. [[CrossRef](#)]
17. Tapaswini, S.; Chakraverty, S.; Behera, D. Numerical solution of the imprecisely defined inverse heat conduction problem. *Chin. Phys. B* **2015**, *24*, 050203. [[CrossRef](#)]
18. Beck, J.V.; Blackwell, B.; St Clair, C.R. *Inverse Heat Conduction, Ill-Posed Problems*; John Wiley & Sons: Hoboken, NJ, USA, 1985.
19. Woodbury, K.A.; Beck, J.V.; Najafi, H. Filter solution of inverse heat conduction problem using measured temperature history as remote boundary condition. *Int. J. Heat Mass Trans.* **2014**, *72*, 139–147. [[CrossRef](#)]
20. Stetina, J.; Mauder, T.; Klimes, L.; Masarik, M.; Kavicka, F. Operational Experiences with the Secondary Cooling Modification of Continuous Slab Casting. In Proceedings of the Metal 2013: 22nd International Conference on Metallurgy And Materials, Brno, Czech Republic, 15–17 May 2013; pp. 62–67.
21. Raudensky, M.; Horský, J. Secondary cooling in continuous casting and Leidenfrost temperature effects. *Ironmak Steelmak* **2005**, *32*, 159–164. [[CrossRef](#)]
22. Timm, W.; Weinzierl, K.; Leipertz, A. Heat transfer in subcooled jet impingement boiling at high wall temperatures. *Int. J. Heat Mass Trans.* **2003**, *46*, 1385–1393. [[CrossRef](#)]
23. Gan, Y. *Practical Manual for Continuous Casting*; Metallurgical Industry Press: Beijing, China, 2010; pp. 68–69, ISBN 978-7-5024-5044-1.
24. Fang, Q.; Ni, H.; Zhang, H.; Wang, B.; Liu, C. Numerical Study on Solidification Behavior and Structure of Continuously Cast U71Mn Steel. *Metals* **2017**, *7*, 483. [[CrossRef](#)]
25. Teodori, E.; Pontes, P.; Moita, A.; Georgoulas, A.; Marengo, M.; Moreira, A. Sensible Heat Transfer during Droplet Cooling: Experimental and Numerical Analysis. *Energies* **2017**, *10*, 790. [[CrossRef](#)]



© 2019 by the authors. Licensee MDPI, Basel, Switzerland. This article is an open access article distributed under the terms and conditions of the Creative Commons Attribution (CC BY) license (<http://creativecommons.org/licenses/by/4.0/>).

Article

Control of Upstream Austenite Grain Coarsening during the Thin-Slab Cast Direct-Rolling (TSCDR) Process

Tihe Zhou ^{1,*}, Ronald J. O'Malley ², Hatem S. Zurob ¹, Mani Subramanian ¹, Sang-Hyun Cho ³ and Peng Zhang ³

¹ Department of Materials Science and Engineering, McMaster University, 1280 Main Street West, Hamilton, ON L8S 4L7, Canada; zurobh@mcmaster.ca (H.S.Z.); subraman@mcmaster.ca (M.S.)

² Department of Materials Science and Engineering, Missouri University of Science & Technology, 1400 N. Bishop Ave., Rolla, MO 65409-0330, USA; omalleyr@mst.edu

³ Algoma Inc. 105 West Street, Sault Ste. Marie, ON P6A 7B4, Canada; Sang-Hyun.Cho@algoma.com (S.-H.C.); peng.zhang@algoma.com (P.Z.)

* Correspondence: tom.zhou@stelco.com; Tel.: +1-519-587-4541 (ext. 5398)

Received: 27 December 2018; Accepted: 29 January 2019; Published: 1 February 2019

Abstract: Thin-slab cast direct-rolling (TSCDR) has become a major process for flat-rolled production. However, the elimination of slab reheating and limited number of thermomechanical deformation passes leave fewer opportunities for austenite grain refinement, resulting in some large grains persisting in the final microstructure. In order to achieve excellent ductile to brittle transition temperature (DBTT) and drop weight tear test (DWTT) properties in thicker gauge high-strength low-alloy products, it is necessary to control austenite grain coarsening prior to the onset of thermomechanical processing. This contribution proposes a suite of methods to refine the austenite grain from both theoretical and practical perspectives, including: increasing cooling rate during casting, liquid core reduction, increasing austenite nucleation sites during the delta-ferrite to austenite phase transformation, controlling holding furnace temperature and time to avoid austenite coarsening, and producing a new alloy with two-phase pinning to arrest grain coarsening. These methodologies can not only refine austenite grain size in the slab center, but also improve the slab homogeneity.

Keywords: thin-slab cast direct-rolling; austenite grain coarsening; grain growth control; liquid core reduction; secondary cooling; two-phase pinning

1. Introduction

Owing to low capital and operating cost, thin-slab cast direct-rolling (TSCDR) has become a major process for hot flat-rolled production since Nucor started the first thin slab caster, directly linked to a hot rolling mill, back in 1989. This process is based on a novel funnel mold caster, which can produce a thin slab of thickness from 50 to 90 mm, instead of the conventional continuous casting slab thicknesses of 200 to 250 mm [1,2]. Figure 1 is an example of the TSCDR process at Algoma Inc. The liquid steel is fed via the ladle and tundish into a funnel-shaped copper mold with primary cooling control. Solidification initiates on the mold wall and the external solidified shell increases in thickness as the steel strand passes through the mold. Based on the steel grades and slab thickness, the casting speed can be from 2.5 to 6.5 m/min. Once leaving the mold, the thin slab passes through the secondary-cooling zone and solidification continues. The secondary-cooling zone has eight segments with multi-point bending and unbending, with 12.7-m containment length, by using air mist cooling. The liquid core reduction system can refine the as-cast microstructure and reduce the centerline segregation and solidification-related defects. The continuous slab is cut to length and then sent to

the roller hearth soaking furnace. To maximize the use of the rolling capacity, the thin slab caster has two strands along with two shuttle furnaces, which can transfer the slab sideways to allow the two strands to feed a single rolling mill. The slab is rolled in a single pass roughing mill after descaling, then goes through the heated transfer table and is rolled in the six-stand finishing mill; the resulting hot strip then passes through the run-out table with a laminar cooling system and is coiled at the down coiler [3].

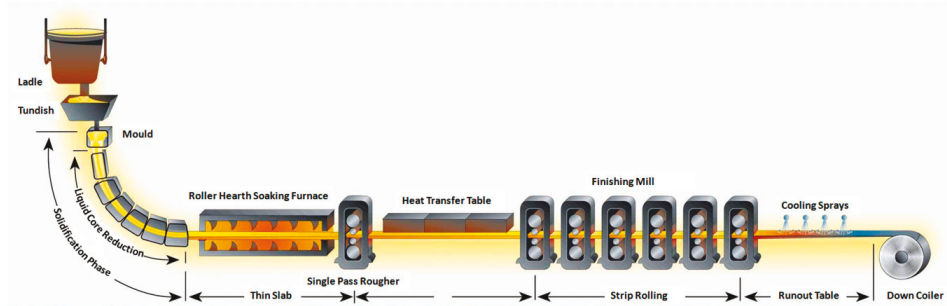


Figure 1. Thin slab casting direct strip production complex at Algoma Inc. [3].

TSCDR mills currently produce a variety of steel grades, including interstitial free steel, low carbon to medium carbon steel, high-strength low-alloy, and advanced high strength multiphase steel grades [1]. Recently, great effort has been placed on using this process to produce high grade micro alloyed steels that can be utilized in bridge guard rails, wind turbine towers, rail cars, and oil and gas pipelines, with stringent low-temperature ductile to brittle transition (DBTT) and drop weight tear test (DWTT) requirements to maintain structural integrity and safety over several decades of service [4,5]. It well established that refining austenite grain size before pancaking can improve DBTT and DWTT properties [6]. In most cases, these applications require a hot band thickness of 10 mm or more. This requirement challenges the TSCDR process, because the ratio of the thickness of the initial as-cast slab to that of the final product is only of the order of 5–7 to 1. It has been proven that production of higher high strength low alloyed (HSLA) grades is very difficult, owing to the presence of extremely large austenite grains in the center of the slab prior to thermomechanical processing [7]. The limited number of thermomechanical deformation passes available in the TSCDR process cannot refine these larger grains [8,9]. In order to achieve uniform and finer microstructure, it is very important to control the upstream austenite grain coarsening before the slab enters the roughing mill. This contribution will focus on refining austenite grain by increasing the cooling rate during solidification, increasing nucleation sites for delta-ferrite by liquid core reduction, and increasing austenite nucleation sites during the delta-ferrite to austenite phase transformation, as well as controlling austenite coarsening inside the holding furnace. In addition, the possibility of rolling new alloy with two-phase pinning is also discussed.

2. Materials, Experimental Procedure, and Model Setup

The experimental materials in this study consisted of an HSLA based American Petroleum Institute (API) X70 cast slab sample from industry, as well as an Fe-Al model alloy with 1.5% Al addition to generate delta/austenite two-phase microstructure at different temperatures. The two chemistries are compared in Table 1. The addition of Al in the Fe-Al model alloy can stabilize delta-ferrite down to room temperature. A two-phase mixture of delta-ferrite and austenite will exist at temperatures between 1310 °C and the eutectoid temperature. The Fe-Al model alloy was prepared by induction melting at CANMET Materials Technology Lab (Hamilton, ON, Canada); the as-received microstructure was delta-ferrite with grain size of approximately 85 μm , after pilot mill hot rolling to the thickness of 10 mm.

Table 1. Chemical composition of the new alloy used in this investigation (wt %).

wt %	C	Mn	Si	Al	Ti	Nb	N
API X70	0.05	1.60	0.30	0.0037	0.0012	0.07	0.0060
Fe-Al model alloy	0.051	1.00	0.36	1.5	0	0	0

In order to quantify the grain coarsening at high temperature, a simple non-isothermal grain growth model [9] was utilized to capture the evolution of grain growth at different stages of the TSCDR process. Starting with the simple equation:

$$\frac{d\bar{R}}{dt} = \alpha M(t) \frac{2\gamma_{gb}}{\bar{R}} \quad (1)$$

then integrating with respect to time, which led to:

$$\bar{R}^2 = \bar{R}_0^2 + 4\gamma_{gb} \int_0^t \alpha M(t) dt \quad (2)$$

where \bar{R} is the mean radius of an individual grain, \bar{R}_0 is the initial grain radius, and γ_{gb} denotes the grain boundary energy per unit of area. A reasonable value of $0.8 \text{ J}\cdot\text{m}^{-2}$ [10] was used for the calculation. α is a shape factor with value of ~ 1.5 [11], and $M(t)$ is the mobility of the grain boundaries [9,12]. Delta-ferrite grain boundary mobility is shown as [9]:

$$M_{\delta}(t) = \frac{0.7075}{T(t)} \times \exp\left(\frac{-20,995.43}{T(t)}\right) \quad (3)$$

While austenite grain boundary mobility is listed as [9]:

$$M_{\gamma}(t) = \frac{0.3072}{T(t)} \times \exp\left(\frac{-20,837.14}{T(t)}\right) \quad (4)$$

In this equation, $T(t)$ is an expression for the temperature as a function of time, which was obtained either experimentally from the data recorded, using a thermocouple, or the temperature profiles during the TSCDR process predicted by the heat transfer model. The details are in the Appendix A.

During a typical TSCDR practice, for instance, Table 1 chemistry, Ti concentration is very low and large TiN particles are formed in the liquid during the late stages of solidification. These particles coarsen during the subsequent solid-state process at high temperature [13,14]. These large TiN particles exert a very small particle pinning effect [15]. Strong particle pinning conditions are not encountered until fine Nb(C,N) precipitates are formed during thermomechanical processing [16–18]. In addition, according to Zurob et al [19], the solute-drag effect of all alloying elements was shown to be negligible at temperatures above $1200 \text{ }^{\circ}\text{C}$. Therefore, Equation (2) can be used to model the grain-size evolution during the TSCDR process up to the point where the slabs exit the homogenization furnace prior to thermomechanical processing at the roughing mill.

To validate the grain growth model, a 70 mm and an 85 mm thickness slab of API X70 were sampled after solidification prior to entering the twin roller hearth tunnel furnaces. The slab crops were sectioned to measure the austenite grain size at various distances from the slab surface. All the samples were prepared using standard metallographic techniques. The prior austenite grain boundaries were revealed using an aqueous solution of picric acid with sodium dodecylbenzene sulfonate, with additions of hydrochloric acid for the different chemistry. Microstructure was investigated using optical and scanning electron microscopy. The image analysis was performed using Clemex PE5.0 software (Clemex Technologies Inc., Longueuil, QC, Canada). The grain size was measured using the area intercept method and the true three-dimensional grain diameter was calculated as 1.382 times the linear intercept diameter [20].

3. Results and Discussions

3.1. Microstructure and Model Validation

The microstructure of the industrially-supplied TSCDR 85- and 70-mm thick slabs of API X70 steel are shown in Figures 2 and 3, respectively. At the surface of the 85 mm API X70 slab, the prior austenite grain size was about 50 μm . At the center of the slab, the prior austenite grain size was as large as 1151 μm . While, the prior austenite grain size at the surface of the 70 mm API X70 slab was about 14 μm , and at the center of the slab was about 858 μm .

Figures 2 and 3 indicated that the industrial TSCDR as-cast microstructure was non-uniform with extremely large grains at the slab center, and that the 70 mm thick slab had a finer austenite grain size compared to the 80 mm slab.

The grain growth model Equation (2) can be used to calculate the delta-ferrite and austenite grain size evolution at different positions in the slab. The important points that are required to be considered is that of the initial grain size \bar{R}_0 and the cooling path ($T(t)$, in Equations (3) and (4)), which varies from the surface to the center of the slab, leading to grain-size variations. To understand the HSLA microstructure evolution during the TSCDR process, THERMO-CALC (Thermo-Calc Software AB, Solna, Sweden) was used to predict the relevant transformation temperatures for API X70 and the Fe-Al model alloy using the TCFE6 database [21]. The results are given in Table 2.

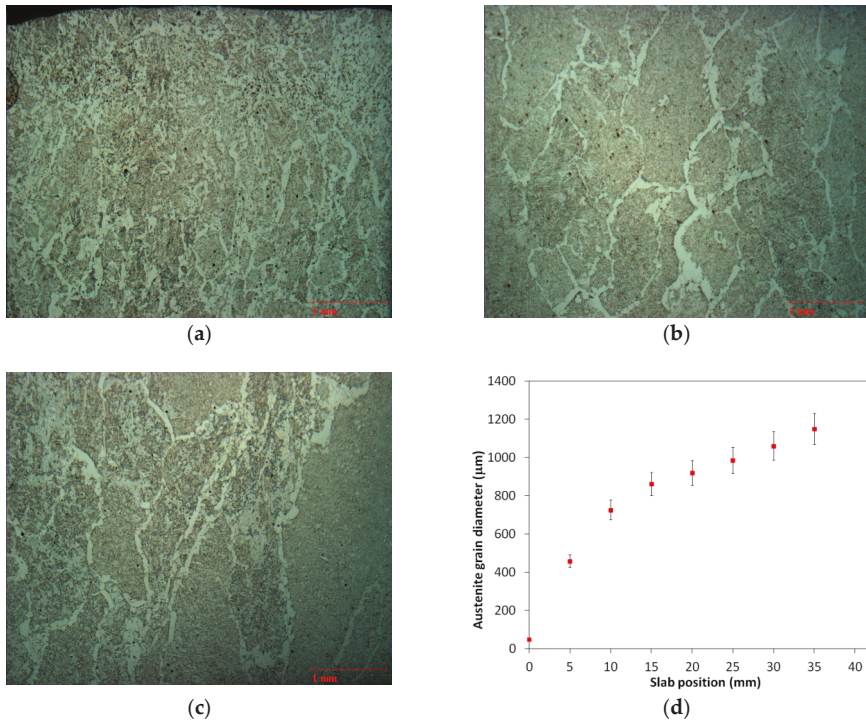


Figure 2. 85-mm slab austenite grain size evolution of American Petroleum Institute (API) X70 from the industrial thin slab casting process: (a) close to slab surface; (b) 20 mm from the slab surface; (c) close to the slab center; and (d) summary of the measured austenite grain size with distance from slab surface to center.

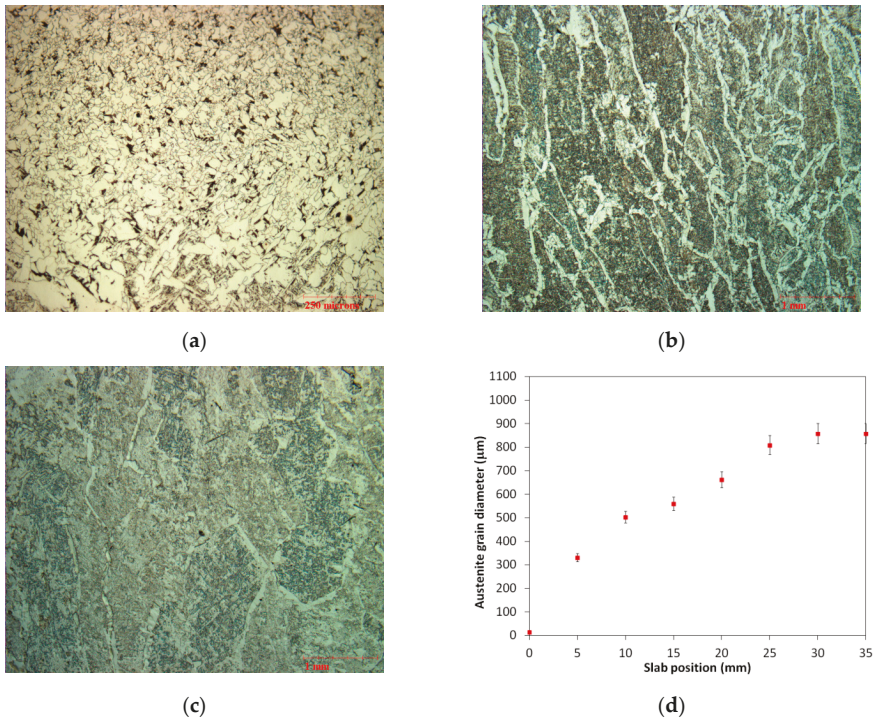


Figure 3. 70-mm slab austenite grain size evolution of API X70 from the industrial thin slab casting process: (a) close to slab surface; (b) 20 mm from the slab surface; (c) close to the slab center; and (d) summary of the measured austenite grain size with distance from slab surface to center.

Table 2. Phase transformation temperature of API X 70.

Phase	Liquid	Liquid + Delta	Delta	Delta + Austenite	Austenite
API X 70 (°C)	>1524	1524–1496	1496–1477	1477–1448	1448–852
Fe-Al alloy (°C)	>1530	1530–1500	1500–1412	1412–734	-

In this study, we have not attempted to model the delta-ferrite to austenite transformation. Instead we simply assumed that the delta grain growth occurred down to 1477 °C and austenite grain growth occurred after the delta-ferrite to austenite phase transformation. The secondary dendrite arm spacing (SDAS) was used as the initial delta-ferrite grain size, \bar{R}_0 , which was calculated using the CON1D V7.0 slab casting heat transfer model, assuming the casting speed of 3.4 m/min [22], as shown in Figure 4a. The initial austenite grain size was presumed to be smaller than the final delta grain size, and was divided by a factor of 3 [23,24] to account for the effect of grain refinement due to the delta-ferrite to austenite transformation in the grain size calculation. Finally, the cooling path $T(t)$ at each point of the slab was also estimated by the CON1D V7.0 model [22]. For example, Figure 4b shows the temperature paths at the surface, 5, 10, and 20 mm below the surface, and the center of the API X70 85 mm slab that was cast with 3.4 m/min casting speed. Due to the spray jet cooling and the high local heat extraction, when the segment rolls directly contacted the slab, the temperature curve on the slab surface showed an irregular trend. Nonetheless, this irregular trend should not interfere with the interpretation of the grain growth with the slab position during the TSCDR process.

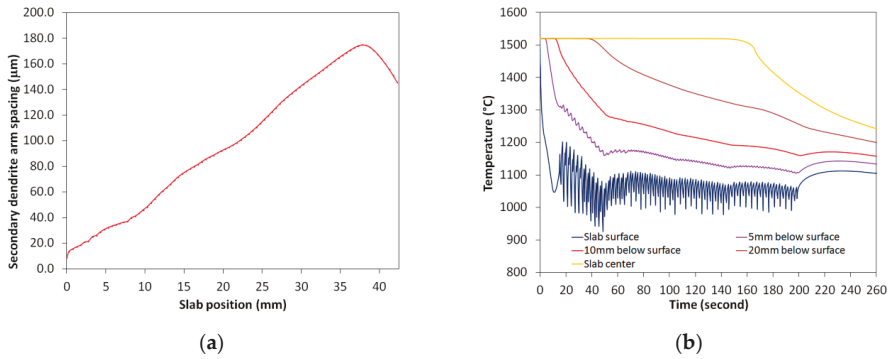


Figure 4. CON1D V7.0 slab casting heat transfer model predicted: (a) secondary dendrite arm spacing as a function of position within the API X70 slab; and (b) temperature paths at the surface, 5, 10, and 20 mm below the surface, and the center of the slab.

Using Equations (2) and (3), an example of delta grain size evolution with time at 5 mm below the slab surface is shown in Figure 5a. The austenite grain size evolution at the same position (5 mm below the surface) with time just before leaving the holding furnace, by using Equations (2) and (4), is shown in Figure 5b. The solid line represents the model predicted austenite grain diameter and the dashed line represents the temperature profile in the TSCDR process at the corresponding slab position.

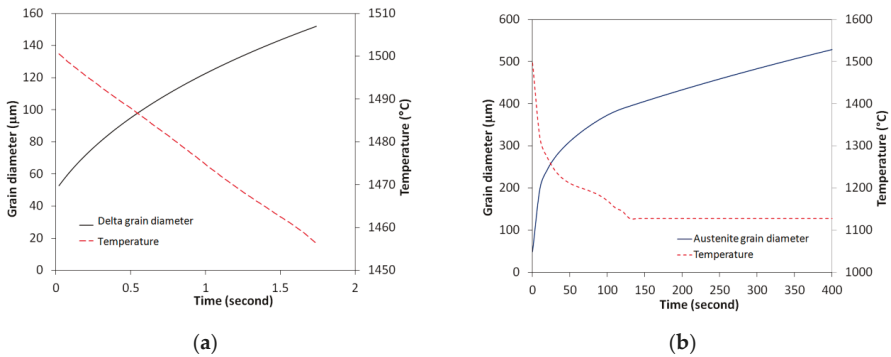


Figure 5. (a) The predicted delta grain size evolution with time 5 mm below the slab surface; and (b) the predicted austenite grain size evolution at the same position before entering the roller hearth holding furnace.

Similar calculations were conducted as a function of the slab thickness. Figure 6a shows the predicted delta grain size as a function of slab position, just before the onset of the delta-ferrite to austenite transformation. The solid diamonds are the calculated delta grain sizes; the solid line is used to highlight the trends of grain size change with distance from the surface to center of the slab. In addition, the austenite grain size could be calculated when the slab was about to enter the holding furnace, and upon leaving the holding furnace prior to entering the roughing mill.

Figure 6b shows the calculated austenite grain size with slab thickness when the slab is about to enter the holding furnace. The solid diamonds and solid lines follow the same notation for delta grains as noted previously. The experimentally measured austenite grain size from the 85 mm slab from Figure 2d (solid squares) is superimposed for comparison. It indicates that very good agreement was obtained between the model prediction and the measured austenite grain size as a function of the slab position. This provides strong support that the normal grain growth model developed here can be used

to predict austenite grain growth at high temperatures prior to the thermomechanical processing. The calculated austenite grain size for the 70 mm slab and the corresponding experimental measurements (Figure 3d) with slab position is shown in Figure 6c. Once again, the predicted austenite grain size was in good agreement with the experimental data as a function of slab position. This agreement further validates the grain growth treatment employed here and supports the applications of the model in the following sections.

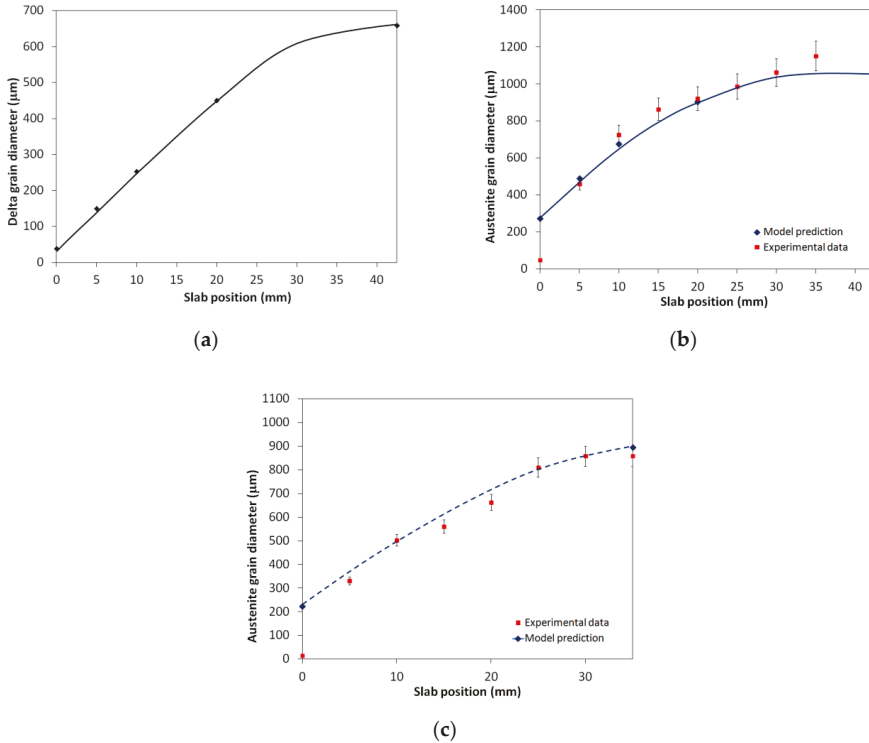


Figure 6. (a) The predicted delta grain size as a function of slab position; (b) comparison of model prediction and experimental measurement of austenite grain size with slab position before the 85 mm slab enters the holding furnace; and (c) comparison of model prediction and experimental measurement of austenite grain size with slab position before the 70 mm slab entering the holding furnace.

3.2. Increasing Cooling Rate to Refine As-Cast Microstructure

Reducing the slab thickness can increase the cooling rate at the slab center, which can refine the austenite grain at the slab center and reduce the non-uniformity of the as-cast microstructure. In what follows, the consequences of reducing the slab thickness from 85 mm to 50 and 30 mm are examined assuming that the only change is the enhanced cooling rate of the slab [25–27]. In order to determine the cooling rate and the initial secondary dendrite arm spacing, the CON1D V7.0 slab casting heat transfer model [22] was used for slabs of 85, 50, and 30 mm slab thicknesses, as shown in Figure 7.

The initial delta-ferrite grain size was, once again, taken to be SDAS; therefore, the model prediction of delta grain size as a function of position for the 30 and 50 mm thin slabs just before the onset of the delta to gamma transformation are shown in Figure 8a, which also includes, for comparison, the results shown earlier for the 70 and 85 mm slabs. The calculated austenite grain size before entering the homogenization furnace is shown in Figure 8b. The symbols in these Figures have the same meaning as discussed previously.

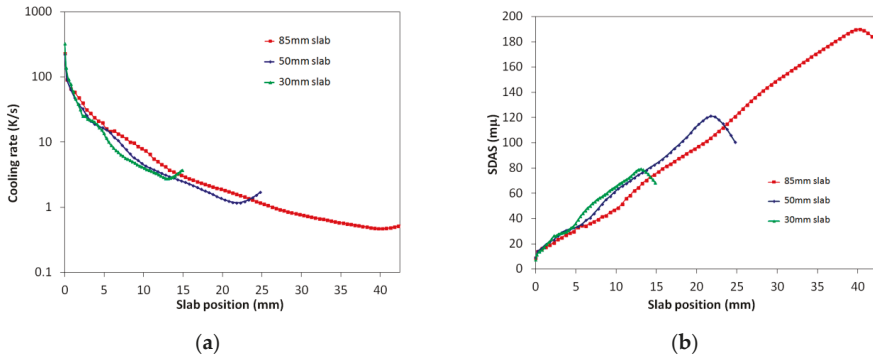


Figure 7. CON1D V7.0 slab casting heat transfer model predicted: (a) cooling curves; and (b) secondary dendrite arm spacing (SDAS) at different positions of 30, 50, and 85 mm slabs.

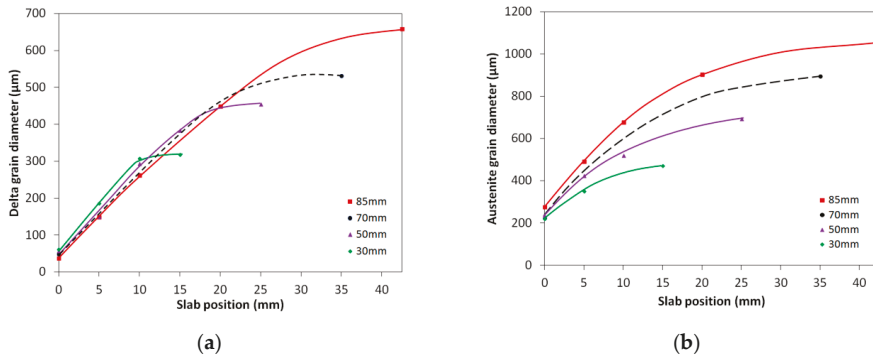


Figure 8. (a) The predicted delta grain size of 30, 50, 70, and 85 mm slabs as a function of slab position just before the onset of the delta to gamma transformation; (b) the predicted austenite grain size of 85, 70, 50, and 30 mm slabs as a function of slab position when the slab is about to enter the homogenization furnace.

It is clear from these calculations that, due to the enhanced cooling rate, austenite grains at the center of the thinner slabs had greatly reduced in size. When the slabs were about to enter the homogenization furnace, the austenite grain size at the center of the 85 mm thick slab was about 1058 μm . However, the grain size was 896 μm at the center of the 70 mm thick slab, 693 μm at the center of the 50 mm thick slab, and 470 μm at the center of the 30 mm slab. In addition, the homogeneity of the microstructure had improved by increasing the cooling rate; the ratio of largest grain size to smallest grain size was 3.8 to 1 for the 85 mm thick slab, 2.8 to 1 for the 50 mm thick slab, and 2.1 to 1 for the 30 mm slab. Therefore, one can conclude that reducing the slab thickness can refine and homogenize the as-cast microstructure due to the enhanced cooling rate at the center of the slab. Experimental measurements of 85 mm (Figure 2) and 70 mm (Figure 3) industrial slab austenite grain sizes, using the distance from the slab surface to center, demonstrated the validity and technological merit of the increased cooling on reducing austenite grains at the center of the slab. The austenite grain size could be reduced from 1151 to 858 μm if the casting slab thickness was reduced from 85 to 70 mm. The main difficulty in applying this method is that it requires changing the layout of the TSCDR process for casting thinner slabs, such as 50 and 30 mm thick slabs. In addition, the smaller slab thickness will further reduce the amount of thermomechanical processing that can be performed downstream, resulting in a larger average grain size, and possibly more grain size non-uniformity despite the improved initial microstructure. Thus, an optimum thickness could be determined by

considering both the solidification and grain growth (as described above) as well as the subsequent thermomechanical processing.

It is well established that as-cast microstructure is a function of the solidification rate (V) and temperature gradient (G) ahead of the solid–liquid front. The effect of the temperature gradient and velocity on the primary dendrite arm spacing can be summarized in the following equation [28,29]:

$$\lambda_1 = A_1 G^{-m} V^{-n} \tag{5}$$

where λ_1 is the primary arm spacing, G is the average temperature gradient in front of tip of dendrite in the liquid side, and V is average solidification velocity. A_1 , m , and n are constants. For the secondary dendrite arm spacing λ_2 , the most widely accepted expression for the relationship between λ_2 and cooling rate (GV) [30,31] is:

$$\lambda_2 = B_1 (GV)^{-n} \tag{6}$$

where B_1 and n are constants. Increasing secondary cooling with restricted casting speed will increase the cooling rate (GV). As a result, the primary and secondary dendrite arm spacing will decrease based on Equations (5) and (6). Figure 9a shows the Algoma DSPC model-predicted slab surface temperatures using different secondary cooling set-ups (the water loops configuration of DSPC is illustrated in Figure 9b). The solid diamonds are the slab surface temperatures for the standard spray cooling set-up used for low carbon steels, 0.6 L/kg of hot steel, and the increased secondary cooling, 1.4 L/kg of hot steel, is used for HSLA steels (solid squares in Figure 9a). When the liquid superheat was above 15 °C, the casting speed was restricted to 3.0 m/min; once the liquid superheat was below 10 °C, the casting speed could be increased to 3.4 m/min. Based on the above setup, the predicted 85-mm slab surface and center temperature profiles using increased secondary cooling, with a casting speed of 3.0 m/min, using the CON1D V7.0 model are shown in Figure 9c. Figure 9d shows austenite grain size with slab position using standard cooling and increased secondary cooling. The solid line highlights the trends of grain refinement with distance from the slab surface to the center. The increased secondary cooling practice was predicted to have a much finer austenite grain size than the standard spray practice at both the surface and center of the slab; austenite grain size was reduced from 276 to 253 μm at the surface and from 1058 to 808 μm at the slab center.

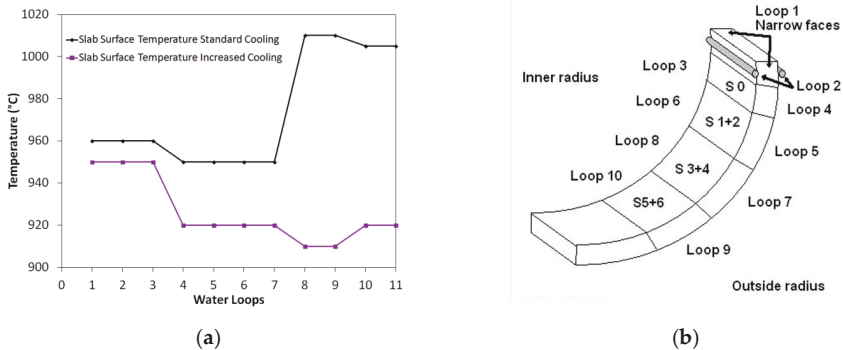


Figure 9. Cont.

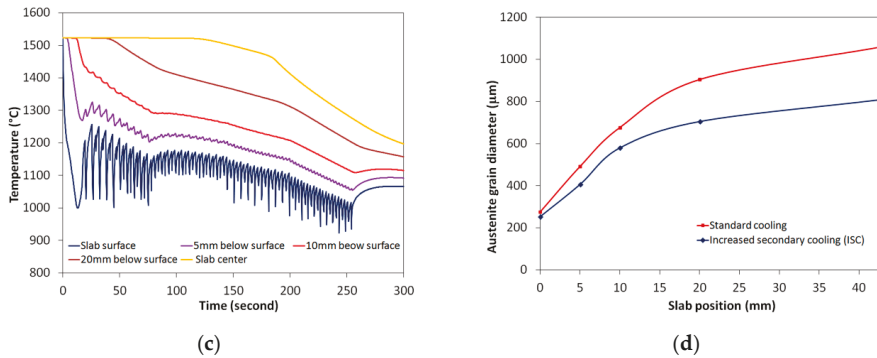


Figure 9. (a) the Algoma direct strip production complex (DSPC) model-predicted slab surface temperature using different secondary cooling set-ups; (b) the water loops configuration at Algoma DSPC; (c) the calculated 85 mm slab temperature profile using increased secondary cooling; and (d) comparison of 85 mm slab austenite grain sizes using standard cooling and increased secondary cooling.

3.3. Liquid Core Reduction

The TSCDR process at Algoma Inc. can adjust the strand gap dynamically during the casting process. The strand thickness can be reduced just below the mold by a tapered roll guide configuration of the “0” segment. Approximately a 10–30 mm strand reduction can be achieved with liquid core by means of many hydraulically-adjustable roll support segments. In this way, the slab thickness can be reduced from 98 mm to either 85 or 70 mm (Figure 10a). The liquid core reduction during casting produces a convective movement, which mixes the solidified dendrite structure and the liquid steel. A melt flow introduced by convection will generate strong shear stresses, which will shed away the newly formed dendrite arms near the solidification front. The newly formed dendrite crystals are then transported into the hot liquid pool by convective movement. Some of the dendrites are re-melted, while others survive and are transported back to the solidifying region. These surviving broken dendrite tips then form additional nucleation sites for delta-ferrite [32]. The finer delta-ferrite, in turn, will provide more nucleation sites for austenite during the delta-ferrite to austenite phase transformation resulting austenite grain refinement. This basic grain multiplication mechanism induced by liquid core reduction is shown schematically in Figure 10b.

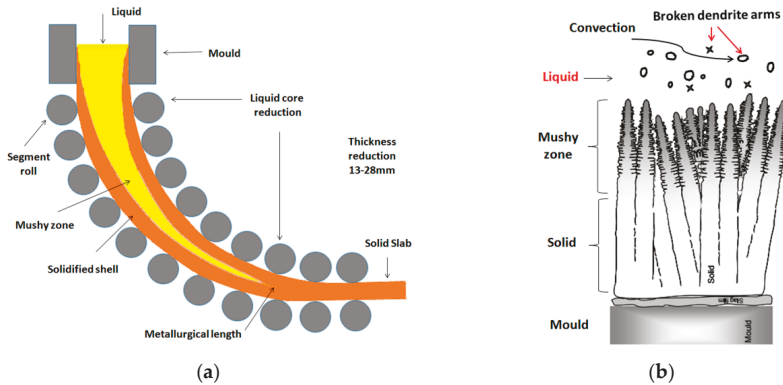
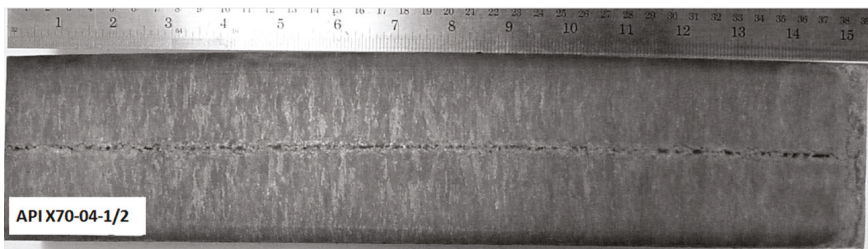
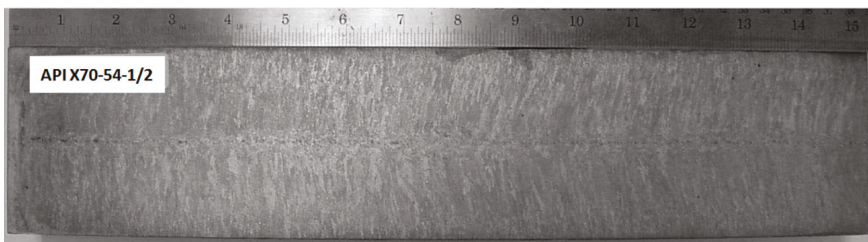


Figure 10. (a) Sketch diagram of liquid core reduction during thin-slab cast direct-rolling (TSCDR) process; (b) the basic mechanism of grain multiplication or grain refinement from liquid core reduction in the solidification region. The convective movement generates shear, to break the dendrite tips, and circulates the debris in the liquid pool.

The liquid core reduction can not only refine as cast microstructure, but also can reduce center line segregation, as well as other solidification-related defects, such as shrinkages and porosity. The metallurgical length for HSLA steels is about 10.0 m which is at the end of segment “6”. The liquid core reduction system together with a dynamic control of the liquid pool length can predict the best squeezing point during casting for these HSLA grades. For API X70, the liquid core reduction was set to occur at the fraction solid between 0.4–0.6. Figure 11a,b show API chemistry slab macro etch from strand 3 and strand 4 at the slab center position, respectively. The strand 3 slab sample shows centerline segregation and solidification shrinkages, which indicates that the squeezing was done late with higher solid fraction; however, the strand 4 sample had the diffused centerline, which confirms that the liquid core reduction was carried out at the optimum set point in the solid fraction.



(a)



(b)

Figure 11. API X70 slab macro etch from: (a) strand 3; and (b) strand 4, with different set points of liquid core reductions.

3.4. Increasing the Number of Austenite Nucleation Sites during Delta-Ferrite to Austenite Phase Transformation

The HSLA steels are low carbon steels (<0.08 wt %) which solidify as delta-ferrite. The ThermoCalc predicted the delta to austenite phase transformation was about 1477 °C (Table 2) and occurred during the liquid core reduction stage. Very little information is available concerning the kinetics of this transformation and its effect on the grain size. To demonstrate the refinement of as-cast microstructure using deformation, the Fe-Al model alloy (Table 1) was studied using a quenching dilatometer at the CANMET Materials Technology Lab [33]. The specimen was reheated into the delta region for 60 s; a compressive strain of 0.2 was applied, and then cooled to 1125 °C at a cooling rate of 50 °C/s. The deformed sample was quenched to room temperature as soon as it reached 1125 °C. Figure 12a shows fine sub-grains that were present within the original delta-ferrite grains. Higher magnification SEM image (Figure 12b) confirmed that the sub-grain boundaries and the delta-ferrite grain boundaries were decorated by fine austenite precipitates. An electron backscatter diffraction (EBSD) map (Figure 12c) showed that austenite grains nucleated along the delta grain and sub-grain boundaries (red line is large angle grain boundary ($\theta > 12^\circ$) and the white is low angle grain boundary

($12^\circ > \theta > 2^\circ$). This demonstration suggested that sub-grains formed as a result of deformation prior to the delta-ferrite to austenite transformation. During this phase transformation, the sub-grain boundaries and the original delta grain boundaries provided nucleation sites for austenite grains, which would lead to the refinement of the austenite grain structure.

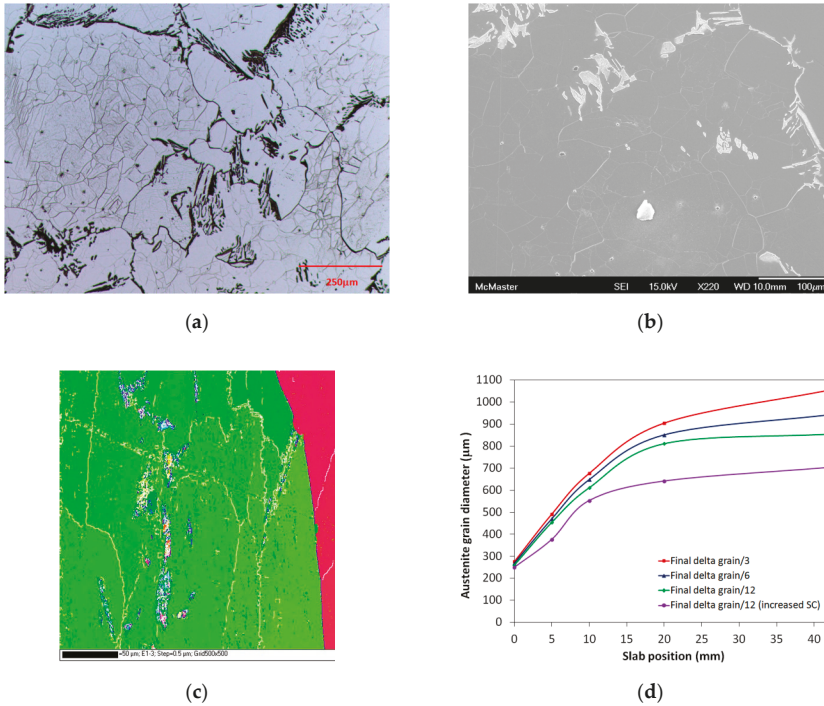


Figure 12. Microstructure of model Fe-Al alloy reheated into the delta region for 60 s, a compressive strain of 0.2 was applied followed by cooling at 50 °C/s to 1125 °C; the sample was quenched to room temperature as soon as it reached 1125 °C: (a) Fine sub-grains present within the original delta-ferrite grains; (b) austenite nucleates along the original delta grain boundaries; (c) electron backscatter diffraction (EBSD) shows austenite grains nucleated along the delta grain and sub-grain boundaries, and (d) predicted austenite grain size when the slab is about to enter the homogenization furnace, with different austenite nucleation sites.

To capture the effect of austenite nucleation sites on the austenite grain coarsening kinetics, the validated grain growth model can be used to calculate austenite grain evolution at different stages of the TSCDR process. Figure 12d summarizes the predicted austenite grain sizes when the slab is about to enter the holding furnace for the different densities of austenite nucleation sites. The various lines represent the grain size achieved when 12, 6, and 3 austenite grains nucleate within each delta grain. The calculation reveals that these extra nucleation sites had little effect on the final grain size at the surface of the slab; however, the austenite grain did decrease with increasing the austenite nucleation sites; the austenite grain in the 85 mm slab center could be reduced from 1058 μm to 945 μm and 856 μm, respectively. The purple line in Figure 12d indicates the austenite grain size trend by using the austenite nucleation density 12 and increased secondary cooling. The austenite grain size in the slab center could be refined from 1058 to 705 μm. The calculated results predicted the potential of increasing the number of austenite nucleation sites during the delta-ferrite to austenite phase transformation to refine the austenite grain size. Much more work is still needed; however,

to design new alloys and the deformation schedule during casting that could take advantage of this novel approach.

3.5. Control of Holding Furnace Temperature and Holding Time

Once the continuous slab leaves the secondary cooling zone it is cut to length and then sent to the roller hearth holding furnace, waiting for thermomechanical processing. The holding furnace standard set-up for HSLA at Algoma DSPC has a holding temperature of 1150 °C for 18 min. Austenite grains continue to coarsen inside the holding furnace. The experimental measurement of austenite grain size from the 85 and 70 mm slabs (Figures 2d and 3d) were used as the initial grain size, and the effects of holding temperature and time on austenite grain coarsening by using Equations (2) and (4) are summarized in Figure 13.

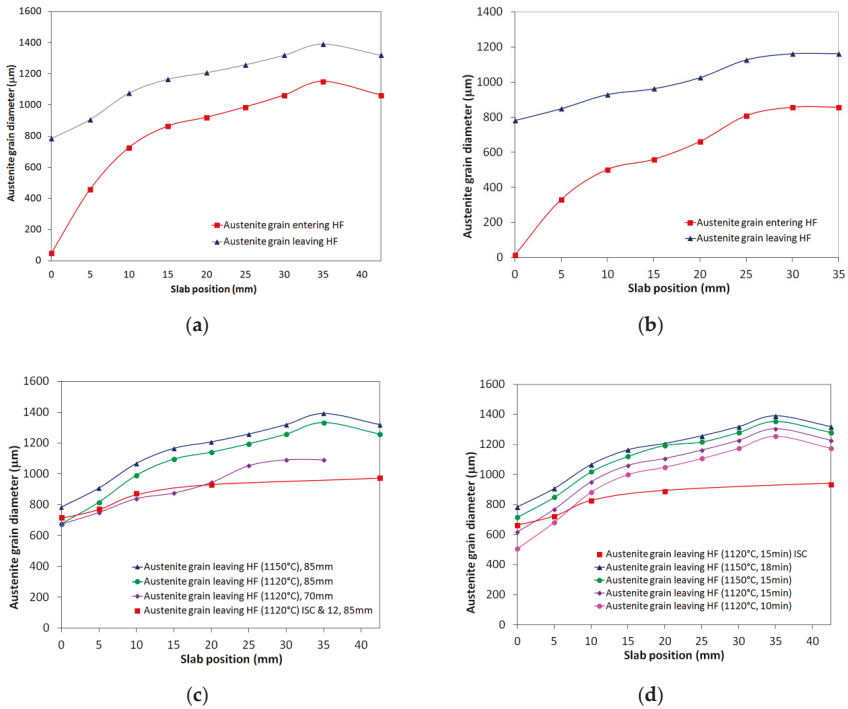


Figure 13. (a) Comparison of DSPC 85-mm thick slab austenite grain size before entering and after leaving the holding furnace (1150 °C, 18 min); (b) comparison of DSPC 70-mm thick slab austenite grain size before entering and after leaving the holding furnace (1150 °C, 18 min); (c) the effect of holding temperature 1120 and 1150 °C on austenite size after leaving the holding furnace; and (d) the effect of holding time and temperature on austenite grain size after leaving the holding furnace.

Figure 13a shows that, for a DSPC 85 mm slab, austenite grain diameter increased from 50 to 784 µm at the slab surface and from 1161 to 1391 µm in the slab center when the slabs were held at 1150 °C for 18 minutes. Extremely large austenite grains existed at the slab center before thermomechanical processing. Austenite grains coarsen much faster on the slab surface than in the slab center due to the larger driving force on the surface. Austenite grain size close to the center of the slab could be reduced from 1391 to 1161 µm by casting a 70 mm slab instead of 85 mm slab (Figure 13b). The effect of holding temperatures on austenite coarsening kinetics is shown in Figure 13c. Once again, the experimental measurement data were used as initial grain size, and the holding time,

18 min, was used for the calculation. The austenite grain size could be reduced from 1391 to 975 μm if increased secondary cooling was used, as well as using the austenite nucleation density 12 during the delta-ferrite to austenite phase transformation when casting an 85 mm slab. The effect of holding time at 1150 and 1120 $^{\circ}\text{C}$ is summarized in Figure 13d. The best combination to control austenite coarsening was to use increased secondary cooling during casting and to set up the holding furnace at 1120 $^{\circ}\text{C}$ for 15 min; thus, the austenite grain size could be reduced from 1391 to 935 μm .

3.6. The Possibility of Producing a New Alloy with Two-Phase Pinning

To refine HSLA steels' austenite grain size during the TSCDR process, carbides/nitrides of Ti, Nb, and V are extensively used to retard grain growth at high temperatures [34,35]. However, these precipitates are ineffective at pinning grain growth when the steel is held at a high temperature for a long time, due to the dissolution of fine particles and rapid particle coarsening. Zhou et al [36,37] proposed a new steel system that can automatically pin the delta grain growth by using a small volume fraction of austenite phase at high temperature. The grain growth is controlled by the austenite phase coarsening rate, which is determined by the bulk diffusion.

Figure 14a shows the CON1D calculated temperature profile at the slab surface as well as those at 5 and 10 mm below the surface of an 85 mm API X70 slab, at Algoma Inc., using the DSPC process cast at a speed of 3.4 m/min. The recorded thermal profile obtained from the laboratory solidification experiment using the new Fe-Al model alloy (Table 1) was superimposed for comparison. The reordered cooling rates, using water quenching, forced air cooling, air cooling, and in mold cooling used in the lab processing were similar to the cooling rates calculated at the slab surface, 5 and 10 mm below the surface, and at the slab center of the TSDCR cast 85 mm slab. In this way, one can compare the average grain sizes obtained from the solidification simulation tests to the grain-sizes measured at 0, 5, and 10 mm below the surface and the center of the industrial slab. These comparisons are shown in Figure 14b, in which the grain-size prior to entry into the soaking furnace was obtained by directly measuring the prior austenite grain size as a function of distance from the surface of the slab (Figure 2d). The data points for the new steel were positioned by matching the cooling rates in the solidification simulation test to the position at which these cooling rates would be observed within the slab. It can be seen that the expected grain size at the center would be 280 μm , compared to 1475 μm for API X70, if the new steel was cast in the form of an 85 mm slab. This clearly demonstrates the potential advantage of this new alloy. One could also compare the grain-sizes within the API X70 slab after exiting the soaking furnace, to those expected in the new alloy, and observe that the grain size of the new alloy was essentially unchanged as a result of soaking, which can prevent excessive grain growth prior to the onset of thermomechanical processing.

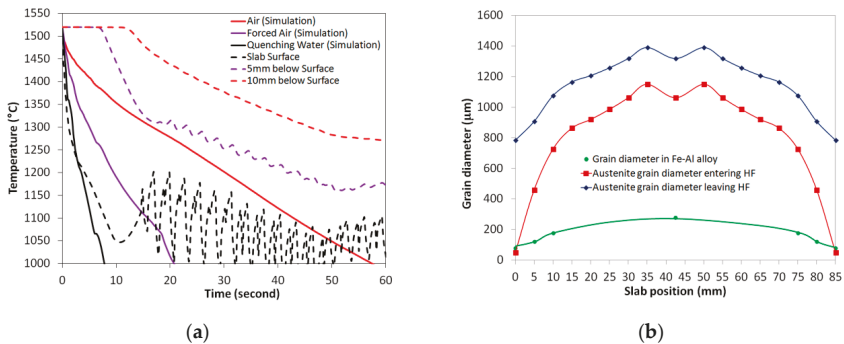


Figure 14. (a) Comparison of CON1D predicted temperature profiles on the surface and 5 and 10 mm below the API X70 85 mm slab, and the recorded thermal profile during simulation process [37]; (b) comparison of grain size evolution with slab distance using the TSCDR process to produce API X70 and Fe-Al new alloy.

4. Conclusions

The developed grain growth model successfully reproduced grain growth as a function of position within the API X70 slab in the TSCDR process. The results suggest that it is essential to control grain coarsening in each step, from solidification to the holding furnace, in order to maintain a required fine and uniform austenite grain size prior to the onset of thermomechanical processing.

Reducing the slab thickness can increase the cooling rate at the slab center during the TSCDR process. Predictions of the grain growth model suggest that austenite grain diameter can be reduced from 1345 to 500 μm if a 30 mm slab high cooling rate is produced. In addition, this would lead to less non-uniformity in the as-cast microstructure by refining the grains at the center of the slab. Increasing secondary cooling with restricted casting speed will increase cooling rate, resulting in primary and secondary dendrite arm spacing refinement. Increased secondary cooling, from 0.6 L/kg of hot steel to 1.4 L/kg of hot steel, can reduce the grain size at the center of an 85-mm thick slab, from 1345 to 942 μm .

Liquid core reduction together with dynamic control of the liquid pool length can not only reduce center line segregation and solidification-related defects, but also provides the potential for generating more nucleation sites for delta-ferrite resulting in austenite grain refinement.

Increasing the number of austenite nucleation sites during the delta-ferrite to austenite phase transformation is an effective method of refining and homogenizing the as-cast microstructure of the TSCDR micro alloyed steels. When the Fe-Al model alloy was deformed prior to the onset of the delta to gamma transformation austenite, nucleated prolifically along the original delta grain boundaries and the newly recrystallized delta grain boundaries. The application of 20% deformation generated more than 30 recrystallized grains in each original delta grain. The calculations confirmed that the austenite grain in the 85 mm slab center can be reduced from 1345 to 1001 μm by doubling the nucleation sites.

Austenite grains continue growing inside the holding furnace. Optimizing the holding temperature and time can control austenite coarsening. The austenite grain size can be reduced from 1475 to 1072 μm if casting a 70 mm slab with a soaking temperature of 1120 $^{\circ}\text{C}$ for 10 min, instead of 1150 $^{\circ}\text{C}$ for 18 min.

The use of a delta-ferrite/austenite duplex microstructure is an effective method to retard grain growth at high temperatures. In the delta-ferrite/austenite duplex microstructure, the delta grain growth rate is very slow and controlled by the rate of coarsening of second phase particles. The developed grain growth model predicts that the delta grain size is 10 times smaller in a duplex microstructure than that in materials without pinning. Laboratory validation shows that the delta grains are pinned throughout the TSCDR process, starting from the final stages of solidification. The concept of dual phase to retard grain coarsening, as demonstrated by the delta-ferrite/austenite duplex microstructure, has great potential for producing more uniform as-cast microstructure for the TSCDR process.

Author Contributions: Conceptualization, T.Z., H.S.Z., and M.S.; methodology, T.Z., H.S.Z., M.S., and R.J.O.; software, R.J.O.; validation, T.Z., H.S.Z., and R.J.O.; formal analysis, T.Z., H.S.Z., and R.J.O.; investigation, T.Z., H.S.Z., and R.J.O.; resources, S.-H.C. and P.Z.; data curation, T.Z. and R.J.O.; writing—original draft preparation, T.Z.; writing—review and editing, R.J.O. and M.S.; visualization, H.S.Z.; supervision, H.S.Z. and M.S.; project administration, M.S.; funding acquisition, M.S.

Funding: This research received no external funding.

Acknowledgments: The authors wish to acknowledge with thanks (i) technical support in making model alloys by CANMET (Hamilton, ON, Canada), (ii) assistance in material characterization from Canadian Centre for Electron Microscopy (CCEM) at McMaster University (Hamilton, ON, Canada), and (iii) the technological support from the DSPC operation team and New Product Development Department at Algoma Inc. (Sault Ste. Marie, ON, Canada).

Conflicts of Interest: The authors declare no conflict of interest.

Appendix A

To calculate the grain boundary mobility $M(t)$ in Equation (A1), the Turnbull mobility was used as an initial estimation:

$$M_{\text{pure}} = \frac{wD_{\text{GB}}V_m}{b^2RT} \quad (\text{A1})$$

In the above equation, w is the grain boundary thickness, D_{GB} is the grain boundary self-diffusion coefficient, V_m is the molar volume, b is the magnitude of the Burgers vector, R is the gas constant and T is the absolute temperature. The delta-ferrite has body-centered-cubic (BCC) crystal structure, the Burgers vector is $b = 1/2\langle 111 \rangle$ and $b = \sqrt{3}a/2$, where a is the lattice parameter of delta-ferrite, 0.286 nm. The molar volume, $V_m = 7.11 \text{ cm}^3$. The activation energy for diffusion along the grain boundary was taken to be $Q_{\text{GB}} = 0.68Q$, where $Q = 256 \text{ kJ/mole}$ is the activation energy for bulk diffusion in BCC. Finally, $w = 1 \text{ nm}$ and $Q_{\text{GB0}} = 1.67 \times 10^{-4} \text{ m}^3/\text{s}$. Given that Turnbull mobility does not take into account attachment kinetics, the grain boundary mobility in this way overestimates the experimental grain growth kinetics. The best fit of the experimental data was obtained using a mobility, which is 1/3 of the Turnbull estimate [9]. Therefore, the delta grain mobility used in this work was:

$$M_{\delta}(t) = \frac{0.7075}{T(t)} \times \exp\left(\frac{-20,995.43}{T(t)}\right) \quad (\text{A2})$$

To estimate the mobility of the austenite grain boundaries, the austenite with face-centered cubic (FCC) crystal structure has $b = 1/2\langle 110 \rangle$; therefore, $b = \sqrt{2}a/2$, where a is 0.357 nm. The molar volume, V_m , is 6.85 cm^3 , the bulk diffusion activation energy in FCC $Q = 284 \text{ kJ/mole}$, and that of grain boundary diffusion is: $Q_{\text{GB}} = 0.61Q$. $w = 1 \text{ nm}$ and $Q_{\text{GB0}} = 0.49 \times 10^{-4} \text{ m}^3/\text{s}$. Once again, the Turnbull mobility leads to an overestimation of the austenite grain growth kinetics. The best fit of the experimental data was obtained with a mobility, which is 0.96 times the Turnbull estimate [9]. Thus, the austenite grain boundary mobility used in this calculation was:

$$M_{\gamma}(t) = \frac{0.3072}{T(t)} \times \exp\left(\frac{-20,837.14}{T(t)}\right) \quad (\text{A3})$$

The cooling path $T(t)$ at each point of the slab and secondary dendrite arm spacing, thermophysical properties, and spray heat transfer coefficients were calculated using the CON1D V7.0 slab casting heat transfer model. The casting speeds for different slab thicknesses used in the simulations are listed as the following:

- (1) 85 mm slab, casting speed 3.0–3.4 m/min;
- (2) 70 mm slab, casting speed 3.4–4.0 m/min;
- (3) 50 mm slab, casting speed 4.5–5.5 m/min;
- (4) 30 mm slab, casting speed 4.5–6.5 m/min.

References

1. Klinkenberg, C.; Kintscher, B.; Hoen, K.; Reifferscheid, M. More than 25 years of experience in thin slab casting and rolling current state of the art and future developments. *Steel Res. Int.* **2017**, *88*, 1700272. [[CrossRef](#)]
2. Arvedi, G.; Mazzolari, F.; Siegl, J.; Hohenbichler, G.; Holleis, G. Arvedi ESP first thin slab endless casting and rolling results. *Ironmak. Steelmak.* **2010**, *37*, 271–275. [[CrossRef](#)]
3. Zhou, T.; Zhang, P.; Kuuskman, K.; Cerilli, E.; Cho, S.H.; Burella, D.; Zurob, H.S. Development of medium-high carbon hot rolled steel strip on a thin slab casting direct strip production complex. *Ironmak. Steelmak.* **2018**, *45*, 603–610. [[CrossRef](#)]
4. Bhattacharya, D.; Misra, S. Development of microalloyed steels through thin slab casting and rolling (TSCR) route. *Trans. Indian Inst. Met.* **2017**, *70*, 1647–1659. [[CrossRef](#)]

5. Challa, V.S.A.; Misra, R.D.K.; O'Malley, R.; Jansto, S.G. The Effect of Coiling Temperature on the Mechanical Properties of Ultrahigh-Strength 700 MPa Grade Processed via Thin-Slab Casting. In Proceedings of the AISTech 2014 Proceedings, Indianapolis, IN, USA, 5–8 May 2014; pp. 2987–2997.
6. Nie, W.J.; Xin, W.F.; Xu, T.M.; Shi, P.J.; Zhang, X.B. Enhancing the toughness of heavy thick X80 pipeline steel plates by microstructure control. *Adv. Mater. Res.* **2011**, *194–196*, 1183–1191. [[CrossRef](#)]
7. Reip, C.P.; Hennig, W.; Kempken, J.; Hagemann, R. Development of CSP processed high strength pipe steels. *Mater. Sci. Forum.* **2005**, *500–501*, 287–294. [[CrossRef](#)]
8. Wang, R.; Garcia, C.I.; Hua, M.; Zhang, H.; DeArdo, A.J. The Microstructure Evolution of Nb,Ti Complex Microalloyed Steel During the CSP Process. *Mater. Sci. Forum.* **2005**, *500–501*, 229–236. [[CrossRef](#)]
9. Zhou, T.; O'Malley, R.J.; Zurob, H.S. Study of grain-growth kinetics in delta-ferrite and austenite with application to thin-slab cast direct-rolling microalloyed steels. *Metall. Mater. Trans. A* **2010**, *41*, 2112–2120. [[CrossRef](#)]
10. Martin, J.W.; Doherty, R.D.; Cantor, B. *Stability of Microstructure in Metallic Systems*; Cambridge University Press: Cambridge, UK, 1997; pp. 219–231.
11. Humphreys, F.J.; Hatherly, M. *Recrystallization and Related Annealing Phenomena*, 2nd ed.; Elsevier Ltd.: Oxford, UK, 2004; pp. 11–25.
12. Turnbull, D. Theory of grain boundary motion. *Trans. AIME* **1951**, *191*, 661–665.
13. Köthe, A.; Kunze, J.; Backmann, G.; Mickel, C. Precipitation of TiN and (Ti,Nb)(C,N) during solidification, cooling and hot direct deformation. *Mater. Sci. Forum.* **1998**, *284–286*, 493–500. [[CrossRef](#)]
14. Nagata, M.T.; Speer, J.G.; Matlock, D.K. Titanium nitride precipitation behavior in thin-slab cast high-strength low-alloy steels. *Metall. Mater. Trans. A* **2002**, *33*, 3099–3109. [[CrossRef](#)]
15. Smith, C.S. Grains, Phases, and interfaces: An interpretation of microstructure. *Trans. Metall. Soc. AIME* **1948**, *175*, 15–51.
16. Kwon, O.; DeArdo, A.J. Interactions between recrystallization and precipitation in hot-deformed microalloyed steels. *Acta Metall.* **1991**, *39*, 529–538. [[CrossRef](#)]
17. Palmiere, E.J.; Garcia, C.I.; DeArdo, A.J. Compositional and microstructural changes which attend reheating and grain coarsening in steels containing niobium. *Metall. Mater. Trans. A* **1994**, *25*, 277–286. [[CrossRef](#)]
18. Poths, R.M.; Rainforth, W.M.; Palmiere, E.J. Strain Induced precipitation in model and conventional microalloyed steels during thermomechanical processing. *Mater. Sci. Forum.* **2005**, *500–501*, 139–145. [[CrossRef](#)]
19. Zurob, H.S.; Hutchinson, C.R.; Brechet, Y.; Purdy, G. Modeling recrystallization of microalloyed austenite: Effect of coupling recovery, precipitation and recrystallization. *Acta Mater.* **2002**, *50*, 3075–3092. [[CrossRef](#)]
20. Gladman, T. *The Physical Metallurgy of Microalloyed Steel*; Institute of Metals: London, UK, 1997.
21. Thermo-Calc Software. Available online: www.thermocalc.com (accessed on 2 November 2018).
22. Meng, Y.; Thomas, B.G. Heat-transfer and solidification model of continuous slab casting: CON1D. *Metall. Mater. Trans. B* **2003**, *34*, 685–705. [[CrossRef](#)]
23. Yin, H.; Emi, T.; Shibara, H. Morphological Instability of δ -ferrite/ γ -austenite interphase boundary in low carbon steel. *Acta Mater.* **1999**, *47*, 1523–1535. [[CrossRef](#)]
24. Kim, H.S.; Kobayashi, Y.; Nagai, K. Prediction of prior austenite grain size of high-phosphorous steels through phase transformation simulation. *ISIJ Int.* **2006**, *46*, 854–858. [[CrossRef](#)]
25. Holzhauser, J.F.; Spitzer, K.H.; Schwerdtfeger, K. Study of heat transfer through layers of casting flux: experiments with a laboratory set-up simulating the conditions in continuous casting. *Steel Res.* **1999**, *70*, 252–257. [[CrossRef](#)]
26. Gonzalez, M.; Goldschmit, M.B.; Assanelli, A.P.; Berdager, E.F.; Dvorkin, E. Modeling of the solidification process in a continuous casting installation for steel slabs. *Metall. Mater. Trans. B* **2003**, *34*, 455–473. [[CrossRef](#)]
27. Louhenkilpi, S.; Makinen, M.; Vapalahti, S.; Raisanen, T.; Laine, J. 3D steady state and transient simulation tools for heat transfer and solidification in continuous casting. *Mater. Sci. Eng. A* **2005**, *413–414*, 135–138. [[CrossRef](#)]
28. McCarmey, D.G.; Hunt, J.D. Measurements of cell and primary dendrite arm spacing in directionally solidified aluminum alloys. *Acta Metall.* **1981**, *29*, 1851–1863. [[CrossRef](#)]
29. Bouchard, D.; Kirkaldy, J.S. Prediction of dendrite arm spacings in unsteady and steady-state heat flow of unidirectionally solidified binary alloys. *Metall. Mater. Trans. B.* **1997**, *28*, 651–663. [[CrossRef](#)]

30. Taha, M.A. Influence of solidification parameters on dendrite arm spacings in low carbon steels. *J. Mater. Sci. Lett.* **1986**, *5*, 307–310. [[CrossRef](#)]
31. Cahn, R.W.; Haasen, P. *Physical Metallurgy*, 4th ed.; North-Holland Physics Publishing: Amsterdam, The Netherlands, 1996.
32. Sobral, M.D.C.; Mei, P.R.; Santos, R.G.; Gentile, F.C.; Bellon, J.C. Laboratory simulation of thin slab casting. *Ironmak. Steelmak.* **2003**, *30*, 412–416. [[CrossRef](#)]
33. Zhou, T.H.; Gheribi, A.E.; Zurob, H.S. Austenite particle coarsening and delta-ferrite grain growth in model Fe-Al alloy. *Can. Metall. Q.* **2013**, *52*, 90–97. [[CrossRef](#)]
34. Zhou, T.; Overby, D.; Badgley, P.; Martin-Root, C.; Wang, X.; Liang, S.L.; Zurob, S.H. Study of processing, microstructure and mechanical properties of hot rolled ultra high strength steel. *Ironmak. Steelmak.* **2018**. [[CrossRef](#)]
35. Hillert, M. Inhibition of grain growth by second-phase particles. *Acta Metall.* **1988**, *36*, 3177–3181. [[CrossRef](#)]
36. Zhou, T.; Zurob, H.S.; O'Malley, R.J.; Rehman, K. Model Fe-Al steel with exceptional resistance to high temperature coarsening. Part I: Coarsening mechanism and particle pinning effects. *Metall. Mater. Trans. A* **2015**, *41*, 178–189. [[CrossRef](#)]
37. Zhou, T.; Zhang, P.; O'Malley, R.J.; Zurob, H.S.; Subramanian, M. Model Fe-Al steel with exceptional resistance to high temperature coarsening. Part II: Experimental validation and applications. *Metall. Mater. Trans. A* **2015**, *41*, 190–198. [[CrossRef](#)]



© 2019 by the authors. Licensee MDPI, Basel, Switzerland. This article is an open access article distributed under the terms and conditions of the Creative Commons Attribution (CC BY) license (<http://creativecommons.org/licenses/by/4.0/>).

Article

Simulation of Crack Initiation and Propagation in the Crystals of a Beam Blank

Gaiyan Yang ^{1,2,3}, Liguang Zhu ^{2,3}, Wei Chen ^{2,3,*}, Gaoxiang Guo ^{2,3} and Baomin He ^{2,3}

¹ School of Metallurgical and Ecological Engineering, University of Science and Technology Beijing, Beijing 100083, China; gaiyanyang-1@163.com

² North China University of Science and Technology, Tangshan 063210, Hebei, China; zhulg@ncst.edu.cn (L.Z.); 17330544382@163.com (G.G.); 18232527312@163.com (B.H.)

³ Hebei Engineering Research Center of High Quality Steel Continuous Casting, Tangshan 063009, Hebei, China

* Correspondence: chenwei@ncst.edu.cn or hblgdzxb@163.com; Tel.: +86-315-880-5053

Received: 5 October 2018; Accepted: 1 November 2018; Published: 5 November 2018

Abstract: Surface cracking seriously affects the quality of beam blanks in continuous casting. To study the mechanism of surface crack initiation and propagation under beam blank mesoscopic condition, this study established a polycrystalline model using MATLAB. Based on mesoscopic damage mechanics, a full implicit stress iterative algorithm was used to simulate the crack propagation and the stress and strain of pores and inclusions of the polycrystalline model using ABAQUS software. The results show that the stress at the crystal boundary is much higher than that in the crystal, cracks occur earlier in the former than in the latter, and cracks extend along the direction perpendicular to the force. When a polycrystalline model with pores is subjected to tensile stress, a stress concentration occurs when the end of the pores is perpendicular to the stress direction, and the propagation and aggregation direction of the pores is basically perpendicular to the direction of the tensile stress. When a polycrystalline model with impurities is subjected to force, the stress concentrates around the impurity but the strain here is minimal, which leads to the crack propagating along the impurity direction. This study can provide theoretical guidance for controlling the generation of macroscopic cracks in beam blanks.

Keywords: polycrystalline model; pores; inclusions; mechanism; beam blank; crystal; propagation

1. Introduction

As the raw material of H-beam production, the beam blank has the advantages of fewer rolling passes, high production capacity, low maintenance cost, and high product quality [1,2]. However, because of the complexity of its section, there are often more quality problems than with other blank types [3], particularly surface cracks [4] as shown in Figures 1 and 2 [5]. To meet the new requirements of a new era in terms of the quality of the beam blank and reduce the surface cracks of the billet, it is urgent to conduct in-depth theoretical research on the surface crack propagation mechanism of the billet at different scales, and thus to play a good guiding role in the production of the beam blanks.

At present, the research on cracks of beam blanks has mainly focused on optimizing the process parameters and improving the equipment structure [6–10]. Numerical simulation of crack initiation and propagation of beam blanks remains less studied and the study of the stress concentration effect on the grain interior and boundary is lacking; study of the effects of inclusions and pores on crack initiation and propagation under mesoscopic conditions does not exist. Lasko et al. simulated the crack generation and expansion process of Al₂O₃/6061 Al composites under different mechanical properties and damage parameters using ABAQUS [11]. Jiang et al. introduced the nodal enrichment functions in the extended finite element method and used the level set method to track the crack

propagation path of the compact tension specimen [12]. Wang and Schwalbe studied the transition from intercrystalline to transcrystalline fatigue crack propagation under different ageing conditions of the alloy Cu-35%Ni-3.5%Cr [13]. Shen simulated the crack propagation of the slab under a mesoscopic condition [14]. Xue et al. used the Abaqus program and its user subroutine UVARM to simulate and analyze the single micro-crack mode in a microcosmic view field, and found that the crack propagation form is different with different presetting angles under different stress states; the higher the stress triaxiality value, the more easily the crack propagates, while the crack tends to close when the value is negative. The deformation energy ratio can precisely reflect the influence degree of stress states on crack propagation [15]. The aforementioned literature addresses crack initiation and propagation. Although some of these studies were completed under microscopic observation, the studies of the Q235B beam blank, particularly under the polycrystalline model, were nearly unable to study the effect of inclusions and pores on crack initiation and propagation. The polycrystalline model combined with metallographic experiments is closer to reality, and can do what other model simulations could not do prior. In this study, through the establishment of a polycrystalline model, the crack propagation process in the crystal of a beam blank is analyzed, and the stress and strain conditions with pores or inclusions are also analyzed, providing theoretical guidance for the generation of macroscopic cracks and process optimization.

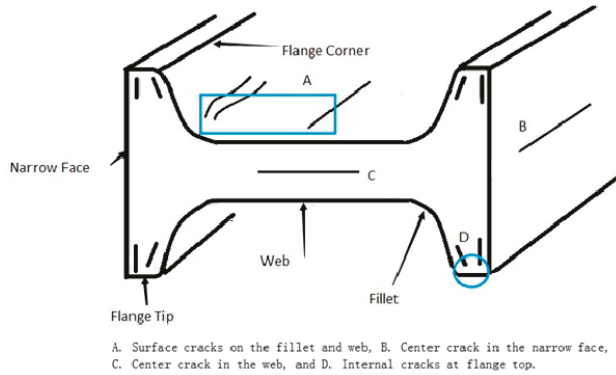


Figure 1. Cross-section schematic of a beam blank [5].



Figure 2. Surface cracks and blowholes on (a) web and (b) fillet of actual beam blank [5].

2. Establishment of a Polycrystalline Model

The polycrystalline model in this study was mainly programmed using MATLAB software (USA). A Voronoi diagram was drawn using the program; its process is shown in Figure 3. The main principle of Voronoi diagram construction is to first randomly generate N points within a certain coordinate range, and then form a triangle with the three points closest to each other, which will generate an infinite number of triangles in the range of coordinates, forming a network. Finally, the midline of the three sides of each triangle in the triangle net is created, and these midlines are connected to form the final polycrystalline model. We termed this method the dual generation method. As can be seen from Figure 4, the polycrystalline model drawn using this method can not only show the irregularity in the size and distribution of grains, but also be consistent in terms of actual grain morphology [16]. Therefore, it is reasonable to draw a polycrystalline model using this method.

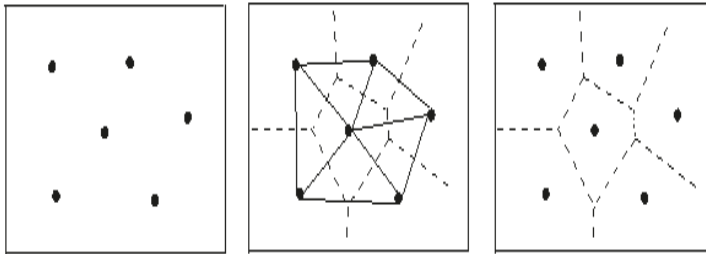


Figure 3. Implementation process of the Voronoi diagram.

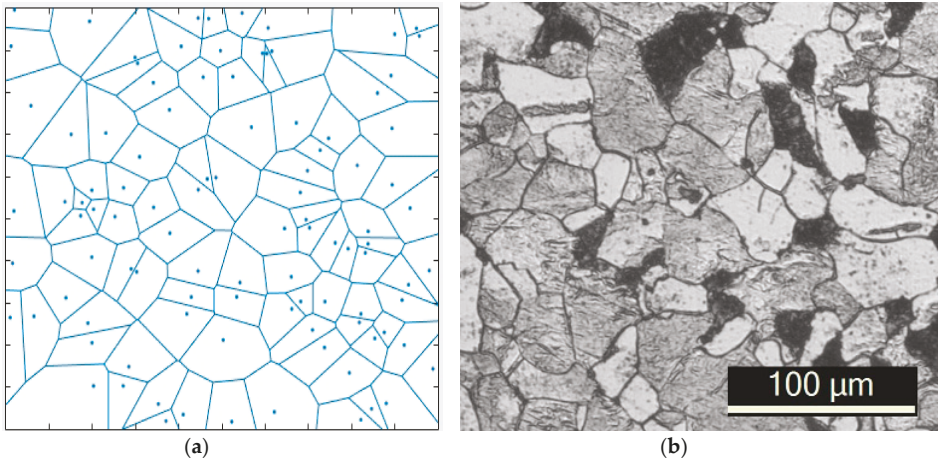


Figure 4. Grain size diagram of (a) polycrystalline Voronoi diagram in MATLAB and (b) actual grain size of the beam blank.

The coordinates of each point obtained from MATLAB are written into the input file and imported into ABAQUS software (6.12 Abaqus, France) to obtain the polycrystalline model. The size of the model area was $0.1 \text{ mm} \times 0.1 \text{ mm}$, as shown in Figure 5; the related parameters of the Q235B materials in the simulation are shown in Table 1.

Table 1. Main parameters used in the simulation.

Parameter	Data
Steel grade	Q235B
Steel compositions	C: 0.19%, Mn: 0.43%, Si: 0.20%, P: 0.025%, S: 0.007%
Elastic Modulus of matrix (E_m)	206 GPa [16]
Elastic Modulus of inclusion (E_i)	20,600 GPa [16]
Poisson's ratio (ν)	0.28 [16]
Specific heat (C_p)	687 J/kg·°C [14]
Thermal conductivity (λ)	32 W/m·°C [14]
Thermal expansion Coefficient (α)	1.30×10^{-5} m/K [14]
Ultimate tensile strength (σ_b)	390 MPa [14]
Yield stress (σ_s)	235 MPa [14]
The density of strand (ρ)	7400 kg/m ³ [14]

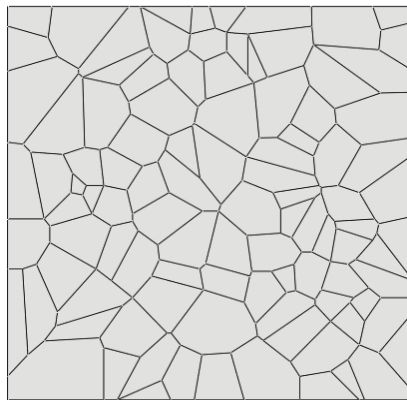


Figure 5. Two-dimensional polycrystalline model in ABAQUS.

2.1. Polycrystalline Model with Cracks

Four types of cracks of different angles and different positions were created on the polycrystalline model of the beam blank. The location of the crack was in the grain interior and the grain boundary; the angles between the crack and tensile stress were 15°, 45°, 75°, and 90°. Figure 6 shows the two typical positions of cracks and loading direction into a 45° angle.

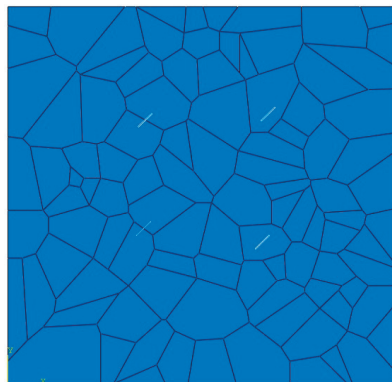


Figure 6. Crack position distribution diagram of the crack with the tensile stress at an angle of 45°.

2.2. Polycrystalline Model with Pores

During the process of casting the beam blank, the generation of pores is mostly caused by improper protective casting, wet raw materials, poor baking in tundish, poor deoxidization of the liquid steel, and poor degassing in refining [17,18]. The existence of pores will have a great impact on the tensile properties of the materials; therefore, the simulation of the stress and strain of a polycrystalline model with pores is of special significance to prevent the generation of cracks.

Models with pores are mainly created in component modules. When creating the model, material properties such as the elastic modulus and Poisson ratio of the model are assigned to the attribute module, while those with holes are not assigned to properties. Based on the original polycrystalline model, a hole was obtained by cutting into the assembly module, and a model with pores was established to simulate the stress and strain. Figure 7 shows the pores distribution on the polycrystalline model components.

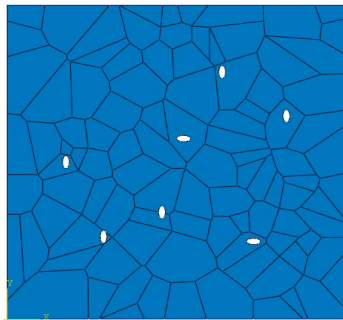


Figure 7. The distribution of pores on the polycrystalline model components.

2.3. Polycrystalline Model with Inclusions

Inclusions in the billet are typically harder than the matrix, which may cause stress concentration around the impurities, leading to metal damage or fractures. Therefore, the study of a polycrystalline model with impurities has a great effect in reducing cracks in the beam blank.

Models with inclusions were also created in the component module. In the attribute module, the matrix was endowed with corresponding elasticity and plasticity. However, because of the high hardness of the inclusions, it was difficult to produce deformation; thus, only the elastic modulus is provided, which is 100 times the size of the matrix [16]. Based on the original polycrystalline model, inclusions were obtained using an incorporating method in the assembly module. Figure 8 shows the distribution of the inclusions on the polycrystalline model components.

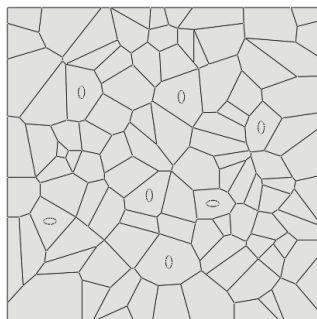


Figure 8. Inclusions distribution on the polycrystalline model components.

2.4. Meshing and Initial Boundary Conditions

By referring to the relevant data, it was found that during the process of elastoplastic analysis, when the object of the study is an incompressible material, non-coordinated units and linear reduction integral units are mainly used. A linear reduction integral can make the calculation easier and save time. The element type selected using this calculation method in ABAQUS was CPS4R, that is, a four-node bilinear plane stress quadrilateral reduced integration element. The control property of the grid was quadrilateral. In this case, the total number of units in the model was 6562; the meshing of the polycrystalline model is shown in Figure 9.

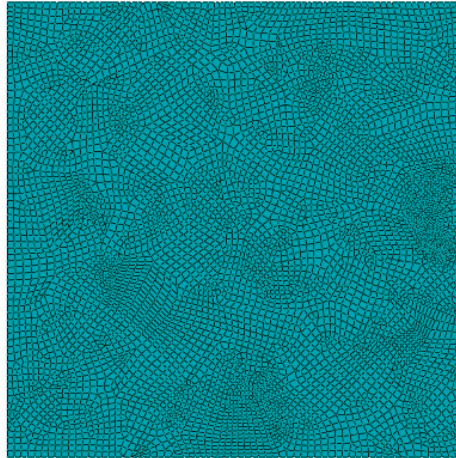


Figure 9. Meshing of the polycrystalline model.

In this study, the boundary condition set in ABAQUS was to select the displacement/rotation angle, the freedom of the boundary UR3 in the X direction was set to 0, velocity loads were separately applied on both sides, and speed/acceleration was selected with a magnitude of 0.05 m/s and a velocity load in the Y direction of 0 [16]. The boundary conditions can better reflect the actual loading conditions. The specific load is shown in Figure 10.

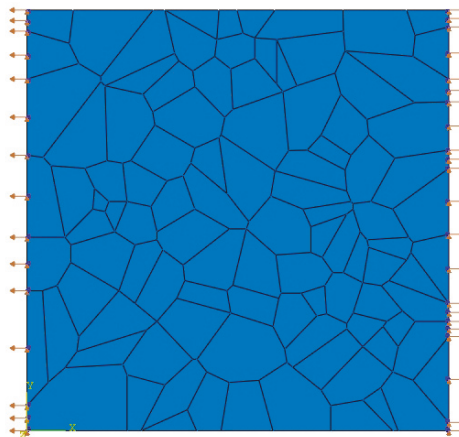


Figure 10. Load distribution.

3. Analysis of Crack Initiation and Propagation in a Crystal

3.1. Stress and Strain Analysis of Defect-Free Crystals

As can be seen in Figures 11 and 12, in the polycrystalline model without any defect, the stress and strain distribution at the boundary of the polycrystalline model is obviously different from that in the crystal, and the stress and strain at the boundary are obviously greater than those in the crystal. This is because of the interaction of external factors and the grain boundary. For example, under a high temperature condition, the grain boundary will undergo a structural change, which will weaken the grain boundary. Another reason is that the properties of the grain boundary and crystal matrix are quite different. As the tensile stress gradually increases, stress corrosion will first occur at the grain boundary, making the grain boundary more prone to fracturing.

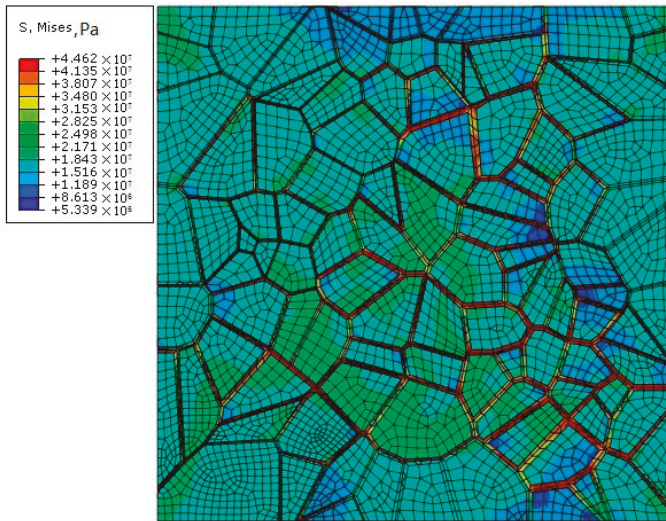


Figure 11. Stress distribution in the polycrystalline model without defects.

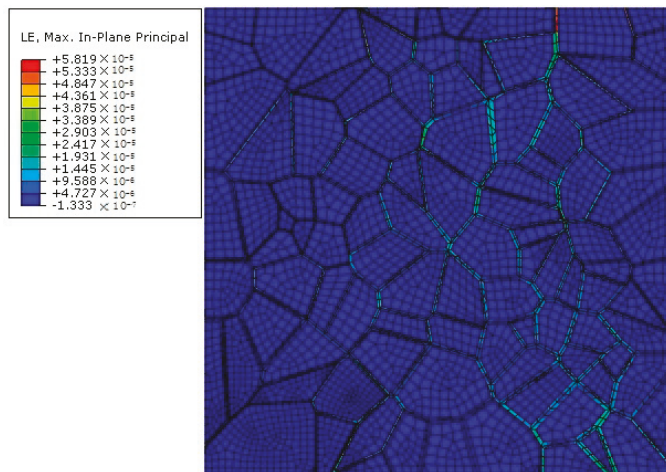


Figure 12. Strain diagram of the polycrystalline model without defects.

3.2. Analysis of a Polycrystalline Model with Multiple Cracks

Cracks are created at two typical positions with four angles, different from the tensile stress. The two typical positions are the crystal interior and boundary, respectively, at four angles between the crack and tensile stress, namely, 15°, 45°, 75°, and 90°. Figures 13–16 show the crack propagation in the two typical positions at different angles from the load direction.

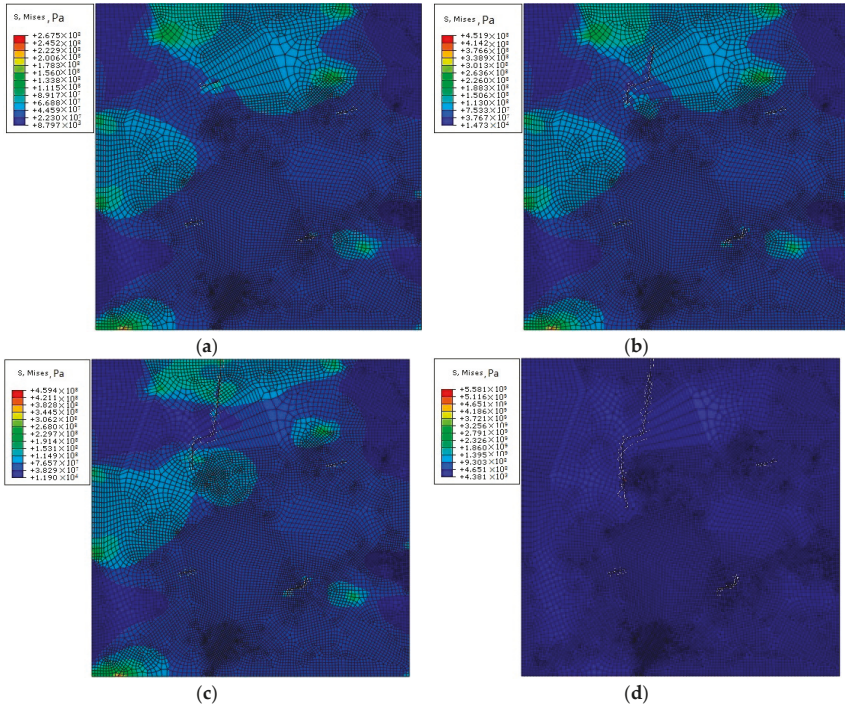


Figure 13. The (a) first stage, (b) second stage, (c) third stage, and (d) fourth stage of crack propagation with a load direction of 15°.

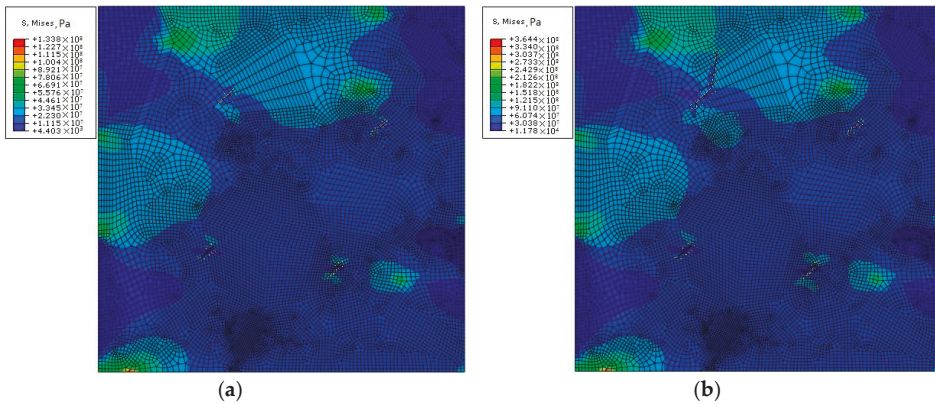


Figure 14. Cont.

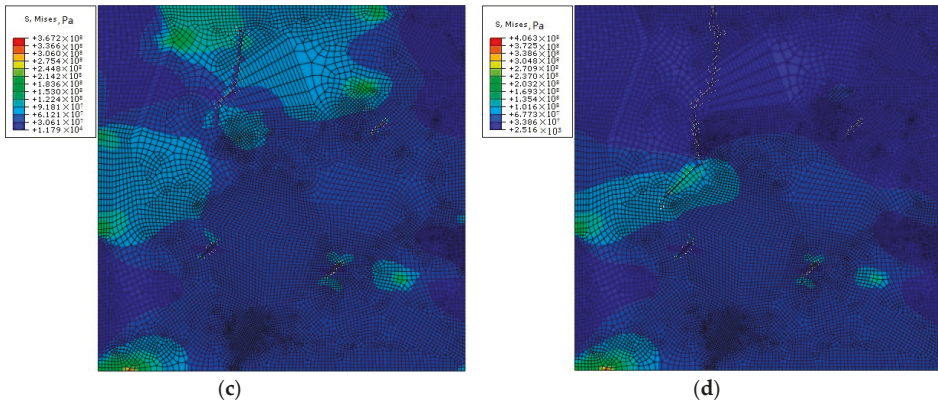


Figure 14. The (a) first stage, (b) second stage, (c) third stage, and (d) fourth stage of crack propagation with a load direction of 45°.

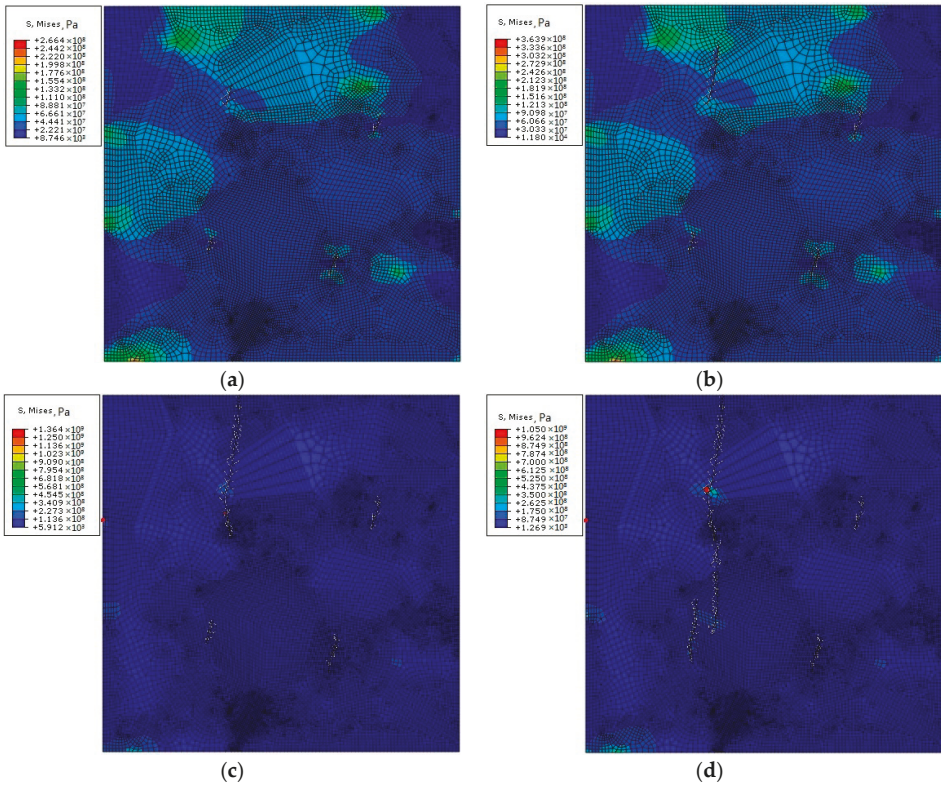


Figure 15. The (a) first stage, (b) second stage, (c) third stage, and (d) fourth stage of crack propagation with a load direction of 75°.

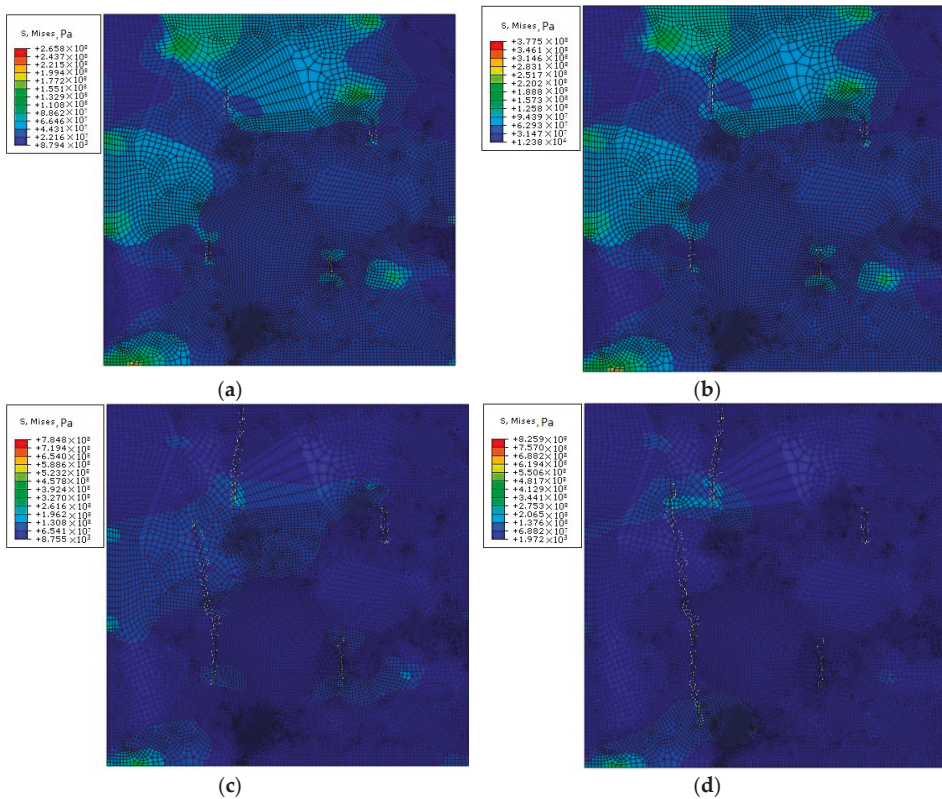


Figure 16. The (a) first stage, (b) second stage, (c) third stage, and (d) fourth stage of crack propagation with a load direction of 90° .

According to the aforementioned Figures 13–16, crack propagation occurs at the crystal boundary prior to that in the crystal, which is a result of crystal interaction that makes the stress at the crystal boundary more concentrated than that in the crystal. Thus, crack propagation is accelerated. Through the analysis of crack propagation under the aforementioned conditions, the following can be found:

- The direction of the crack propagation is basically along with the direction perpendicular to the tensile stress, and the amount of crack propagation along this direction is also the greatest, consistent with the study of Yang et al. [19], Wang and Schwalbe [13].
- The amount of crack propagation at the grain boundary is higher than that in the crystal.
- The angle and tensile stress of the crack are unrelated to the direction of crack propagation, and their influence on crack propagation is mainly reflected in the time and sequence of the crack propagation and the final crack propagation displacement.

3.3. Analysis of a Polycrystalline Model of Different Porosities

Damage to metallic materials when they contain pores can be approximately divided into three processes: first, nucleation occurs around the grain boundary or the second phase particle, then the holes begin to grow, and finally they connect together to form cracks. Therefore, it is of great significance to study the stress and strain process of a polycrystalline model with holes to show the mechanism of crack formation.

Figure 17 shows the stress distribution of the polycrystalline model with different porosities, from which certain regularity can be found in pores. In the direction perpendicular to tensile stress, the maximum stress can be observed at the end of pores; while in the same direction of the force, the minimum stress and strain can be calculated around other pores with insignificant deformation. It indicates that when the polycrystalline model deforms, stress concentration at the end of the pores is mostly perpendicular to the direction of tensile stress.

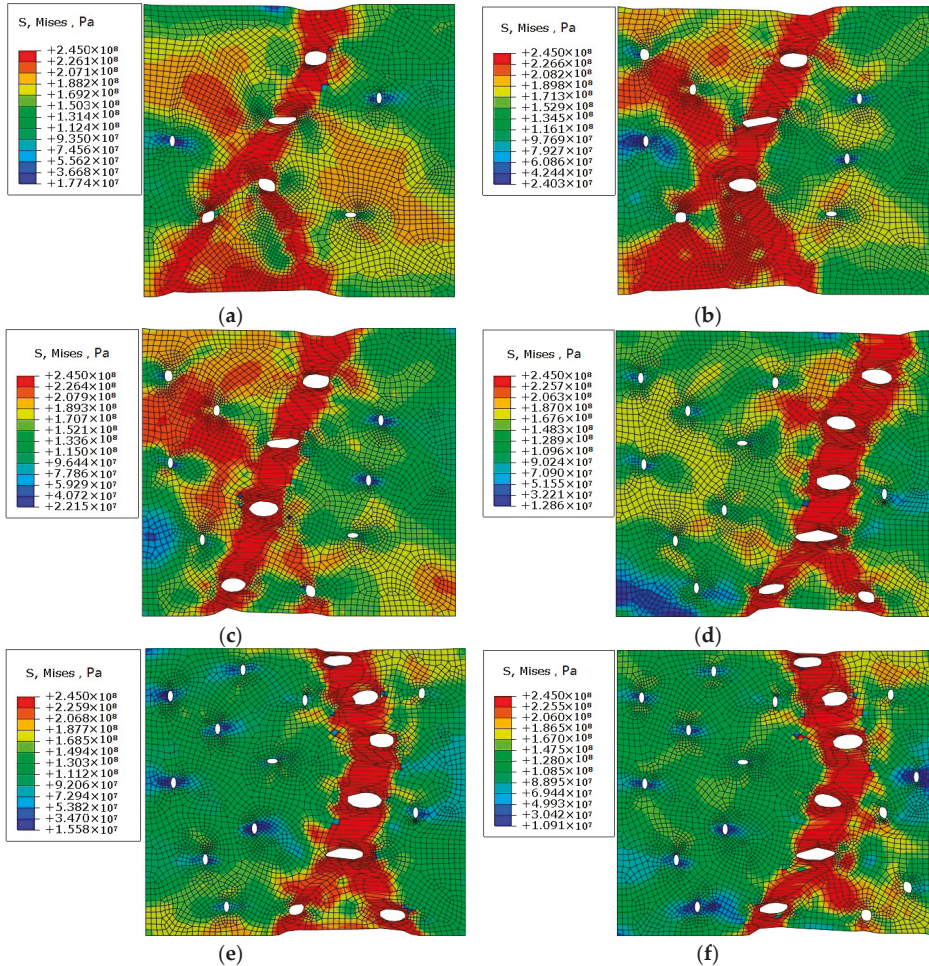


Figure 17. Stress distribution diagram of a polycrystalline model with different porosity of (a) 0.40%, (b) 0.60%, (c) 0.75%, (d) 0.90%, (e) 1.10%, and (f) 1.30%.

Figure 18 shows the strain results of polycrystalline models when the porosity is 0.4% and 1.3%, respectively. It can be found from the variation diagram of strain that the plastic strain is more concentrated around the pores than the matrix, and the polycrystalline model with a porosity of 1.3% is significantly larger than the polycrystalline model with a porosity of 0.4%, which indicates that the effects of different porosity on metal damage are different. At the same time, under different porosity, the pores begin to propagate and aggregate in the direction perpendicular to the tensile stress. The main reason for this phenomenon is that in the direction perpendicular to the tensile stress,

the stress concentration occurs at the end of the pores, which resulting in larger equivalent plastic strain around the pores, and the localization of the strain results in continuous aggregation and propagation of the pores, so the crack always starts from this direction.

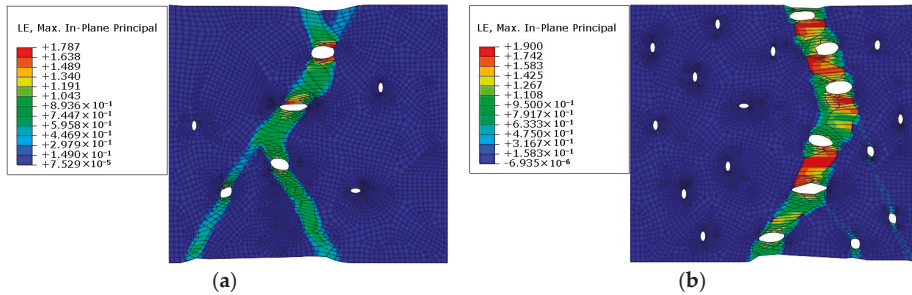


Figure 18. Tensile strain diagram with porosity of (a) 0.4% and (b) 1.3%.

3.4. Analysis of Polycrystal Model with Different Proportion Inclusions

The size and number of inclusions in steel is not only an important condition to evaluate steel quality, but also one of the main factors causing defects, and is the unavoidable existence in steel materials. Because the properties of the inclusions are different from the properties of the steel matrix materials, it has a great influence on the deformation and fracture process of the steel materials. In this paper, the stress and strain behavior of polycrystalline model with different percentage of inclusions is simulated to analyze its effect on material failure.

On the polycrystalline model parts, different proportion areas are divided as inclusions, and then inclusions material properties are given in the property module. Because it is a hard phase relative to the matrix of the polycrystalline model, only elastic properties are assigned to it. In this method, models with 0.44%, 0.57%, 0.70%, and 0.82% percentage of impurities were created respectively, and the same boundary conditions were set for simulation. Figure 18 shows the stress distribution in matrix with inclusions. As can be seen from the figure, the stress mainly concentrates at the inclusions, and the stress at the inclusions is much larger than that at the matrix. The reason for this phenomenon is that the elasticity and plasticity differences between impurities and the matrix are relatively large in the polycrystalline model. When the polycrystalline model is under stress, impurities can hardly meet the deformation requirements when the matrix deforms. Therefore, the impurities cannot deform simultaneously with the matrix, as a result, the stress accumulates in and around impurities, making the stress distribution at the impurities more obvious. Combined with Figures 17 and 19, it can be seen that the influence of pores on the crack is greater than that of inclusions.

As can be seen from the strain of a polycrystalline model of different impurity percentages in Figure 20, the deformation of the matrix of the polycrystalline model is much different from that of the impurities; the deformation of the impurities is much less than that of the matrix. This is because of the large differences in the elasticity and plasticity of the impurities and polycrystalline matrix. After the loading is applied, the impurity cannot deform because of its properties; thus the stress concentration will occur around the impurity and the stress value will be increasingly greater, resulting in the separation of the impurity and the matrix, and thus a hole. Therefore, when a metal material is subjected to a large external force, the crack will often expand along the direction of the impurities, resulting in the material damage and fracture.

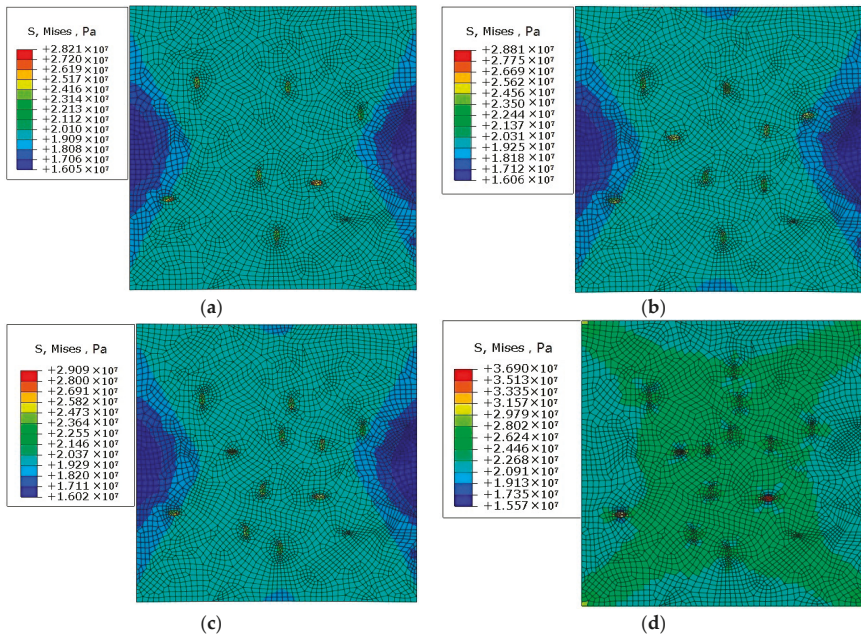


Figure 19. Stress distribution diagram of a polycrystalline model with different impurity percentages of (a) 0.44%, (b) 0.57%, (c) 0.70%, and (d) 0.82%.

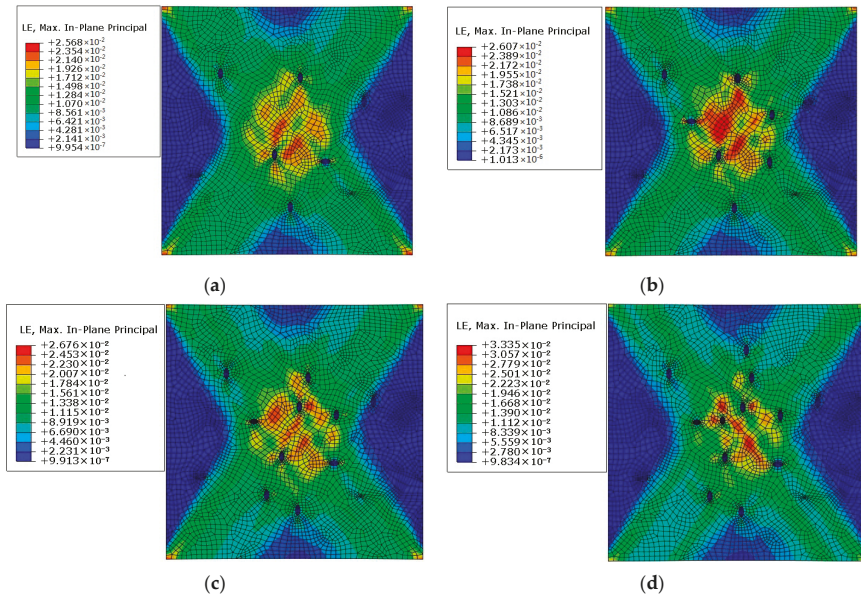


Figure 20. Strain distribution diagram of a polycrystalline model with different impurity percentages of (a) 0.44%, (b) 0.57%, (c) 0.70%, and (d) 0.82%.

4. Conclusions

In this study, a polycrystalline model of a beam blank was established using MATLAB. Based on mesoscopic damage mechanics, the full implicit stress iterative algorithm was used to simulate the crack propagation of the polycrystalline model using ABAQUS software, as well as a stress and strain simulation of a polycrystalline model with pores and impurities. The conclusions are as follows:

1. The stress at the crystal boundary is much greater than that in the crystal after loading on the defect-free polycrystalline model.
2. Crack propagation occurs at the crystal boundary prior to that in the crystal, and the propagation of the former is greater than that of the latter.
3. The direction of crack propagation is basically along the direction perpendicular to the tensile stress, and the amount of crack propagation along this direction is also the greatest.
4. When a polycrystalline model with pores is subjected to tensile stress, stress concentration occurs at the position where the end of pores is perpendicular to the stress direction, and the propagation and aggregation direction of the pores are basically perpendicular to the direction of the tensile stress. When the pores ends are parallel to the stress direction, the stress values at these locations are relatively small.
5. When a polycrystalline model with impurities is subjected to a force, a large stress concentration will occur at the impurities, while the strain generated by the impurities is the smallest. This often causes the crack to propagate along the direction of the impurities, thus causing damage to and fracturing of the material.
6. Both inclusions and pores affect crack initiation and propagation. Through mesoscopic simulation, it was found that the influence of pores on cracks is greater than that of inclusions.
7. The simulation of mesoscopic crack initiation and propagation of a beam blank can provide theoretical guidance for the generation of macrocracks and process optimization.

Author Contributions: W.C. and L.Z. conceived and designed the experiments and research ideas; G.Y., G.G., and B.H. performed the experiments, the simulations, the early stage of the investigation, and the data collection; W.C. and G.Y. analyzed the data and graphics; W.C. and L.Z. supervised the whole work; G.Y. wrote and revised the paper.

Funding: This research was funded by the National Natural Science Foundation of China (51574103 and 51574106).

Acknowledgments: The authors would like to thank the technical support of Hebei Engineering Research Center of High Quality Steel Continuous Casting.

Conflicts of Interest: The authors declare no conflict of interest.

References

1. Xu, M.G.; Zhu, M.Y. Transport Phenomena in a Beam-Blank Continuous Casting Mold and a New Design of Submerged Entry Nozzle. *ISIJ Int.* **2015**, *55*, 791–798. [[CrossRef](#)]
2. Xu, H.L.; Wen, G.H.; Sun, W.; Wang, K.Z.; Yan, B. Analysis of thermal behavior for beam blank continuous casting mold. *J. Iron Steel Res. Int.* **2010**, *17*, 17–22. [[CrossRef](#)]
3. Lee, J.E.; Yeo, T.J.; Kyu Hwan, O.H.; Yoon, J.K.; Yoon, U.S. Prediction of cracks in continuously cast steel beam blank through fully coupled analysis of fluid flow, heat transfer, and deformation behavior of a solidifying shell. *Metall. Mater. Trans. A* **2000**, *31*, 225–237. [[CrossRef](#)]
4. Xu, H.L. Simulation and Optimization of Cooling Process for Continuous Casting Beam Blank. Ph.D. Thesis, Chongqing University, Chongqing, China, 2010.
5. Yang, G.Y.; Zhu, L.G.; Chen, W.; Yu, X.W.; He, B.M. Initiation of Surface Cracks on Beam Blank in the Mold during Continuous Casting. *Metals* **2018**, *8*, 712. [[CrossRef](#)]
6. Lv, M.; Lu, B.; Wang, X.X.; Shan, Z.G.; Zhang, Q.; Chen, Y.S. Research and control on web plate crack of the large type beam blank. *Iron Steel* **2010**, *45*, 99–102. [[CrossRef](#)]
7. Wu, J.; Xu, W.; Yang, Y.D. Technics study of reducing longitudinal surface crack of beam blank. *Iron Steel* **2009**, *45*, 95–97. [[CrossRef](#)]

8. Xu, H.L.; Wen, G.H.; Sun, W.; Wang, K.Z.; Yan, B.; Luo, W. Thermal behaviour of moulds with different water channels and their influence on quality in continuous casting of beam blanks. *Ironmak. Steelmak.* **2013**, *37*, 380–386. [[CrossRef](#)]
9. Du, Y.P.; Yang, J.W.; Shi, R.; Cui, X.C. Effect of submerged entry nozzle (sen) parameters and shape on 3-d fluid flow in mould for beam blank continuous casting. *Acta Metall. Sin.* **2004**, *17*, 705–712.
10. De Santis, M.; Cristallini, A.; Rinaldi, M.; Sgrò, A. Modelling-based innovative feeding strategy for beam blanks mould casting aimed at as-cast surface quality improvement. *ISIJ Int.* **2014**, *54*, 496–503. [[CrossRef](#)]
11. Lasko, G.; Weber, U.; Schmauder, S. Finite Element Simulations of Crack Propagation in Al₂O₃/6061 Al Composites. *Acta Metall. Sin.* **2014**, *27*, 853–861. [[CrossRef](#)]
12. Jiang, Z.W.; Wan, S.; Cheng, C. Analysis of the Crack Propagation Based on Extended Finite Method. *Appl. Mech. Mater.* **2013**, *275–277*, 169–173. [[CrossRef](#)]
13. Wang, G.X.; Schwalbe, K.H. A study of the transition from intercrystalline to transcrystalline fatigue crack propagation in different ageing conditions of the alloy Cu-35%Ni-3.5%Cr. *Int. J. Fatigue* **1993**, *15*, 3–8. [[CrossRef](#)]
14. Shen, J.L. Study on Simulation of Surface Cracks Growth for Continuous Casting Q235 Slab. Mater's Thesis, Chongqing University, Chongqing, China, 2013.
15. Xue, F.M.; Li, F.G.; Li, J.; He, M.; Yuan, Z.W.; Wang, R.T. Numerical modeling crack propagation of sheet metal forming based on stress state parameters using xfem method. *Comput. Mater. Sci.* **2013**, *69*, 311–326. [[CrossRef](#)]
16. Wang, F.G. Crack Initiation and Propagation of Duplex Stainless Steel Finite Element Simulation. Master's Thesis, Xi'an Technological University, Xi'an, China, 2014.
17. Chen, L.Y.; Zhu, Y.C. Cause for bubbles occurring in top CC slab & countermeasures. *Contin. Cast.* **1999**, *2*, 19–20. [[CrossRef](#)]
18. Geng, M.S.; Wang, X.H.; Zhang, J.M.; Wang, W.J.; Liu, Z.M. Study of Surface Blow Hole Defects of Continuous Casting Slab. *Iron Steel* **2010**, *45*, 45–50. [[CrossRef](#)]
19. Yang, G.Y.; Zhu, L.G.; Chen, W.; Yu, X.W.; Guo, G.X. Propagation of Surface Cracks on Beam Blank in the Mould during Continuous Casting. *Ironmak. Steelmak.* **2018**. [[CrossRef](#)]



© 2018 by the authors. Licensee MDPI, Basel, Switzerland. This article is an open access article distributed under the terms and conditions of the Creative Commons Attribution (CC BY) license (<http://creativecommons.org/licenses/by/4.0/>).

Article

Applied Mathematical Modelling of Continuous Casting Processes: A Review

Michael Vynnycky [†]

Division of Processes, Department of Materials Science and Engineering, Brinellvägen 23, KTH Royal Institute of Technology, 100 44 Stockholm, Sweden; michaelv@kth.se; Tel.: +46-73-765-2037

[†] Current address: Department of Applied Mathematics and Statistics, Institute of Mathematical and Computer Sciences, University of São Paulo at São Carlos, P.O. Box 668, São Carlos 13560-970, São Paulo, Brazil.

Received: 21 October 2018; Accepted: 2 November 2018; Published: 9 November 2018

Abstract: With readily available and ever-increasing computational resources, the modelling of continuous casting processes—mainly for steel, but also for copper and aluminium alloys—has predominantly focused on large-scale numerical simulation. Whilst there is certainly a need for this type of modelling, this paper highlights an alternative approach more grounded in applied mathematics, which lies between overly simplified analytical models and multi-dimensional simulations. In this approach, the governing equations are nondimensionalized and systematically simplified to obtain a formulation which is numerically much cheaper to compute, yet does not sacrifice any of the physics that was present in the original problem; in addition, the results should agree also quantitatively with those of the original model. This approach is well-suited to the modelling of continuous casting processes, which often involve the interaction of complex multiphysics. Recent examples involving mould taper, oscillation-mark formation, solidification shrinkage-induced macrosegregation and electromagnetic stirring are considered, as are the possibilities for the modelling of exudation, columnar-to-equiaxed transition, V-segregation, centreline porosity and mechanical soft reduction.

Keywords: asymptotic analysis; numerical simulation; continuous casting

1. Introduction

Continuous casting is a process whereby molten metal is solidified into semi-finished billets, blooms, slabs or strips for subsequent rolling in finishing mills; it is the most frequently used process to cast not only steel, but also aluminum and copper alloys, with the main configurations being as shown in Figure 1. Although originally a process that was developed on an industrial scale in the early decades of the 20th century for the casting of non-ferrous alloys, its use has been widespread also for steel since the 1950s. Compared to casting in moulds, continuous casting is more economical, as it consumes less energy and produces less scrap. Furthermore, the properties of the products can be easily modified by changing the casting parameters. As all operations can be automated and controlled, continuous casting offers numerous possibilities to adapt production flexibly and rapidly to changing market requirements and to combine it with digitization technologies. Nevertheless, new challenges continuously arise, as ways are sought to minimize casting defects and to cast new alloys.

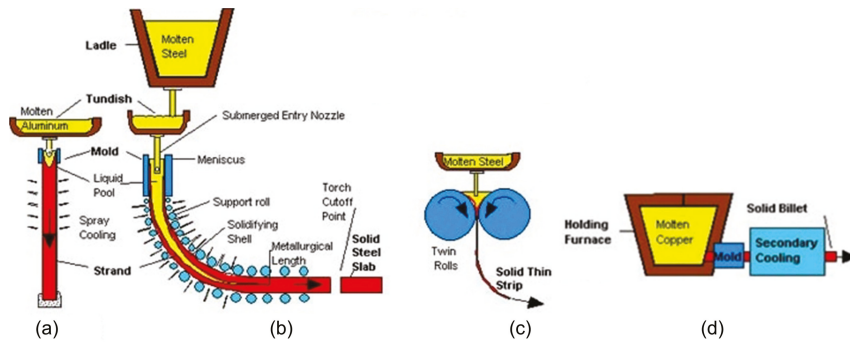


Figure 1. Continuous casting: (a) vertical; (b) curved; (c) strip; and (d) horizontal. Reproduced with permission from Brian G. Thomas, 2018 [1].

An important aspect in meeting these challenges is the use of modelling and simulation, as reviewed recently for the case of steel in [2]. With readily available and ever-increasing computational resources, the majority of modelling and simulation activity for continuous casting processes focuses on large-scale numerical simulation. Whilst there is certainly a need for this type of modelling, the focus in this paper is on an alternative approach more grounded in applied mathematics, asymptotic methods in particular, which lies between overly simplified analytical models and multi-dimensional simulations. In this approach, the governing equations are nondimensionalized and systematically simplified to obtain a formulation which is numerically much cheaper to compute, yet does not sacrifice any of the physics that was present in the original problem; in addition, the results should agree also quantitatively with those of the original model. This approach is well-suited to the modelling of continuous casting processes, which often involve the interaction of complex multiphysics.

There are several motivations for this hybrid asymptotic/numerical approach. The first is that it has been applied successfully in other areas of science and technology, as witnessed by the growth of an activity known as practical asymptotics [3–8]; note, however, that this is not identical to the model order-reduction approach [9], which is also prevalent in industrial mathematics. The second is the Moore’s law effect in modelling [10]: namely, that, although computational power doubles every 18 months, it will still be many years before all the length scales in a casting process will be numerically resolved [11]. Moreover, although the use of asymptotic methods for the modelling of continuous casting is not unknown, it remains somewhat limited to fluid flow and heat transfer aspects [12–20]. Thus, the goal here is to review recent activity in this area, based primarily on the activities of the author and co-workers [21–33].

The layout of the paper is as follows. Section 2 focuses on models for the determination of metallurgical length. Section 3 is on the role of the air gap and implementation of mould taper. Section 4 focuses on oscillation-mark formation in the continuous casting of steel, whereas Section 5 is on solidification shrinkage-induced macrosegregation. Section 6 is on electromagnetic stirring, with conclusions being drawn in Section 7. Finally, Appendix A shows in more detail how the practical asymptotics approach is applied to one of the sub-problems considered in the paper.

2. Metallurgical Length

2.1. Pure Metals or Eutectic Alloys

To be able to correctly dimension a continuous casting process, it is of primary importance to have an estimate of where complete solidification will occur. This requires a model that takes into account fluid flow, heat transfer and phase change; a generalized two-dimensional (2D) schematic for this is shown in Figure 2. The inlet drawn here does not correctly reflect the situation in all continuous casting processes. For example, for the continuous casting of steel blooms or billets, a submerged entry

nozzle is used, whereas, for the strip casting of copper and its alloys, multiple jets are located above the molten metal surface. For the latter, a 2D model was considered in [34,35] which employed the $k-\epsilon$ model to describe the turbulent flow of molten metal; in addition, experimental measurements were carried out to obtain data necessary for modelling the heat transfer between the solidified copper shell and the surrounding cooling mould. The resulting equations were solved using the commercial software CFX [36]. In much later work [21], the original model equations were reconsidered in the light of a much simpler model which simply took account of the streaming of the melt at the casting speed, V_{cast} ; through asymptotic reduction, the original 2D time-independent model becomes effectively a 1D time-dependent, model, with the usual understanding that the coordinate in the casting direction corresponds to the product of V_{cast} and time, if the casting geometry is slender. Moreover, since the original model was for an almost pure copper melt, the simpler model was formulated in terms of a sharp interface between liquid and solid phases [21]; this approach would also be suitable for eutectic alloys.

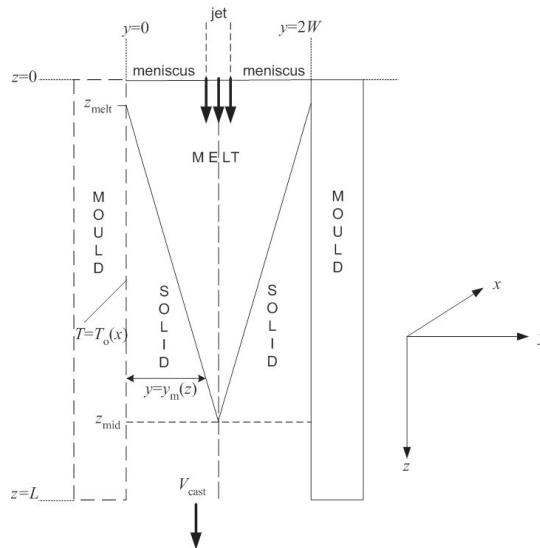


Figure 2. Schematic of a vertical continuous casting process.

Figure 3 shows a comparison of the key results from [21,34,35]. Thus, although significantly more computational effort was required in generating the results in [34,35], there is scant difference between them. Whilst this may be due to the limited effects of turbulence lower down in the caster, it is notable that all quantities agree well even near the top, where the effects of turbulence should still be quite strong.

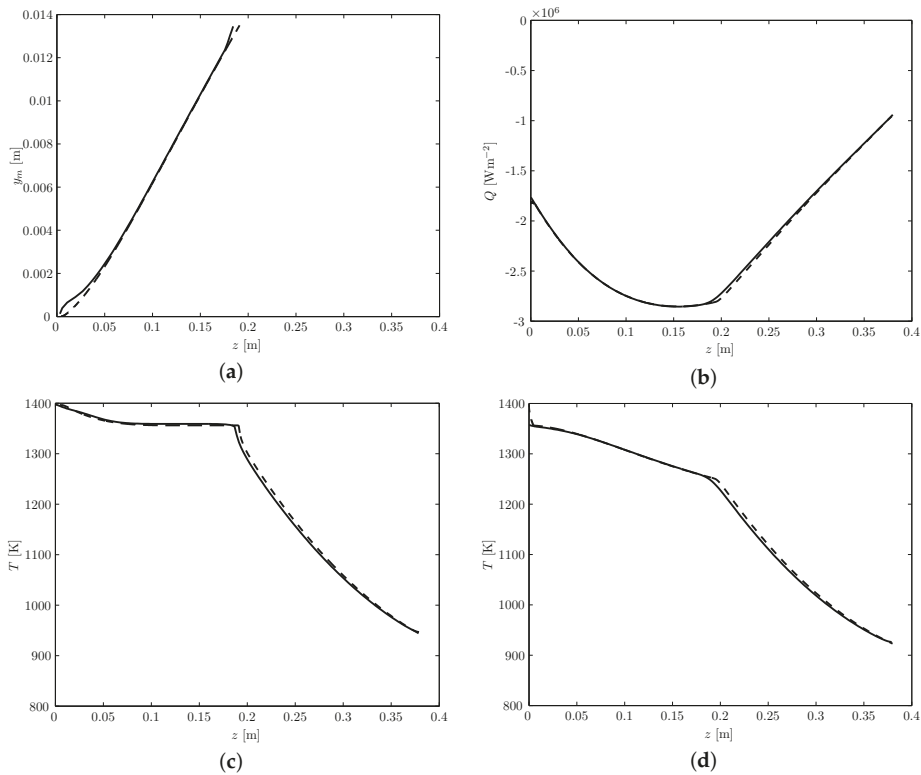


Figure 3. Comparison of: (a) the location of the solidification front, y_m ; (b) the heat flux, Q , at the outer edge of the copper strip; (c) the temperature at the centreline ($y = W$); and (d) the temperature at the outer edge of the copper strip. In all cases, the solid line is for the full model, and the dashed line is for the reduced model; z denotes the distance along the casting direction from the meniscus. Reproduced from [21], with copyright permission from Elsevier, 2017.

2.2. Alloys

In general of course, the alloys that are cast have a substantial solidification interval, leading to the formation of a mushy zone between the melt and the solid, in which both coexist; thus, the situation is now more akin to Figure 4 than Figure 2. Typically, the numerical solution of the governing equations is handled by introducing an auxiliary variable, commonly the local liquid fraction, and using an enthalpy formulation on a fixed grid [37–41]. This generally functions well enough if a basic description of fluid flow and heat transfer is required—all the more so if the solidification interval of the alloy is large. However, it is often required to determine quantities that affect the quality of the final solidified alloy, such as the degree of macrosegregation of an alloy’s solute elements, the ratio of equiaxed-to-columnar crystals or the thermomechanical stress; all of these are associated with processes in the mush. Thus, to compute all of these quantities accurately in the region where they really matter, it would be convenient to be able to resolve the locations of the solid-mush and mush-liquid interfaces explicitly.

The methodology to address this situation for the case of continuous casting processes was developed in [22]. This was done by applying a boundary immobilization method for the solidus and liquidus isotherms, transforming from (y, z) to (η, z) variables, as shown in Figure 5, with η given by

$$\eta = \begin{cases} y/y_s(z), & 0 \leq y \leq y_s(z) \\ 1 + \frac{y-y_s(z)}{y_1(z)-y_s(z)}, & y_s(z) \leq y \leq y_1(z) \\ 2 + \frac{y-y_1(z)}{W-y_1(z)}, & y_1(z) \leq y \leq W \end{cases}$$

where y_1 and y_s denote the locations of the liquidus and solidus isotherms, respectively. A benchmark problem was solved using three different formulations:

- (A) an enthalpy-like formulation just mentioned using the full 2D time-independent equations;
- (B) an enthalpy-like formulation using a reduction of the full 2D time-independent equations to a 1D transient-like formulation of the type used in [21];
- (C) the proposed new formulation, which is also 1D transient-like but resolves the locations of the solidus and liquidus isotherms explicitly.

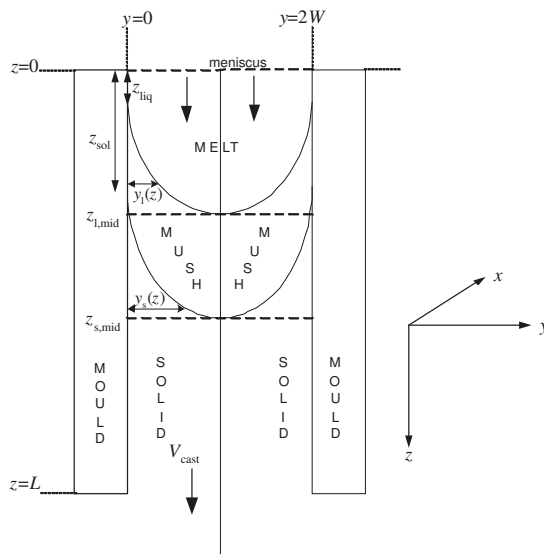


Figure 4. 2D schematic of the vertical continuous casting of an alloy.

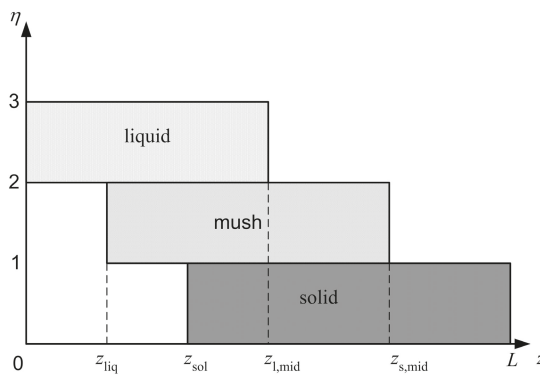


Figure 5. Computational domain in (η, z) variables.

The key results are summarized in Figure 6. Figure 6a–f shows, respectively, the location of the liquidus isotherm (y_1), the location of the solidus isotherm (y_s), the mould wall temperature, the

heat flux at the mould wall, the centreline temperature and the temperature gradient in the casting direction at the centreline, and indicates that the novel formulation *C* gives results that agree very well with those of the more conventional formulations *A* and *B*. In future, it is therefore hoped to extend this formulation for modelling the multiphysical phenomena that are present in the mushy zone, as mentioned above.

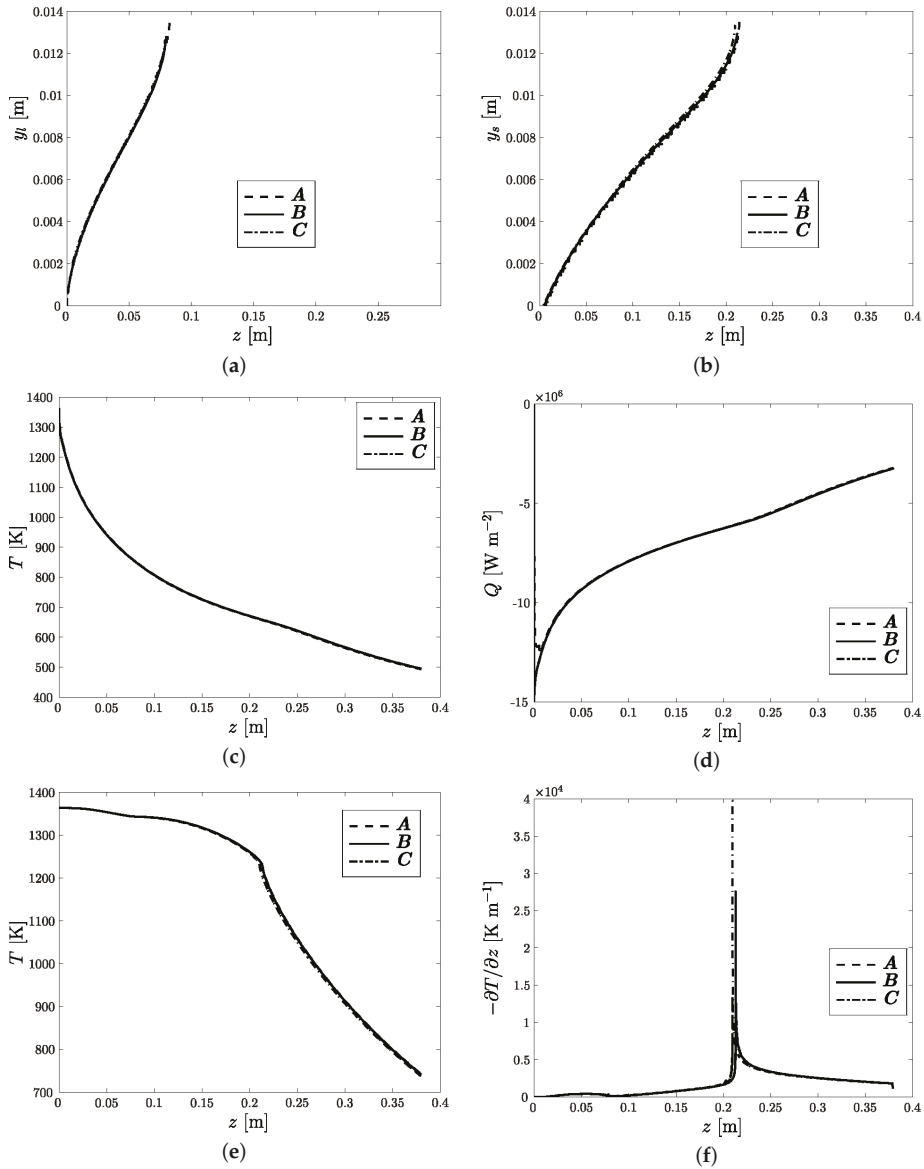


Figure 6. (a) The location of the liquidus isotherm, y_l ; (b) the location of the solidus isotherm, y_s ; (c) mould wall temperature; (d) mould wall heat flux, Q ; (e) centreline temperature; and (f) $-\partial T/\partial z$ at the centreline. All quantities are given as functions of z . Reproduced from [22], with copyright permission from Elsevier, 2017.

3. Air Gap and Mould Taper

In the models presented thus far, heat transfer between the solidified shell and the mould wall is characterized by an experimentally measured heat transfer coefficient and the surface of the mould wall is assumed to be parallel to the casting direction. In practice, however, it is thought that an air gap forms between the mould wall and the solidified shell when the latter, in going from a plastic to elastic state, is strong enough to withstand the metalstatic pressure of the adjacent molten metal, thereby receding from the mould as a result of contraction; a contributing factor is also thought to be the expansion of the mould itself. Air-gap formation prohibits effective heat transfer between the mould and shell, leading to longer solidification lengths and requiring supplementary process design considerations, such as mould tapering. Consequently, the actual situation is more similar to that shown in Figure 7, which shows the idea for the case of the casting of pure metal or eutectic alloy. Now, in addition to determining the location of the solid/melt interface, it is also necessary to determine the location where the air gap begins to form, denoted by z_{gap} , as well as the width of the air gap as a function of z , given in the figure as $r_w(z) - r_a(z)$.

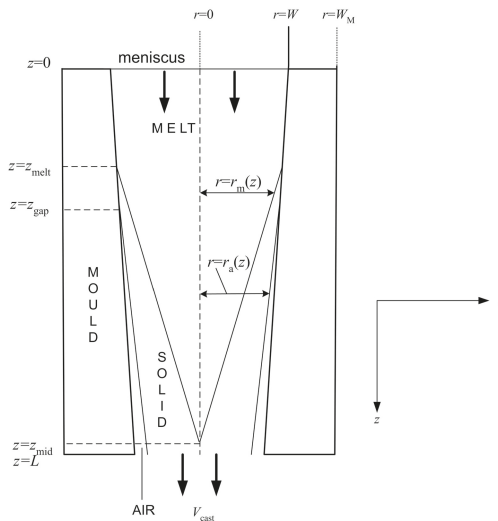


Figure 7. A 2D schematic of the continuous casting process with tapered mould walls and superheat.

Early analytical models made preliminary headway on the air gap problem [42–45]. Later papers have been solely numerical studies [46–52]. In the latter, the common approach is to employ multidimensional finite element models to describe the coupled thermomechanical interaction that occurs between the solidified shell and the mould wall. However, in contrast to all of these, in [24–27], the fact that the air gap is slender was used, together with the generalized plane strain approximation, to derive an asymptotic model for the aforementioned interaction in the case of an untapered mould; in particular, closed-form expressions can be found for the stress and strain components. Ultimately, the only numerical burden is the computation of a moving boundary problem for the temperature, although with back-coupling to the structure mechanical problem via the boundary conditions; the case of a tapered mould fits easily into this framework, since the taper is always small enough to be amenable to asymptotic methods: for example, in the case of steel casters, the taper is usually of the order of 2%/m [47].

In [28,29], the interplay of melt superheat and mould taper was considered for an axisymmetric continuous casting geometry, although we just focus on the effect of mould taper itself for one particular value of superheat here. Figure 8a shows the different taper profiles considered; here, M is a dimensionless parameter related to the actual mould taper, in per cent/m, by

$$M = \frac{LX}{100\alpha\Delta T}$$

where

$$X = \frac{100}{L} \left(\frac{r_w(0) - r_w(L)}{r_w(0)} \right),$$

where α is the thermal expansion coefficient of the metal and ΔT is an appropriate temperature scale for the problem (see [28,29] for exact details). Figure 8b–d shows, respectively, how the position of the solid/air interface (r_m), the position of the solid/air interface (r_a) and the width of the air gap, $a_g := r_w(z) - r_a(z)$, vary with z for different values of M . Lastly, Figure 9 gives an idealized result: the minimum taper necessary to avoid any air gap at all, with Figure 8b also showing the profile for r_m , denoted there by \bar{r}_w , that this would correspond to. However, in Figure 9, a taper profile that is much more extreme than those currently in use would be required.

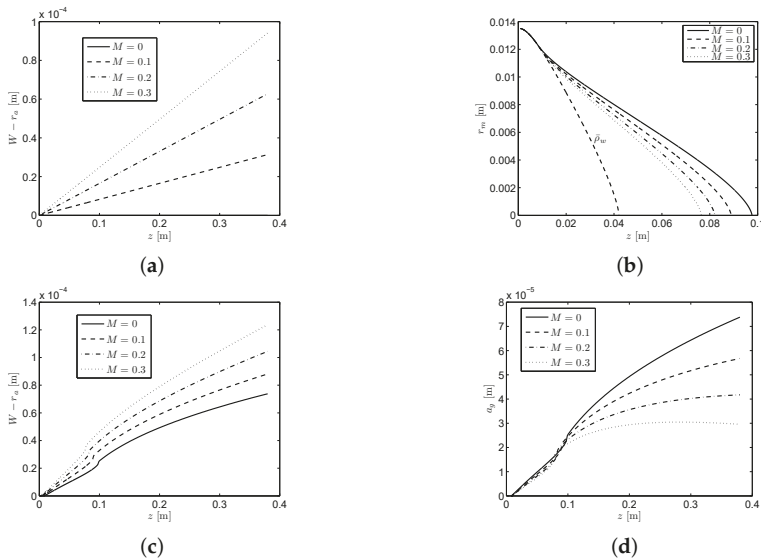


Figure 8. Dependence on M of: (a) the taper profile, $r_w(z)$, relative to W ; (b) the position of the solid/air interface, $r_m(z)$; (c) the position of the solid/air interface, $r_a(z)$; and (d) the width of the air gap, $a_g(z)$.

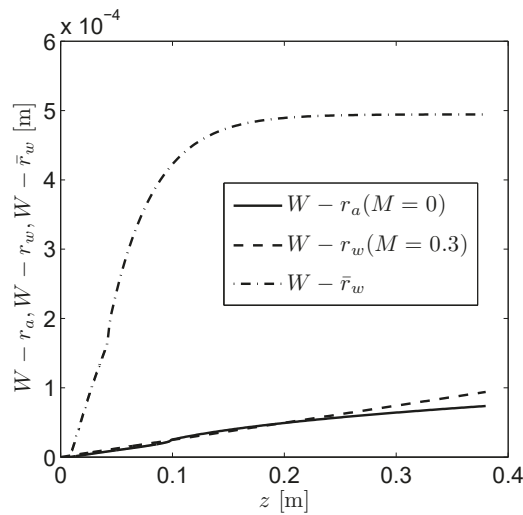


Figure 9. Comparison of the size of the air gap for the untapered system (solid line) with the $M = 0.3$ linear taper (dotted line), and the ideal taper required to completely eliminate the air gap (dashed line).

Finally, we note that, although the results in Figures 8 and 9 are for a somewhat fictitious situation, work is nevertheless underway to extend the results to the more realistic case of the continuous casting of round steel billets; a good source for validating the approach will be the experimental and theoretical results in [47]. A further future extension would then be for mould taper for blooms, billets and slabs, in which the generalized plane strain approximation can also be used, as well as the fact that the air gap is slender and the taper is small enough for asymptotic methods to be applicable.

4. Oscillation-Mark Formation

Although the continuous casting configurations shown in Figures 2, 4 and 7 indicate a mould that is stationary, in reality, it is made to oscillate in the casting direction; this is particularly so for the continuous casting of steel. Moreover, a mould powder, often termed flux, is introduced over the steel melt; the powder becomes molten and the flows between the steel and the oscillating mould, with the resulting configuration being as in Figure 10, which depicts the initial stages of solidification in continuous casting. In this way, solidified steel is prevented from contacting the mould directly and resolidified flux is shaken from the surface of the mould. However, as is well-known and hinted at in Figure 10, a detrimental effect of this construct is the formation of depressions on the surface of the solidified steel, commonly referred to as oscillation marks; an experimental example is shown in Figure 11. Moreover, although the mould oscillation is normally periodic in time, this does not in general mean that the marks which form are identical and periodically spaced. For example, Figure 12 shows the spacing between thirteen marks, also termed as the pitch, taken from a continuously cast steel sample, from which it is clear that, more often than not, the pitch obtained was close to the average value. This may in itself not be noteworthy, other than that this average value is also close to the theoretical value, as we show below. Further samples of experimental oscillation-mark data, arguably the largest ever collected from a single continuous casting process, can be found in [53,54].

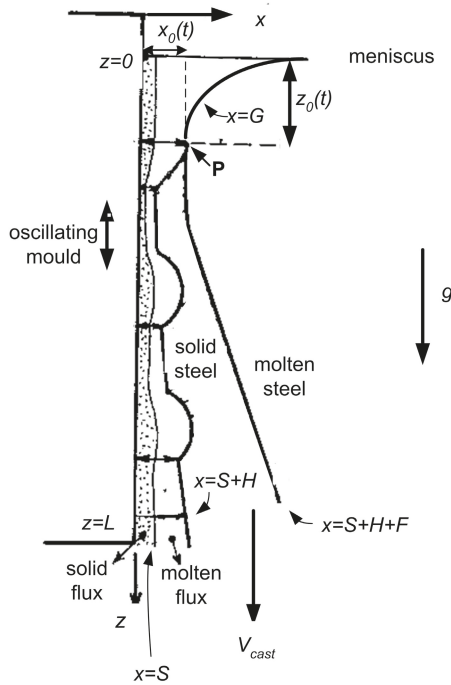


Figure 10. A sketch showing how an oscillation mark forms.



Figure 11. Two adjacent oscillation marks and typically observed microstructure underneath them.

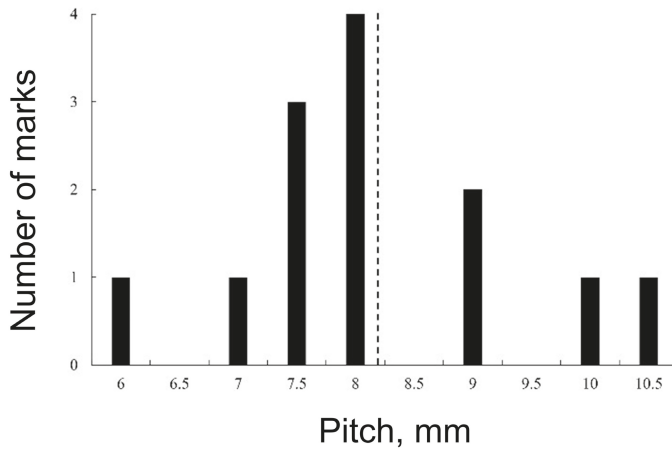


Figure 12. Experimental results showing the number of marks associated with a given pitch, taken from [30]. The vertical dashed line shows the average value.

Oscillation marks have been subject of modelling in the continuous casting literature since the early 1980s [55], with the most recent review being given in [56]. At the centre of this modelling is the need to relate it to the early experimental work of Tomono [57], which classified oscillation marks as being either of overflow-type, in which case the solidified shell is strong enough to avoid deformation, causing the steel meniscus to overflow the solid tip, or fold-type, in which case the solid shell is too thin to prevent its tip from bending back under the rim pressure. Recent attempts at modelling this problem have tended towards the use of computational fluid dynamics [56,58–61], although results which give either fold or overflow marks remain elusive, as is a criterion, in terms of process parameters, for when one or the other should occur.

In this context, Vynnycky et al. [30] recently revisited an earlier model for oscillation-mark formation by Hill et al. [18], with a view to providing a detailed and systematic asymptotic analysis; the model used lubrication theory coupled to heat conduction in the solid flux, molten flux and solid steel regions, and was able to predict the oscillation-mark shape. This resulted in a model involving fifteen dimensionless parameters which was able to give good agreement with the experimental oscillation-mark profiles shown in Figure 11; the comparison is shown in Figure 13. Note that the pitch in this figure is given by V_{cast}/f , where f is the mould oscillation frequency, and that this is close to the dashed line in Figure 11 for the values $V_{cast} = 0.013 \text{ ms}^{-1}$ and $f = 19/12 \text{ s}^{-1}$ used in [30,53]. Furthermore, the profiles and the character of the model, which neglects the presence of the meniscus completely, indicated that the marks were of fold-type.

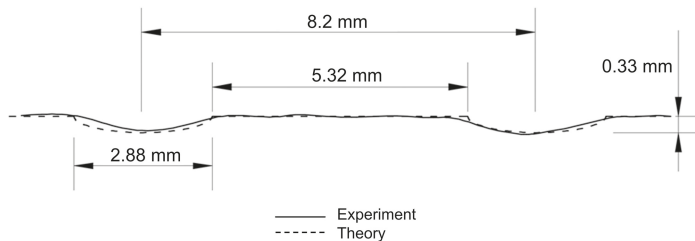


Figure 13. Comparison of the theoretically calculated oscillation mark profiles and those measured experimentally by Saleem [53].

In further work [32], an attempt was made to extend the model to include the effect of the meniscus, thereby allowing the possibility of model parameters to drive whether the model predicts fold-type or overflow-type marks. For this purpose, a novel “moving-point” formulation was derived, which unlike the volume-of-fluid (VOF) formulation adopted in [56,58–61], attempts to track explicitly the location of the point at which solidification first begins. This approach suggests that if solidification has not occurred within a capillary length from the top of the meniscus, then the meniscus profile predicted by Bikerman [62], and which emerges naturally in the asymptotic analysis in [32], will collapse, leading to overflow; however, further work is required to extend the isothermal model derived in [32] to determine where the temperature first becomes low enough for the steel to start to solidify.

5. Macrosegregation

Macrosegregation is the term used to denote to variations in composition that occur in alloy castings or ingots and range in scale from several millimetres to even metres; it is a central problem, since it strongly influences the further workability of the cast products and their mechanical properties. As was already well-established as early as the 1960s [63,64], it arises as a consequence of the nature of the solidification process for alloys, which involves the formation of a mushy network of solid dendrites through which there is the slow flow of interdendritic melt, and the transport of alloying elements. In particular, as solidification occurs, if the solute—for example, Cu in an Al-4.5 wt% Cu

alloy [65] or Sn in a Cu-8 wt% Sn alloy [66]—is more soluble in the liquid phase than it is in the solid phase, then it is rejected into the melt, resulting in a non-uniform distribution of solute in the final solidified casting.

Over the years, there has developed a substantial body of modelling work on macrosegregation in one-dimensional transient solidification [67–72], some of which is of relevance to steady-state continuous or direct chill casting processes. In higher dimensions, computational fluid dynamics (CFD) is often used, although, as indicated in [73], numerical dispersion and diffusion are present in the simulated macrosegregation profiles reported in the literature, hindering the interpretation of CFD results. In particular, it has been found that unstructured computational meshes can eliminate the numerical dispersion that is present when structured meshes are used; however, undesirable numerical diffusion is introduced instead. On the other hand, refining a structured mesh alleviates problems with numerical oscillations, but instead results in a dramatic increase in computation time [74]. More details on recent efforts to come to grips with these difficulties can be found in [73,75–79].

One particular cause of macrosegregation in continuous casting is due to solidification shrinkage, which tends to dominate that due to natural convection induced by thermal and solutal gradients. The modelling of this phenomenon is particularly amenable to asymptotic methods since the macrosegregation is driven by a dimensionless parameter, $\varepsilon = \rho_s / \rho_l - 1$, that is often no greater than around 0.1; here, ρ_s and ρ_l are the solid and liquid densities, respectively. Consequently, the resulting non-uniform solute profile can be obtained as the second term in a regular perturbation series in ε . As a result, and as shown in [23], there is therefore no need to resort to CFD to compute the Darcy-damped Navier–Stokes equations for modelling the melt and the mushy zone. Although the analysis is algebraically somewhat lengthy, the computational load is not; moreover, because of the hybrid analytical-numerical method used, there is no possibility for any numerical diffusion or dispersion. The situation considered in [23] is similar to that in Figure 4, although with no superheat, so that there is only a mushy zone and a fully solidified region. Moreover, the lever rule is assumed for macrosegregation at the microscale, and it is demonstrated analytically that the leading-order solute at the macroscale is also given by the lever rule.

The results of the approach were compared with those obtained in [80] using CFD for the continuous casting of an Al-4.5 wt% Cu alloy, and are shown in Figure 14. Several features are noteworthy in this figure. First, we see so-called inverse segregation at $y = 0$: this is the well-established phenomenon wherein the solute concentration is higher at the outer surface of the casting than it is elsewhere [65,74,81]. Moreover, near $y = W$, we would expect to see negative segregation, i.e., the concentration would be less than the initial composition. Note that two curves have been included from [80]: one using the linearized phase diagram for the Al-Cu system, and one using the non-linearized phase diagram. As can be seen, the agreement with the results of the asymptotic model is very reasonable for $y \leq 0.02$ m, although rather less so thereafter. This could be due to a variety of factors:

- the fact that the model in [23] does not include superheat, whereas the model in [80] had a superheat of 27 K;
- in [80], numerical issues associated with the use of CFD, of the type mentioned earlier; and
- the fact that the geometry in question, which has an aspect ratio of six, is not slender enough for the asymptotic approach to be valid.

It is clear that the method based on the asymptotic approach is far from complete, with the most urgent extensions being the inclusion of superheat and the possibility to assume Scheil equation- or back diffusion-based macrosegregation at the microscale.

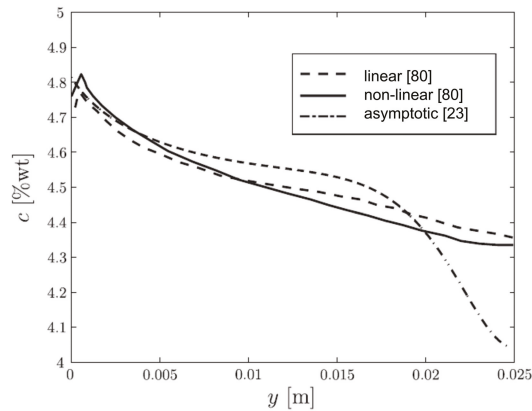


Figure 14. Comparison of the macrosegregation profiles obtained in [80], using the linearized and non-linearized phase diagrams for the Al-Cu system, and using the asymptotic model in [23].

6. Electromagnetic Stirring

Electromagnetic stirring (EMS) has been used in the continuous casting of steel [82] since the 1970s as a way to control solidification structures. Since roughly the same time, mathematical modelling has been used to elucidate the actual role of EMS in affecting the motion of the steel melt; most noteworthy is a sequence of papers by Schwerdtfeger and co-workers [83–88] which explore, both experimentally and theoretically, the effect of stirring in the round-billet, rectangular-bloom and slab geometries that are characteristic for the continuous casting of steel. In particular, the models considered consist of the turbulent Navier–Stokes equations for the velocity field of the molten metal and Maxwell’s equations for the induced magnetic flux density. In principle, there is two-way coupling between the models, since the alternating magnetic field gives rise to a Lorentz force which drives the velocity field, which can in turn affect the magnetic field. Typically, the magnetic Reynolds number is rather low, and rarely greater than unity, meaning that the velocity-free Maxwell’s equations can be solved; the output is then used to constitute the Lorentz force which drives the velocity field. Moreover, the frequency of the magnetic field is typically great enough to allow the use of the time average of the Lorentz force as input to the Navier–Stokes equations.

In calculating the induced magnetic field, an assumption is necessary as regards the applied oscillating field surrounding the domain of interest, typically the steel strand. In the models mentioned above [83–88], the assumption comes in the form of a boundary condition for the normal component of the magnetic flux density at the surface of the strand. However, revisiting the problem for the continuous casting of round billets [83,88], the configuration for which is shown in Figure 15a, Vynnycky [31] showed that prescribing the normal component of the magnetic flux density at the surface of the strand leads to a non-unique solution for the components of the magnetic flux density, and hence for the components of the time-averaged Lorentz force. On the other hand, it was found that prescribing the tangential component of the magnetic flux density would lead to a unique solution. Moreover, for the circular configuration, it was found that it was possible to choose the tangential component so that the original expressions for the components of the time-averaged Lorentz force, first given in [83,88], would be recovered. In addition, although the analysis was carried out for when the magnetic Reynolds number is small enough that there is only one-way coupling between the fluid flow to the magnetic field, the result concerning non-uniqueness would hold even when there is genuine two-way coupling.

At present, work is under way to re-evaluate the corresponding situation for rectangular strands [84], which is algebraically more complex. Nevertheless, a resolution of the issue is timely, since the expressions derived in [83,88] for the components of the time-averaged Lorentz force have

been cited and used on numerous occasions since, even up to the present day [89–94]. Moreover, the results are even more significant in the case of modulated EMS [95–97], where magnetic fields of different frequencies are applied and it is the intention that the resulting Lorentz force should have a constant time-averaged and a time-varying component; in this case, posing the correct boundary conditions for the magnetic field is vital for obtaining meaningful results from modelling.

A further activity concerns obtaining a better idea of how the solid and mushy zones that form during continuous casting, giving the situation shown in Figure 15b, affect the ability of the applied magnetic field to stir the remaining melt [33]. Some preliminary results are given in Figure 16 for the case of round billets. For these results, the model parameters from [83,88] have been used. The axisymmetric Navier–Stokes equations have been solved, although a Darcy-like damping term has been included so as to take into account the effect of the mushy zone. In Figure 16a, the outer radius of the mushy zone, r_m , has been taken to be 60% of the radius of the mould; note that this value of r_m corresponds to the value used for the radius of the melt in [88]. Figure 16a compares solutions for the azimuthal velocity, v_θ , for three different values of the inner radius of the mushy zone, $r_0 = 0$, $r_m/3$, $2r_m/3$ —with the solution when the Darcy term is neglected completely, so that there is no mush. Here, the curve for the no-mush case corresponds to that computed in [88]. It turns out that the profile given here has a maximum value that is around six times lower than that in [88], which was around 1.5 m s^{-1} , as well as having its maximum displaced further away from $r = r_m$; it is not surprising that there is a difference, since the turbulence model used, which adopts the Prandtl mixing length hypothesis [98], was one of simplest possible, whereas a more sophisticated two-equation k - W model was used in [88]. Nevertheless, even the value obtained here is not unreasonable in the context of electromagnetically-stirred melts. As regards the other curves in this plot, it is clear that the presence of the mushy layer reduces v_θ significantly: for example, for $r_0 = 0$, corresponding to mush occupying the entire region from $r = 0$ to r_m , the maximum value of v_θ is around 0.02 m s^{-1} . For Figure 16b, $r_m = r_b$; here, the profile for the no-mush curve resembles much more closely that computed in [88], with even the maximum value for v_θ comparing favourably. There is also a proportionately greater drop in v_θ when going from the no-mush case to when $r_0 = 2r_m/3$.

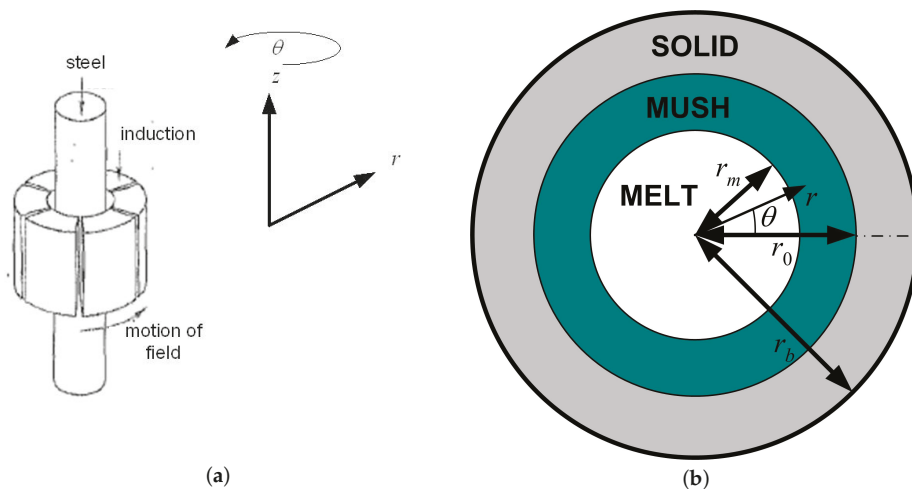


Figure 15. (a) Schematic of an arrangement of an inductor around a circular steel strand for inducing rotating fields; and (b) schematic of circular solid, mush and melt regions in the cross-section of the strand.

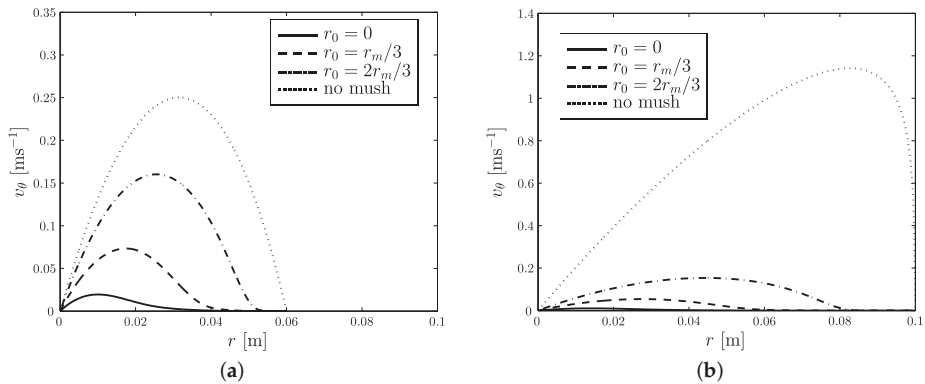


Figure 16. Azimuthal velocity, v_θ , vs. radial distance, r , for $r_0 = 0$, $r_m/3$, $2r_m/3$ and no mush, with: (a) $r_m = 0.06$ m; and (b) $r_m = 0.1$ m.

The model in [33] can be extended in a number of ways. First, although the casting velocity was not included in this analysis, it can be incorporated without affecting the analysis. After that, it would be of interest to include an equation for the conservation of heat, so that the temperature and hence the liquid fraction are computed as part of the model, rather than the liquid fraction simply being prescribed, as was the case in [33]. A nondimensional analysis would make it clear whether the effect of the magnetic field affects the heat transfer in the problem, through either Joule heating or convection. Once these models are in place, it should be possible to assess the role of stirring in macrosegregation and crystal structure formation: with respect to white-band formation in the case of the former [87,99,100], and columnar-to-equiaxed crystal transition in the case of the latter. A parallel line of activity would be to adapt these ideas to linear travelling magnetic fields for rectangular slabs, billets and blooms.

7. Conclusions

This paper has reviewed recent efforts in employing applied mathematical techniques, predominantly analysis and asymptotic methods, for the modelling of continuous casting processes. The focus has been on using these techniques in order not only to infer the qualitative behaviour of models, but also with a view to obtaining reduced-model formulations that require considerably less computational time than the original models, whilst still retaining their salient physical features. The work presented was divided into five topics: metallurgical length; air-gap formation and mould taper; oscillation-mark formation; macrosegregation; and electromagnetic stirring. Whilst work on all of these is still ongoing, a certain degree of validation has already been achieved:

- For the determination of metallurgical length, the proposed approach already yielded good agreement with a more computationally intensive approach using CFD and turbulence modelling [21], for the case of a pure metal, and with a more conventional enthalpy-formulation approach for alloys [22].
- For solidification shrinkage-induced macrosegregation in a binary alloy, reasonably good quantitative agreement was achieved for the cross-sectional macrosegregation profile, and even better agreement is to be expected when the model has been developed to include superheat [23].
- For oscillation-mark formation, very good agreement was obtained with experimental results for fold-type marks [30].

For air-gap formation and mould taper, validation will soon be attempted against the results of Kelly et al. [47] for the continuous casting of round billets. For electromagnetic stirring, validation will be possible against the original experimental results of Dubke et al. [84], although this work is

perhaps more embryonic, in view of an anomaly in the modelling of EMS in continuous casting that was recently found in [31].

In addition to the possible extensions of the work already carried out in each of these topics, which are detailed towards the end of Sections 2–6, these topics also form the starting points of investigations into a variety of as yet under-researched areas in continuous casting. Amongst these are the following:

Exudation For the case of alloys that have a long solidification interval—for example, alloys of copper or aluminium [41,66,70,101,102]—interdendritic melt seeps out through the air gap that forms between the solidifying shell and the chilled mould surface; this is known as exudation. Mathematically, this means that the region $z_{\text{liq}} \leq z \leq z_{\text{sol}}$ at $y = 0$ in Figure 4 is effectively an outlet for the interdendritic melt. The situation is an example of macrosegregation that requires the methods developed in Sections 2 and 5.

Columnar-equiaxed transition In the continuous casting of steel, it is well-established that the solidified structure consists of equiaxed crystals in the centre of the casting, surrounded by a columnar crystals, and that EMS is often used to increase the extent of the equiaxed zone, by means, it is believed, of dendrite fragmentation. However, models which can predict the columnar-to-equiaxed transition (CET) and how it can be affected by EMS are non-existent, although there is some work on CET using the cellular automaton method [103–105].

V-segregation V-segregation is the name given to the eponymously-shaped channels that are formed in the centre of the equiaxed zone of continuously cast steel slabs, blooms and billets, in which the macrosegregation level of interstitial elements such as carbon and sulphur, and of substitutional elements such as molybdenum and chromium, can be quite extensive. Even today, the mechanism behind the development of V-shaped segregate channels or lines is still not well understood [106]. The appearance of the V-segregates differs between different cast sizes, width of the equiaxed zone and casting speed. V-segregates can be found in low alloyed steels, as well as in stainless and high-alloyed steels.

Centreline porosity Continuously cast products develop centreline porosity along the strand direction, as a result of an extended mushy zone in the centre of the solidifying material. The length of the mushy zone depends mainly on solidification mode, degree of solidification shrinkage, extent of the equiaxed zone, cross section dimensions and casting speed. In particular, the centre pore develops due to a lack of feeding to compensate for the solidification shrinkage. When the pressure in the centre decreases below the equilibrium pressure for gas phase, porosity will develop, with the pore growing along the centre line. Although internal porosity is well-studied for ingot and component casting [107–109], this is far from the case for continuous casting [110].

Mechanical soft reduction A method used to counteract V-segregations, centreline porosity and centreline segregation is mechanical soft reduction [111–113], whereby the cast steel cross section is reduced by pinch rollers to compensate for the downward liquid flow in the mushy zone due to solidification shrinkage.

Lastly, we point out the relevance of the above to the thermo-fluid dynamics topics that are relevant to as-cast quality, particularly in the continuous casting of steel. Although such topics are numerous, the work on oscillation-mark formation begins to address surface quality; moreover, it provides a relatively cheap computational framework for considering the formation and propagation of surface cracks, as are known to occur, for example, in peritectic steels [114]. Furthermore, although the work on macrosegregation considered only solidification shrinkage, it already contains the full array of momentum, heat and solute conservation equations that would be required to model macrosegregation due to other causes: for example, thermosolutal convection [115], or electromagnetic stirring, which is known to produce so-called white bands in the casting of steel [87,99,100,116,117], but which has never been properly modelled. Moreover, the work on solidification shrinkage-induced macrosegregation may help to inform on centreline porosity. Although the analysis in [23] did not dwell on the second term in the regular perturbation series for pressure, this quantity becomes negative and unbounded as full solidification is reached at the centreline, if the lever rule is used to describe

segregation at the microscale; this would indicate that the pressure as a whole tends to zero, meaning the appearance of a pore. In addition, it is apparent that the pressure does not behave in this way for other microsegregation rules. It would be impossible to deduce this qualitative behaviour from numerical simulations alone, which further highlights the benefit of thinking asymptotically.

Funding: The author would like to thank FAPESP (Fundação de Amparo a Pesquisa do Estado de São Paulo) for the award of a visiting researcher grant [Grant Number 2018/07643-8].

Conflicts of Interest: The author declares no conflict of interest.

Appendix A. Notes on Practical Asymptotics

As indicated in Section 1, this article has been underpinned by the use of practical asymptotics; however, there has not been space to show details of how it works, and this issue is now addressed here.

To begin with, one would need to demonstrate the following four steps in action in the topics considered in Sections 2–6:

- (a) Nondimensionalization of the original governing equations;
- (b) Analysis of the nondimensionalized governing equations, and identification of the key dimensionless parameters and asymptotic reduction;
- (c) Evidence that the computation of the reduced model is cheaper than the computation of the original model would have been (if the reduced model does not have an analytical solution); and
- (d) Evidence of agreement between the results of the original model and the asymptotically reduced model.

Moreover, point (c) presupposes that one has indeed solved the problem in both the computationally intensive way and the cheap way; however, in practice, the visibility of “computational cheapness” comes from the observation that it ought to be cheaper to compute the numerical solutions for:

1. Fewer partial differential equations (PDEs) rather than more;
2. One-dimensional models rather than two-dimensional models, and two-dimensional models rather than three-dimensional models;
3. Ordinary differential equations (ODEs) rather than PDEs; and
4. Problems having fewer model parameters rather than more, with regard to the need for parameter studies to obtain a complete understanding of model behaviour.

Even so, there are examples in other areas of science and technology where a given problem has been solved both ways and the computational cost, in terms of CPU (central processing unit) time and RAM (random access memory), has been compared [118–123], although this was not done for the problems considered here.

In this context, we return to the problem of determining the metallurgical length in Section 2.1:

- The original model was two-dimensional steady-state, consisted of six PDEs and contained 32 model parameters [34,35].
- After nondimensionalization and asymptotic reduction, the model was one-dimensional and transient-like, consisted of two PDEs (or effectively different representations of the same PDE) and contained six model parameters [21].
- A direct comparison of CPU time and RAM was not carried out, but we note that one computation in [35] required 30 h of CPU time on a Cray J932 Supercomputer—with current computational architectures, this would no doubt take much less, but still would not be as short as the few seconds required for the formulation in [21].
- The agreement between the model results was very good, as shown in Figure 3.

Thus, this example demonstrates quite concretely how the asymptotic approach has been successfully applied.

References

1. Return to Introduction to Continuous Casting. Available online: <http://ccc.illinois.edu/introduction/overview.html#fig1> (accessed on 6 November 2018).
2. Thomas, B.G. Review on modeling and simulation of continuous casting. *Steel Res. Int.* **2018**, *89*, 1700312. [[CrossRef](#)]
3. Kuiken, H.K. *Practical Asymptotics*; Kluwer Academic Publishers: Dordrecht, The Netherlands, 2001.
4. Holmes, M.H.; King, J.R. Practical Asymptotics II. *J. Eng. Math.* **2003**, *45*, 155–404. [[CrossRef](#)]
5. Witelski, T.P.; Rienstra, S.W. Introduction to Practical Asymptotics III. *J. Eng. Math.* **2005**, *53*, 199. [[CrossRef](#)]
6. McCue, S.W. Preface to the fourth special issue on practical asymptotics. *J. Eng. Math.* **2009**, *63*, 153–154. [[CrossRef](#)]
7. Korobkin, A. Preface to the fifth special issue on practical asymptotics. *J. Eng. Math.* **2011**, *69*, 111–112. [[CrossRef](#)]
8. Smith, W.R. Preface to the sixth special issue on “Practical Asymptotics”. *J. Eng. Math.* **2017**, *102*, 1–2. [[CrossRef](#)]
9. Schilders, W.H.A.; van der Vorst, H.A.; Rommes, J. (Eds.) *Model Order Reduction: Theory, Research Aspects and Applications*, 1st ed.; Mathematics in Industry 13; Springer: Berlin/Heidelberg, Germany, 2008.
10. Voller, V.R.; Porte-Agel, F. Moore’s law and numerical modeling. *J. Comput. Phys.* **2002**, *179*, 698–703. [[CrossRef](#)]
11. Pickering, E.J.; Chesman, C.; Al-Bermani, S.; Holland, M.; Davies, P.; Talamantes-Silva, J. A comprehensive case study of macrosegregation in a steel ingot. *Metall. Mater. Trans. B* **2015**, *46*, 1860–1874. [[CrossRef](#)]
12. DiLellio, J.A.; Young, G.W. An asymptotic model of the mold region in a continuous steel caster. *Metall. Mater. Trans. B* **1995**, *26B*, 1225–1241. [[CrossRef](#)]
13. Smelser, R.E.; Johnson, R.E. An asymptotic model of slab casting. *Int. J. Mech. Sci.* **1995**, *37*, 793–814. [[CrossRef](#)]
14. Johnson, R.E.; Cherukuri, H.P. Vertical continuous casting of bars. *Proc. R. Soc. A* **1999**, *455*, 227–244. [[CrossRef](#)]
15. Cherukuri, H.P.; Johnson, R.E. Modelling vertical continuous casting with temperature-dependent material properties. *Int. J. Mech. Sci.* **2001**, *43*, 1243–1257. [[CrossRef](#)]
16. Bland, D.R. Flux and the continuous casting of steel. *IMA J. Appl. Maths* **1984**, *32*, 89–112. [[CrossRef](#)]
17. Hill, J.M.; Wu, Y.H. On a nonlinear Stefan problem in the continuous casting of steel. *Acta Mech.* **1994**, *107*, 183–198. [[CrossRef](#)]
18. Hill, J.M.; Wu, Y.H.; Wiwatanapataphee, B. Analysis of flux flow and the formation of oscillation marks in the continuous caster. *J. Eng. Math.* **1999**, *36*, 311–326. [[CrossRef](#)]
19. King, J.R.; Lacey, A.A.; Please, C.P.; Wilmott, P.; Zoryk, A. The formation of oscillation marks on continuously cast steel. *Math. Eng. Ind.* **1993**, *4*, 91–106.
20. Howison, S.D. *Practical Applied Mathematics: Modelling, Analysis, Approximation*; Cambridge University Press: Cambridge, UK, 2005.
21. Mitchell, S.L.; Vynnycky, M. Verified reduction of a model for a continuous casting process. *Appl. Math. Mod.* **2017**, *48*, 476–490. [[CrossRef](#)]
22. Vynnycky, M.; Saleem, S. On the explicit resolution of the mushy zone in the modelling of the continuous casting of alloys. *Appl. Math. Mod.* **2017**, *50*, 544–568. [[CrossRef](#)]
23. Vynnycky, M.; Saleem, S.; Fredriksson, H. An asymptotic approach to solidification shrinkage-induced macrosegregation in the continuous casting of binary alloys. *Appl. Math. Mod.* **2018**, *54*, 605–626. [[CrossRef](#)]
24. Vynnycky, M. An asymptotic model for the formation and evolution of air gaps in vertical continuous casting. *Proc. R. Soc. A* **2009**, *465*, 1617–1644. [[CrossRef](#)]
25. Vynnycky, M. Air gaps in vertical continuous casting in round moulds. *J. Eng. Math.* **2010**, *68*, 129–152. [[CrossRef](#)]
26. Vynnycky, M. On the role of radiative heat transfer in air gaps in vertical continuous casting. *Appl. Math. Mod.* **2013**, *37*, 2178–2188. [[CrossRef](#)]
27. Vynnycky, M. On the onset of air-gap formation in vertical continuous casting with superheat. *Int. J. Mech. Sci.* **2013**, *73*, 69–76. [[CrossRef](#)]

28. Florio, B.J.; Vynnycky, M.; Mitchell, S.L.; O'Brien, S.B.G. Mould-taper asymptotics and air gap formation in continuous casting. *Appl. Math. Comput.* **2015**, *268*, 1122–1139. [[CrossRef](#)]
29. Florio, B.J.; Vynnycky, M.; Mitchell, S.L.; O'Brien, S.B.G. On the interactive effects of mould taper and superheat on air gaps in continuous casting. *Acta Mech.* **2017**, *228*, 233–254. [[CrossRef](#)]
30. Vynnycky, M.; Saleem, S.; Devine, K.M.; Florio, B.J.; Mitchell, S.L.; O'Brien, S.B.G. On the formation of fold-type oscillation marks in the continuous casting of steel. *R. Soc. Open Sci.* **2017**, *4*, 176002. [[CrossRef](#)] [[PubMed](#)]
31. Vynnycky, M. On an anomaly in the modeling of electromagnetic stirring in continuous casting. *Metall. Mater. Trans. B* **2018**, *49B*, 399–410. [[CrossRef](#)]
32. Vynnycky, M.; Zambrano, M. Towards a “moving-point” formulation for the modelling of oscillation-mark formation in the continuous casting of steel. *Appl. Math. Mod.* **2018**, *63*, 243–265. [[CrossRef](#)]
33. Vynnycky, M. Porous-media braking of electromagnetic stirring in the continuous casting of steel. In Proceedings of the 24th ABCM International Congress of Mechanical Engineering, Curitiba, Brazil, 3–8 December 2017.
34. Mahmoudi, J.; Vynnycky, M.; Fredriksson, H. Modelling of fluid flow, heat transfer and solidification in the strip casting of a copper base alloy: (III). Solidification—A theoretical study. *Scand. J. Metall.* **2001**, *30*, 136–145. [[CrossRef](#)]
35. Mahmoudi, J.; Vynnycky, M.; Sivesson, P.; Fredriksson, H. An experimental and numerical study on the modelling of fluid flow, heat transfer and solidification in a copper continuous strip casting process. *Mater. Trans.* **2003**, *44*, 1741–1751. [[CrossRef](#)]
36. AEA Technology. *CFX 4.2 Flow Solver User Guide*; AEA Technology: Harwell, UK, 1995.
37. Swaminathan, C.R.; Voller, V.R. A general enthalpy method for modeling solidification processes. *Met. Trans. B* **1992**, *23B*, 651–664. [[CrossRef](#)]
38. Voller, V.R.; Peng, S. An enthalpy formulation based on an arbitrarily deforming mesh for solution of the Stefan problem. *Comput. Mech.* **1994**, *14*, 492–502. [[CrossRef](#)]
39. Aboutalebi, M.R.; Hasan, M.; Guthrie, R.I.L. Numerical study of coupled turbulent flow and solidification for steel slab casters. *Numer. Heat Transf.* **1995**, *28*, 279–297. [[CrossRef](#)]
40. Aboutalebi, M.R.; Hasan, M.; Guthrie, R.I.L. Coupled turbulent flow, heat and solute transport in continuous casting processes. *Metall. Mater. Trans. B* **1995**, *26*, 731–744. [[CrossRef](#)]
41. Thevik, H.J.; Mo, A.; Rusten, T. A mathematical model for surface segregation in aluminum direct chill casting. *Metall. Mater. Trans. B* **1999**, *30*, 135–142. [[CrossRef](#)]
42. Savage, J. A theory of heat transfer and air gap formation in continuous casting molds. *J. Iron Steel Inst.* **1962**, *198*, 41–47.
43. Richmond, O.; Tien, R.H. Theory of thermal stresses and air-gap formation during the early stages of solidification in a rectangular mold. *J. Mech. Phys. Solids* **1971**, *19*, 273–284. [[CrossRef](#)]
44. Kristiansson, J.O. Thermal stresses in the early stage of the solidification of steel. *J. Therm. Stresses* **1982**, *5*, 315–330. [[CrossRef](#)]
45. Tien, R.H.; Richmond, O. Theory of maximum tensile stresses in the solidifying shell of a constrained regular casting. *J. Appl. Mech.* **1982**, *49*, 481–486. [[CrossRef](#)]
46. Kim, K.Y. Analysis of gap formation at mold-shell interface during solidification of aluminium alloy plate. *ISIJ Int.* **2003**, *43*, 647–652. [[CrossRef](#)]
47. Kelly, J.E.; Michalek, K.P.; O'Connor, T.G.; Thomas, B.G.; Dantzig, J.A. Initial development of thermal and stress fields in continuously cast steel billets. *Metall. Mater. Trans. A* **1988**, *19A*, 2589–2602. [[CrossRef](#)]
48. Grill, A.; Sorimachi, K.; Brimacombe, J.K. Heat flow, gap formation and break-outs in the continuous casting of steel slabs. *Metall. Mater. Trans. B* **1976**, *7B*, 177–189. [[CrossRef](#)]
49. Bellet, M.; Decultieux, F.; Menai, M.; Bay, F.; Levaillant, C.; Chenot, J.L.; Schmidt, P.; Svensson, I.L. Thermomechanics of the cooling stage in casting processes: Three-dimensional finite element analysis and experimental validation. *Metall. Mater. Trans. B* **1996**, *27*, 81–99. [[CrossRef](#)]
50. Huespe, A.E.; Cardona, A.; Fachinotti, V. Thermomechanical model of a continuous casting process. *Comput. Methods Appl. Mech. Eng.* **2000**, *182*, 439–455. [[CrossRef](#)]

51. Li, C.; Thomas, B.G. Thermomechanical finite-element model of shell behavior in continuous casting of steel. *Metall. Mater. Trans. B* **2004**, *35B*, 1151–1172. [[CrossRef](#)]
52. Sun, D.; Annapragada, S.R.; Garimella, S.V.; Singh, S.K. Analysis of gap formation in the casting of energetic materials. *Numer. Heat Transf.* **2007**, *51*, 415–444. [[CrossRef](#)]
53. Saleem, S. On the Surface Quality of Continuously Cast Steels and Phosphor Bronzes. Ph.D. Thesis, KTH Royal Institute of Technology, Stockholm, Sweden, 2016.
54. Saleem, S.; Vynnycky, M.; Fredriksson, H. A study of the oscillation marks' characteristics of continuously cast Incoloy alloy 825 blooms. *Metall. Mater. Trans. A* **2016**, *47*, 4068–4079. [[CrossRef](#)]
55. Takeuchi, E.; Brimacombe, J.K. The formation of oscillation marks in the continuous casting of steel slabs. *Metall. Mater. Trans. B* **1984**, *15*, 493–509. [[CrossRef](#)]
56. Jonayat, A.S.M.; Thomas, B.G. Transient thermo-fluid model of meniscus behavior and slag consumption in steel continuous casting. *Metall. Mater. Trans. A* **2014**, *45*, 1842–1864. [[CrossRef](#)]
57. Tomono, H. Elements of Oscillation Mark Formation and Their Effect on Transverse Fine Cracks in Continuous Casting of Steel. Ph.D. Thesis, École Polytechnique Fédérale de Lausanne, Lausanne, Switzerland, 1979.
58. Ramirez-Lopez, P.E.; Lee, P.D.; Mills, K.C. Explicit modelling of slag infiltration and shell formation during mould oscillation in continuous casting. *ISIJ Int.* **2010**, *50*, 425–434. [[CrossRef](#)]
59. Ramirez-Lopez, P.E.; Lee, P.D.; Mills, K.C.; Santillana, B. A new approach for modelling slag infiltration and solidification in a continuous casting mould. *ISIJ Int.* **2010**, *50*, 1797–1804. [[CrossRef](#)]
60. Lee, P.D.; Ramirez-Lopez, P.E.; Mills, K.C.; Santillana, B. Review: The “butterfly effect” in continuous casting. *Ironmak. Steelmak.* **2012**, *39*, 244–253. [[CrossRef](#)]
61. Ramirez-Lopez, P.E.; Mills, K.C.; Lee, P.D.; Santillana, B. A unified mechanism for the formation of oscillation marks. *Metall. Mater. Trans. B* **2012**, *43B*, 109–122. [[CrossRef](#)]
62. Bikerman, J.J. *Physical Surfaces*; Academic Press: New York, NY, USA, 1970.
63. Flemings, M.C.; Nereo, G.E. Macrosegregation. I. *AIME Met. Soc. Trans.* **1967**, *239*, 1449–1461.
64. Flemings, M.C.; Mehrabian, R.; Nereo, G.E. Macrosegregation. PT. 2. *AIME Met. Soc. Trans.* **1968**, *242*, 41–49.
65. Reddy, A.V.; Beckermann, C. Modeling of macrosegregation due to thermosolutal convection and contraction-driven flow in direct chill continuous casting of an Al-Cu round ingot. *Metall. Mater. Trans. B* **1997**, *28*, 479–489. [[CrossRef](#)]
66. Saleem, S.; Vynnycky, M.; Fredriksson, H. Formation of the tin rich layer and inverse segregation in phosphor bronzes during continuous casting. In Proceedings of the Minerals, Metals and Materials Society (TMS) 2015: 144th Annual Meeting and Exhibition, Orlando, FL, USA, 15–19 March 2015; pp. 15–22.
67. Diao, Q.Z.; Tsai, H.L. Modelling of solute redistribution in the mushy zone during solidification of aluminium-copper alloys. *Metall. Trans.* **1993**, *24A*, 963–973. [[CrossRef](#)]
68. Chen, J.H.; Tsai, H.L. Inverse segregation for a unidirectional solidification of aluminium-copper alloys. *Int. J. Heat Mass Transf.* **1993**, *36*, 3069–3075. [[CrossRef](#)]
69. Diao, Q.Z.; Tsai, H.L. The formation of negative- and positive-segregated bands during solidification of aluminum-copper alloys. *Int. J. Heat Mass Transf.* **1993**, *36*, 4299–4305. [[CrossRef](#)]
70. Mo, A. Mathematical modelling of surface segregation in aluminum DC casting caused by exudation. *Int. J. Heat Mass Transf.* **1993**, *36*, 4335–4340. [[CrossRef](#)]
71. Voller, V.R.; Sundarraj, S. A model of inverse segregation: The role of microporosity. *Int. J. Heat Mass Transf.* **1995**, *38*, 1009–1018. [[CrossRef](#)]
72. Minakawa, S.; Samarasekera, I.V.; Weinberg, F. Inverse segregation. *Metall. Trans.* **1985**, *16*, 595–604. [[CrossRef](#)]
73. Du, Q.; Eskin, D.G.; Katgerman, L. Numerical issues in modelling macrosegregation during DC casting of a multi-component aluminium alloy. *Int. J. Numer. Methods Heat Fluid Flow* **2009**, *19*, 917–930. [[CrossRef](#)]
74. Jalanti, T.; Swierkosz, M.; Gremaud, M.; Rappaz, M. Modelling of macrosegregation in continuous casting of aluminium. In *Continuous Casting*; Ehrke, K., Schneider, W., Eds.; WILEY-VCH Verlag GmbH: Weinheim, Germany, 2006; pp. 191–198.
75. Založnik, M.; Xin, S.; Šarler, B. Verification of a numerical model of macrosegregation in direct chill casting. *Int. J. Numer. Methods Heat Fluid Flow* **2008**, *18*, 308–324. [[CrossRef](#)]

76. Venneker, B.C.H.; Katgerman, L. Modelling issues in macrosegregation predictions in direct chill castings. *J. Light Met.* **2002**, *2*, 149–159. [[CrossRef](#)]
77. Eskin, D.G.; Zuidema, J.; Savran, V.I.; Katgerman, L. Structure formation and macrosegregation under different process conditions during DC casting. *Mater. Sci. Eng. A* **2004**, *384*, 232–244. [[CrossRef](#)]
78. Eskin, D.G.; Du, Q.; Katgerman, L. Relationship between shrinkage-induced macrosegregation and the sump profile upon direct-chill casting. *Scr. Mater.* **2006**, *55*, 715–718. [[CrossRef](#)]
79. Du, Q.; Eskin, D.G.; Katgerman, L. Modeling macrosegregation during direct-chill casting of multicomponent aluminum alloys. *Metall. Mater. Trans. A* **2007**, *38A*, 180–189. [[CrossRef](#)]
80. Jalanti, T. Etude et Modélisation de la Macroségrégation dans la Coulée Semi-Continue des Alliages d'Aluminium. Ph.D. Thesis, École Polytechnique Fédérale de Lausanne, Lausanne, Switzerland, 2000.
81. Fredriksson, H.; Åkerlind, U. *Materials Processing during Casting*; Wiley: Chichester, UK, 2006.
82. Tzavaras, A.A.; Brody, H.D. Electromagnetic stirring and continuous-casting—Achievements, problems, and goals. *J. Met.* **1984**, *36*, 31–37. [[CrossRef](#)]
83. Spitzer, K.H.; Dubke, M.; Schwerdtfeger, K. Rotational electromagnetic stirring in continuous-casting of round strands. *Metall. Mater. Trans. B* **1986**, *17*, 119–131. [[CrossRef](#)]
84. Dubke, M.; Tacke, K.H.; Spitzer, K.H.; Schwerdtfeger, K. Flow fields in electromagnetic stirring of rectangular strands with linear inductors: Part I. Theory and experiments with cold models. *Metall. Mater. Trans. B* **1988**, *19B*, 581–593. [[CrossRef](#)]
85. Dubke, M.; Tacke, K.H.; Spitzer, K.H.; Schwerdtfeger, K. Flow fields in electromagnetic stirring of rectangular strands with linear inductors: Part II. Computation of flow fields in billets, blooms, and slabs of steel. *Metall. Mater. Trans. B* **1988**, *19*, 595–602. [[CrossRef](#)]
86. Dubke, M.; Spitzer, K.H.; Schwerdtfeger, K. Spatial-distribution of magnetic-field of linear inductors used for electromagnetic stirring in continuous-casting of steel. *Ironmak. Steelmak.* **1991**, *18*, 347–353.
87. Tacke, K.H.; Grill, A.; Miyazawa, K.; Schwerdtfeger, K. Macroscgregation in strand cast steel—Computation of concentration profiles with a diffusion-model. *Arch. Eisenhüttenw.* **1981**, *52*, 15–20. [[CrossRef](#)]
88. Tacke, K.H.; Schwerdtfeger, K. Stirring velocities in continuously cast round billets as induced with rotating electromagnetic-fields. *Stahl und Eisen* **1979**, *99*, 7–12.
89. Zhang, C.; Shatrov, V.; Priede, J.; Eckert, S.; Gerbeth, G. Intermittent behavior caused by surface oxidation in a liquid metal flow driven by a rotating magnetic field. *Metall. Mater. Trans. B* **2011**, *42*, 1188–1200. [[CrossRef](#)]
90. Liu, H.; Xu, M.; Qiu, S.; Zhang, H. Numerical simulation of fluid flow in a round bloom mold with in-mold rotary electromagnetic stirring. *Metall. Mater. Trans. B* **2012**, *43*, 1657–1675. [[CrossRef](#)]
91. Yang, J.; Xie, Z.; Ning, J.; Liu, W.; Ji, Z. A framework for soft sensing of liquid pool length of continuous casting round blooms. *Metall. Mater. Trans. B* **2014**, *45*, 1545–1556. [[CrossRef](#)]
92. Poole, G.M.; Heyen, M.; Nastac, L.; El-Kaddah, N. Numerical modeling of macrosegregation in binary alloys solidifying in the presence of electromagnetic stirring. *Metall. Mater. Trans. B* **2014**, *45*, 1834–1841. [[CrossRef](#)]
93. Ren, B.Z.; Chen, D.F.; Wang, H.D.; Long, M.J.; Han, Z.W. Numerical simulation of fluid flow and solidification in bloom continuous casting mould with electromagnetic stirring. *Ironmak. Steelmak.* **2015**, *42*, 401–408. [[CrossRef](#)]
94. Fang, Q.; Ni, H.; Zhang, H.; Wang, B.; Lv, Z. The effects of a submerged entry nozzle on flow and initial solidification in a continuous casting bloom mold with electromagnetic stirring. *Metals* **2017**, *7*, 146. [[CrossRef](#)]
95. Wang, X.; Fautrelle, Y.; Etay, J.; Moreau, R. A periodically reversed flow driven by a modulated traveling magnetic field: Part I. Experiments with GaInSn. *Metall. Mater. Trans. B* **2009**, *40*, 82–90. [[CrossRef](#)]
96. Eckert, S.; Nikrityuk, P.A.; Raebiger, D.; Eckert, K.; Gerbeth, G. Efficient melt stirring using pulse sequences of a rotating magnetic field: Part I. Flow field in a liquid metal column. *Metall. Mater. Trans. B* **2007**, *38*, 977–988. [[CrossRef](#)]
97. Beitelman, L.S.; Curran, C.P.; Lavers, J.D.; Tallback, G. Modulated Electromagnetic Stirring of Metals at Advanced Stage of Solidification. EP Patent EP080783247, 22 August 2011.
98. Versteeg, H.; Malalasekera, W. *An Introduction to Computational Fluid Dynamics: The Finite Volume Method*, 2nd ed.; Pearson: Harlow, UK, 2007.
99. Bridge, M.R.; Rogers, G.D. Structural effects and band segregate formation during the electromagnetic stirring of strand-cast steel. *Met. Trans. B* **1984**, *15*, 581–589. [[CrossRef](#)]

100. Kor, G.J.W. Influence of circumferential electromagnetic stirring on macrosegregation in steel. *Ironmak. Steelmak.* **1982**, *9*, 244–251.
101. M'Hamdi, M.; Håkonsen, A. Experimental and numerical study of surface macrosegregation in DC casting of aluminium sheet ingots. In *Modeling of Casting, Welding and Advanced Solidification Processes-X, Proceedings of the 10th International Conference on Modeling of Casting, Welding and Advanced Solidification Processes, Destin, FL, USA, 25–30 May 2003*; Stefanescu, D.M., Warren, J.A., Jolly, M.R., Krane, M.J.M., Eds.; Minerals, Metals & Materials Soc.: Warrendale, PA, USA, 2003; pp. 505–512.
102. Haug, E.; Mo, A.; Thevik, H.J. Macrosegregation near a cast surface caused by exudation and solidification shrinkage. *Int. J. Heat Mass Transf.* **1995**, *38*, 1553–1563. [[CrossRef](#)]
103. Luo, Y.Z.; Zhang, J.M.; Wei, X.D.; Xiao, C.; Hu, Z.F.; Yuan, Y.Y.; Chen, S.D. Numerical simulation of solidification structure of high carbon SWRH77B billet based on the CAFE method. *Ironmak. Steelmak.* **2012**, *39*, 26–30. [[CrossRef](#)]
104. Luo, S.; Zhu, M.; Louhenkilpi, S. Numerical simulation of solidification structure of high carbon steel in continuous casting using cellular automaton method. *ISIJ Int.* **2012**, *52*, 823–830. [[CrossRef](#)]
105. Wang, W.; Ji, C.; Luo, S.; Zhu, M. Modeling of dendritic evolution of continuously cast steel billet with cellular automaton. *Metall. Mater. Trans. B* **2018**, *49*, 200–212. [[CrossRef](#)]
106. Guan, R.; Ji, C.; Zhu, M.; Deng, S. Numerical simulation of V-shaped segregation in continuous casting blooms based on a microsegregation model. *Metall. Mater. Trans. B* **2018**, *49*, 2571–2583. [[CrossRef](#)]
107. Lee, P.; Chirazi, A.; See, D. Modeling microporosity in aluminum-silicon alloys: A review. *J. Light Met.* **2001**, *1*, 15–30. [[CrossRef](#)]
108. Dantzig, J.A.; Rappaz, M. *Solidification*; EPFL Press: Lausanne, Switzerland, 2009.
109. Stefanescu, D.M. Computer simulation of shrinkage related defects in metal castings—A review. *Int. J. Cast Met. Res.* **2005**, *18*, 129–143. [[CrossRef](#)]
110. Du, P. Numerical Modeling of Porosity and Macrosegregation in Continuous Casting of Steel. Ph.D. Thesis, University of Iowa, Iowa City, IA, USA, 2013.
111. Rogberg, B.; Ek, L. Influence of soft reduction on the fluid flow, porosity and center segregation in CC high carbon- and stainless steel blooms. *ISIJ Int.* **2018**, *58*, 478–487. [[CrossRef](#)]
112. Domitner, J.; Wu, M.; Kharicha, A.; Ludwig, A.; Kaufmann, B.; Reiter, J.; Schaden, T. Modeling the effects of strand surface bulging and mechanical softreduction on the macrosegregation formation in steel continuous casting. *Metall. Mater. Trans. A* **2014**, *45*, 1415–1434. [[CrossRef](#)]
113. Mayer, F.; Wu, M.; Ludwig, A. On the formation of centreline segregation in continuous slab casting of steel due to bulging and/or feeding. *Steel Res. Int.* **2010**, *81*, 660–667. [[CrossRef](#)]
114. Saleem, S.; Vynnycky, M.; Fredriksson, H. The influence of peritectic reaction/transformation on crack susceptibility in the continuous casting of steels. *Metall. Mater. Trans. B* **2017**, *48*, 1625–1635. [[CrossRef](#)]
115. Sun, H.; Zhang, J. Study on the macrosegregation behavior for the bloom continuous casting: Model development and validation. *Metall. Mater. Trans. B* **2014**, *45B*, 1133–1149. [[CrossRef](#)]
116. Hurtuk, D.J.; Tzavaras, A.A. Some effects of electromagnetically induced fluid-flow on macrosegregation in continuously cast steel. *Metall. Trans. B Proc. Met.* **1977**, *8*, 243–251. [[CrossRef](#)]
117. Sasaki, K.; Sugitani, Y.; Kobayashi, S.; Ishimura, S. The effect of fluid flow on the formation of the negative segregation zone in steel ingots. *Tetsu Hagane* **1979**, *65*, 60–69. [[CrossRef](#)]
118. Vynnycky, M.; Shugai, G.; Yakubenko, P.; Mellgren, N. Asymptotic reduction for numerical modeling of polymer electrolyte fuel cells. *SIAM J. Appl. Math.* **2009**, *70*, 455–487. [[CrossRef](#)]
119. Ly, H.; Birgersson, E.; Vynnycky, M.; Sasmito, A.P. Validated reduction and accelerated numerical computation of a model for the proton exchange membrane fuel cell. *J. Electrochem. Soc.* **2009**, *156*, B1156–B1168. [[CrossRef](#)]
120. Ly, H.; Birgersson, E.; Vynnycky, M. Asymptotically reduced model for a proton exchange membrane fuel cell stack: Automated model generation and verification. *J. Electrochem. Soc.* **2010**, *157*, B982–B992. [[CrossRef](#)]
121. Ly, H.; Birgersson, E.; Vynnycky, M. Computationally efficient multi-phase models for a proton exchange membrane fuel cell: Asymptotic reduction and thermal decoupling. *Int. J. Hydrog. Energy* **2011**, *36*, 14573–14589. [[CrossRef](#)]

122. Vynnycky, M.; Sharma, A.K.; Birgersson, E. A finite-element method for the weakly compressible parabolized steady 3D Navier-Stokes equations in a channel with a permeable wall. *Comput. Fluids* **2013**, *81*, 152–161. [[CrossRef](#)]
123. Sharma, A.K.; Birgersson, E.; Vynnycky, M. Towards computationally-efficient modeling of transport phenomena in three-dimensional monolithic channels. *Appl. Math. Comput.* **2015**, *254*, 392–407. [[CrossRef](#)]



© 2018 by the author. Licensee MDPI, Basel, Switzerland. This article is an open access article distributed under the terms and conditions of the Creative Commons Attribution (CC BY) license (<http://creativecommons.org/licenses/by/4.0/>).

MDPI
St. Alban-Anlage 66
4052 Basel
Switzerland
Tel. +41 61 683 77 34
Fax +41 61 302 89 18
www.mdpi.com

Metals Editorial Office
E-mail: metals@mdpi.com
www.mdpi.com/journal/metals



MDPI
St. Alban-Anlage 66
4052 Basel
Switzerland

Tel: +41 61 683 77 34
Fax: +41 61 302 89 18

www.mdpi.com



ISBN 978-3-03921-322-1